Title
Dust and Black Carbon Radiative Forcing Controls on Snowmelt in the Colorado River Basin

Author
Skiles, Sara McKenzie

Publication Date
2014

Peer reviewed|Thesis/dissertation

UNIVERSITY OF CALIFORNIA

Los Angeles

Dust and Black Carbon Radiative Forcing Controls on Snowmelt in the Colorado River Basin

A dissertation submitted in partial satisfaction of the

requirements for the degree of Doctor of Philosophy

in Geography

by

Sara McKenzie Skiles

2014

ABSTRACT OF THE DISSERTATION

Dust and Black Carbon Radiative Forcing Controls on Snowmelt in the Colorado River Basin

by

Sara McKenzie Skiles

Doctor of Philosophy in Geography

University of California, Los Angeles, 2014

Professor Gregory S. Okin, Chair

Light absorbing impurities (LAIs), like dust and black carbon (BC), initiate powerful albedo feedbacks when deposited on snow cover, yet due to a scarcity of observations radiative forcing by LAIs is often neglected, or poorly constrained, in climate and hydrological models. This has important consequences for regions like the Colorado River Basin, where dust deposition to mountain snow cover frequently occurs in the upper basin in the springtime, a relatively new phenomenon since western expansion of the US. Previous work showed that dust on snow (DOS) enhances snowmelt by 3-7 weeks, shifts timing and intensity of runoff, and reduces total water yield.

Here, advanced methods are presented to measure, model, and monitor DOS in the hydrologically sensitive Colorado River Basin. A multi-year multi-site spatial variability analysis indicates the heaviest dust loading comes from point sources in the southern Colorado Plateau, but also shows that lower levels of dust loading from diffuse sources still advances melt by 3-4 weeks. A high-resolution snow property dataset,

including vertically resolved measurements of snow optical grain size and dust/BC concentrations, confirms that impurity layers remain in the layer in which they are deposited and converge at the surface as snow melts: influencing snow properties, rapidly reducing snow albedo, and increasing snowmelt rates. The optical properties of deposited impurities, which are mainly dust, are determined using an inversion technique from measurements of hemispherical reflectance and particle size distributions. Using updated optical properties in the snow+aerosols radiative transfer model SNICAR improves snow albedo modeling over a more general dust characterization, reducing errors by 50% across the full range of snow reflectance. Radiative forcing by LAIs in the CRB, estimated directly from measurements and updated optical properties, is most strongly controlled by dust concentrations in the uppermost surface layer, as dust comprises 99%+ of the impurity mixture, and therefore, dominates absorption. Coupling the physically based snow model SNOWPACK, modified to track dust layers, to SNICAR, simulates the impacts of DOS radiative forcing on snow properties. This improved understanding, and representation, of DOS processes has important implications for assessing regional impacts of LAIs, for representing LAIs in climate and hydrologic models, for remote sensing of these processes.

The dissertation of Sara McKenzie Skiles is approved.

Laurence Smith

Yongkang Xue

Steven A. Margulis

Thomas H. Painter

Gregory S. Okin, Committee Chair

University of California, Los Angeles

2014

Dedications

To Tom Painter, for believing in me, funding me, and paving the way for me to become what every half motivated ski bum dreams of- a legitimate snow scientist. Words cannot express my appreciation for what you have taught me, and the opportunities you have provided.

To my family:

My father, the most amazing man I have ever known, for giving us puzzles instead of toys, spending summer vacations in tents instead of hotels, and for eating out of coolers instead of at restaurants. For instilling in us our wanderlust, curiosity, and sense of adventure (not to mention, a deep and enduring love of science fiction and a healthy appreciation for math). For always trusting my sometimes questionable decision making, and never letting me believe I was not capable of achieving my goals. And for my stepmom Molly, for creating a home for us, for making Dad a very happy man, and for dropping everything to take care of him when he needed it most.

My mother, for giving us a childhood in Alaska and teaching us to ski, hike, bike and love the outdoors. For making us kind hearted and open minded. For putting up with our shenanigans and always taking our side (unless, of course, it was in our best interest to not take our side). For going it alone, enduring, and coming out the side with six productive and self-sufficient human beings. It wasn't always easy, but smooth waters do not a good sailor make.

My brother Seth, for getting me into trouble, and getting me out of it, for camping trips, forest fairs, train ride and cruises, and the pirate summer. For always putting everyone else first, no matter what. My sister Sadie, for supporting me for an entire

summer before college (even though we slept on a mattress on the floor, and ate only potatoes and oatmeal), for knowing enough Spanish to not get us kidnapped by a drug cartel in Central America, and for bikes, beers, and baking. Cierra, my beautiful baby sister, for her bright eyes and kind heart, and adorable texts at just the right moment. Chris and Connor, for letting me treat them like baby brothers, even though they have long since grown taller than me.

To Ralph Patterson, for producing and mentoring a whole gaggle of official, and unofficial, but always thirsty, snow scientist. And for Jodi Patterson, for putting up with said crowd and letting me sleep upstairs when the scotch bottle was bottomless. And, for Leah and Kris, for also loving snow enough to be teaching assistants with only knowledge for compensation, and by knowledge, I mean beer. We had a good run.

To Phylis and Eric Fagrelius, first, for willingly housing an unknown graduate student, and then, for being the most fun people ever. Thanks for the gin and tonics, Glee nights, blues and brews, freezer space, and for being my Ouray family.

To Jeff Deems, for being patient enough to do fieldwork with a splitboarder. For hikes, bike rides, beers, and sanity (and help with research, of course).

And last, but not least, to Tom Ghelli, my love and partner in crime, for well timed camping trips to Moab, for being my personal mechanic, for moving to California, and for ski tours, dog walks, and mountain bike rides. And our dogs, Yuko and Molly, for frequently rousing me from a dissertation trance with demands for walks and food, for sleeping under the desk and keeping my feet warm, and for endless affection and adoration.

Table of Contents

Chapter 2

A high-resolution snow property dataset including surface albedo and vertically resolved measurements of snow optical grain size and LAI concentrations

List of Figures

Introduction

Chapter 1

Chapter 2

Chapter 3

Chapter 4

Chapter 5

List of Tables

Acknowledgements

Chapter 1 is a version of Skiles, S.M., T.H. Painter, J. Belnap, J. Li, L. Holland. Spatial variability in dust-on snow processes and impacts: a multi-year multi-site study in the Colorado River Basin. In preparation for submission to Hydrologic Processes, 2014.

Skiles processed and analyzed the data and wrote the paper. Li and Holland carried out STILT model runs. Painter and Belnap funded and advised the work.

Chapter 2 is a version of Skiles, S.M., T.H. Painter. Light Absorbing Impurities in Snow: Monitoring temporal variability in surface dust loading, black carbon content, grain size, and albedo. In preparation for submission to Journal of Glaciology, 2014.

Skiles collected, processed, and analyzed data and wrote the paper. Painter funded and advised the work. Ian Delaney and Jeff Deems (not co-authors) are acknowledged for fieldwork assistance.

Chapter 3 is a version of Skiles, S.M., T.H. Painter, G. Okin, A method to retrieve the imaginary part of the complex refractive index and single scattering optical properties of dust deposited in mountain snow cover. In preparation for submission to Journal of Glaciology, 2014.

Skiles implemented the method, carried out the analysis, and wrote the paper. Painter and Okin funded and advised the work.

Chapter 4 is a version of Skiles, S.M., T.H. Painter. Light Absorbing Impurities in Snow: Modeling the evolution in radiative forcing by dust and black carbon over an ablation season. In preparation for submission to Journal of Glaciology, 2014.

Skiles carried out the analysis and wrote the paper. Painter funded and advised the work.

Chapter 5 is a version of Skiles, S.M., T.H. Painter. Coupling a physically based snowmelt model and radiative transfer model to track dust stratigraphy and changes in surface albedo during snow ablation. In preparation for submission to Geophysical Research Letters, 2014.

Skiles implemented model coupling, analyzed results, and wrote the paper. Painter funded and advised the work.

This work was funded by the NASA project NNX10AO97G. Part of this work was performed at the Jet Propulsion Laboratory, California Institute of Technology under a contract from NASA.

Curriculum Vitae

2008 B.S., *Geography*, University of Utah

2008 B.S., *Environmental Studies*, University of Utah

2008 GIS Certificate, University of Utah

2010 M.S., *Geography*, University of Utah

Publications

Masters Thesis

Interannual Variability in Radiative Forcing by Desert Dust in Snowcover in the Colorado River Basin. *University of Utah*, 2010.

Conference Proceedings

Skiles, S.M., T.H. Painter. 2014. A 9-yr record of dust-on-snow in the Colorado River Basin, *Proceedings of the 12th Biennial Conference of Science and Management on the Colorado Plateau (2013)*.

Journal Articles

Painter, T.H., **S.M. Skiles**, J. Deems, C. C. Landry, Dust Radiative Forcing in snow of the Upper Colorado River Basin: Part I. 2012. A 6 year record of energy balance, radiation, and dust concentrations. *Water Resources Research.* 48, W07521, doi:10.1029/2012WR011985.

Skiles, S.M., T. H. Painter, J. Deems, C. C. Landry, 2012. Dust Radiative Forcing in snow of the Upper Colorado River Basin: Part II. Interannual variability in radiative forcing and snowmelt rates. *Water Resources Research*. 48, W07522, doi:10.1029/2012WR011986.

Painter, T. H., A. C. Bryant, **S.M. Skiles**. 2013. Radiative Forcing by light absorbing impurities in snow from MODIS surface reflectance data, *Geophysical Research Letters*, 39, L17502, doi:10.1029/2012GL052457.

Painter, T. H., F. Seidel, A.C. Bryant, **S.M. Skiles**, K. Rittger. 2013. Imaging Spectroscopy of albedo and radiative forcing by light-absorbing impurities in mountain snow, *Journal of Geophysical Research: Atmospheres*, 118(17), doi: 10.1002/jgrd.50520.

Reynolds, R.L., H. L. Goldstein, B. M. Moskowitz, **S. M. Skiles**, R.F. Kokaly, C.B. Flagg, K. Yauk, T. Berquó, G. Breit, M. Ketterer, D. Fernandez, M.E. Miller, T.H. Painter. 2013. Composition of dust deposited to snow cover in the Wasatch Range (Utah, USA): Controls on radiative properties and snow cover and comparison to some dust source sediments, *Aeolian Research*, doi: 10.1016/j.aeolia.2013.08.001.

Li, J., G.S. Okin, **S.M. Skiles**, T.H. Painter. 2013. Relating variation of dust on snow to bare soil dynamics in the western United States, *Environmental Research Letters*, 8(4), doi: 10.1088/1748-9326/8/4/044054.

Kaspari, S., T.H. Painter, M. Gysel, **S.M. Skiles**, M. Schwikowski, 2014. Seasonal and elevational variations of black carbon and dust in snow an ice in the Solu-Khumbu, Nepal and estimated radiative forcings, *Atmospheric Chemistry and Physics*, 13, doi:10.5194/acpd-13-33491-2013.

Oaida, C., Y. Xue, M. Flanner, **S.M. Skiles**, F. De Sales, T.H. Painter. 2014. Investigating Physical Snow Processes Including Aerosols Using An Enhanced WRF/SSiB Model. *Submitted to Journal of Geophysical Research – Atmospheres.*

Awards

American Geophysical Union (AGU) Outstanding Student Paper Award, 2010.

Water Resources Research Editor' Choice Award, *Skiles et al*., 2012.

UCLA Department of Geography Graduate Student Publication Award, *Skiles et al*., 2012.

Introduction

Snow is a unique and important land cover type that, in addition to its contribution to climate through its high albedo and low thermal conductivity, acts as a natural fresh water reservoir, storing water in mountains over the winter months for release in the spring and summer. This is an important process that dominates regional hydrology in many locations and provides water resources to $1/6^{th}$ of the world's population [*Barnett et al.*, 2008]. In addition to supplying water for drinking, agriculture, and hydropower snow cover also influences local ecology [*Steltzer et al.*, 2009] and forest fire regimes [*Westerling et al.*, 2006]. The economic value of adequate and clean water is already high and will continue to increase, and as the world faces a warming climate, growing populations, and wide spread land use change, accurate knowledge of water resources held in the form of snow in mountain environments will grow in demand [*Bales et al.*, 2006].

In recent decades, the ability to monitor and model trends in mountain snow cover has advanced with improved *in situ* observations, expanded remote sensing capability, and increased computation capability that has facilitated physically based modeling and data assimilation. This has led to an improved understanding of snow energy balance, and particularly snow albedo; the property that describes how much solar radiation is reflected by the snow surface. Snow can have the highest albedo of any naturally occurring surface, reflecting up to 90% of incoming solar radiation when first deposited, and even slight changes in albedo have a large impact on snow cover evolution.

Reduction of snow albedo is controlled mainly by light absorbing impurity (LAI) content and snow grain size. Of the two, the greater impact can come from LAIs because

they first impact the visible wavelengths (VIS) where half of at-surface solar irradiance occurs. In these wavelengths, ice is transparent and even small amounts of dark impurities act to increase absorption (Figure 1). The impact due to grain size comes in the near infrared (NIR) wavelengths where ice is more absorptive; as snow grains grow the absorbing path length is increased and absorption is increased (Figure 2). When LAIs are deposited at the snow surface the energy contribution due to surface darkening enhances the rate of snow grain growth, initiating a feedback process that reduces snow albedo over the full range of snow reflectance.

Unfortunately, despite advancements in monitoring and modeling, current process simulations and model prediction of albedo evolution rely on oversimplifications and crude parameterizations of the processes. While it is well established that LAIs, like mineral dust and black carbon, reduce snow cover albedo [*Conway et al.*, 1996; *Painter et al.*, 2012b; *Warren and Wiscombe*, 1980], measurements are sparse many of the dynamics of the process remain unresolved. Model improvements require detailed quantification of impurity optical properties, layer evolution, and influence on snow microstructure. The research proposed here aims to improve how these processes are measured and modeled, in order to more accurately represent them in snow energy and mass balance models, and facilitate the ability to detect and monitor LAIs in snow from remote sensing imagery.

1. Dust on Snow in the Colorado River Basin

Understanding how LAIs impact snow cover is especially important in areas like the western US, where 70-90% of water resources come from snowmelt, and retention of mountain snow cover is a crucial component of sustaining water security. The Colorado

River is one of the most heavily allocated river ways in the world. Referred to as the lifeblood of the western US [*Christensen et al.*, 2004], it replenishes lower basin reservoirs in the spring and summer as snow melts from mountains in the upper basin. The mountain snow cover that makes up the headwaters of the Colorado River, the Rocky Mountains of Colorado, Wyoming, and New Mexico and Uintah Mountains of Utah, are at high risk for dust deposition in the spring when emission rates peak in the nearby Colorado Plateau [*Flagg et al.*, 2013; *Painter et al.*, 2012b], an erosional landscape that is one the main dust producers in North America [*Neff et al.*, 2008].

Deposited dust darkens the snow surface, lowers albedo, and increases the amount of energy available to drive snowmelt. The efficacy of dust radiative forcing is further enhanced because (1) dust deposition events mainly occur in the spring, when solar irradiance is increasing and most snow accumulation has already happened, leaving the LAI closer to sunlight, and (2) dust and larger BC particles are not entrained in melt water, so previously deposited dust layers converge at the snow surface during spring melt, thus compounding albedo reduction [*Conway et al.*, 1996]. This process is enhancing the springtime reduction in snow-covered area, shifting runoff timing and intensity, and reducing total water yield [*Painter et al.*, 2012b; *Painter et al.*, 2007; *Skiles et al.*, 2012].

2. Previous Work

Using detailed radiation measurements from two instrumentation sites within Senator Beck Basin Study Area (SBBSA), San Juan Mountains, CO (Figure 3) *Painter et al.* [2007] determined the relative contributions of changes in dust concentration and grain size to changes in snow albedo. From this partitioning the radiative forcing of dust in

snow was estimated, and in turn, the evolution of snow cover and its melt in the absence of dust was modeled. Applying this over two years *Painter et al.* [2007b] found that dust radiative forcings of 17-59 W m^{-2} advanced melt by 18-35 days.

This study was extended by *Skiles et al.* [2012] to a 6-year (2005-2010) record, over which end of year dust concentrations ranged from 0.2 mg g^{-1} (2005) to 4.6 mg g^{-1} (2009). Corresponding springtime daily radiative forcing were between 30-75 W m^{-2}, but as high as 214 W m^{-2} with hourly peaks as high as 409 W m^{-2}. The average springtime incoming solar radiation is ~ 800 W m^{-2} in this region, and dust radiative forcings that account for nearly half of the absorption of this incoming radiation are unprecedented. The results confirmed that dust in this region advances snowmelt by about four weeks on average, but also found that in an extreme dust years (2009, 2010) the impact could be as great as 6-7 weeks. In all years snowmelt runoff peaked earlier and was more intense than it would be in the absence of dust, with a doubling of snowmelt rates in the heaviest dust years.

Additionally, this study compared the relative contribution of dust radiative forcing and increasing temperatures of 2^{o} and 4^{o} C, the projected warming in the region, to enhanced melt. Higher temperatures enhanced melt in the absence of dust by 5-18 days, but in the presence of dust this impact was reduced to 0-6 days [*Skiles et al.,* 2012], a result which confirms the importance of snow albedo and the efficacy of dust radiative forcing. This lesser impact of increased temperatures is attributed to the fact that the impact comes in the sensible and longwave energy flux terms, which contribute less energy to melt than solar radiation.

The current degree of dust accelerated snowmelt is a relatively new factor in the western US, this was shown by *Neff et al.* [2008], who used proxy records of dust deposition from high-elevation lakes in the same study area. This study found that dust load levels increased by 500% above the late Holocene average; this follows the timeline of Anglo settlement of the western United States during the 19th century. The larger dust flux persisted into the early 21st century; a slight decline in the mass accumulation rate was exhibited in the early 20th century. This has been attributed to a reduction in sheep populations and perhaps the enactment of the Taylor Grazing Act of 1934, which imposed regulations that restricted grazing activities on public lands. Together these trends strongly suggests that increased accumulation rates can be attributed to disturbance of dryland soil surfaces in the western United States, especially disturbance by grazing [*Neff et al.*, 2005]. Lake sediments collected in the Uintah Mountains, Utah by *Reynolds et al.* [2010] similarly exhibited indications of alteration due to settlement of the Western US.

The historical impact of increased dust deposition on the hydrology of the Colorado River was investigated by *Painter et al.* [2010]. Radiative forcing due to dust at SBBSA was expanded to the entire basin, and then a hydrological model was run between 1916 and 2003 for pre-disturbance and post-disturbance albedo schemes [*Painter et al.*, 2010]. It was found that current dust levels shift peak runoff three weeks earlier, and due to increased evapotranspiration rates upon earlier removal of snow cover- dust has reduced total annual runoff by ~5%. The albedo parameterization for dusty snow only took into account data from lower dust years (2005-2008). *Deems et al.* [2013] updated the model runs to account for extreme dust loading (2009, 2010) and found that melt was advanced

by 6 weeks, and total annual runoff was reduced by an additional 1%, for total reduction in runoff at Lee's Ferry, AZ of 6%.

3. Current Study

The work presented here is effort to advance our understanding of dust on snow processes in the Colorado River Basin through high-resolution measurements and physically based modeling. First, a regional perspective is established by analyzing spatial variability in dust on snow processes in the Colorado River Basin. The work of *Painter et al.* [2012b; 2007] and *Skiles et al.* [2012] is expanded to include an additional study area, Grand Mesa Study Plot, established in 2009 and located 150 km to the north of SBBSA. Spatiotemporal variability in dust loading, radiative forcing, and advanced melt is analyzed over the coincident four year record (2010-2013) at GMSP and SBBSA, and additionally, back trajectory footprints are used to assess spatial variability in source region.

Next, the study focus shifts from the regional to micro scale, to investigate the physical interaction between dust and snow grains, in order to gain a better understanding of dust-in-snow dynamics, and support physically based modeling of LAI processes. Accurate modeling of radiative transfer in snow requires field measurements of snow impurities and optical snow grain size for relationship development and model validation [*Flanner et al.*, 2007], measurements of which sparse and inconsistent. Here, a dataset is presented that contains near daily measurements of snow albedo, vertically resolved dust and black carbon concentrations across the top 30 cm, and snow optical grain size stratigraphy across the full snow profile, collected over the 2013 ablation season at Swamp Angel Study Plot, the subalpine study in SBBSA.

Modeling the radiative impacts of dust deposited in snow requires knowledge of the optical properties of both dust and snow. While the optical properties of snow are fairly well established and spatially consistent, those of dust are not, and have never been determined for dust in snow, which would be region specific. Using dust filtered from snow samples at SBBSA, the effective optical properties of Colorado River Basin dust are determined with a radiative transfer inversion technique, from measurements of hemispherical dust reflectance and particle size distributions.

The vertically resolved high-resolution snow property measurement dataset and dust optical properties are used to model LAI radiative forcing directly using the snow/aerosol radiative transfer model SNICAR [*Flanner and Zender*, 2005; 2006]. Previous work has assumed that LAIs are primarily mineral dust, but measurements were not made to establish the presence or absence of black carbon, a widespread highly absorbing aerosol found in snow and ice cover all over the world. Black carbon concentrations, determined for the first time from SBBSA snow samples, are used to force unique models run for only BC, only dust, and dust+BC to investigate the radiative contribution from both dust and black carbon and partition radiative forcing ratios. Additionally, radiative forcing estimated directly from measurements are compared to radiative forcing estimated indirectly from changes in surface reflectance following the method presented in *Painter et al.* [2007].

The current study is concluded by coupling SNICAR, with CRB dust optical properties incorporated, to the physically based multi-layer snow process model SNOWPACK. The SNOWPACK model is updated to track dust mass upon deposition, and uses SNICAR to calculate the reflected shortwave radiation input at each time step

from model variables at the previous time step. SNOWPACK variables used in SNICAR include snow density, optical grain size, and dust concentrations (which is dust mass divided by snow density). An external file provides solar zenith angles. The other inputs to SNOWPACK (solar irradiance, wind speed, vapor pressure, and net longwave radiation) are taken from measurements at the SASP instrumentation tower. The impact due to dust is determined by comparing model outputs from runs that contain dust (representing observed conditions) to no dust runs (representing a clean snowpack). Compared variables include snow density, optical grain size, dust concentrations, and radiation balance. Using model outputs for individual model runs additionally allows for the partitioning of radiative forcing impacts due to direct and indirect effects, i.e. substituting clean snow grain size into dust model runs, to determine the impact due only to dust, and substituting dust influenced grain size into clean snow model runs, to determine the impact due only to changes in grain size.

4. Future Work and Outlook

The current work focuses on modeling processes at a point, which is useful for high-resolution method and model development, but does not inform about the surrounding heterogeneous mountain environment. Satellite platforms may bridge the gap between point measurements and spatially distributed impacts in the future. Two recent studies presented methods to quantify radiative forcing by light absorbing impurities in snow using the Airborne Visible/Infrared Imaging Spectrometer (AVIRIS) and the earth orbiting Moderate Resolution Imaging Spectrometer (MODIS) [*Painter et al.*, 2012a; *Painter et al.*, 2012b]. Both studies validated results using albedo and radiative forcing from SBBSA.

The outlook for the work presented here is to contribute to constraining and validating the algorithms that drive remote sensing retrievals, like those from the Imaging Spectrometer-Snow Albedo and Radiative Forcing (IS-SnARF) algorithm [*Painter et al.*, 2013], which is used by the Airborne Snow Observatory (ASO; www.aso.jpl.nasa.gov), a snow mapping effort by NASAs Jet Propulsion Laboratory that is currently in the demonstration phase. ASO is able to return spatially distributed snow water equivalent, grain size, albedo, and radiative forcing by impurities from the combination of a visible/near infrared imaging spectrometer and LiDAR. Currently, ASO is flying weekly in the spring over the Tuolumne River Basin, where water managers for the city of San Francisco are using retrievals to make informed decisions about water storage and release.

A platform like ASO would be ideal for monitoring the impacts LAI deposition in other, more remote regions, such as the Himalaya, where snow and glacier cover is vulnerable to LAI deposition from mid-latitude dust storms mixing with pollutant rich atmospheric brown clouds. Carrying out fieldwork in the Himalaya is logistically more difficult than that in the Western US, as snow covered areas are more remote, dangerous to access, and sample analysis is complicated by long travel times. Additionally, snow covered areas lack the necessary infrastructure to carry out detailed point based snow energy balance and snow process studies, like the work presented here. Therefore, remote sensing is the ideal method to monitor snowpack trends in these remote regions. The potential exists to not only constrain and validate retrievals using methods like the ones presented here, but also to use remote sensing retrievals as inputs for the modeling-

coupling scheme presented here, to partition radiative forcing impacts and forecast snow cover evolution between flights.

References

Barnett, T. P., et al. (2008), Human-induced changes in the hydrology of the western United States, *Science*, *319*(5866), 1080-1083.

Conway, H., A. Gades, and C. F. Raymond (1996), Albedo of dirty snow during conditions of melt, *Water Resources Research*, *32*(6), 1713-1718.

Deems, J., T. H. Painter, J. Barsugli, J. Belnap, and B. Udall (2013), Combined impacts of current and future dust deposition and regional warming on Colorado River Basin snow dynamics and hydrology, *Hydrology and Earth System Sciences Discussions*, *10*.

Flagg, C. B., J. C. Neff, R. L. Reynolds, and J. Belnap (2013), Spatial and temporal patterns of dust emissions (2004-2012) in semi-arid landscapes, southeastern Utah, USA, *Aeolian Research*.

Flanner, M. G., and C. Zender (2005), Snowpack radiative heating: Influence on the Tibetan Plateau climate, *Geophysical Research Letters*, *32*.

Flanner, M. G., and C. Zender (2006), Linking snowpack microphysics and albedo evolution, *Journal of Geophysical Research*, *111*(D12), doi:10.1029/2005JD006834.

Flanner, M. G., C. S. Zender, J. T. Randerson, and P. J. Rasch (2007), Present-day climate forcing and response from black carbon in snow, *Journal of Geophysical Research*, *112*.

Neff, J. C., R. Reynolds, J. Belnap, and P. Lamothe (2005), Multi-decadal impacts of grazing on soil physical and biogeochemical properties in Southeast Utah, *Ecological Applications*, *15*(1), 87-95.

Neff, J. C., A. P. Ballantyne, G. L. Farmer, N. M. Mahowald, J. L. Conroy, C. C. Landry, J. T. Overpeck, T. H. Painter, C. R. Lawrence, and R. L. Reynolds (2008), Increasing

eolian dust deposition in the western United States linked to human activity, *Nature Geosciences*.

Painter, T. H., A. Bryant, and S. M. Skiles (2012a), Radiative forcing by light abosrbing impurities in snow from MODIS surface reflectance data, *Geophysical Research Letters*, *39*(17).

Painter, T. H., S. M. Skiles, J. Deems, A. Bryant, and C. Landry (2012b), Dust Radiative Forcing in snow of the Upper Colorado River Basin: Part 1. A 6 year record of energy balance, radiation, and dust concentrations, *Water Resources Research*.

Painter, T. H., F. Seidel, S. M. Skiles, A. Bryant, and K. Rittger (2013), Imaging spectroscopy of albedo and radiative forcing by light absorbing impurities in mountain snow, *Journal of Geophysical Research: Atmospheres*, *118*(17).

Painter, T. H., J. S. Deems, J. Belnap, B. Udall, A. F. Hamlet, and C. C. Landry (2010), Decreased water yield from the Colorado River Basin under dust-accelerated snowmelt, *PNAS*.

Painter, T. H., A. P. Barrett, C. C. Landry, J. C. Neff, M. P. Cassidy, C. R. Lawrence, K. E. McBride, and G. L. Farmer (2007), Impact of disturbed desert soils on duration of mountain snow cover, *Geophysical Research Letters*, *34*.

Reynolds, R. L., J. S. Mordecai, J. G. Rosenbaum, M. E. Ketterer, M. K. Walsh, and K. A. Moser (2010), Compositional changes in sediments of subalpine lakes, Uinta Mountains (Utah): evidence for the effects of human activity on atmospheric dust inputs, *Journal of Paleolimnology*, *44*, 161-175.

Skiles, S. M., T. H. Painter, J. Deems, C. Landry, and A. Bryant (2012), Dust radiative forcing in snow of the Upper Colorado River Basin: Part II. Interannual variability in radiative forcing and snowmelt rates, *Water Resources Research*, *48*.

Steltzer, H., C. C. Landry, T. H. Painter, J. Anderson, and E. Ayres (2009), Dust-induced early snowmelt synchronizes phenology across an alpine landscape, *Proceedings of the National Academy of Sciences*, *106*(28), 11629-11634.

Warren, S. G., and W. J. Wiscombe (1980), A model for the spectral albedo of snow, II, Snow containing atmospheric aerosols, *J. Atmos. Sci. (USA)*, *37*(12), 2734-2745.

Westerling, A. L., H. G. Hidalgo, D. R. Cayan, and T. W. Swetnam (2006), Warming and Earlier Spring Increase Western US Forest Wildfire Activity, *Science*, *313*(5789), 940.

Figures

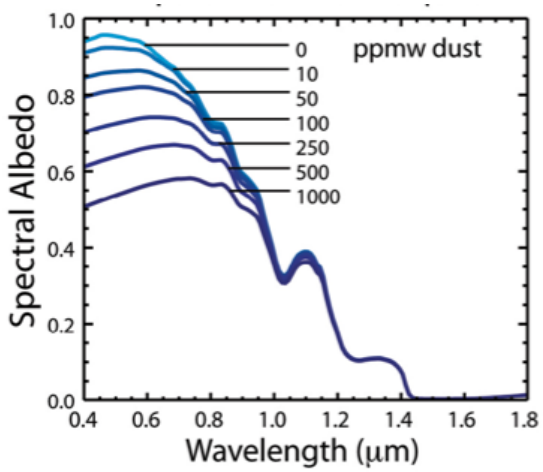

Figure 1 The impact of increasing dust concentration on albedo in the visible wavelengths.

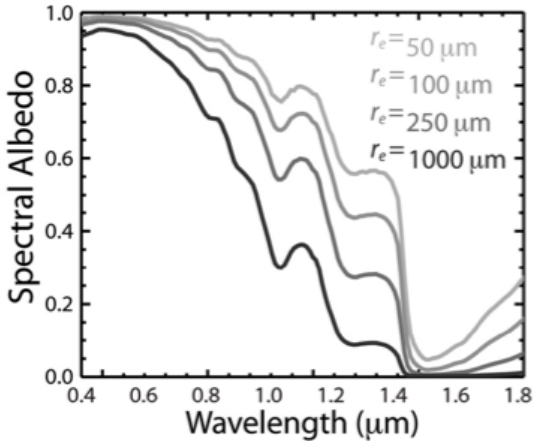

Figure 2 The impact of increasing grain size on albedo in the NIR wavelengths.

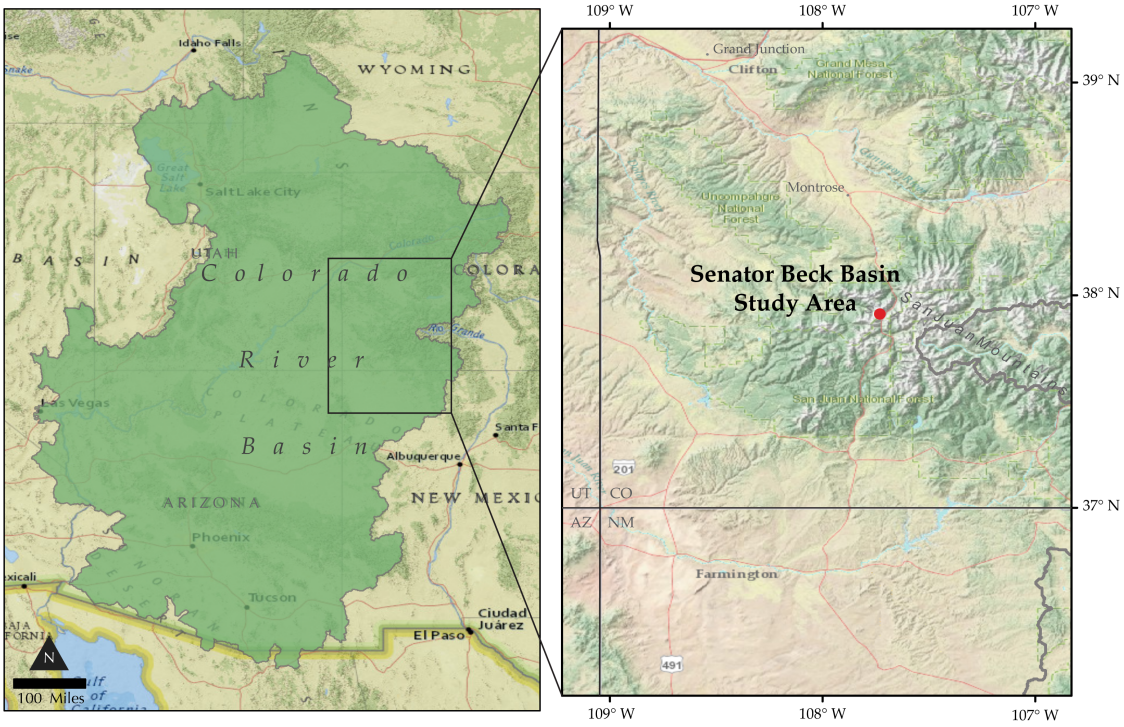

Figure 3 Overview of study region.

Chapter 1

Spatial variability in dust-on-snow processes and impacts: a multi-year multi-site study in the Colorado River Basin

Abstract

The observed level of dust loading to the mountain snow cover of the Colorado River Basin is a relatively new phenomenon, occurring only after the expansion of development in the western US in the mid 1880's. The darkening of the snow surface by mineral dust depresses snow albedo and advances melt. Interannual variability in dust deposition, dust radiative forcing, and advanced snowmelt was analyzed by *Skiles et al.* [2012] using a six-year record of dust concentration and energy balance fluxes at alpine and subalpine towers in Senator Beck Basin Study Area (SBBSA), San Juan Mountains, southwestern Colorado, USA. Dust loading enhanced springtime melt by 21 to 51 days, and was found to be more effective at advancing melt than increases in temperature of 2-4^{o} C. Here we utilize the Grand Mesa Study Plot (GMSP), established in 2009 and located 150 km to the north of SBBSA, to assess spatial variability in these processes. Snow albedo and dust stratigraphy records suggest coincident deposition timing, with some variability in source region as GMSP back-trajectory footprints are shifted to the north relative to SBBSA. End of year dust concentrations at GMSP are 0.04-2.70 mg g^{-1} less, and correspondingly, dust radiative forcing is lower in magnitude but similar in behavior with daily mean RF of 32-50 W m^{-2} advancing melt by 15-30 days. As exhibited at SBBSA dust advances melt at more than double the rate of warming temperatures; on average dust advances melt by 24 days at GMSP, while in the absence of dust, temperatures of 2-4^{o}C advanced melt by 10 days. In the presence of dust, warming temperatures are less effective, advancing melt by an additional average of four days.

1. Introduction

The semi-arid Colorado Plateau region of the western United States is an erosional landscape that is one of the main dust producers in North America, along with the Great Basin, Mojave, and Sonoran deserts [*Neff et al.,* 2008]. Biological and physical soil crusts inherently stabilize the soils in this region, but mechanical disturbance of these surfaces, from activities such as grazing, oil and gas development, and off highway vehicles decreases threshold frictional velocity below typically observed wind speeds, making sediments more available for transport [*Belnap and Gillette*, 1998]. Beginning with the disturbance of the Western US by Anglo settlement in the mid 19th century, the mountain snow cover of the Colorado River Basin (CRB) has been subject to five-fold or greater dust loading from this region [*Neff et al.*, 2008].

When deposited at the snow surface, dust accelerates snowmelt through albedo feedbacks: the darkening of the snow surface directly reduces albedo and this indirectly reduces albedo by accelerating the growth of snow effective grain size. This dust-induced snow albedo feedback advances melt, shifts timing and intensity of peak runoff, and reduces total water yield [*Deems et al.*, 2013; *Painter et al.*, 2010; *Skiles et al.*, 2012]. Recent research indicates that neglecting dust-on-snow processes may be a factor contributing to operational river runoff forecast errors in the Colorado River Basin (CRB) [*Bryant et al.*, 2013]. This has important hydrologic implications in a region where mountain snow melt is a critical resource that contributes over 70% of flow to the Colorado River, a heavily allocated waterway that provides water to seven basin states and Mexico.

Here we present detailed measurements of energy fluxes, energy balance, and dust radiative forcing at two study areas in the upper Colorado River Basin. This expands upon previous work presented in *Painter et al.* [2012b] and *Skiles et al.* [2012], a double study which assessed interannual variability in energy balance, dust loading/radiative forcing, and snowmelt runoff between 2005 and 2010 using energy balance fluxes and snow measurements from two study areas in a single basin in southwestern CO, USA. The work presented here includes an additional study area to assess spatial variability in dust-on-snow impacts for this region.

2. Previous Work

The understanding of impacts from dust-on-snow in the upper Colorado River Basin (CRB) has increased with detailed study of processes at two well-instrumented study plots in Senator Beck Basin Study Area (SBBSA) in southwestern, CO. The SBBSA was established to study and monitor the hydrologic impacts of dust-on-snow, and instrumentation suites were installed to capture snow energy balance fluxes (latent and sensible heating/ net solar and longwave radiation) to improve measurement and modeling of dust-on-snow processes. The study area, instrumentation, and data record are described in detail by *Painter et al*. [2012b].

Painter et al. [2007] utilized the first two years of data from SBBSA to isolate the effects of dust from other controls and showed that the acceleration of melt by the shortwave radiative forcing of dust resulted in a shortening of snow cover duration in this region by about a month. *Skiles et al.* [2012] expanded this analysis to assess the interannual variability in dust loading, radiative forcing, and snowmelt rates over a 6-yr record (2005-2010); mean springtime dust radiative forcing across the period ranged

from 31 to 75 W m-2 shortening snow cover duration by 21 to 51 days. The dust-advanced loss of snow cover was found to be linearly related to total dust concentration at the end of snow cover, despite temporal variability in dust exposure and solar irradiance. The advanced melt due to dust resulted in faster and earlier peak snowmelt outflow, with daily mean snowpack outflow doubling under the heaviest dust conditions. This study also compared the relative capacity of dust and warmer temperatures to advance melt and found dust efficacy to be greater: increases of 2 - 4^{o}C advanced melt by 5-18 days in the absence of dust and 0-6 days in the presence of dust.

The snow cover of the San Juan Mountains is the first high altitude point of contact for predominantly southwesterly winds transporting dust from the semi-arid landscapes of the Four Corners region (where Utah, Arizona, Colorado, and New Mexico intersect) making SBBSA an ideal location to study the impacts of dust deposition to mountain snow cover. Multiple strands of evidence point to the source region for dust-on-snow in the Colorado River Basin as the Colorado Plateau physiographic region. These include particle size and isotopic analysis of deposited dust to remote sensing imagery of dust plumes and back-trajectory analysis [*Goldstein et al.*, 2014; *Neff et al.*, 2008; *Painter et al.*, 2007]. The majority of dust deposition events at SBBSA are observed during spring (March-June), as wind speeds and dust emission are at their peak during those months [*Flagg et al.*, 2013; *Lawrence et al.*, 2010]. These events are also the most effective at initiating snow albedo feedbacks, as they coincide with increasing solar irradiance and onset of snowmelt.

Until recently the two study plots in SBBSA have been the only sites with the necessary instrumentation to facilitate modeling of the impacts of dust-on-snow in the

Colorado River Basin. A third snow energy balance site, Grand Mesa Study Plot (GMSP), located to the north of SBBSA, was installed in 2009 specifically to begin to capture variability in the dust source area within the broader Colorado Plateau emission region. In this paper, we assess spatial variability in dust-on-snow processes by comparing the 4-yr dust source, deposition, and radiative forcing record at GMSP with the SBBSA record over the same time period.

3. Methods

3.1 Study Areas and Instrumentation

The relative location of the study areas and their location within the Colorado River Basin are shown in Figure 1. Senator Beck Study Plot (SBSP) is located in the alpine tundra (3719 m) above tree line, at a level site near the center of SBBSA. Swamp Angel Study Plot (SASP) is located in the lower part of SBBSA, in a clearing below tree line in a subalpine forest at 3368 m. Grand Mesa Study Plot (GMSP) is located in an opening in a pine forest on the northern rim of the Grand Mesa in west central Colorado. At 3239 m it is only slightly lower in elevation (129 m) than SASP. All three sites consist of a snow profile plot that contains a tower holding the instrumentation array. Tower measurements include wind speed and direction (at two heights), air temperature and relative humidity (at two heights), snowpack depth, incoming and outgoing broadband and near-infrared/shortwave-infrared (NIR/SWIR) solar radiation, and incoming longwave radiation values. Incoming and outgoing visible solar radiation is calculated as the difference between the broadband and NIR/SWIR. Outgoing longwave radiation is inferred from measurement of snow surface temperature from infrared sensor. Reflected radiation measured at the towers is corrected for slope and aspect via a

hexagonal array of vertical snow depth measurement stakes deployed around the tower [*Painter et al.*, 2012b]. Study plots and instrumentation arrays are pictured in Figure 1. The main difference between the sites is precipitation measurements, which occur only at SASP. Precipitation is not measured at SBSP due to the high winds that would exacerbate undercatch, and is inferred from SASP. Precipitation at GMSP is inferred from the nearby 'Mesa Lakes' Snow Telemetry site (SNOTEL; NRCS).

3.2 Observations and Snow Sampling

The presence of airborne dust and subsequent deposition in snow at SBBSA are visually identified as dust events and recorded by Center For Snow and Avalanche Studies (CSAS) observers. After sampling of a deposition event occurs, surface collections of dust concentrations, referred to as bulk samples, are collected per event by sampling the snow in a shallow layer over a 0.5 m^2 area. These samples are melted and sent to the Geosciences and Environmental Change Science Center of the United States Geological Survey in Denver, CO where snow is evaporated from samples, and dust is dried and preserved for composition and particle size analysis. There are currently three full seasons (2011-2013) that have a consistent per-event dust loading record. This excludes dust layers that are deposited on dust already at the surface, as these cannot be uniquely sampled. This dataset is made available through the CSAS (www.snowstudies.org).

In addition to specific dust-event snow sampling, the snowpack at SBBSA is monitored through regular excavation of snow pits to the ground. Sampling intervals are once a month while snowpack is accumulating, increasing to weekly intervals beginning no later than April 15th, which is the average date of peak snow water equivalent. Weekly

measurements begin earlier if significant dust deposition has occurred. Snow sampling is most frequent at SASP, the easiest site to access. Measurements in the snow pits include: temperature profile, snowpack stratigraphy, liquid water content, and measurements of snow density. Snow water equivalent (SWE), the amount of water that is held within the snowpack, is calculated from depth and density measurements. Dust stratigraphy is measured and quantified in the top 30 cm of the snow column at 3 cm intervals for a total of 10 samples, with accurate sample volumes maintained by use of a gravimetric board. (The sampling depth of 30 cm is the approximate maximum depth to which dust and other light absorbing impurities can influence radiative forcing.) Snow samples are sent to the Snow Optics Laboratory at NASA's Jet Propulsion Laboratory (SOL/JPL), where they are filtered and weighed to find dust concentration in mg g^{-1} of melted sample, which is equivalent to parts per thousand by weight (pptw).

The distance between SBBSA and GMSP inhibits regular observations at the latter, more northern site. Snow is sampled at GMSP at minimum once a month beginning in March by either CSAS or SOL/JPL. The temporal resolution of sampling does not allow for individual dust event collections, but otherwise snow sampling and observations are identical to that described for SBBSA.

3.3 Modeling

3.3.1 Dust Source Region

Dust sources in the Colorado Plateau and across the western US are dispersed, and therefore we chose back-trajectories footprints over vectors to investigate source region variability. These footprints were produced for each spring dust event with the Stochastic Time-Inverted Lagrangian Transport (STILT) model [*Lin et al.*, 2003].

Conceptually, footprints can be thought of changes in concentration at the receptor site that can be attributed to different upwind source areas along the back-trajectories. In this interpretation, the footprints indicate the sensitivity in concentrations at the receptor site to surface fluxes along the back-trajectories for each modeled grid cell and time (units of ppm/(μmole m^{-2} s^{-1})$^{-1}$). Further discussion of the derivation of footprints can be found in *Lin et al.* [2003].

As a Lagrangian particle dispersion model, STILT uses an air parcel-following coordinate system, which offers distinct numerical and computational advantages over fixed-coordinate Eulerian models. Among these advantages are robustness against numerical diffusion, increased computational efficiency, and improved representation of atmospheric boundary layer transport effects [*Lin*, 2012] STILT calculates back-trajectories from wind fields produced by a different gridded meteorological model. These back-trajectories represent the paths air parcels (i.e. fictitious particles) followed over the course of the simulation to arrive at a receptor site (location of interest) at the time the simulation was initialized.

The STILT simulations here were driven with meteorological fields from the Eta Data Assimilation System (EDAS) at 40-km horizontal resolution with an initial release of 3000 particles at a height of 30 m AGL over each receptor site. Three thousand particles were released every six hours for the duration of each event. Back-trajectories out to -24 hr were produced for each release. Footprints were derived for each release on a 1/6° latitude and 1/4° longitude horizontal grid, over which the particle number densities were time-integrated for each grid cell volume. Multiple six-hourly releases were then averaged to produce a footprint representative for the duration of the event.

These simulations were run without the explicit consideration of a settling velocity to account for dust loading within the back-trajectory model, meaning that the spatial extent of footprints may be overestimated.

3.3.2 Radiative Forcing

The range of potential radiative forcing due to dust is estimated using the treatment described in *Painter at al*. [2007]. Briefly, to bracket the potential dust impact, radiative forcing is calculated using two scenarios. The minimum scenario addresses the first direct effect of dust in snow by accounting for the reduction in visible albedo. The maximum scenario addresses both the first direct effect as well as the first indirect effect by accounting for reduction in visible albedo due to dust and changes in grain size.

Minimum surface radiative forcing $F_{d\min}$ (W m^{-2}) is calculated as

$$F_{d\min} = E_{vis}\Delta_{vis} \quad (1)$$

where E_{VIS} is the visible irradiance (W m^{-2}), $\Delta_{vis} = 0.92 - \alpha_{vis}$, α_{vis} is calculated visible albedo (from tower measurements) and 0.92 is the mean visible albedo for dust event free snow.

Maximum surface radiative forcing $F_{d\max+i1}$ is calculated as:

$$F_{d\max+i1} = 0.5(E_{vis}\Delta_{vis} + E_{nir}\alpha_{nir}((1/\xi) - 1) \quad (2)$$

where if

$\Delta_{vis} \le 0.17$ then $\xi = 1 - 1.689\Delta_{vis}$

else if,

$\Delta_{vis} > 0.17$ then $\xi = 0.67$

where the subscript '+*i*1' indicates that this accounts for the first indirect effect, E_{NIR} is the NIR/SWIR net shortwave flux, and α_{NIR} is the NIR/SWIR albedo. The latter relationship gives the proportion of the change in NIR/SWIR albedo due to the presence of dust versus grain coarsening in the absence of dust [*Marks et al.*, 1998; *Painter et al.*, 2007].

3.3.3 Temperature Increases

To address the spatial variability in the relative capacities of radiative forcing by dust and temperature increases to accelerate snowmelt, we follow the same method that is presented in *Skiles et al.* [2012]. Briefly, snowmelt was reconstructed during the ablation season with simulated uniform, hourly temperature perturbations of +2 and +4^{o} C, both with and without dust. There is an associated increase in sensible heating and longwave irradiance to the snow surface with higher air temperatures. Sensible heating is directly related to the increase in temperature, whereas increased longwave is dependent on both increases in temperature and the fraction of sky that is cloud covered [*Konzelmann et al.*, 1994]. This method brackets the increase in longwave by modeling longwave emissions with complete cloud cover and cloud free skies using parameterizations presented in *Konzelmann et al.* [1994].

3.3.4 Snowmelt Modeling

The point snow energy balance model, SNOBAL, was used to reconstruct snowmelt at each of the three sites [Marks *and Dozier,* 1992; *Marks et al.,* 1992]. The model represents the snow pack as two layers: an active 25 cm first layer and then remainder of the snowpack as the second layer. Energy exchanges are calculated in the active upper layer and then energy transfer is determined for the snowpack as a whole,

from which the energy available for phase changes in both layers is determined. The model utilizes site elevation, measurement heights, roughness length, and initial snow state variables (snow depth, snow density, snow surface temperature, average snowpack temperature, and liquid water content) as starting inputs. The starting snowpack conditions, or state variables, are determined from the manual snow measurements performed closest in time to April 15 (the date of average peak snow for the region) at each site. Changes in state variables, updated at an hourly time step, are driven by the observed forcing variables (hourly averages of net shortwave, longwave irradiance, air temperature, relative humidity, and wind speed), which are measured at the towers.

A detailed description of SNOBAL can be found in *Marks et al.* [1998]. An extended discussion of how SNOBAL is applied to assess dust advanced snowmelt, as well as a model sensitivity study completed using SBBSA instrumentation accuracy ranges, can be found in *Skiles et al.* [2012]. Briefly, the largest sensitivity occurs with uncertainty ranges associated with longwave irradiance, net solar radiation, and wind speed measurements with 1-2 days difference in melt out date. The maximum uncertainty is 2-3 days for all combined uncertainty ranges (+,-). The model surface roughness parameter was also assessed, as this value is set to a constant (1 mm). It was found that the SNOBAL is not highly sensitive to alterations in this parameter if surface roughness values typically observed at the study plots are used. Overall, SNOBAL reconstructs snowpack evolution well, consistently melting out snow cover to within a day of observed snow all gone (SAG) across all years.

The model was used to predict snowmelt for 15 combinations of dust and temperature scenarios over the springtime melt season. To simplify the presentation of

these results, scenarios are averaged and consolidated to a set of 6 scenarios: observed conditions (D_0), observed conditions with dust radiative forcings removed (C_0), and each of these scenarios with the 2^o C (D_2, C_2) and 4^o C (D_4, C_4) temperature increases.

4. Results

4.1 Measurements

4.1.1 Energy Balance and Snow Cover

Four-year daily mean (2010-2013) meteorological and radiation fluxes at each of the three sites are plotted in Figure 2. Climatologically GMSP and SASP are very similar, which is not surprising given their relative elevations and site environments. They both exhibit mean relative humidity (60%) and similar mean temperatures. The GMSP site is, on average, 0.3^{o}C warmer than SASP. The GMSP and SASP sites both have mean maximum summertime temperatures of 20^o C and mean minimum wintertime temperatures of -18^o C. The largest meteorological variation between the two sites is wind speed. While both sites are well protected and exhibit relatively low yearly average wind speeds (1 ms^{-1} at SASP, 2 ms^{-1} GMSP), wind speeds are consistently higher at GMSP. Over the full year, GMSP averages 1 m s^{-1} windier than SASP, yet hourly wind speeds can reach 10 m s^{-1} at GMSP while they do not exceed 5 m s^{-1} at SASP. Radiation fluxes are slightly higher at GMSP, as on average there is 8 W m^{-2} greater solar contribution and 6 W m^{-2} thermal contribution (longwave) at GMSP than SASP.

The alpine exposure at SBSP results in windier, colder, and less humid conditions than SASP and GMSP. The mean wind speed at SBSP is 4 m s^{-1}, with mean hourly values peaking around 15 m s^{-1}. Mean temperature is -1^{o}C; with an average summertime high of 16 ^{o}C and wintertime low of -20 ^{o}C. While the solar irradiance is ~ 25 W m^{-2}

greater at SBSP than the lower elevation sites, the incoming longwave radiation is ~ 25 W m^{-2} less due to the colder air temperatures.

The accumulation and duration of snow cover are controlled by these fluxes. Snow typically begins to accumulate at all three sites in November as solar irradiance decreases and temperatures decline. Snow cover reaches a maximum depth in March or April, and then decreases with increasing solar irradiance to SAG in May or June. Both GMSP and SASP have similar snow accumulation and ablation patterns, with 1.0 m average seasonal snow depths. There is some variation exhibited, as the date of maximum snow depth, which marks the transition between snow accumulation and ablation, typically occurs later at GMSP. In 2011 and 2012 this was only by a day, but in 2012 it was by 12 days, and in 2013 it was by nearly 40 days. While there was not significantly more snow at GMSP in 2013, on average only 10 cm more than SASP, snow accumulation was maintained for longer and peaked higher at GMSP relative to SASP. The SBSP site accumulates 20 cm less snow on average than GMSP or SASP, primarily due to wind redistribution, but in all years snow cover is maintained for longer relative to the lower elevation sites and, on average, snow depth peaks 3 weeks later.

Ablation season coincides with the seasonal increase of solar irradiance in the spring, because among the snow energy balance terms, it is net solar flux that contributes the most energy toward driving snowmelt [*Marks and Dozier*, 1992; *Oerlemans*, 2000]. In Figure 3 we have plotted broadband, NIR/SWIR, and visible albedo over the ablation season for each site. These are the ratios between measured incoming and outgoing solar flux, where the reflected flux has been corrected for slope and aspect following the method described in *Painter et al.* [2012b]. Increases in albedo over this time period were

due to new snowfall and decreases were due to dust being at or near the snow surface. The albedos at GMSP and SASP co-vary closely with each other, as illustrated by the derivatives of daily broadband albedo with respect to time plots (Figure 4). This indicates that dust and new snowfall events occur at each site coincidentally, which is also observed in snow stratigraphy.

4.1.2 Dust Deposition

Since 2003, a total of 87 dust events coincident with snow have been recorded in SBBSA. There is an average of eight events per season, although events are not evenly distributed over the record as shown in Figure 5. The number of events exhibited an increasing trend through 2009, when the number of events peaked at 12. From 2009-2013 the number has varied between nine and 12 events. Dust events are not distributed evenly across the snow-covered season, as 80% of them occur in March, April, and May (Figure 5). This is not unexpected, as the drying of arid landscapes and atmospheric momentum exchange coincide to increase dust event frequency in the spring. The number of spring events follows a similar pattern as season total events, increasing from 2003-2008 and then becoming less variable over the last 5 years with an average of nine (+/-1) events each spring.

The timing of impurity deposition is important for the radiative impact, as dust that is deposited in winter is usually buried by additional snow accumulation, thus limiting the amount of time additional solar radiation is being absorbed at the surface. In contrast, dust deposited in the spring has the largest impact, because solar irradiance is increasing and the internal energy in the pack is great enough to initiate snowmelt. Additionally, dust remains in the layer in which it was deposited and is not entrained in

melt water, a process which results in newly deposited spring dust layers persisting at the surface and previously buried layers resurfacing and converging over snow cover depletion. This further darkens the surface and compounds albedo decay. The stationary behavior of dust layers as snow melts has been consistently observed at SBBSA and has also been reported for light absorbing impurities in other regions [*Conway et al.*, 1996; *Doherty et al.*, 2013].

4.1.3 Dust Concentrations

The amount of dust entrained in each event is variable and therefore the number of events each season is not a predictor of total dust loading. The season total dust concentrations reported here are the values from last collection of the season. This end of year sample is collected just prior to snow depletion when all dust has combined at the surface, in no year has additional dust been deposited in the time between the last sample collection and SAG.

End of year dust concentrations exhibit greater interannual variability than number of seasonal dust events (Fig 6). Over the nine year SBBSA record, it appears seasonal loading exhibits two modes extreme dust years (2009, 2010, 2013) with average loading at SASP of 4.6 mg g^{-1} and lower dust years (2005-2008, 2100-2012) with average loadings of 0.8 mg g^{-1}. Concentrations at the windy SBSP site tend to be slightly lower than SASP, with an average concentration of 3.6 mg g^{-1} in the high dust years and 0.7 mg g^{-1} in the lower years. Dust loading at GMSP was lower than SBBSA, with 1.65 mg g^{-1}, 1.04 mg g^{-1}, and 0.6 mg g^{-1} in 2010, 2011, and 2012 and an average loading of 1.0 mg g^{-1}, 1.1 mg g^{-1} less than SASP. The largest difference between SASP and GMSP occurred in 2010, when SASP had an additional 2.7 mg g^{-1} of dust at the end of the year.

The highest end of year dust concentration was sampled at SASP in 2013, with 4.8 mg g^{-1}. We cannot compare this directly to the other sites, as both SBSP and GMSP were inaccessible for an end of year sample collection in 2013. Using the variation between dust concentrations at each site for 2005-2012 we can estimate the EOY dust concentration at SBSP; variation in dust loading between SBSP and SASP is greatest in heavy dust loading years, with an average difference of -1.2 mg g^{-1} for 2009 and 2010, if averaged across the 8 years, the difference minimizes to -0.4 mg g^{-1}. This would result in an end of year dust concentrations between 3.6 and 4.4 mg g^{-1}. We do not make an estimate at GMSP due to the short record and the variation in that record.

It is outside the scope of this paper to discuss in detail the factors that contribute to this high interannual variability in dust loading, as it relates to surface dynamics in the source region and synoptic meteorology. A recent study by *Li et al.* [2013] found a relationship between the amounts of bare ground, as identified from remote sensing imagery, and dust loading at SBBSA. *Flagg et al.* [2013] monitored emission in southeastern UT between 2003 and 2012 and found wind speeds to be the strongest predictor of dust flux patterns, with the strong prolonged winds that occur across the Colorado Plateau in the spring producing the highest fluxes. Other factors, like vegetation cover/type and soil type, also played a role in emission fluxes [*Flagg et al.*, 2013]. Likely heavy dust-on-snow years cannot be attributed to a single factor and additional study is needed better understand the relationships between source region, atmospheric transport, and deposition processes.

4.2 Modeling

4.2.1 Dust Source Region

We classified the directional extent of each footprint in Table 1 and plotted representative events for these classifications Figure 7. The majority of spring events can be classified as extending to the southwest. Relative to SBBSA footprints, GMSP footprints are shifted to the north and more frequently classified as extending to the west. The potential source regions are most similar between the two sites when footprints extend to the south and are most divergent when footprints extend to the west, when trajectories are latitudinal to the sites. There are no footprints that extend directly to the north or east for either of the study areas. Full season averages (Figure 7) mirror the general southwest direction of the individual events. The exception is 2013, when individual events and the seasonal average were more western than the other years. This may be related to the three events in 2013 that were reported as multi-day events, resulting in broader footprint extents.

When individual event dust loading at SASP is compared to back trajectory footprints for the same events, it is the south/southwesterly events that tend deposit the most dust, though not every southwesterly event brings heavy dust loading. There were 12 springtime events between 2011 and 2013 for which per event loading could be uniquely sampled at SASP. These are summarized in Table 1 and loading ranges from 0.13 g m^{-2} (March 17th, 2011) to 23.7 g m^{-2} (April 8th, 2013) with a median value of 0.6 g m^{-2} (April 8th, 2011).

The heaviest single event dust load was associated with the April 8th, 2013 (D6) event. The dust deposited during D6 accounted for over 90% of the total dust loading in

2013 and deposited more dust in the single event than has been deposited across entire other seasons. We currently have no knowledge of the factors that forced this uniquely large event. The back trajectory footprint, shown in Figure 8, is west to southwest and differs from the more constrained footprints exhibited by other major events. The footprint for GMSP was distinctly more northern for this event and the albedo record suggests the dust loading at GMSP was not as heavy.

The main dust source region for SBBSA has been identified as northeastern Arizona mainly because the dust plumes from this region are visible from remote sensing imagery [*Li et al.*, 2013; *Painter et al.*, 2007]. The GMSP site location was selected outside of these plume paths to try and parse out the dust loading from large point sources, northeastern AZ, from more diffuse sources like southern UT. The footprints support the hypothesis that a broader area is contributing to dust loading and therefore it is of interest to partition the level of contribution from these diffuse sources. If we make a simple assumption that dust deposition at GMSP represents diffuse dust loading, comparing end of dust concentrations allows us to make a first order estimate of the partitioning between point source and diffuse dust contributions.

In lower dust years, 2011 and 2012, dust loading at all sites is similar, with GMSP receiving ~0.1 mg g^{-1} less than SBBSA. Whereas in the extreme dust year, 2010, the difference in dust concentrations is far greater, SASP and SBSP received 2.7 mg g^{-1} and 1.0 mg g^{-1} more dust, respectively. While anecdotal, this suggests that deposition in lower dust years may be accounted for mainly by diffuse loading and the additional loading to SBBSA in extreme dust years is contributed by point source plumes. This hypothesis is supported in part by the fact that the 2010 diffuse contribution at SBBSA (0.8 mg g^{-1}),

calculated by taking the difference between the point source contributions in 2010 at SASP/SBSP (2.7 mg g^{-1}/1.0 mg g^{-1}) and subtracting from the total 2010 dust loading (4.3 mg g^{-1}/2.7 mg g^{-1}), corresponds to average dust loading at SASP/SBSP in non-extreme dust years (0.8 mg g^{-1}/0.7 mg g^{-1}). For all three extreme dust years at SASP (2009, 2010, 2013) 0.8 mg g^{-1} represents 18% of the total dust loading, suggesting a ~ 80% point source contribution.

4.2.2 Radiative Forcing

Dust radiative forcing typically initiates in March with the deposition of spring dust events, and increases over the ablation season with additional dust deposition and snow albedo feedbacks. To capture this rise in spring radiative forcing, we calculate it for each year from March 15 to the date of modeled clean SAG. Spring radiative forcing is controlled by the amount of dust at, or near, the snow surface and is modulated by new snowfall. Theoretically a number of cloudy days would decrease dust radiative forcing by reducing incoming solar irradiance, but *Skiles et al.* [2012] found no relationship between cumulative broadband irradiance and daily mean radiative forcing at SBBSA. We have plotted daily means radiative forcing along with precipitation, snow depth, and dust events in Figure 9.

Radiative forcing from April 15 to observed date of SAG gives an indication of how much additional energy dust is contributing toward melts over the ablation season. The highest daily mean values consistently occur at SASP, which receives the most dust. In 2013, with the highest observed end of year dust concentration on record, the daily mean radiative forcing was 65 W m^{-2} between April 15th and SAG, and peaked at 141 W m^{-2} just prior to melt. Despite the slightly lower dust concentration the highest mean

radiative forcing occurred in 2009 (75 W m^{-2}) at SASP. Radiative forcing was elevated in 2009, when the lack of new snowfall at the end of the season resulted in a reduction of snow albedo to an unprecedented 0.33 for the last week of snow cover. The average daily radiative forcing in 2009 was 125 W m^{-2} during the last 7 days of snow cover, whereas in spring 2013 it was 108 W m^{-2} over this same time period. Over the full record, the lowest ablation season radiative forcing (35 W m^{-2}) occurred in 2005, the lowest dust concentration year.

The patterns exhibited at SBSP are similar to SASP, though as with total dust loading, radiative forcing values tend to slightly lower at SBSP. The highest ablation season radiative forcing occurred in 2013 (59 W m^{-2}) and the lowest between 2010 and 2013 occurred in 2011 (32 W m^{-2}). The lowest radiative forcing at any site (19 W m^{-2}) occurred at SBSP also in 2005. In lower dust years, the difference in radiative forcing between SASP and SBSP is greater, SASP received almost 20 W m^{-2} more than SBSP in 2011 and 2012, whereas it was only an additional 5-7 W m^{-2} in 2010 and 2013.

Similar evolution in radiative forcing is exhibited at GMSP relative to SASP and SBSP, but lower magnitude, with 16 W m^{-2} less than SASP and 3 W m^{-2} less than SBSP. The highest daily mean radiative forcing occurred in 2010 (50 W m^{-2}) and was lowest in 2012 (35 W m^{-2}). These coincide with the highest and lowest end of year dust concentrations measured at GMSP. Unfortunately, we do not have measured end of year dust concentration at GMSP for either 2009 or 2013, the highest dust years at SBBSA. Radiative forcing values would indicate that 2010 could have been the heaviest dust year GMSP, as ablation season radiative forcing in 2013 (39 W m^{-2}) was lower than in in 2010 (50 W m^{-2}). This is also the year with the largest difference between SBBSA and GMSP,

with 25 W m^{-2} and 19 W m^{-2} greater daily mean radiative forcing at SASP and SBSP, respectively.

In Figure 9 we continue to plot radiative forcing after SAG, over the time period when there would still be snow cover in the absence of radiative forcing by dust. These values provide a measure of how much additional solar radiation the ground is absorbing in the absence of snow. The daily mean radiative forcing was similar at all three sites over this period (~ 150 W m^{-2}). At SASP it ranged from 132 W m^{-2} (2011) to 174 W m^{-2} (2013), with an average of 155 W m^{-2}, while at SBSP it ranged from 137 W m^{-2} (2011) to 165 W m^{-2} (2013), with an average of 153 W m^{-2}. At GMSP it ranged from 128 W m^{-2} (2012) to 167 W m^{-2} (2010), with an average of 153 W m^{-2}.

Mean daily radiative forcing from April 15 to clean scenario SAG provides an encompassing measure of dust forced snow albedo feedbacks, including enhanced grain growth and earlier removal of snow cover. The daily mean radiative forcing over this period was again highest in 2013 with 130 W m^{-2} at the SASP, 100 W m^{-2} at SBSP, and 95 W m^{-2} at GMSP. Average values for the SASP, SBSP, and GMSP were 105 W m^{-2}, 87 W m^{-2}, and 88 W $m^{-}2$, respectively. In all cases there was an additional 28 – 65 W m^{-2} of radiative forcing for the period of April 15 to clean scenario SAG relative to dust scenario SAG, with this additional forcing coming from the earlier reduction in snow covered area.

4.2.3 Advanced Snowmelt

The additional energy contribution from dust radiative forcing contributes to earlier snowmelt (a) by reducing cold content of the snow column when snow temperature is < 0 °C and (b) immediately to melt when snow temperature is at 0 °C

[*Painter et al.*, 2012b; *Skiles et al.*, 2012]. We refer to the difference in the number of days between the snow all gone dates of the dust and clean scenarios as $\Delta SAG_{D_0,C_0}$. Evolution in SWE over the ablation season is plotted in Figure 10. As discussed in the Methods section, the clean snowpack is modeled by removing the minimum and maximum radiative forcing due to dust, then averaging the daily values of these two scenarios to represent a conservatively clean snowpack. Without direct observation of zero-dust conditions, the modeled clean snow scenario is our best understanding of the evolution of the snowpack in the absence of dust.

Radiative forcing by dust varies on multiple temporal scales, and degree to which it advances snowmelt can be influenced by factors such as the amount of SWE the ground at the beginning of the ablation season [*Painter et al.*, 2007], the amount of new snow fall atop dust layers in the spring [*Skiles et al.*, 2012], and the variation in solar irradiance by cloud cover [*Skiles et al*, 2012]. We find that the impact of these tempering factors does not influence the linear relationship we find between $\Delta SAG_{D_0,C_0}$ and end-of-year dust concentrations exhibited at SBBSA over the full 9-yr record (Figure 11; R^2 values of 0.94 and 0.95 at the SASP and SBSP site, respectively).

As might be expected the greatest degree of dust advanced melt took place at SASP in the extreme dust years of 2009, 2010, and 2013, with $\Delta SAG_{D_0,C_0}$ values of 51, 48, and 49 days at SASP, respectively. The ΔSAG at SBSP was, on average, 6 days less, due to the lower dust concentrations and radiative forcing values. In the high dust years $\Delta SAG_{D_0,C_0}$ are 44, 37, and 38 days for 2009, 2010, and 2013 respectively. The average of both site gives an idea of the basin wide $\Delta SAG_{D_0,C_0}$, which would be 44 days for these

extreme dust years. The lower dust years, 2005-2008 and 2011-2012, exhibit advanced melt on the scale of about a month with 24-34 days (SASP) and 23-28 days (SBSP).

There is a similar linear $\Delta SAG_{D_0,C_0}$ response at GMSP to EOY dust concentrations, as seen in Figure 11. Over the three years with measured dust loading, 2010 had the greatest advanced melt (27 days) and 2012 had the lowest (15 days). The largest advanced melt occurred in 2013, when EOY dust was not measured. We suggested previously that the loading at GMSP was greatest in 2010, based on higher ablation season radiative forcing. Given the clear relationship between $\Delta SAG_{D_0,C_0}$ we suggest the dust loading in 2013 may have been slightly higher and the lower radiative forcing in 2013 maybe have resulted from the two clean snow events over the ablation season. A longer record at GMSP will help us better understand the variation at this site.

The ability of the snowmelt model to accurately reconstruct snow cover can be assessed by comparing measured to modeled SWE (Figure 10). The root mean square difference of modeled to measured SWE over the ablation season at SASP is 49 mm across all years (2005-2013). At SBSP, we calculate measured SWE using snow depth from the tower and density from the snow pits, due to variation in snow depth between the pit site and tower, resulting in a slightly higher average RMSD of 52 mm. Due to sparse measurements of ablation season SWE at GMSP we refrain from calculating RMSD's, but we are confident that the model robustly simulates snow cover at this site, with modeled SAG occurring within 1 day of observed SAG across all four years.

The difference among C_2, and C_4, and C_0 SAG in Figure 10 is the number of days that the temperature increases would advance loss of snow cover in the absence of dust ($\Delta SAG_{C_2,C_0}$ and $\Delta SAG_{C_4,C_0}$, respectively). The differences of D_2 and D_4 SAG from D_0

SAG represent the number of days temperature increases would further shorten snow cover in the presence of dust ($\Delta SAG_{D_2,D_0}$ and $\Delta SAG_{D_4,D_0}$, respectively).

All sites exhibit a similar response to increases in temperature. Temperature increases of +2 and +4°C under dust-free scenarios induce $\Delta SAG_{C_2,C_0}$ and $\Delta SAG_{C_4,C_0}$ of 4-18 days at GMSP, 6-20 days at SASP, and 7-20 days at SBSP – a lesser melt forcing than the observed dust radiative forcing in this region. The lowest $\Delta SAG_{D_0,C_0}$ occurred at GMSP in 2012, being only 15 days. In the absence of dust, a temperature increase of 4°C still would have been fairly ineffectual, advancing melt by only 8 days. Combined with observed dust conditions, the increases in temperature shortened snow cover duration by 1 to 8 additional days ($\Delta SAG_{D_2,D_0}$, $\Delta SAG_{D_4,D_0}$). The reduced impact of increased temperature under dusty conditions is due to the reduced snow cover duration over which the increased sensible heating and longwave irradiance can affect a difference in SAG. The lowest melt forcing by increased temperature in the dusty case occurred in 2009 at SASP, corresponding to the greatest mean dust radiative forcing. In these scenarios, $\Delta SAG_{D_2,D_0}$, $\Delta SAG_{D_4,D_0}$ were < 1 day.

5. Concluding Thoughts

Dust loading at SBBSA exhibits two modes: extreme dust years, 2009, 2010, and 2013, where loading is ~4.0 mg g^{-1}, and lower dust years, 2011 and 2012, with dust loading of ~1 mg g^{-1}. This holds true across the full 9-yr record at SBBSA, not just the 4-yr record discussed here [*Skiles and Painter*, 2014]. The average daily mean radiative forcings in these extreme dust years ranged from 50-75 W m^{-2} advancing melt by 48-51 days at SASP and 37-44 days at SBSP. Dust still accelerates melt at SBBSA in

less extreme dust loading years by 27 days on average. This advanced melt shifts runoff timing and intensity, which can results in a doubling of snowpack outflow in extreme dust years [*Skiles et al.*, 2012].

Dust deposition at GMSP between 2010 and 2013 resulted in average daily mean radiative forcings of 35-50 W m^{-2} advancing melt by 15-30 days. While evidence suggests that timing of dust events is roughly coincident between the two sites, the dust loading at GMSP is on average ~1 mg g^{-1} less than SASP. This is not unexpected, given the site location was selected to capture diffuse dust loading patterns in this region. The behavior of melt response is similar to both SASP and SBSP, with the magnitude of advanced melt exhibiting a linear relationship with end of year dust concentrations. The lower dust concentrations and daily mean radiative forcings at GMSP suggests the degree of dust impact across the Colorado River Basin may not be as extreme as what is exhibited to SBBSA, which analysis here suggests may receive up to 80% of heavy dust loading from plumes originating in north eastern Arizona. That is not to discount of the impact of dust-on-snow deposition, as dust accelerates snowmelt at GMSP by 24 days on average.

Temperature increases of 2-4^0 C that are projected for this region are less effective at forcing snowmelt, but could further accelerate snowmelt by 1-8 days in the presence of dust. The degree of this impact depends on the amount of dust loading and depth of snow cover, with the temperature advanced melt being the smallest in high dust years and low snow years. This is not to say that warmer temperatures will not have impact on mountain snow cover in this region. The impact from temperature comes

mainly during the accumulation season when warmer temperatures cause precipitation to fall as rain instead of snow.

Field and in situ measurements can be used to refine our understanding of dust on snow processes at the point scale, but the high spatial and interannual variability in the radiative impact from dust and inaccessible nature of snow covered mountain environments makes remote sensing the ideal method to monitor impacts and assess spatial variability both in this and other regions. *Painter et al.* [2012a] presented the MODIS dust radiative forcing model (MODDRFS) that retrieves the radiative impact by dust and other light absorbing impurities from space. *Painter et al.* [2013] presented the Imaging Spectrometer-Snow Albedo and Radiative Forcing (IS-SnARF) algorithm, which retrieves dust radiative forcing from AVIRIS and similar hyperspectral airborne instrument platforms. The development and validation of the algorithms driving these remote sensing retrievals would not have been possible without the unprecedented data record at SBBSA.

The data from SBBSA are also being utilized to force and validate hydrologic models. *Painter et al.* [2010] used data from SBBSA to investigate the dust impact on the hydrology of the Colorado River by expanding the radiative forcing due to dust to the entire basin and then running a hydrological model between 1916 and 2003 for pre-disturbance and post-disturbance albedo schemes [*Painter et al.*, 2010]. It was found that current dust levels shift peak runoff three weeks earlier, and due to increased evapotranspiration rates upon earlier removal of snow cover, dust has reduced total annual runoff by ~5%. The albedo parameterization for snow with dust only took into account data from lower dust years (2005-2008). *Deems et al.* [2013] updated the model

runs to account for extreme dust loading and found that melt was advanced by 6 weeks, and total annual runoff was reduced by an additional 1%, for total reduction in runoff at Lee's Ferry, AZ of 6%.Given the heavy demand for water from the Colorado River, the impact of dust loading on the snow is likely to critically affect the quantity and quality of water available from the river to meet future needs. Heavy dust loading years will likely become more frequent in the future as expected warming and decreased precipitation will create deeper and longer droughts, reducing plant cover and increasing dust emissions [*Li et al.*, 2013; *Munson et al.*, 2011].

6. References

Belnap, J., and D. Gillette (1998), Vulnerability of desert biological soil crusts to wind erosion: The influences of crust development, soil texture, and disturbance, *Journal of Arid Environments*, *39*(2), 133-142.

Bryant, A., T. H. Painter, J. Deems, and S. M. Bender (2013), Hydrologic Response to Dust Radiative Forcing in Snow in the Upper Colorado River Basin, *Geophysical Research Letters*, *40*(15).

Conway, H., A. Gades, and C. F. Raymond (1996), Albedo of dirty snow during conditions of melt, *Water Resources Research*, *32*(6), 1713-1718.

Deems, J., T. H. Painter, J. Barsugli, J. Belnap, and B. Udall (2013), Combined impacts of current and future dust deposition and regional warming on Colorado River Basin snow dynamics and hydrology, *Hydrology and Earth System Sciences Discussions*, *10*.

Doherty, S. J., T. C. Grenfell, S. Forsstrom, D. Hegg, R. E. Brandt, and S. Warren (2013), Observed vertical redistribution of black carbon and other insoluble light-absorbing particles in melting snow, *Journal of Geophysical Research: Atmosphere*, *118*.

Flagg, C. B., J. C. Neff, R. L. Reynolds, and J. Belnap (2013), Spatial and temporal patterns of dust emissions (2004-2012) in semi-arid landscapes, southeastern Utah, USA, *Aeolian Research*.

Goldstein, H. L., R. Reynolds, and C. Landry (2014), Properties of dust deposited on Colorado mountain snow cover: effects on snow albedo*Rep.*, U.S. Geological Survey.

Konzelmann, T., R. van der Wal, G. Wouter, R. Bintanja, E. Hennekin, and A. Abe-Ouchi (1994), Parameterization of global and longwave incoming radiation for the Greenland Ice Sheet, *Global and Planetary Change*, *9*(1-2).

Lawrence, C. R., T. H. Painter, C. Landry, and J. C. Neff (2010), The contemporary composition of aeolian dust deposited in the San Juan Mountains, Colorado, USA, *Journal of Geophysical Research*, *115*.

Li, J., G. S. Okin, S. M. Skiles, and T. H. Painter (2013), Relating variation of dust on snow to bare soil dynamics in the western Unites States, *Environmental Research Letters*(8).

Lin, J. C. (2012), Lagrangian modeling of the atmosphere: an introduction, in *Lagrangian Modeling of the Atmosphere*, edited by J. C. Lin, D. Brunner, C. Gerbig, A. Stohl, A. Luhar and P. Websley, pp. 1-11, American Geophysical Union Monographs.

Lin, J. C., C. Gerbig, S. C. Wofsy, A. E. Andrews, B. C. Daube, K. J. Davis, and C. A. Grainger (2003), A near-field tool for simulating the upstream influence of atmospheric observations: The Stochastic Time-Inverted Lagrangian Transport (STILT) model, *Journal of Geophysical Research: Atmospheres*, *108*(D16).

Marks, D., and J. Dozier (1992), Climate and energy exchange at the snow surface in the alpine region of the Sierra Nevada 2. Snow cover energy balance, *Water Resources Research*, *28*(11), 3043-3054.

Marks, D., J. Kimball, D. Tingey, and T. Link (1998), The sensitivity of snowmelt processes to climate conditions and forest cover during rain-on-snow: a case study of the 1996 Pacific Northwest flood, *Hydrological Processes*, *12*, 24.

Munson, S. M., J. Belnap, and G. S. Okin (2011), Responses of wind erosion to climate-induced vegetation changes on the Colorado Plateau, *PNAS*, *108*(10), 3854-3859.

Neff, J. C., A. P. Ballantyne, G. L. Farmer, N. M. Mahowald, J. L. Conroy, C. C. Landry, J. T. Overpeck, T. H. Painter, C. R. Lawrence, and R. L. Reynolds (2008), Increasing

eolian dust deposition in the western United States linked to human activity, *Nature Geosciences*.

Oerlemans, J. (2000), Analysis of a 3 year meteorological record from the ablation zone of Morteratschgletscher, Switzerland: Energy and mass balance, *Journal of Glaciology*, *46*(155), 571-579.

Painter, T. H., A. Bryant, and S. M. Skiles (2012a), Radiative forcing by light abosrbing impurities in snow from MODIS surface reflectance data, *Geophysical Research Letters*, *39*(17).

Painter, T. H., S. M. Skiles, J. Deems, A. Bryant, and C. Landry (2012b), Dust Radiative Forcing in snow of the Upper Colorado River Basin: Part 1. A 6 year record of energy balance, radiation, and dust concentrations, *Water Resources Research*.

Painter, T. H., F. Seidel, S. M. Skiles, A. Bryant, and K. Rittger (2013), Imaging spectroscopy of albedo and radiative forcing by light absorbing impurities in mountain snow, *Journal of Geophysical Research: Atmospheres*, *118*(17).

Painter, T. H., J. S. Deems, J. Belnap, B. Udall, A. F. Hamlet, and C. C. Landry (2010), Decreased water yield from the Colorado River Basin under dust-accelerated snowmelt, *PNAS*.

Painter, T. H., A. P. Barrett, C. C. Landry, J. C. Neff, M. P. Cassidy, C. R. Lawrence, K. E. McBride, and G. L. Farmer (2007), Impact of disturbed desert soils on duration of mountain snow cover, *Geophysical Research Letters*, *34*.

Skiles, S. M., and T. H. Painter (2014), A 9-yr record of dust on snow in the Colorado River Basin, paper presented at 12th Biennial Conference of Science and Management on the Colorado Plateau, Flagstaff, AZ.

Skiles, S. M., T. H. Painter, J. Deems, C. Landry, and A. Bryant (2012), Dust radiative forcing in snow of the Upper Colorado River Basin: Part II. Interannual variability in radiative forcing and snowmelt rates, *Water Resources Research*, *48*.

Figures

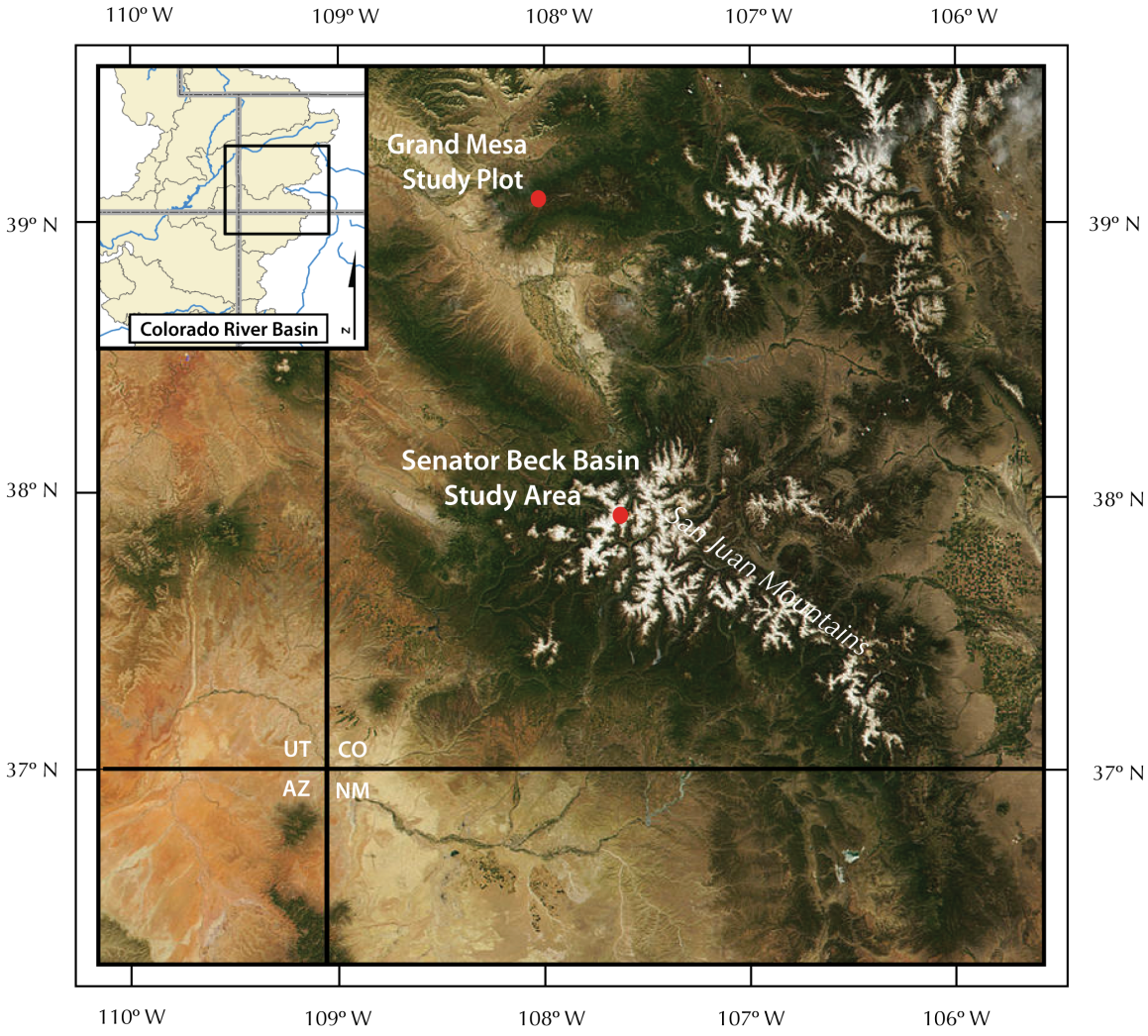
110° W
109° W
108° W
107° W
106° W
39° N
38° N
37° N
Grand Mesa
Study Plot
Colorado River Basin
N
Senator Beck Basin
Study Area
San Juan Mountains
UT
CO
AZ
NM


Senator Beck
Study Plot
(SBSP)
Swamp Angel
Study Plot
(SASP)
Grand Mesa
Study Plot
(GMSP)

Figure 1 Map of study areas, inset indicated location relative to the Colorado River Basin. Instrumentation towers and study plots for each of the three study plots pictured below.

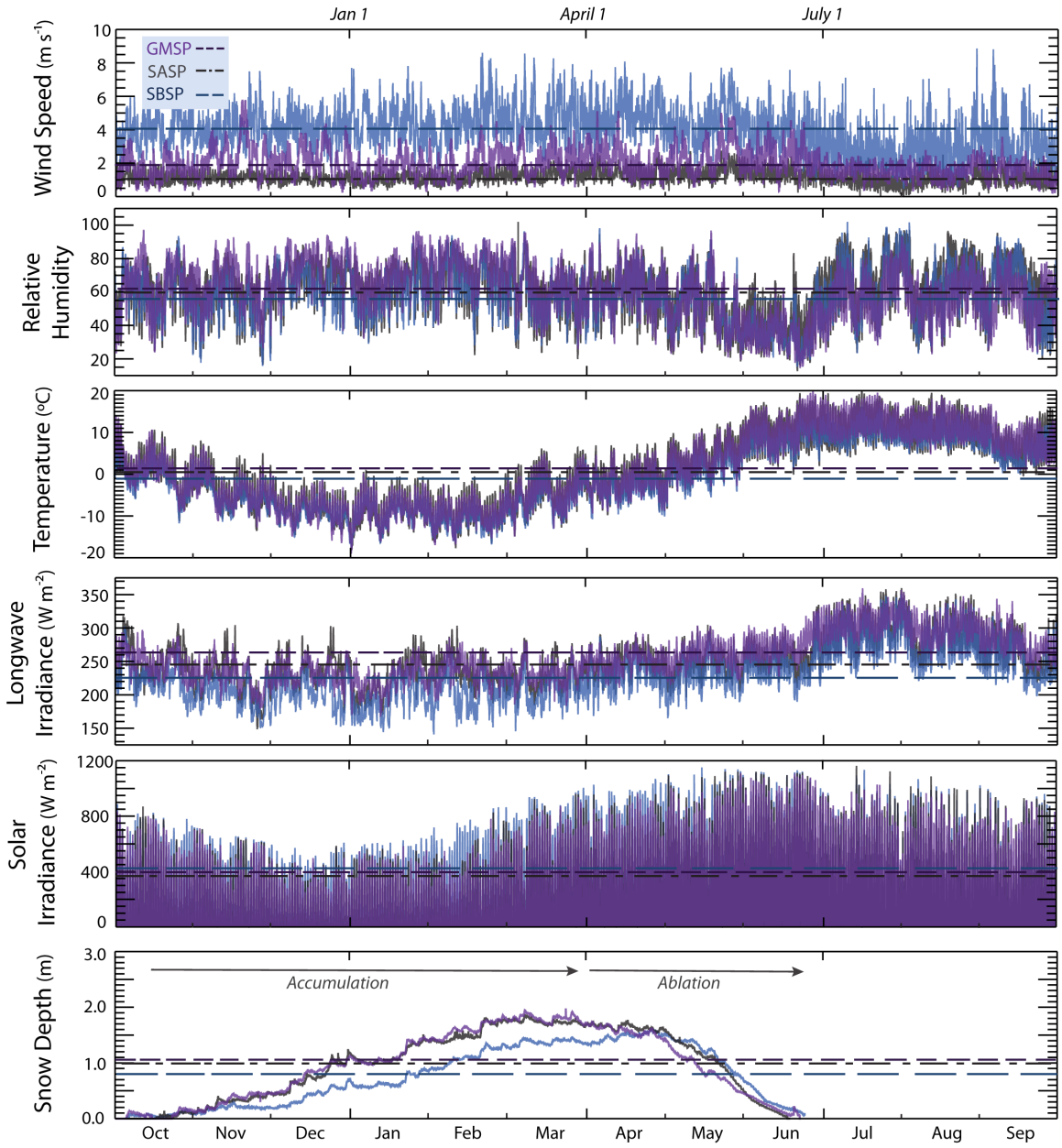

Figure 2 Daily mean fluxes and snow depth from instrumentation tower measurements plotted as four-year means, with full record mean value indicated by the dotted lines.

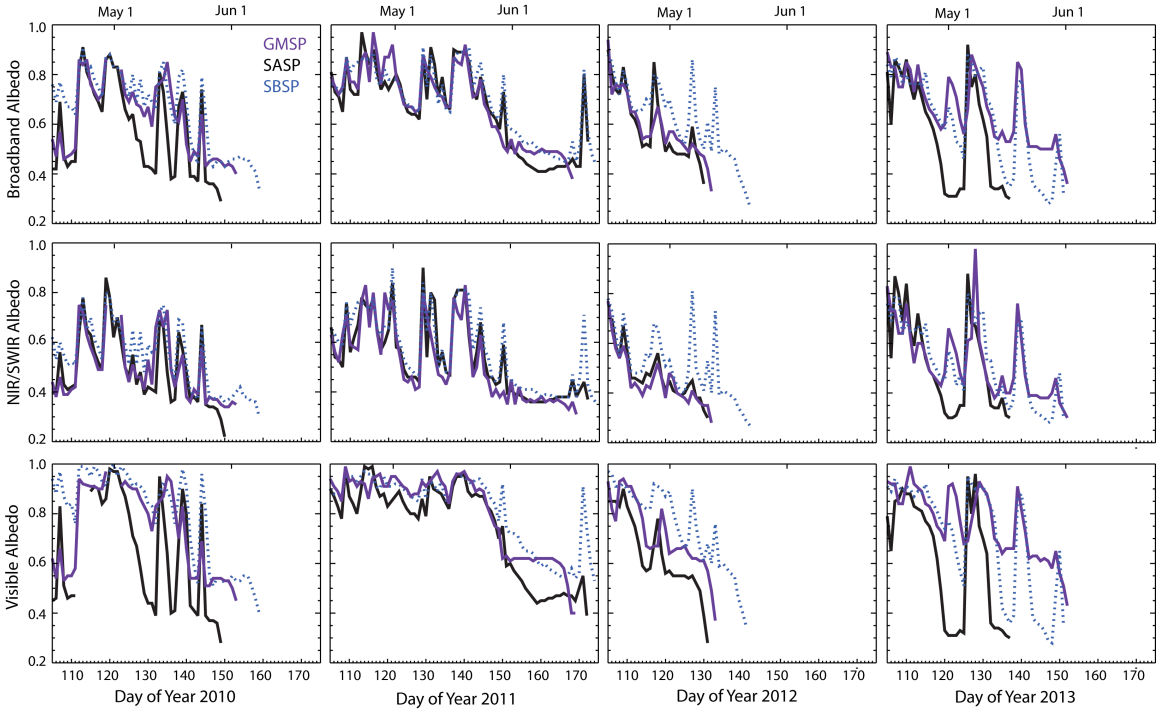

Figure 3 Broadband, NIR/SWIR, and visible albedo plotted from April 15th to snow all gone (SAG).

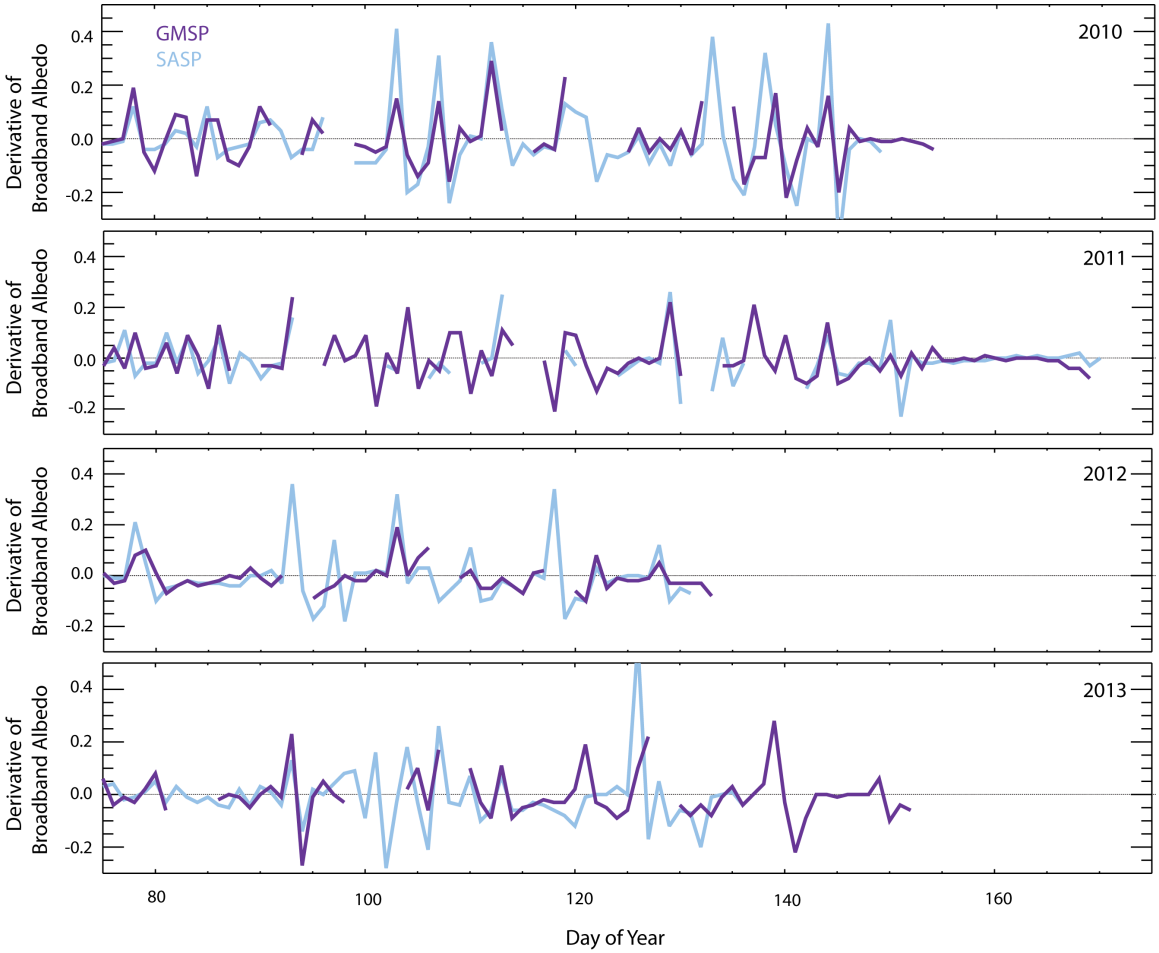

Figure 4 The derivative of broadband albedo with respect to time for SASP and GMSP from March 15th through SAG. With a few exceptions the reflectance at the sites show positive covariance.

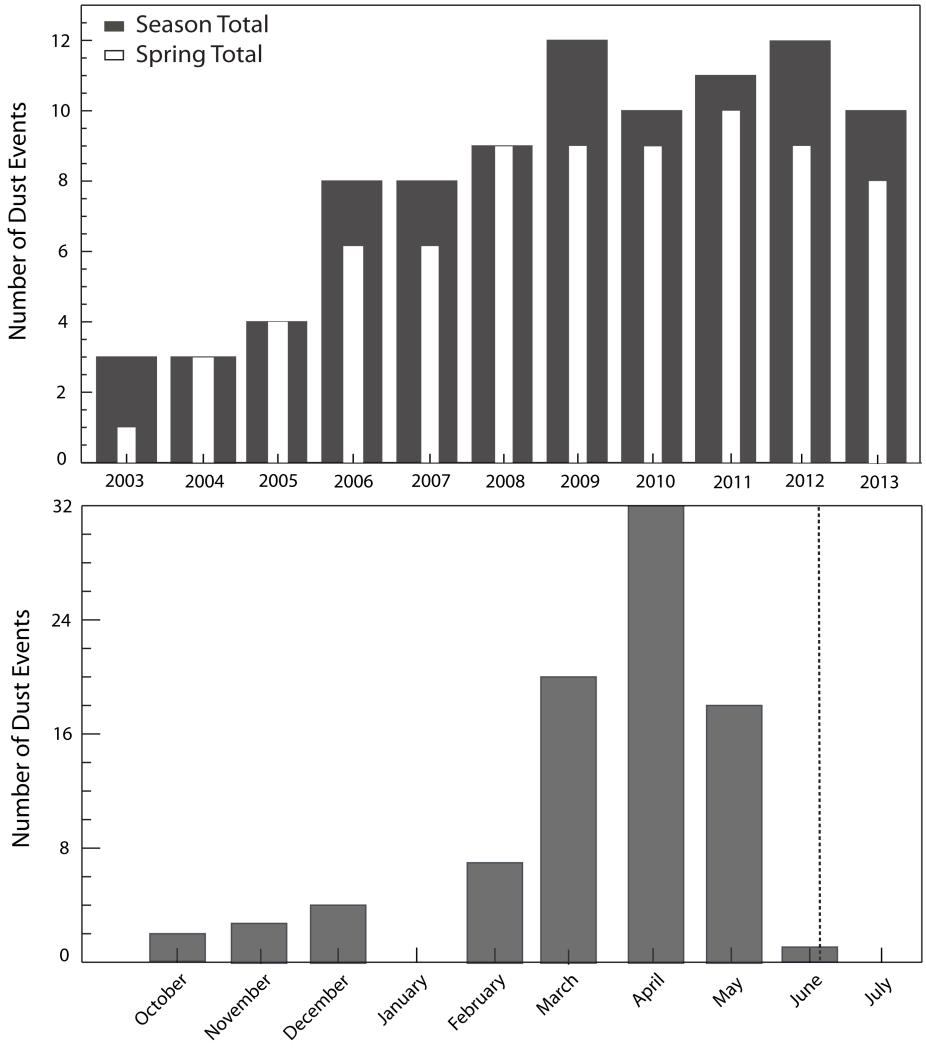

Figure 5 Dust event record at SBBSA over the full record. The plot above shows the number of events for each season, as well as how many of those events occurred in the spring. The plot below shows the monthly distribution of events, with basin average SAG date indicated by the dotted line.

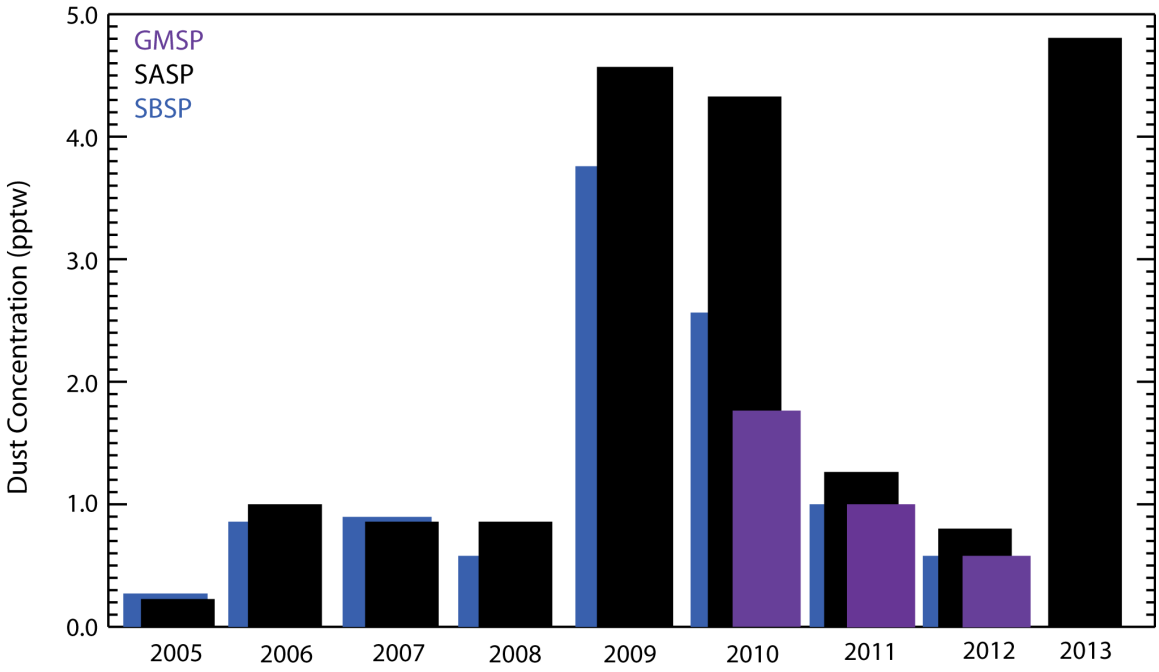

Figure 6 End of year dust concentrations.

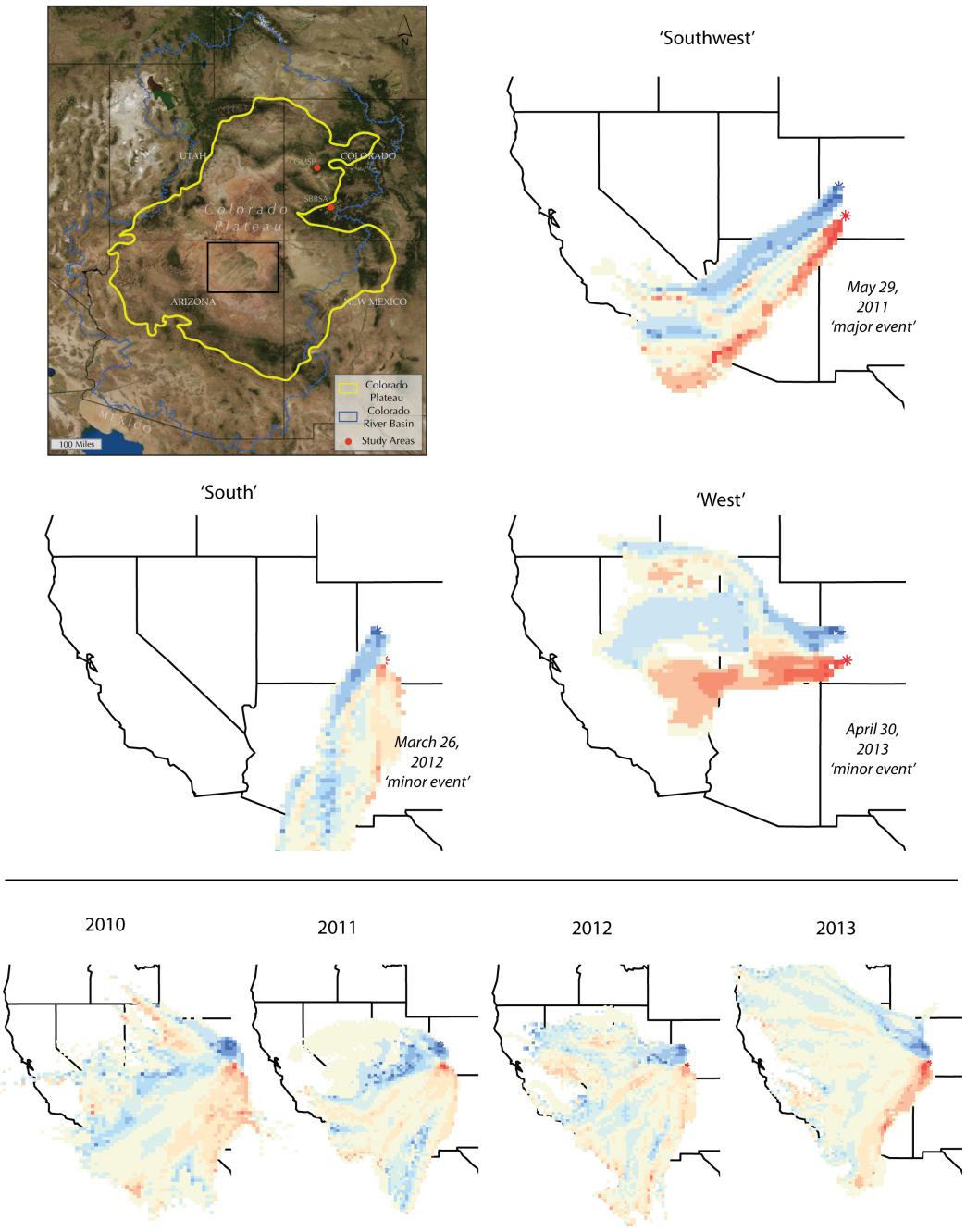

Figure 7 Above, 24 hr-back-trajectory footprints that are representative of trajectory classifications from table 1. Below, 24-hr back-trajectory averages of each year's springtime events. All plots represent footprint differences; where beige is the area GMSP and SBBSA have in common, blue is GMSP only, and red is SBBSA only. For reference we show map of the Colorado Plateau, with the square indicating the region where visible dust plumes originate.

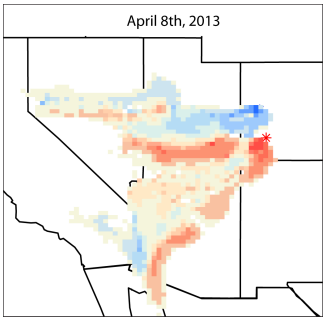

Figure 8 The 24-hr back-trajectory for the single largest dust event recorded since 2005, where blue is GMSP only, red is SBBSA only, beige represents a common source region.

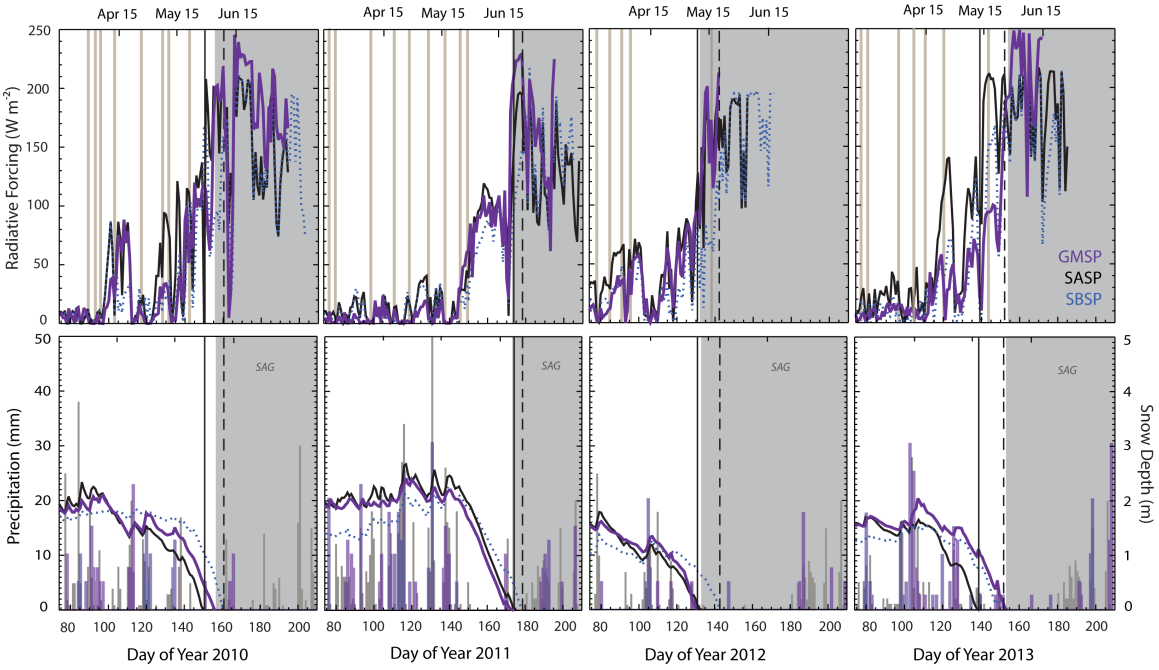

Figure 9 Springtime dust radiative forcing and dust event timing (above). Springtime snow cover depletion and precipitation (below). The observed SAG date at GMSP is indicated by the gray shading, the solid black vertical line is SAG at SASP, and the dotted black vertical line is SAG at SBSP.

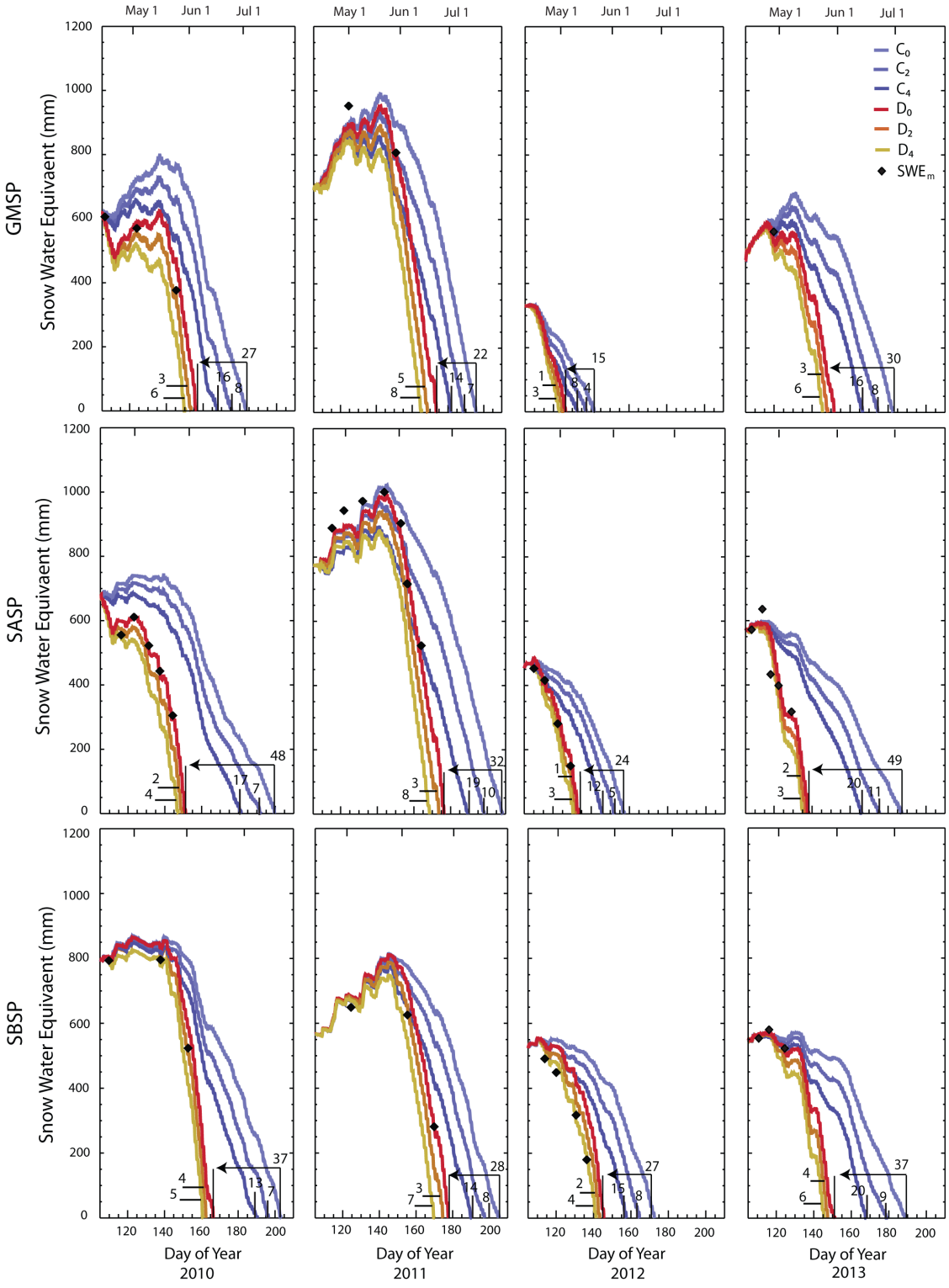

Figure 10 Depletion of snow water equivalent plotted from April 15th. The red line (modeled SWE under observed conditions) matches well with measured SWE (black diamonds), indicating the model does a good job of reconstructing of snowmelt.

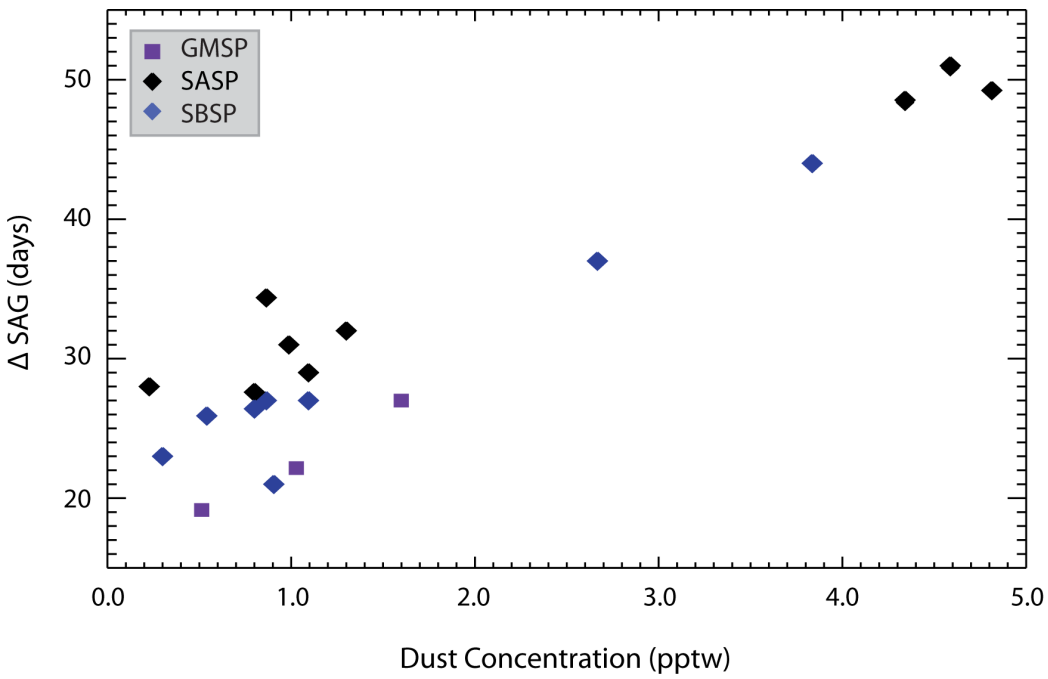

Figure 11 The relationship between end of year dust concentration and the number days dust advances snowmelt.

Table 1 Summary of spring dust events, source region, and dust loading 2010-2013. If dust events were uniquely sampled, dust loading is noted. If dust events were deposited when dust was already at the surface, visual event identification is noted. These observations are not available for 2010. Events that took place after SAG at one more sites are not listed.

Event Date	Event #	Dust Loading ($g\ cm^{-2}$)	Visual Identification	Source Region	
2010				*SBBSA*	*GMSP*
30-Mar	D2			southwest	southwest
3-Apr	D3			west southwest	west northwest
5-Apr	D4			southwest	southwest
12-Apr	D5			south	south
28-Apr	D6			southwest	southwest
9-May	D7			southwest	southwest
11-May	D8			southwest	west southwest
22-May	D9			southwest	southwest
2011					
17-Mar	D3	0.1378		southwest	west southwest
21-Mar	D4	2.562		south	south
8-Apr	D5	0.608		southwest	southwest
21-Apr	D6	0.3355		southwest	southwest
29-Apr	D7	0.2391		southwest	west
9-May	D8	0.5393		southwest	southwest
18-May	D9		Minor Event	southwest	southwest
26-May	D10		Minor Event	west southwest	west
29-May	D11		Major Event	southwest	southwest
2012					
18-Mar	D5	1.6387		south	south
26-Mar	D6		Minor Event	south	south
1-Apr	D7		-	southwest	southwest
6-Apr	D8		Major Event	southwest	southwest
2013					
17-18-Mar	D4	0.1951		west	west
21-22-Mar	D5	0.6025		west southwest	west
8-Apr	D6	23.7302		southwest	west
13-14-Apr	D7	1.5988		west southwest	west
15-17-Apr	D8	4.5765		southwest	west southwest
30-Apr	D9		Minor Event	west	west

Chapter 2

A high-resolution snow property dataset including surface albedo and vertically resolved measurements of snow optical grain size and LAI concentrations

Abstract

Light absorbing impurities can initiate powerful albedo feedbacks when deposited on snow and ice cover, yet due to a scarcity of observations and measurements, radiative forcing by aerosols is often neglected or poorly constrained in climate and hydrological models. To gain a better understanding of dust-in-snow dynamics and support physically based modeling of LAI processes near daily measurements of dust and black carbon stratigraphy, optical snow grain size, and snow albedo were collected over the 2013 ablation season at Swamp Angel Study Plot in Senator Beck Basin Study Area, San Juan Mountains, southwestern CO. Surface dust concentrations exhibited a wide range of values, from 0.02 to 6.0 mg g^{-1} (pptw) with 98% of mass being deposited by three events over two weeks in mid- April. Dust and black carbon concentrations co-varied indicating an association between LAI particles, but BC concentrations were 4-6 orders of magnitude lower than dust concentrations and likely play only a minor role in radiative forcing in this region. An accelerated rate of grain growth corresponded to this time period of heavy dust deposition. When these dust events converged at the surface, albedo was reduced to 0.3 for nearly two weeks, leading to rapid melt in the surface layers. This process appeared to scavenge mass from individual grains leading to an unexpected reduction in both grain size and density. End of season dust emergence also forced rapid snow depth reduction at rates 40-50% faster than other years with similar snow depth but less dust. Even minor dust loading initiated albedo decline and the relationship between dust concentrations at the surface and albedo is log-linear.

1. Introduction

The arid Colorado Plateau region of the western United States is one of the main dust producers in North America [*Neff et al.*, 2008]. The predominantly southwesterly winds entrain sediment and deposit it downwind in the snow-covered Colorado Rocky Mountains, with peak of dust emission coinciding with snowmelt onset in the spring [*Flagg et al.*, 2013; *Painter et al.*, 2012b]. Snowmelt runoff from these high elevation mountains provides over 70% of flow to the Colorado River, a critical resource that provides water to 7 basin states and Mexico. The level of springtime dust loading in the Western US is elevated in the Anthropocene. Sediment cores from high elevation lakes show that dust deposition increased 5 fold over background dust coinciding with Anglo settlement and grazing disturbance in the mid 19th century [*Neff et al.*, 2008].

Radiative forcing by this increased dust deposition has been shown to advance melt by 1-2 months, shift timing and intensity of peak runoff, and reduce total water yield [*Deems et al.*, 2013; *Painter et al.*, 2010; *Painter et al.*, 2007b; *Skiles et al.*, 2012]. The powerful impact on snow albedo has been documented with field, in-situ, and remote sensing measurements [*Painter et al.*, 2012a; *Painter et al.*, 2012b; *Painter et al.*, 2013; *Painter et al.*, 2007b], and ongoing research indicates that this may be a major factor contributing to operational river runoff forecast errors in the Colorado River Basin (CRB) [*Bryant et al.*, 2013]. This suite of studies, focusing on understanding the impacts of dust on snow in the hydrologically sensitive Colorado River Basin, have utilized a semi-empirical determination of dust radiative forcing based on changes in surface reflectance [*Painter et al.*, 2007b]. While very useful to constrain the relationship between dust and albedo, and investigate its impact on runoff, it is of interest to represent these processes

explicitly in physically based radiative transfer and snowmelt models. This requires measurements which have been previously unavailable; an extended high-resolution dataset of snow physical and optical properties to force, validate, and calibrate models.

Additionally, these studies have assumed that these LAIs are primarily mineral dust and have not considered the contribution of carbonaceous particles from industrial and urban sources. There has been a push to limit short-lived climate pollutants, like black carbon (BC) a by-product of the incomplete combustion of fossil and bio fuels, on a global scale. The 2007 IPCC synthesis report lists BC on snow as a contributor to anthropogenic climate change through reduction of snow covered area (SCA) [*IPCC*, 2007]. Another recent study found BC [atmosphere+snow] processes to be second only to CO_2 in climate forcing effectiveness [*Bond et al.*, 2013]. While the presence of BC can be inferred from the preliminary analysis of chemical and optical data that confirms the presence of BC in snow samples from this region [*Reynolds et al.*, 2013], actual BC content in snow and its contribution to radiative forcing in the CRB is currently unknown. Therefore, the known profound dust contribution, and preliminary evidence of presence of BC, motivates us to quantify the temporal variability in BC content, its coincident presence with dust, and their relative and combined contributions to radiative forcing in snow at the point to basin scales.

A field campaign conducted in the San Juan Mountains of southwestern, CO in spring 2013 collected data to assess dust and BC content and physically model radiative and hydrologic forcing by dust+BC. Here we present the measurement record; daily evolution in dust and black carbon content in the top 30 cm of the snowpack, optical grain size, depth, density, temperature over the full profile, and surface albedo over the

last two months of snow cover. This sampling window captured the transition from a relatively clean and cold snowpack to a dust laden melting one. In chapter 3 we use measurements to determine the optical properties of deposited dust, and in chapter 4 we use the dust optical properties and these measurements to force and validate a snow and ice radiative transfer model to accurately quantify, and partition, radiative forcing by these LAI components.

2. Methods

2.1 Study Site

Measurements were collected in the Senator Beck Basin Study Area (SBBSA) in the San Juan Mountains of southwestern Colorado, USA. This area contains two energy balance flux towers, one alpine and one subalpine, which have been collecting net solar radiation fluxes, net longwave radiation, snow depth, wind speed, wind direction, air temperature, and relative humidity at two heights since 2005. Regular snow pit measurements, monthly in the winter and weekly in the spring, for dust stratigraphy/concentrations, snow temperature, grain type, density, and SWE have been carried out over this same time period by the Center for Snow and Avalanche Studies in Silverton, CO, who manages the sites. An overview of the basin location is shown in Figure 1, and detailed site description and discussion of the data record can be found in *Painter et al.* [2012b].

The daily snow measurements presented here were collected at Swamp Angel Study Plot, the subalpine study plot of SBBSA. This site is located in a clearing below tree line at 3368 m near the lower end of SBBSA (Figure 1). It is a protected site with low wind speeds and is easily accessed on skis, making it a useful location to monitor

snow cover evolution. The snow profile plot, which is pictured in Figure 2, is 30 m x 30 m and contains a stand-alone precipitation gauge and 6 m tower holding the instrumentation array.

2.2 Snow Sampling

For this particular study, snow measurements began March 11th, 2013 and continued until the depletion of snow cover on May 18th, 2013. Approximately 80% of observed dust events occur in March, April, or May [*Skiles and Painter*, 2014]. To reduce variability in snow conditions snow pit excavation began around 10:00 am every day, with measurements commencing ~ 11:00 am. Additionally, most measurements were collected by the same observer [lead author Skiles], with two time periods of assistance from trained snow observers. Some gaps exist over the measurement period due to inclement weather and/or the limitations of having a single observer. Sampling days, and measurements made on those days, are summarized in Table 1.

Measurements were made in snow pits excavated on the north side of the SASP instrumentation tower within study plot boundaries as shown in Figure 2. The first snow pit was located at the front of the study plot with consecutive pits being excavated, at minimum, a meter behind the previous pit face. All pits were back filled when measurements were completed to reduce influence on grain growth from radiative and turbulent fluxes on the pit face. Examples of sampling methods are pictured in Figure 3. Sampling occurred in the following order: (1) collect spectral snow albedo over the pit site; (2) excavate pit, record snow depth, and collect 2 cm vertical increment profile of snow optical grain radius (OGR); (3) collect 10 cm temperature profile along shaded pit wall, noting visual snow and dust stratigraphy; (4) measure snow density in 10 cm

increments using a density cutter and field scale; and (5) gravimetric sampling for LAI stratigraphy in 3 cm increments in the top 30 cm of the snow column. Accurate sample volumes were maintained by use of a gravimetrics board [*Painter et al.*, 2012b]. To reduce scavenging of impurities by sample container, these individually bagged snow samples were kept frozen after collection, packed in coolers with dry ice, and shipped overnight to the Snow Optics Laboratory at NASA's Jet Propulsion Laboratory (SOL-JPL) where they were stored in the cold room at -20^{o} C until time of analysis. Albedo and OGR were retrieved with an Analytical Spectral Devices (ASD) field spectroradiometer (i.e. spectrometer; FieldSpec3), which contiguously samples the spectral range 0.35-2.5 μm. OGR is inferred from snow reflectance via contact spectroscopy, discussed in section 2.3. We chose to collect OGR, and not visual grain size/shape, because these measurements will be used for radiative transfer/albedo modeling which require the optically relevant metric as an input.

2.3 Optical Snow Grain Size

2.3.1 Field Collection

We used contact spectroscopy to monitor the evolution in optical grain size, the methodology of which is outlined in detail in *Painter et al*. [2007a]. Briefly, this method couples a field spectrometer and contact probe to collect optical grain radius, i.e. the radius of the sphere that returns the same hemispherical flux, along a vertical snow pit profile. The contact probe has its own light source with a known irradiance and illumination angle which allows it to be used under variable conditions at any time of day [*Painter et al.*, 2007a]. To reduce grain growth through conduction from the light source a circular matte black spacer is attached to the end of the probe to maintain a constant

distance from the snow surface, which doubles the field of view to 2 cm. When placed flat against the snow surface, the spacer also helps eliminate outside light from being collected at the sensor, maintaining the known irradiance from the contact probe light source. To further reduce outside light, the snow pit is covered by an opaque tarp during collection, extending out to a minimum of 30 cm past pit edges.

To begin the collection, the probe with spacer attached is placed onto a white standard Spectralon panel (http://www.labsphere.com), the instrument is optimized, and 10 spectra are collected. It is then placed on the pit face and 2 collections are made along the profile every 2 cm vertically to collect OGR stratigraphy. The resolution is limited by the field of view, and layers that are thinner than 2 cm are averaged with the snow in the same field of view [*Painter et al.*, 2007a]. An additional ten white standard spectra are collected once the full profile has been collected in order to understand variation in instrument sensitivity. During processing the two collections per depth are averaged and the white standard spectra are interpolated across the acquisitions to account for instrument drift [*Painter et al.*, 2007a]. This method is ideal for these measurements because it quick, accurate, does not suffer from calibration and variable illumination issues, and can be carried out by a solo observer [Figure 3]. Additionally, utilizing grain size retrievals from contact spectroscopy, *Painter et al.* [2007a] found that it improved shortwave spectral albedo modeling by an order of magnitude relative to grain size retrievals from a hand lens.

2.3.2 Grain Size Retrieval

After the initial processing step the spectra are output in ENVI [www.exelisvis.com] spectral library format, visually inspected, resampled, and then

spectra are inverted for optical grain radius via the Nolin-Dozier (N-D) model. Briefly, *Nolin and Dozier* [1993] presented a method for grain size retrieval from remote sensing using the ice absorption feature centered at 1030 nm, and validated it in *Nolin and Dozier* [2000]. The collected spectra are inverted for OGR by taking the integral across the continuum-normalized spectrum (950 to 1090 nm). OGR is then determined through best match to theoretical OGR's contained within a look up table, generated through repetitive runs of the DISORT [*Stamnes et al.*, 1988], an algorithm which simulates the radiative transfer through a homogenous snowpack comprised of spherical grains of pure ice of a given grain size and specified illumination and reflection geometry. *Nolin and Dozier* [2000] validated this model with hand lens, field spectrometer, and stereology measurements and determined uncertainty of ±10-50 μm for grain size between 50 and 900 μm. *Painter et al.* [2007a] suggested this error could be as great as 100 μm for grain sizes smaller than 300 μm.

2.3.3 Variability and Sensitivity

Variability and sensitivity in grain size retrievals from this relatively new method was assessed from a series of grain sizes collections at a snow pit site just below Putney Study Plot (PTSP; Center for Snow and Avalanche Studies) in the San Juan Mountains on May 18-19th, 2012. This meteorological study plot is across Highway 550 from Senator Beck Basin Study Area, and was selected because snow had already melted away at SASP by mid-May 2012. Snow conditions were ideal for a sensitivity/variability study; the snowpack was warm but not saturated resulting in a consistent, relatively shallow, profile of larger rounded grains. Sets of profiles were collected in succession under prescribed scenarios, which were chosen to quantify grain size variation under the

following conditions; 1) variability across the north facing pit wall, 2) on east and west facing walls, relative to north wall, 3) without tarp cover, 4) over time with the pit open, and finally, 5) over time with the pit open but the face shaved back. The first two were chosen to bracket sensitivity of retrieval when SOL-JPL contact spectroscopy protocol (tarp cover, shaved back, timely retrieval) is followed. The others were chosen to test sensitivity of the method if protocol is not followed. Of particular interest are the no tarp retrievals as *Painter et al. [2007a]* did not utilize tarp cover but suggested that it could be used to reduce influence from outside irradiance. Variability was quantified with two metrics- differences in mean OGR relative to the reference profile, and root mean square deviation (RMSD) from the reference profile, where the reference profile is the first collected on the north-facing wall.

2.2 Lab Analysis for LAI Concentrations

2.2.1 Dust

After being removed from the cold room, snow samples were allowed to melt completely. To ensure samples were well mixed, they were then placed in a sonicator to agitate settled particles for 20 minutes in the Nasco brand Whirlpak bags used to collect the samples. After sonication, sample mass was recorded and then a 50 mL subsample was drawn off into a polypropylene vial for black carbon analysis. The remaining sample was then re-weighed and vacuum filtered through individual pre-weighed 0.495 μm Nuclepore pore diameter filters. Filters containing impurities were fully dried and then reweighed to return impurity mass. The large majority of this mass is mineral dust and dust concentration is recorded in milligrams of impurity per gram of snow sample (mg g^{-1} or parts per thousand by weight) by taking the ratio between the differential dust mass

and the snow sample mass [*Painter et al.*, 2012b]. Black carbon mass, determined by the method described in section 2.2.2, was removed from dust mass reported here but the dust mass is so much greater that the difference in concentration in negligible. Samples are always analyzed as daily sets, at a maximum of 20 samples (2 sample sets) per day, with both dust and black carbon analysis taking place the same day they were melted.

2.2.2 Black Carbon

We utilize an intra-cavity laser-induced single particle incandescence soot photometer (SP2; Droplet Measurement Technology, Inc.) coupled to an ultrasonic nebulizer (A5000T; Cetac) to determine black carbon concentration from the discrete 50 mL liquid subsamples. The SP2 is the only instrument that directly measures BC in individual aerosol particles. It was designed to sample atmospheric black carbon but was adapted to measure black carbon in liquid samples by coupling the instrument to a nebulizer, and has now been used in multiple studies to analyze for BC content in snow and ice samples [*Bisiaux et al.*, 2011; *Bisiaux et al.*, 2012; *Kaspari et al.*, 2011; *McConnell et al.*, 2007; *Sterle et al.*, 2013].

There are different system setups; here the SOL-JPL method is summarized. Liquid samples were prepared following the suggestions in *Wendl et al.* [2014]; 50 mL polypropylene vials (having already been sonicated) were placed in a glass beaker on a stirring plate to ensure the samples remained well mixed during analysis. The sample was fed into the nebulizer through 0.5 mm Teflon tubing at 0.5 mL min^{-1} using a peristaltic pump. An ultrasonic transducer aerosolizes the liquid allowing BC particles to become suspended. Ultra clean compressed air carries the aerosol stream through a heating and cooling element to dry the aerosol flow. This is fed through the SP2 at known rate, and as

the aerosol stream crosses the laser path particles containing black carbon are heated to the point of incandescence; the emission from this is measured and correlated to the particles BC mass through comparison to BC standard (Aquadag). The mass of individual BC particles was then summed and divided by the volume of liquid that was analyzed (reconstructed from water and air flows). Concentrations are then reported in ug L^{-1} (ng g^{-1} or ppb equivalent).

Detailed discussions relating to the uncertainties of this method can be found in *Schwarz et al.* [2012], *Kaspari et al.* [2013], and *Wendl et al.* [2014]. It is recognized that due to nebulizer efficiency, the SP2 underestimates black carbon concentrations in liquid samples by not measuring the smallest and largest particles [*Kaspari et al.*, 2013; *Wendl et al.*, 2014]. It is also possible that there may be some overestimation of BC content in samples that contain high dust concentrations [*Schwarz et al.*, 2012]. BC concentrations reported here have background values removed and have been corrected for losses using external calibration [*Wendl et al.*, 2014]. Background concentrations were determined through analysis of ultrapure DI water, and for external calibration Aquadag standards in concentrations ranging from 0.5 to 100 ug L^{-1} were used. These standards were freshly prepared each week, sonicated before use, and stored in glass containers in a refrigerator. Based on replication analysis of 5 sample sets over a range of dust concentrations and 10 'dusty' (visible dust content) environmental snow samples collected from other locations in the San Juan Mountains, uncertainty in the concentrations reported here are estimated to range from 2 - 7% for samples visually identified as clean and 6 - 15% for those visually identified as dusty.

3. Results and Discussion

3.1 Water Year 2013

Water year 2013 (WY13) was a unique year in that it was both the dustiest and driest year over the SBBSA data record (2005-2013). The record of dust events at SBBSA, as recorded by the Center for Snow Avalanche Studies while snow cover is retained in SBBSA, and end of year dust concentrations are plotted in Figure 4. While the total number of dust events and the timing of those events were not abnormal relative to other years, the amount of dust deposited in WY13 was more than 30 times the amount of dust deposited in the lowest dust year (2005) and a third greater than the next highest dust year (2009). Over 98% of the total WY13 dust mass was deposited in April, and therefore our measurements capture the transition from a relatively clean to dusty snowpack.

Record mean and WY13 monthly precipitation is plotted in Figure 5. October was the only month to set a new monthly low in WY13, but consistently lower rain/snowfall resulted in 300 mm less precipitation than the record mean and almost 400 mm less than 2008, the wettest year. The only month where precipitation exceeded the record mean was July, and over the time that precipitation typically falls as snow WY13 was on average 26 mm less than the record mean, resulting in a low snow year; it had the latest accumulation date, the lowest peak snow depth (1.78 m), and an average snow depth (1.19 m) that was only slightly higher than the lowest snow year (2012, 1.07 m).

In terms of turbulent and radiative fluxes, WY13 was a near-average year (**Error! Reference source not found.**). Relative to the previous 8-yr mean WY13 had the same average wind speed, air temperature, relative humidity, and longwave/solar irradiance. Over the time period that snow cover was present, mean solar irradiance was slightly

higher (~40 Wm^{-2}) than the previous 8-yr mean, but this did not impact air temperatures which were ~1^0 C cooler, and none of the other fluxes showed significant variation. This indicates that at the beginning of our measurements period the snowpack was typical of mid-March snowpack, despite the slightly lower than average snow depth.

During the measurement period, which is highlighted in gray in

Figure 6, there was lower than average air temperatures and higher than average wind speeds. We believe this is due in part to a major spring storm cycle, which deposited 50 mm of precipitation (22 cm new snowfall) between April 14th and 18th. This event was associated with peak wind speeds of up to 5 m s^{-1} (average ~1 m s^{-1}) and drops in nighttime air temperature to nearly -20° C. Another storm event on April 30th, while not associated with any precipitation, again brought higher than normal wind speeds and another drop in air temperatures. Dust deposition was observed during both of these events.

3.2 LAI Concentrations

Daily measured values of snow depth, density, black carbon and dust concentration, optical grain size, and surface albedo are plotted in Figure 7 over the two-month time period between March 20th and May 20th, 2013. While snow pit observations began before this time period (March 11th) repairs to the field spectrometer delayed measurement of optical grain radius until March 25th (Table 1), at which point consistent observations of all parameters began. We include precipitation, measured from the nearby collector, in these plots to show the influence of new snowfall on these values.

3.2.1 Dust

There were 10 dust events while snow cover was present in WY13 (see Figure 4), 3 of which occurred before measurements began (Nov 9, Feb 8-9, and Mar 6-7), and 1 which occurred while snow cover was still present at higher elevations in SBBSA but after snow all gone at SASP (May 23rd). In the first pit (P1; March 11th) we bagged all 1-L density cuts to capture concentrations across the full profile, from which dust events 1-3 were identified. Dust event 1 'D1' was 150 cm below the surface, just above the ground, D2 was 75 cm below the surface, and D3 was 18 cm below the surface. All of these events were minor, and D3 was not dark enough to be visually identified. Other than these minor dust layers, the bulk snowpack portion of P1 (early season snow) was the cleanest snow sampled, with dust concentrations as low as 0.0004 mg g^{-1}.

After P1, we limited analysis to the 10 gravimetric samples in the top 30-cm. Dust content in individual layers exhibited a wide variation, from 0.001 g m^{-2} to 54 g m^{-2} for dust loading and 0.002 mg g^{-1} to 5.9 mg g^{-1} for dust concentrations. Over the measurement period there was an increasing trend in dust content across all surface layers, shown in Figure 8, even in those with new snow. This could be due in part to the increased atmospheric dust loading in this region, which peaks in April-May-June [*Sorooshian et al.*, 2013], coinciding with peak dust emission in the Colorado Plateau source regions. The marked increases in dust mass were always associated with an observed dust event, and these remained in the deposition layer and then converged with other layers at the surface as snow melt progressed. Scavenging of mass from the surface was only observed at the very end of the season when 15-25% of total dust mass was scavenged by melt water. This process is expressed in Figure 9, which is depth-resolved

evolution in dust concentration for individual layers in the top 30 cm from March 25th-May 18th. In Figures 8 and 9, we also plot albedo to show the strong relationship between trends in dust content in the surface layers and albedo, discussed in more detail in section 3.5.

Dust event 4 (D4) was the first dust event that occurred during our sampling period, a minor event that deposited 0.07 g m^{-2} of dust on March 17th increasing the surface concentration from 0.010 mg g^{-1} on Mar 14th to 0.014 mg g^{-1} on Mar 18th. The next event, D5, began on Mar 21st and was also minor, depositing 0.11 g m^{-2} of dust before being buried by new snowfall on Mar 23rd. On Mar 25th, both D4 and D5 were identified below the newer snow in the visual stratigraphy as 'very faint' with sampled dust concentration of 0.02 mg g^{-1} 10 cm below the surface (D4) and 0.03 mg g^{-1} 5 cm below that (D5). Over the next few days, these layers came closer to the surface and led to the development of melt/freeze crust in the near surface. These layers converged and then surfaced on March 31st, remaining at or in the near surface until April 6th. In Figure 8 dust concentrations are plotted on a log scale and the increase in dust at the surface from these two minor events is more visible.

The next dust event, D6, occurred on April 8th and was the first significant deposition event of the season. There was 48 g m^{-2} of dust deposited over the duration of D6, which is the most mass associated with any dust event since measurements began in 2005 and 90% of the total dust mass deposited in 2013. The impact of D6 on albedo was delayed because it was deposited by a prefrontal wind event and was buried by the precipitation that followed it. Visual stratigraphy in P16 (April 10th) noted the 'significant dust layer' beneath 20 cm of new snow and the sampled dust concentration in this layer

was over 4.0 mg g^{-1} of snow. This single layer concentration was higher than end of year concentrations for six of the other years on record (see Figure 4).

As the new snow became denser and snow depth decreased, the snow surface came closer to D6, but it was further buried by the April 14th-18th precipitation. This storm cycle was associated with two additional dust events; D7, which deposited 2.0 g m^{-2} on April 14th, was noted 16 cm below new snow in the April 14th stratigraphy, D8 deposited 3.5 g m^{-2} between the 15th and 17th of April and was noted at the snow surface on April 16th. In the next pit on April 24th the new snow at the surface had a very low surface concentration of 0.02 mg g^{-1}, and D6-8 were still individual dust layers below it. Dust in the top 3 cm then increased at an exponential rate as dust layers converged; D8 surfaced on April 28th bringing the surface concentration up to 0.2 mg g^{-1}. On April 30th D7 and D8 merged at the surface and the final dust event of the season (D9) deposited an additional ~1 g m^{-2} of dust, increasing the surface concentration to 1.1 mg g^{-1}. D6 began to surface on May 2nd combining with D7–D9, resulting in a surface concentration of 5.07 mg g^{-1}.

The combination of clear, sunny days and emergence/convergence of dust over this time period initiated a rapid melt cycle in the surface layers, leading to high surface roughness and development of melt flow pathways. During the period when surface roughness persisted, the total amount of dust mass at the surface remained the same (54 g m^{-2}), but surface density decreased leading to an increase in dust concentration values. This decrease in surface density was also observed in the 1-L density measurements, discussed in section 3.3.3.

New snowfall from the 5th-10th of May buried D6-9. Clear skies and higher air temperatures led to the rapid emergence of these layers, increasing surface concentrations from 0.2 mg g^{-1} May 9th to 4.3 mg g^{-1} on May 14th. After this point dust loading in the surface decreased from 43 g m^{-2} (May 14th) to 37 g m^{-2} on May 18th (the day before snow all gone) as melt water flushed through the pack. Surface concentrations were more variable than surface loading over this time period, corresponding to a decrease in snow density, similar to the earlier period of rapid melt. The final surface concentration measured was 4.4 mg g^{-1}, 1.5 mg g^{-1} less than the peak surface concentration measured on May 3rd when D6-9 first combined at the surface. In previous studies the assumption has been made that dust persists at the surface over melt and therefore the last gravimetric collection of the season (i.e. end of year dust concentration) represents the total mass deposited over the season. This result indicates that while most of the mass does remain at the surface, some may be scavenged by melt water. It is also possible that scavenging may be more efficient in heavy dust years with rapid end of season melt rates.

3.2.2 Black Carbon

We would like to point out that in discussion and in Figure 7 we report black carbon concentrations in ug L^{-1} or parts per *billion*, whereas dust concentrations are in mg g^{-1} or parts per *thousand* (by weight). In Figure 11 we plot both on the ppb scale to illustrate that the BC concentrations are 4-7 orders of magnitude less than the dust concentrations over the measurement period. Sampled black carbon (BC) concentrations ranged from 0.5 to 26 ug L^{-1} and exhibited strong association with dust concentrations. Like dust, the lowest concentrations were sampled in the first pit on March 11th, which had an average BC concentration of 2.6 ug L^{-1} in the bulk snowpack. Dust and BC co-

varied across the full measurement period, and to avoid being repetitive we quickly summarize; BC values were low in the first part of the measurements period, and rise with deposition of D6-9. Peak values are observed during periods of melt when D6-9 converge at the surface. We do not observe a decrease in concentration with decreasing surface density during periods of heavy melt, because the SP2 concentrations are not dependent on sample mass only on the amount of liquid water analyzed. We also did not observe a loss of concentrations to melt water scavenging at the end of the season.

Black carbon is typically not present in high enough concentrations to be visually identifiable; therefore we have no record of stratigraphy or deposition events outside of what can be reconstructed from concentrations. The range in concentration values was not as great for BC, but the co-variation suggests an association with dust (Figure 11). Except for a very few circumstances dust and black carbon emission are not related processes; one is produced from arid and/or disturbed landscapes and the other is produced via the incomplete combustion of fossil and bio fuels. Potential processes are:

- Synoptic level events that deposit dust also bring black carbon from distal sources.
- Or, BC particles are associated with dust particles in arid source regions prior to emission.

Reynolds et al. [2013] found conglomerations of carbonaceous particles with embedded mineral composition in dust from snow in the nearby Wasatch Mountain Range, UT. These could form prior to emission, during atmospheric transport, or after deposition into the snow cover. The relationship we found could also be an artifact of the

way samples are prepared and analyzed. Additional measurements and further analysis are needed to better understand this relationship.

Measurements of black carbon at other mid-latitude mountain snow cover sites are sparse, and this was the first year BC has been quantified at SBBSA, so there was limited data against which to compare the WY13 concentrations. *Sterle et al.* [2013], the only other study that we are aware of that has used an SP2 to quantify BC concentrations in snow in the Western US, sampled concentrations in surface snow from 25 ug L^{-1} in new accumulation to 135 ug L^{-1} in melting snow in the Eastern Sierra Nevada, CA. These concentrations are 5-12 times greater than what is presented here under similar conditions. They also found that dust and BC concentrations co-varied, and that dust, even in much smaller quantities than occur at SASP, accounted for a greater portion of LAI radiative forcing [*Sterle et al.*, 2013]. If the BC concentrations we sampled in WY13 are representative, it is unlikely that BC is playing a significant role in radiative forcing in this region, especially in the presence of such extensive and heavy dust loading.

3.3 Full Profile Measurements

3.3.1 Temperature

Average snow temperature in P1 was -5^{o}C, and the temperature profile was warmest near the ground, coldest in the mid-pack to in the near surface, and warmer in the top 10 cm typical for a wintertime mid-latitude snowpack. This was the coldest snowpack, from this point the bulk of the snowpack continued to warm reaching 0^{o} C on April 12th, marking a transition toward a melting snowpack. After this, temperatures in the active surface layers varied with surface temperature, but remained around -0.5 ^{o} C, dropping only during the mid-April storm to below -1.0 ^{o} C. After this point, surface

layer temperature increased, corresponding to clearer skies and warmer temperatures that led to the convergence of D6-9 in the near surface. The first fully isothermal snowpack was measured on April 24th but had likely transitioned in the days prior to this. Our measurements indicate that the snowpack remained fully isothermal for the rest of measurements period, with exception of new snow deposited between May 6-8th.

3.3.2 Depth

Peak accumulation occurred at the SASP tower just prior to time period plotted in Figure 7 on March 21st (1.78 cm). The deepest snow pit depth at the measurement site also occurred on March 21st at 1.77 cm. While new snowfall did increase snow depth after this point, the overall trend was decreasing. Prior to D6 this average rate of decline was -2.8 cm/day. This is likely attributable mainly to densification as the snowpack retained cold content (below 0°C) at this point. Over the time period that D6 was at or near the surface, and D7-9 was deposited, this rate increased to -4.3 cm/day. When D6 combined with D7-9 at the surface on May 2nd this rate nearly doubled to -8.0 cm/day until melt out on May 19th. The greatest daily change in snow depth occurred between 15th-17th of May, with -10 cm/day. This rate of depth reduction is 40% greater relative to the last 2 weeks of snow cover in WY06 and 50% faster than WY12, both low snow years with less dust deposition.

3.3.3 Density

Profile trends in density were fairly typical of an intermountain west snowpack, usually less dense and more variable in the surface layers, more consistent and most dense in the mid pack, with decreasing density into the depth hoar above the ground. As would be expected due to metamorphic process mean snowpack density in all layers

exhibited an increasing trend over the measurements period (Figure 11). There were steeper trend lines in the active surface layers (top 10 and 30 cm) where atmosphere/radiation interactions take place. The rate of this increase was tempered by new snowfall, which will almost always lower surface density. The largest decrease in surface density was associated with the April 14th-18th storm cycle when 50 cm of precipitation reduced surface density from 305 kg m^{-3} on April 13th to 182 on April 14th, and then further to 109 kg m^{-3} on April 18th. The next largest decrease came with new snowfall deposited during the May 5-8th storm when surface density decreases from 457 kg m^{-3} on May 3rd to 295 kg m^{-3} on May 8th. The earlier storm was more effective at reducing surface density because it was colder storm with more precipitation, which was deposited on a snowpack that still retained cold content in the surface layers.

Our measurements show the rate at which snow becomes denser is not constant, and plateaus over time during the ablation season. If the increases in density due to new snowfall are removed the average rate of densification across the full profile was 6 kg m^{-3}/day over the first 3 weeks of measurements, 4 kg m^{-3}/day over the next 2.5 weeks when D6-9 was deposited and the snowpack transitioned to isothermal, and then 0.3 kg m^{-3}/day in the last two weeks, when the snowpack was melting and dust was at the surface. Trends in surface layers densities are more variable, in the top 30 cm (top 10 cm) density increased by 12 kg m^{-3}/day (20 kg m^{-3}/day) on average over the first 3 weeks. Over the next 2.5 weeks, densification rates in the top 30 cm increased to 13 kg m^{-3}/day but decreased in the top 10 cm to 17 kg m^{-3}/day. During the last two weeks of melt, densification rates slowed to 2 kg m^{-3}/day in the top 30 cm, and 15 kg m^{-3}/day in the top 10 cm.

This slowing in densification rate is not unexpected; snow metamorphism is an active process driven by temperature and vapor pressure gradients that act to increase both grain size and density over time. In the beginning of the measurement period a high temperature gradient was still present, which lessened as the snowpack transitioned to a melting snowpack during the middle of the measurement period, and slowed further as the control of snow metamorphism shifted toward the presence of liquid water in the absence of a temperature gradient in the last two weeks of snow cover.

Counterintuitive to the general understanding of snow densification over time in the snow free time period between April 27th and May 2nd surface density exhibited a decreasing trend. This decrease in snow density was observed again at the very end of the season between May 14th-18th. We suggest that the heavy dust loading near or at the surface may play a role in these unexpected trends. Increasing surface roughness and the formation of melt pathways was observed over this time (Figure 11) indicating rapid melting in the surface layers could remove mass from individual grains surrounding impurities preferentially, and without enough time for metamorphism to compensate this would result in high surface roughness and decreased density. This impact has not been observed in other years, but neither have sampling intervals been so close together. Additional measurements during melt periods of heavy dust years will give us a better understanding of this process.

3.4 Grain Size

In Figure 12, we show example grain size profiles for four days, plotted with density, temperatures, and visual stratigraphy. At the beginning of the measurement period the snowpack could have been generally described as a meter deep slab of small

rounded sintered grains above nearly 60 cm of faceted depth hoar. The development of this extensive depth hoar was driven by the steep temperature/vapor pressure gradient between air and ground in the early season shallow snowpack, which persisted until more significant snowfall in January. This stratigraphy is visualized in the P5 (March 26th) profile; a relatively clean, consistent, cold snowpack with the exception of D4 and D5 at the near surface driving the formation of ice and melt freeze layers. The P20 (April 14th) profile was warmer and more variable with cold new snow at the surface above D6. While it had not surfaced at this point, a series of melt/freeze layers had formed below D6 indicating that it was still absorbing solar radiation and influencing grain evolution. Below these, the snow cover consisted of a fairly consistent slab of denser larger rounded grains above depth hoar. The P28 (April 29th) profile was an isothermal snowpack with D6-8 in the surface layers. During this period the snowpack was very complex, consisting of melt freeze crusts and infiltrating liquid water to wetting fronts. The P35 (May 11th) profile is a fully melting snowpack with newer snow rapidly rounding/warming above D6-9.

These profiles capture dust-influenced snow cover evolution; melt freeze or ice layers are consistently observed beneath dust layers, even with minor events. In a cold temperature gradient snowpack these layers can influence vapor pressure gradients, leading to the formation of unique dust influenced stratigraphy. This could be a concern on steeper slope angles as these micro temperature gradients can lead to the formation of weak layers that would increase avalanche danger. In the transition to a warmer snowpack, large melt freeze agglomerations typically form around or below dust layers that are in the near surface. In an isothermal snowpack the rapid melting associated with

surfaced dust layers leads to the formation of flow pathways and wetting fronts, particularly above former ice layers.

It should be emphasized that optical grain radius is not a measure of grain shape, but is the radius of an optically equivalent sphere that returns the same hemispherical flux. Typically, OGR profiles track visual stratigraphy well and therefore profiles tend to be intuitive representations of snowpack properties. Occasionally optical grain sizes can be counter-intuitive, for example, with depth hoar. The large striated grains are visually very large, but typically OGR is the same or smaller in these layers than in the well rounded sintered grain layers above- this is because despite the large variation in grain shape the specific surface area (the surface area to volume ratio) is similar in these layers. Larger grain sizes in depth hoar layers do manifest as layers became wetter (see P29), but decrease again as snow flushes through the pack (P35).

The smallest particles we measured (OGR <100 μm) were always associated with new snowfall. The largest grain sizes (OGR 450+ μm) were always associated with melt/freeze conglomerate and ice/wetting front layers. The fastest changes in grain size were measured in aging new snow at the surface, but all layers exhibited increasing trends over the season (Figure 13). Over the first 2.5 weeks, when the snowpack was still cold, growth was slowest (~1 μm/day). Over the next 2.5 weeks, with dust deposition and the transition to an isothermal snowpack, it increased to ~10 μm/day. In the last two weeks as the snowpack melts it lessened again to ~5 μm/day.

Larger changes were associated with grain growth rates in the surface layers. Over the first two weeks the mean rate of OGR growth was 10 μm/day and 19 μm/day for the top 10 cm and top 4 cm, respectively. These rates increased over the next two and

half weeks to 17 μm/day and 27 μm/day over the time period during which dust deposition occurred and the snowpack transitioned to isothermal. Over the last two weeks, the growth slowed to 1 μm/day and 3 μm/day, with a negative trend just prior to snow depletion as discussed below. We suggest the enhanced rates of growth over the middle to end of April correspond with enhanced grain growth by dust deposition, whereas a slowing in the growth rates at the end of the season correspond to the shift in control of snow metamorphism to liquid water.

As with density, a decrease in surface grain size was observed in the absence of snowfall over the two time periods when D6-9 was at the surface. Between May 2nd -5th OGR at the surface (top 2 cm) dropped from 320 to 272 μm while increasing from 245 to 299 μm in the top 30 cm, and 294 to 306 μm across the full profile. In the last week of snow cover surface grain size decreased from 284 μm on May 9th, to 221 μm on May 17th. Even when averaged with lower surface layers, the drop in grain size was still exhibited at the end of snow cover; 329 to 244 μm in the top 10 cm. Again, we suggest that impurities/impurities clusters enhance the transition of phase rate from solid to liquid in the surrounding grains, as water infiltrates the snowpack both grain size and density in the surface layers is reduced. If the lower elevation snow cover receives heavier dust loading than alpine snow cover, which is suggested by the SBBSA dust record [*Painter et al.*, 2012b], this reduction in grain size at the end of the season could help explain the count-intuitive elevational grain size trend detected in remote sensing imagery in *Painter et al.* [2013].

3.4.1 Variability and Sensitivity in Grain Size Retrievals

Given natural variability in snow properties and the 2 cm field of view of the contact probe, we would expect variation between profiles in natural snow, and we wanted to capture this variability in our profiles. Profile descriptions and profile locations are shown in Figure 14. Profiles did exhibit variability (Figure 15), yet when protocol was followed mean variation in OGR was relatively small across all profiles, with an average interquartile range of 46.761 μm, a mean difference of - 0.025 μm, and a RMSD of 46.445 μm. The range in variability, both for mean difference and deviation, never exceeded the error range suggested by *Painter et al.* [2007a] and often fell near or below that of the N-D model. Box plots (1st, 2nd, 3rd Quartile, Max and Min) for profiles are plotted in Figure 16. Profile means, mean differences, and RMSD are summarized in Table 2.

The largest variation occurred for the outside of protocol scenarios, which exhibited an increase in mean OGR of 33.765 μm and a RMSD of 73.986 μm. The largest mean difference in OGR occurred when the pit was allowed to remain open and the face was not shaved back before collection. This confirms the impact of reflected solar radiation, longwave radiation, and turbulent fluxes on grain growth in an open pit, after an hour mean OGR had increased by 71.419 μm. A pit could easily remain open at these time steps (20 minutes to an hour) during fieldwork, and often do. In scenario $Norths_{120}$ the pit had been open for 2 hours, but shaving back the face just 30 cm returned a ~80 μm reduction in mean grain size relative to the profile an hour prior, and was within 8 μm of the reference profile.

While variability was exhibited in grain size retrievals, the range of variability was small, and for within protocol scenarios the difference was well under reported uncertainty for the N-D model. We suggest from these results that if protocol is being followed sensitivity of this method, under similar conditions, is ± 15 μm if collections are occurring on a shaded (typically north) facing wall, which increases to ± 20 μm if collections are taking place on partially shaded or exposed faces (east/west walls). The very small mean difference (- 0.025 μm) between within protocol collections found in this study suggests that variability could average out across multiple profiles. Due to the study plot setup at SASP, our snow pits were southeast facing, and suggest ± 20 μm is a reasonable uncertainty for the measurements presented here. We made all efforts to minimize variability by collecting profile always along the left hand (shaded) portion of the pit face, additionally OGR was always collected first after excavation, and prior to collection the profile portion of the pit face was shaved back ~ 5cm after placement of the tarp.

3.5 Surface Albedo

Retrieving an accurate surface albedo with a field spectrometer requires consistent sky conditions during up-looking and down-looking acquisitions. This limitation resulted in a sparser surface spectral albedo record relative to the other measurements (Table 1). While we do utilize these spectral albedos in Chapter 3 and Chapter 4 to validate radiative transfer model results, here we present the evolution in visible (VIS; 0.285-0.695), near infrared (NIR; 0.695–2.800 μm), and broadband (BB; 0.285–2.800 μm) shortwave albedo measurements from the tower sensors. These are particularly useful because it is a continuous record, and the albedo values are already spectrally integrated

across the wavelength ranges of interest, as LAI concentrations and grain size are negatively correlated with albedo across the visible and NIR wavelengths, respectively. We selected the hourly albedo values for 11:00 AM local hour each day, typically the time frame over which we could be collecting snow pit measurements. The albedos are corrected for slope and aspect following the method described in *Painter et al.* [2012b].

Albedo evolution closely tracks dust patterns in the snowpack, particularly in the surface layer as shown in Figure 8 (dust loading) and Figure 9 (dust concentrations). In the beginning of the measurement period albedos are high, but slowly decay (BB; -0.004/day) as D4 and D5 are in the surface/near surface layers. New snowfall after the deposition of D6 on April 8-9th refreshed albedo to new snowfall values (BB 0.9, VIS 0.95, NIR 0.84). Over the next few days when D6 was in the near surface layers, albedos exhibit a quick decline (BB; 0.9 to 0.66) but increase again with new snowfall on April 14th. Another drop was associated with the deposition of D8 on April 15th, but again, new snowfall over the next few days retained high albedo values. Following snowfall on April 23rd, 12 days of relatively clear skies and the surfacing of D6-8, there was a quick decline in albedo (BB -0.045/day, VIS -0.057/day, NIR -0.035/day) to ~0.3 in all wavelength ranges on April 30th, the day D9 was deposited. The new precipitation on May 5th -8th slowed the radiative impact from the extremely low albedo briefly. As D6-9 resurfaced, albedo decay quickly resumed with VIS albedo dropping from 0.96 to 0.36 in 5 days (BB; 0.8 to 0.35). Values remained around 0.3 for 6 days, forcing the rapid melt and decrease of snow depth at the end of the season.

In WY13, there were two weeklong periods when snow albedo was reduced to 0.3 (70% absorption of incoming solar radiation); between April 30th and May 5th, and then

again between May 12th and May 18th (snow all gone at tower). These time frames correspond to the counter-intuitive observations in surface density/grain size reduction. This supports our hypothesis that the additional energy contribution from dust radiative forcing forces rapid melt in the surfaces layers; scavenging mass from individual grains at a faster rate than snow metamorphism can compensate, reducing grain size and density. NIR albedo values (0.35) were actually higher than VIS albedo values (0.32) on May 4th and 5th, and again on May 15th (0.38, 0.33) supporting the hypothesis of grain size reduction. The only other year that this low of an albedo was measured for this long was WY09, the year with the second greatest dust loading.

The relationships between near-surface grain size (resampled to top 3 cm) and dust (log scale surface concentrations) with VIS, NIR, and BB albedo are plotted in Figure 17. We chose to plot the near-surface layers for these plots, as this is where the first interactions between solar radiation and LAIs/snow grains take place. The strongest is the log-linear relationship between increasing surface dust concentrations and decreasing VIS albedo [R^2 = -0.93], indicating even minor additions of dust mass accelerate albedo reduction. In the absence of impurities, BB albedo would be dominated by ice absorption in the NIR wavelengths, but in the presence of dark impurities, the control of the BB signal shifts to the visible wavelengths due to absorption by LAIs. Our measurements reflect this understanding of snow albedo. Broadband albedo is more strongly related to dust concentrations (R^2=-0.9) than grain size (R^2=-0.58). While NIR albedo generally decreases with increasing grain size the relationship is not as strong as that between dust concentrations and VIS albedo (R^2=-0.65). This could be due to spatial variation in surface grain sizes between the pit site and the tower.

4. Concluding Thoughts

Here, a dataset was presented which contains measured dust and black carbon concentrations, optical grain size, albedo, and other full profile snow properties over a full ablation season. These measurements will allow us to partition radiative forcing between dust and black carbon, develop algorithms to improve detection and modeling of LAI radiative forcing, assess how well models handle snow evolution in the presence of dust, and compare explicit representations of dust radiative forcing to semi-empirical methods.

To summarize, dust content in the bulk snowpack- early season snow- was low- and increased over the spring season. Dust concentrations in the surface layers exhibited high variability, decreasing with new snowfall and increasing with dust deposition. The mass deposited with each event was conserved in the layer in which it is deposited, and individual layers converged at the surface as snow melted. Additional studies have observed this stationary behavior of light absorbing impurities [*Conway et al.*, 1996; *Doherty et al.*, 2013]. A decrease in total dust mass was only observed in the last few days before snow cover depletion, as rapid melt flushed through the pack. Albedo closely tracked dust behavior, reaching very low values during periods when dust layers converged at the surface. This rapid contribution of energy into the snowpack appeared to lead to rapid melt at the surface, decreasing both mass and grain size, and rapid end of season melt that reduced snow pack depth by up to 10 cm per day. Outside of these rapid melt events, grain sizes exhibited an increasing trend over the measurement period, with the highest rate of grain growth occurring over the time period when 98% of the total dust

mass was deposited. Black carbon closely tracked dust patterns, but is present only in minor quantities and likely plays no prominent role in radiative forcing.

Previous studies have shown dust deposition on mountain snow cover can alter timing and amount of peak flow and reduce water availability in the Western US [Painter *et al.,* 2010; *Skiles et al.,* 2012], and the data record indicates that extreme dust years like WY13 may become more frequent. Modeling efforts that will utilize the measurements presented here should contribute toward more accurate quantification of LAI in snow processes as well as improved modeling of energy and mass balance, not only in the western US but also in other regions that experience dust and BC deposition. As disturbance of arid lands increases and the amount of black carbon from incomplete combustion continue to rise, mountain snow cover is at increased risk for deposition of light absorbing impurities, making this effort not only important, but also urgent.

5. References

Bisiaux, M. M., R. Edwards, J. R. McConnell, M. Albert, H. Anschutz, T. A. Neumann, E. Isaksson, and J. E. Penner (2011), Variability of black carbon deposition to the East Antarctic Plateau, AD 1800-2000, *Atmospheric Chemistry and Physics Discussions*, *11*, 31091-31114.

Bisiaux, M. M., R. Edwards, J. R. McConnell, M. A. J. Curran, T. D. Ommen, A. M. Smith, T. A. Neumann, D. R. Pasteris, J. E. Penner, and K. C. Taylor (2012), Changes in black carbon deposition to Antartica from two high-resolution ice core records, 1850-2000 AD, *Atmospheric Chemistry and Physics*, *12*, 4107-4115.

Bond, T. C., S. J. Doherty, D. W. Fahey, and P. Forster (2013), Bounding the role of black carbon in the climate system: A scientific assessment, *Journal of Geophysical Research-Atmospheres*.

Bryant, A., T. H. Painter, J. Deems, and S. M. Bender (2013), Hydrologic Response to Dust Radiative Forcing in Snow in the Upper Colorado River Basin, *Geophysical Research Letters*, *40*(15).

Conway, H., A. Gades, and C. F. Raymond (1996), Albedo of dirty snow during conditions of melt, *Water Resources Research*, *32*(6), 1713-1718.

Deems, J., T. H. Painter, J. Barsugli, J. Belnap, and B. Udall (2013), Combined impacts of current and future dust deposition and regional warming on Colorado River Basin snow dynamics and hydrology, *Hydrology and Earth System Sciences Discussions*, *10*.

Doherty, S. J., T. C. Grenfell, S. Forsstrom, D. Hegg, R. E. Brandt, and S. Warren (2013), Observed vertical redistribution of black carbon and other insoluble light-absorbing particles in melting snow, *Journal of Geophysical Research: Atmosphere*, *118*.

Flagg, C. B., J. C. Neff, R. L. Reynolds, and J. Belnap (2013), Spatial and temporal patterns of dust emissions (2004-2012) in semi-arid landscapes, southeastern Utah, USA, *Aeolian Research*.

IPCC (2007), Climate Change 2007: A Synthesis Report*Rep.*

Kaspari, S., T. H. Painter, M. Gysel, and M. Schwikowski (2013), Seasonal and elevational variations of black carbon and dust in snow and ice in the Solu-Khombu, Nepa and estimated radiative forcings, *Atmospheric Chemistry and Physics Discussions*(13).

Kaspari, S., M. Schwikowski, M. Gysel, M. Flanner, S. Kang, S. Hou, and P. A. Mayewski (2011), Recent increases in black carbon concentrations from a Mt. Everest ice core spanning 1860-2000 AD, *Geophysical Research Letters*, *38*.

McConnell, J. R., R. Edwards, G. L. Kok, M. G. Flanner, C. S. Zender, E. S. Saltzman, J. R. Banta, D. R. Pasteris, M. M. Carter, and J. D. W. Kahl (2007), 20th-century industrial black carbon emissions altered Arctic climate forcing, *Science*, *317*, 1381-1384.

Neff, J. C., A. P. Ballantyne, G. L. Farmer, N. M. Mahowald, J. L. Conroy, C. C. Landry, J. T. Overpeck, T. H. Painter, C. R. Lawrence, and R. L. Reynolds (2008), Increasing eolian dust deposition in the western United States linked to human activity, *Nature Geosciences*.

Nolin, A. W., and J. Dozier (1993), Estimating snow grain size using AVIRIS data, *Remote Sens Environ*, *44*, 231-238.

Nolin, A. W., and J. Dozier (2000), A hyperspectral method for remotely sensing the grain size of snow, *Remote Sens Environ*, *74*(2), 207-216.

Painter, T. H., A. Bryant, and S. M. Skiles (2012a), Radiative forcing by light abosrbing impurities in snow from MODIS surface reflectance data, *Geophysical Research Letters*, *39*(17).

Painter, T. H., N. P. Molotch, M. P. Cassidy, M. G. Flanner, and K. Steffen (2007a), Contact spectroscopy for the determination of stratigraphy of snow grain size, *Journal of Glaciology*, *53*(180), 6.

Painter, T. H., S. M. Skiles, J. Deems, A. Bryant, and C. Landry (2012b), Dust Radiative Forcing in snow of the Upper Colorado River Basin: Part 1. A 6 year record of energy balance, radiation, and dust concentrations, *Water Resources Research*.

Painter, T. H., F. Seidel, S. M. Skiles, A. Bryant, and K. Rittger (2013), Imaging spectroscopy of albedo and radiative forcing by light absorbing impurities in mountain snow, *Journal of Geophysical Research: Atmospheres*, *118*(17).

Painter, T. H., J. S. Deems, J. Belnap, B. Udall, A. F. Hamlet, and C. C. Landry (2010), Decreased water yield from the Colorado River Basin under dust-accelerated snowmelt, *PNAS*.

Painter, T. H., A. P. Barrett, C. C. Landry, J. C. Neff, M. P. Cassidy, C. R. Lawrence, K. E. McBride, and G. L. Farmer (2007b), Impact of disturbed desert soils on duration of mountain snow cover, *Geophysical Research Letters*, *34*.

Reynolds, R., et al. (2013), Composition od dust deposited on snow cover in the Wasatch Range (Utah, USA): Controls on radiative properties of snow cover and comparison to some dust-source sediments, *Aeolian Research*, *In Press*.

Schwarz, J. P., S. J. Doherty, F. Li, S. T. Ruggerio, C. E. Tanner, A. E. Perring, R. S. Gao, and D. W. Fahey (2012), Assessing Single Particle Soot Photometer and Integrating

Sphere/Integrating Sandwich Spectrophotometer measurement techniques for quantifying black carbon concentration in snow, *Atmospheric Measurement Techniques* (5).

Skiles, S. M., and T. H. Painter (2014), A 9-yr record of dust on snow in the Colorado River Basin, paper presented at 12th Biennial Conference of Science and Management on the Colorado Plateau, Flagstaff, AZ.

Skiles, S. M., T. H. Painter, J. Deems, C. Landry, and A. Bryant (2012), Dust radiative forcing in snow of the Upper Colorado River Basin: Part II. Interannual variability in radiative forcing and snowmelt rates, *Water Resources Research*, *48*.

Sorooshian, S., T. Shingler, A. Harpold, C. W. Feagles, T. Meixner, and P. D. Brooks (2013), Aerosol and precipitation chemistry in the southwestern United States: spatiotemporal trends and interrelationships, *Atmospheric Chemistry and Physics*(13).

Stamnes, K., S.-C. Tsay, W. J. Wiscombe, and K. Jayaweera (1988), Numerically stable algorithm for discrete-ordinate-method radiative transfer in multiple scattering and emitting layered media, *Applied Optics*, *27*, 2502-2509.

Sterle, K. M., J. R. McConnell, J. Dozier, R. Edwards, and M. Flanner (2013), Retention and radiative forcing of black carbon in the Eastern Sierra Nevada snow, *The Cryosphere*, *7*.

Wendl, I. A., J. A. Menking, R. Farber, M. Gysel, S. Kaspari, M. J. G. Laborde, and M. Schwikowski (2014), Optimized method for black carbon analysis in ice and snow using the Single Particle Soot Photometer, *Atmospheric Measurement Techniques Discussions*(7).

Figures

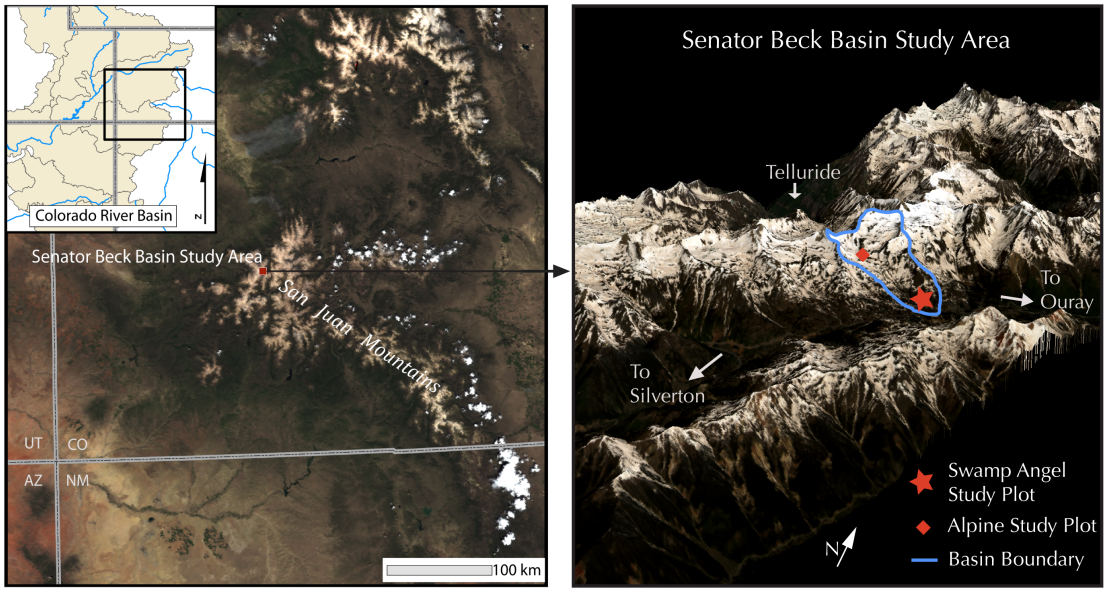

Figure 1 Regional overview of Senator Beck Basin Study Area (SBBSA) at two scales. Inset on left shows location relative to Colorado River Basin.

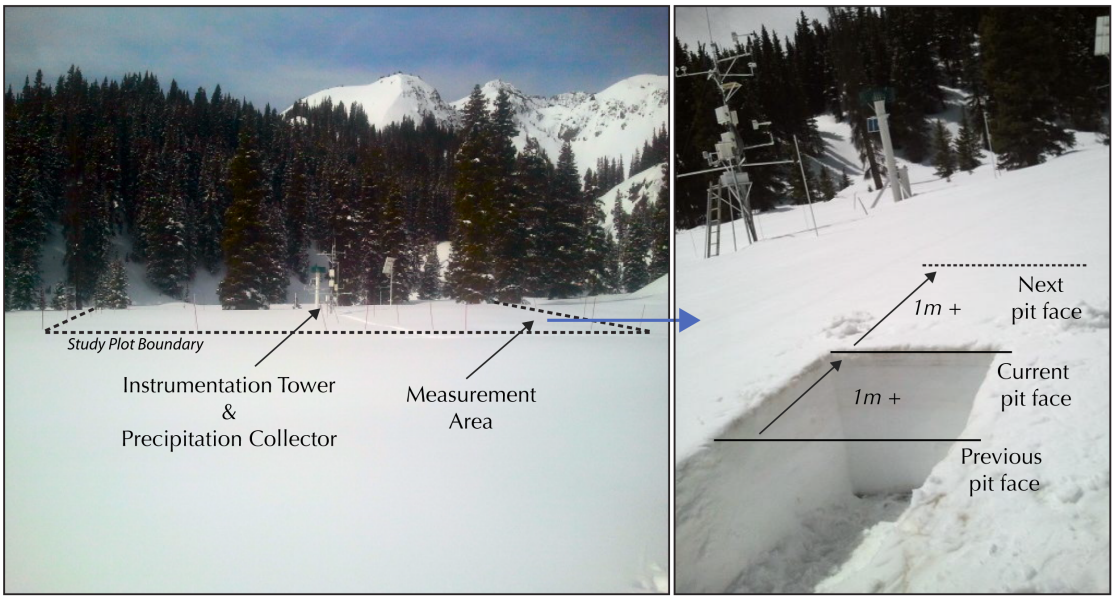

Figure 2 (Left) Photograph of Swamp Angel Study Plot with plot boundaries outlined. (Right) Snow sampling took place on the right hand side of the study plot, progressing from the front toward the back of the study plot with 1m or more between each successive pit face

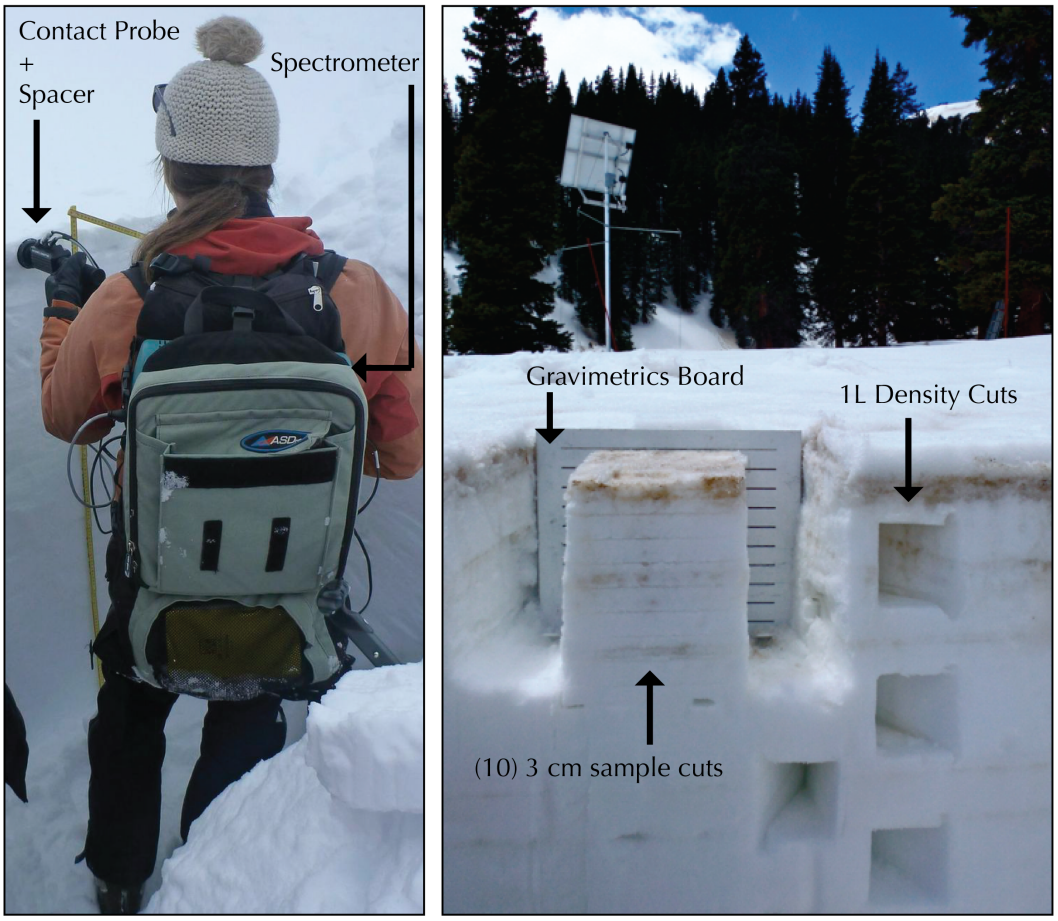

Figure 3 (Left) Solo contact spectroscopy collection; if the spectrometer is worn on the back, and the computer that controls the collections is held by a brace in front, that leaves one hand free to hold the contact probe up against the snow face. Typically the snow pit would be covered by a tarp to reduce outside illumination. (Right) Snow pit face showing density cuts and top 30cm gravimetric sampling, the 3 cm cuts are made using a white powder coated saw (not pictured).

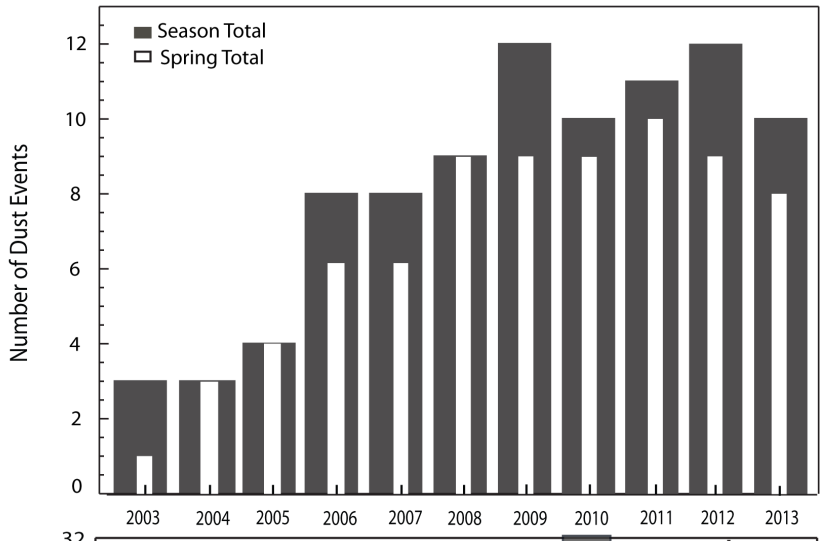
Season Total
Spring Total
Number of Dust Events
0
2
4
6
8
10
12
2003
2004
2005
2006
2007
2008
2009
2010
2011
2012
2013

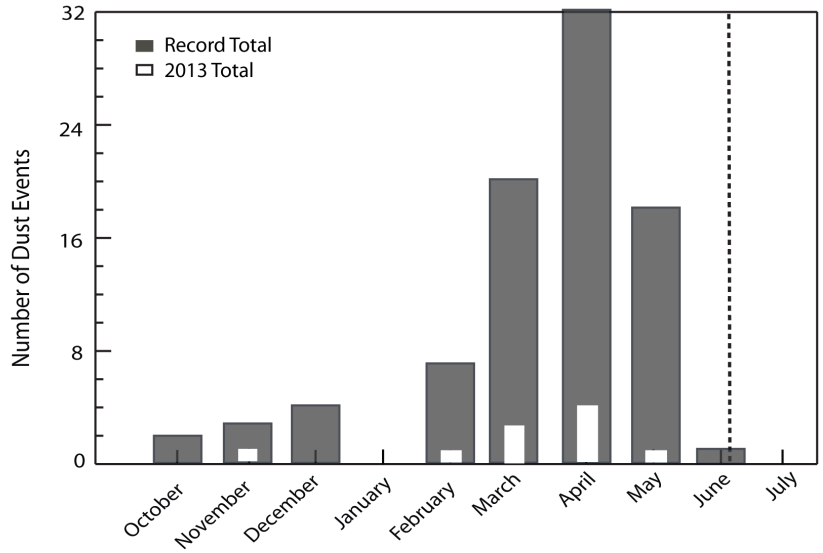
Record Total
2013 Total
Number of Dust Events
0
8
16
24
32
October
November
December
January
February
March
April
May
June
July

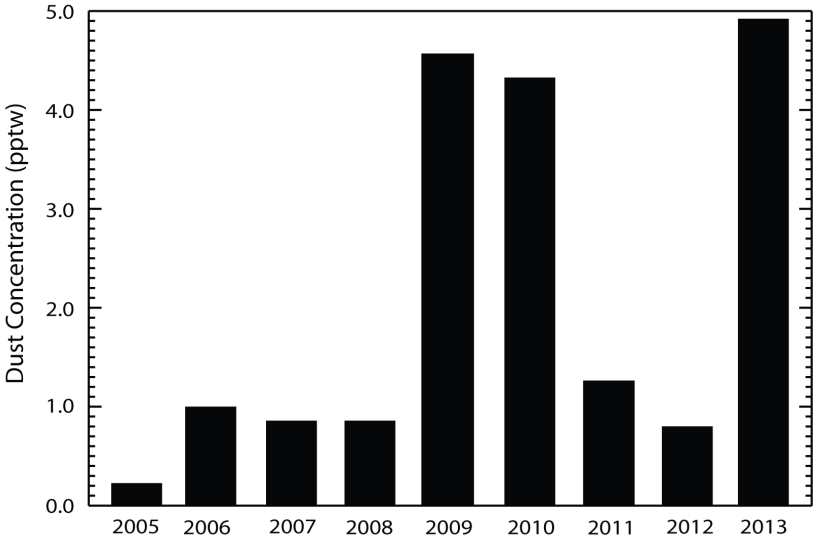
Dust Concentration (pptw)
0.0
1.0
2.0
3.0
4.0
5.0
2005
2006
2007
2008
2009
2010
2011
2012
2013

Figure 4 (Above) Yearly and monthly distributions of dust events in SBBSA, the dotted line indicated average basin-wind snow all gone date. (Below) End of year dust concentrations at SASP.

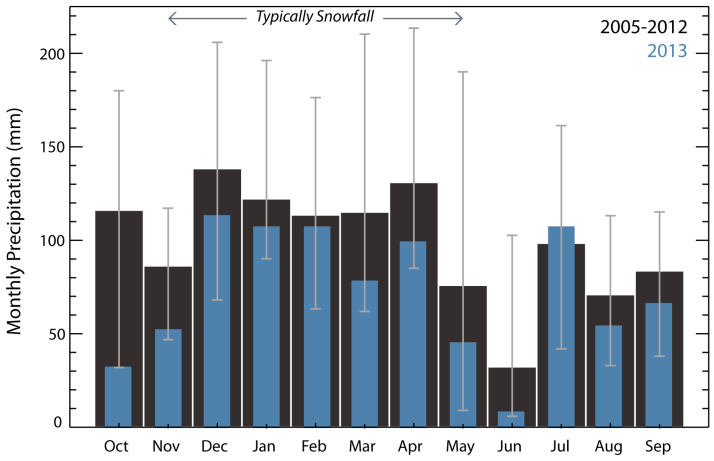

Figure 5 WY13 monthly precipitation relative to previous 8-yr record mean. Full record maximum and minimum precipitation values for each month in gray.

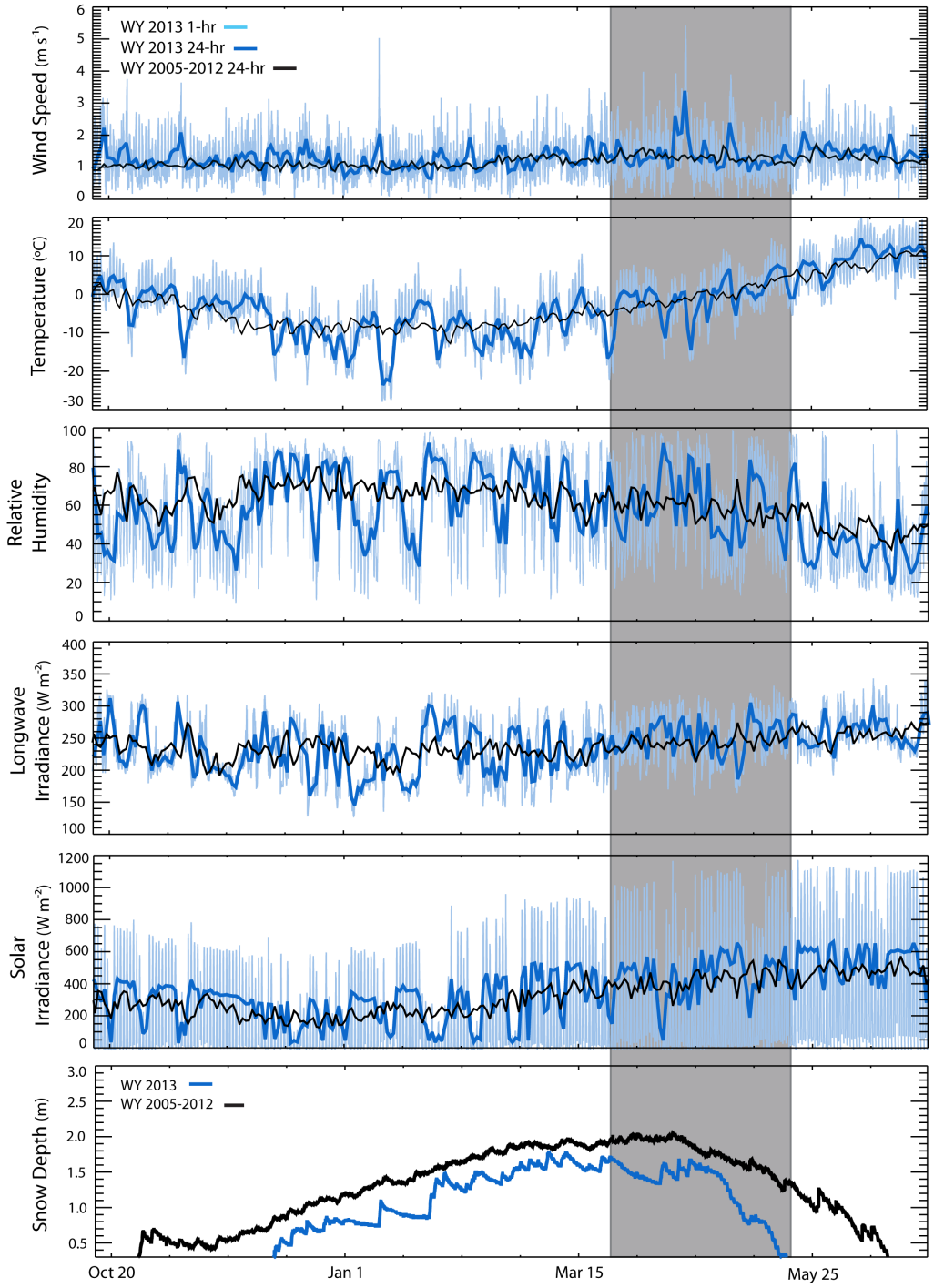
WY 2013 1-hr
WY 2013 24-hr
WY 2005-2012 24-hr
Wind Speed (m s-1)
Temperature (oC)
Relative Humidity
Longwave Irradiance (W m-2)
Solar Irradiance (W m-2)
WY 2013
WY 2005-2012
Snow Depth (m)
Oct 20
Jan 1
Mar 15
May 25

Figure 6 Snow energy balance fluxes and snow depth for WY13 (1-hr, 24-hr) relative to the record mean (24-hr) from the SASP instrumentation tower. Other than lower than normal precipitation resulting in later and lower than average snow accumulation, WY13 was an average year in terms of meteorological and radiative fluxes. The highlighted area represents the measurement time period presented here.

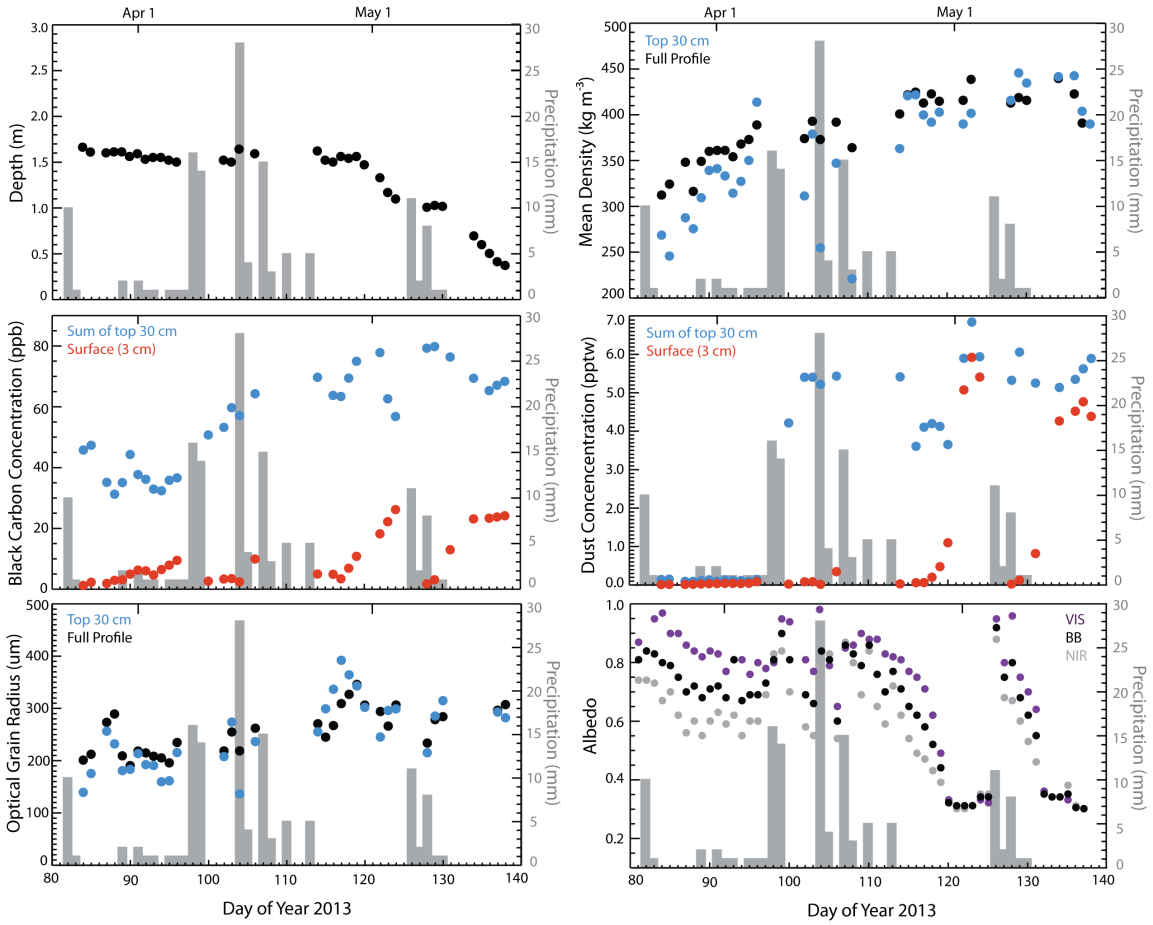

Figure 7 Evolution in snow properties at SASP between March 25th and May 18th, 2013. Depth, density, and optical grain size are from snow pit measurements. Dust and black carbon concentrations are from analysis of gravimetric snow samples. Albedo and precipitation are from the nearby SASP instrumentation suite.

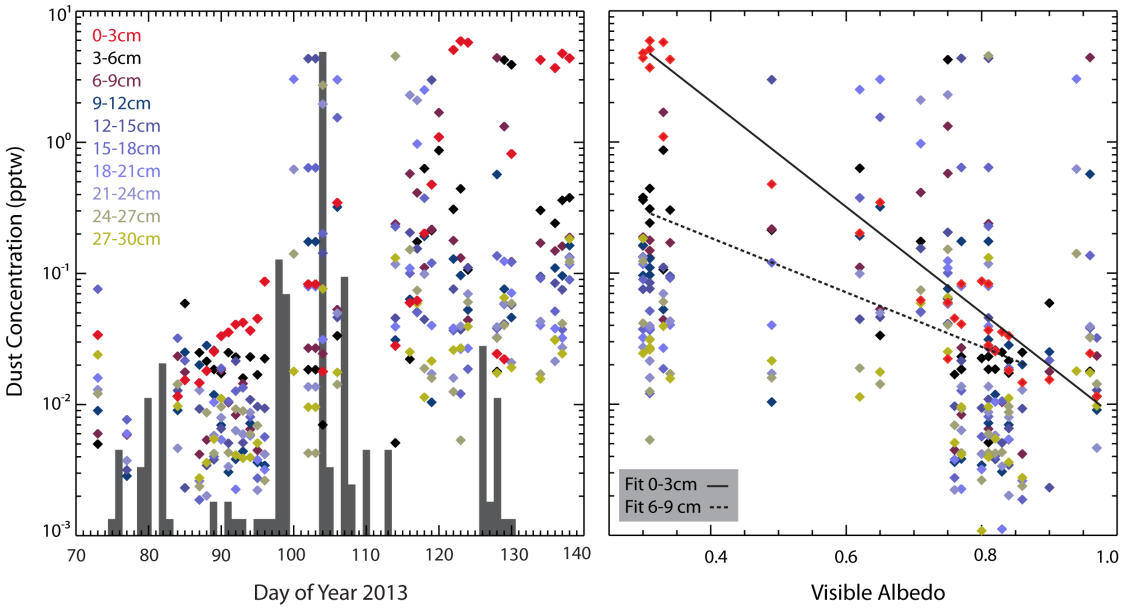

Figure 8 (Left) Log scale evolution in dust concentrations for individual layers in the top 30 cm. (Right) Relationship between log scale dust concentrations and surface albedo (VIS), as would be expected, surface albedo is most strongly related to dust content in the surface layers (exponential fits; R^2 values of 0.94 for 0-3 cm and 0.54 for 3-6 cm).

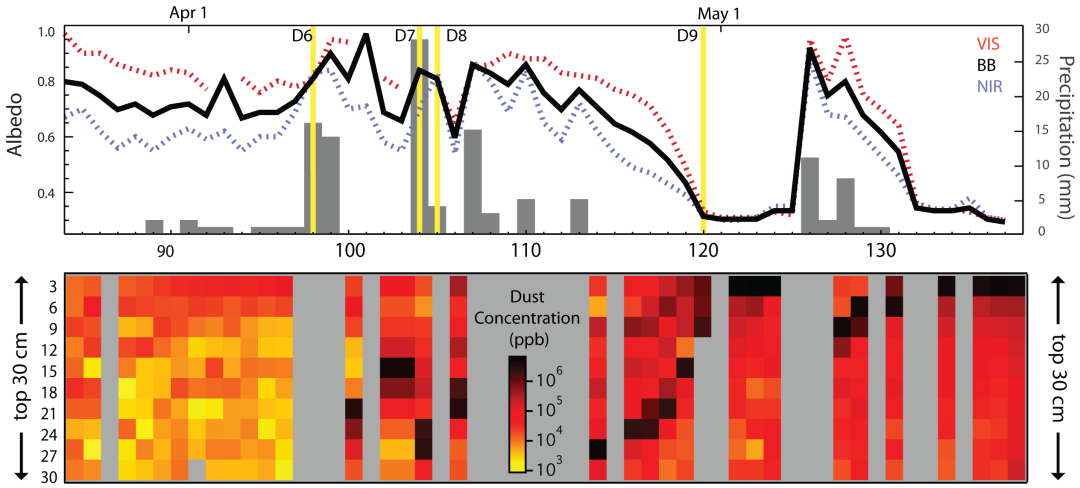

Figure 9 Evolution in snow albedo (above) and dust concentrations in individual gravimetric cuts over the top 30cm (below) by depth. This exhibits the convergence of dust layers from individual dust events (yellow lines) at the surface with melt, and the coincident decrease in surface albedo. Increases in surface albedo are always due to new snowfall; a peak in broadband albedo occurs on DOY 101 with no precipitation recorded at the collector, but field notes indicate it was snowing on this day.

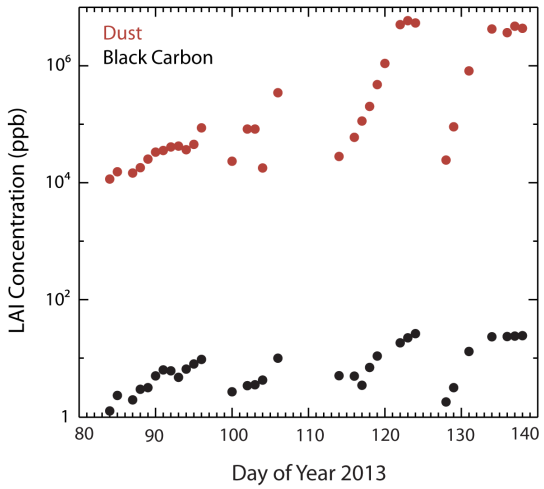

Figure 10 Dust and BC with equivalent concentration units.

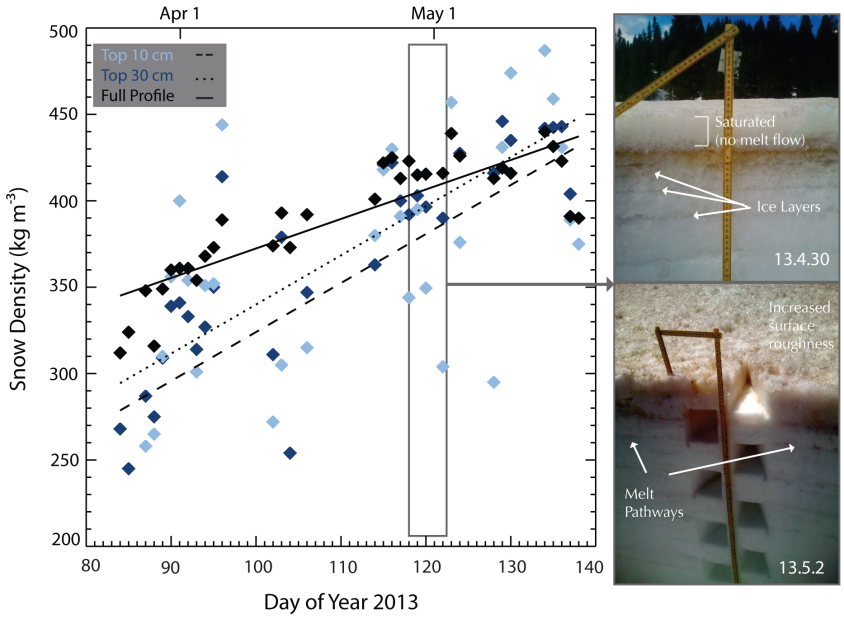

Figure 11 Increasing density trends across the full profile and surface layers. Outline highlights the time period when a decrease in surface density was observed in the absence of new snowfall but in the presence of heavy dust loading. The transitioning snowpack is shown on the right, illustrating the rapid melt from the surface layers and resulting surface roughness.

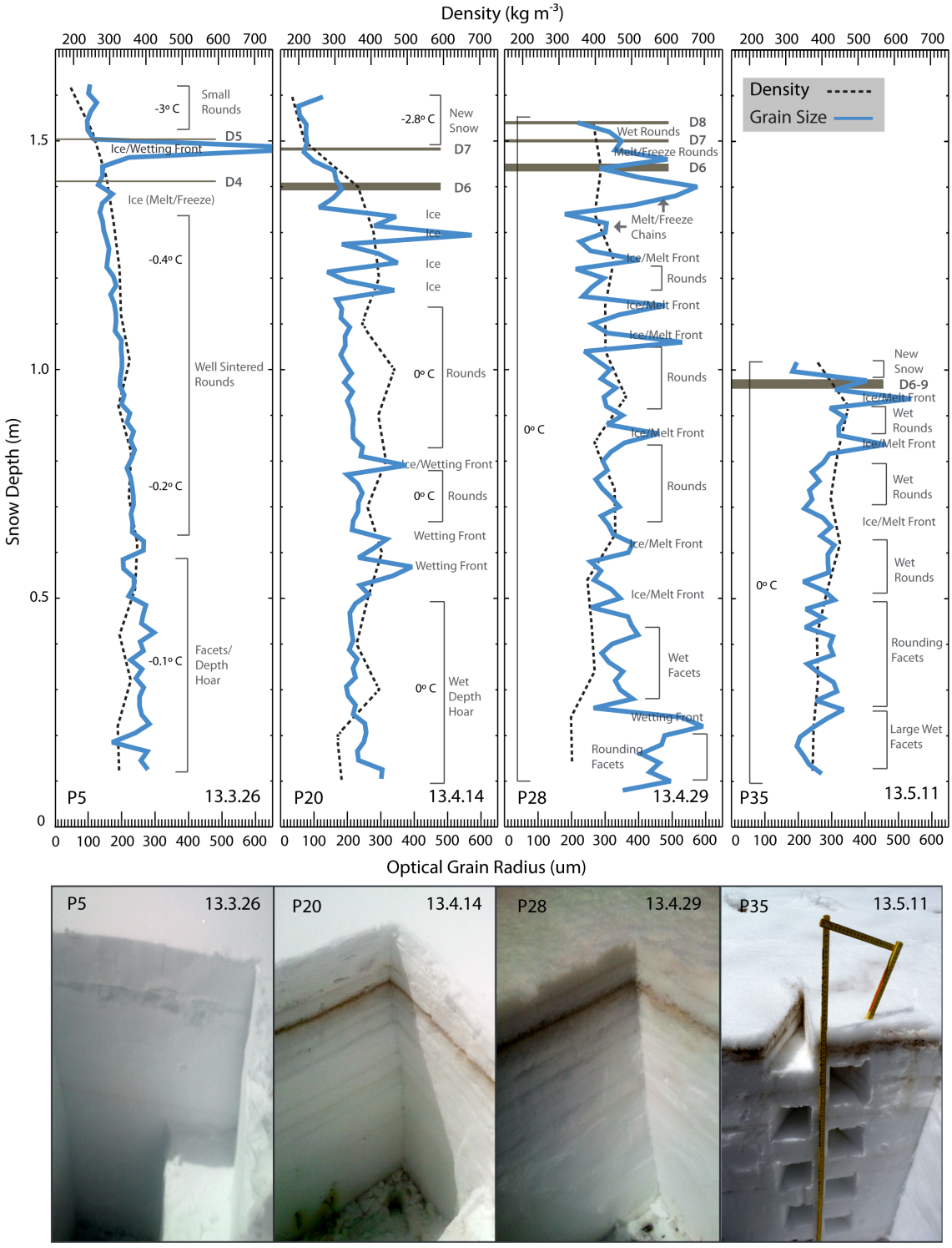

Figure 12 Grain size, density and temperature profiles with visual stratigraphy identifying prominent features. Pits are labeled with corresponding pit number and date of collection. Pictures from these field days are show below.

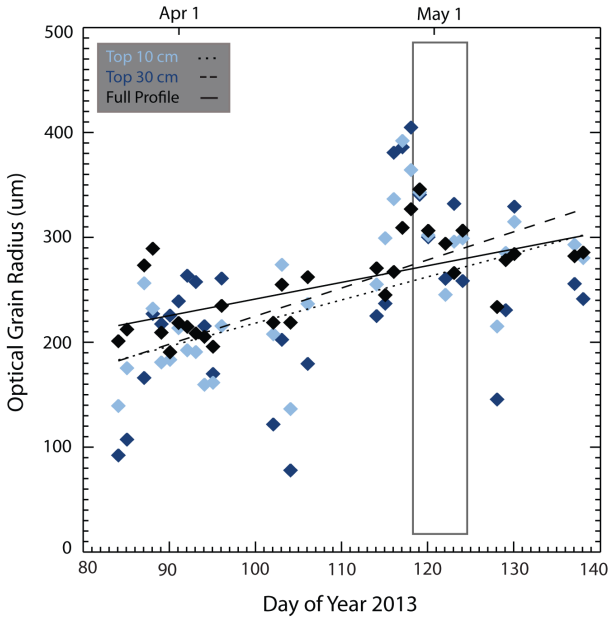

Figure 13 Increasing trend in snow optical grain radius in the surface layers and over the full profile. The outline corresponds to the time period outlined in Figure 9, when a decrease in grain size (and density) was observed in the absence of new snowfall but in the presence of heavy dust loading.

Scenario Name	Description	
12.5.18		
North $_1$	Reference Profile- first collected	*Elapsed time ~5 min*
North $_2$	Collected immediately after North$_1$, to right	
North $_3$	Collected immediately after North$_2$, to left of North$_1$	
West	Collected immediately after North$_3$ on West Wall	
No Tarp	Tarp removed, face shaved back 5cm, North$_1$ recollected	
12.5.19	*Pit excavated back 1m from 12.5.18 pit face*	
North $_1$	Reference Profile- first collected	*Elapsed time ~7 min*
North $_2$	Collected immediately after North$_1$, to right	
North $_3$	Collected immediately after North$_2$, to left of North$_1$	
West	Collected immediately after North$_3$ on West Wall	
East	Collected immediately after West on East Wall	
No Tarp	Tarp removed, face shaved back 10cm, North$_1$ recollected	
North $_{20}$	Pit open 20 min, tarp replaced, North$_1$ recollected	
North $_{60}$	Pit open 60 min, tarp replaced, North$_1$ recollected	
Norths $_{120}$	Pit open 120 min, face shaved back 30 cm, North$_1$ recollected	

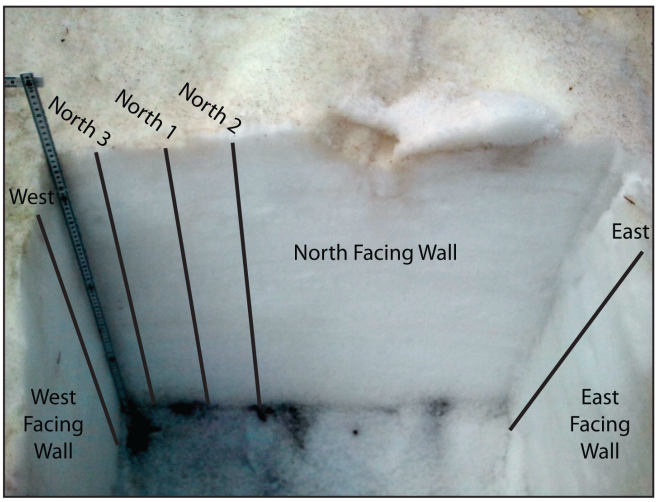

Figure 14 Variability and sensitivity scenarios (top) and a picture showing snow pit on 12.5.19 with pit orientation and profile locations annotated (bottom).

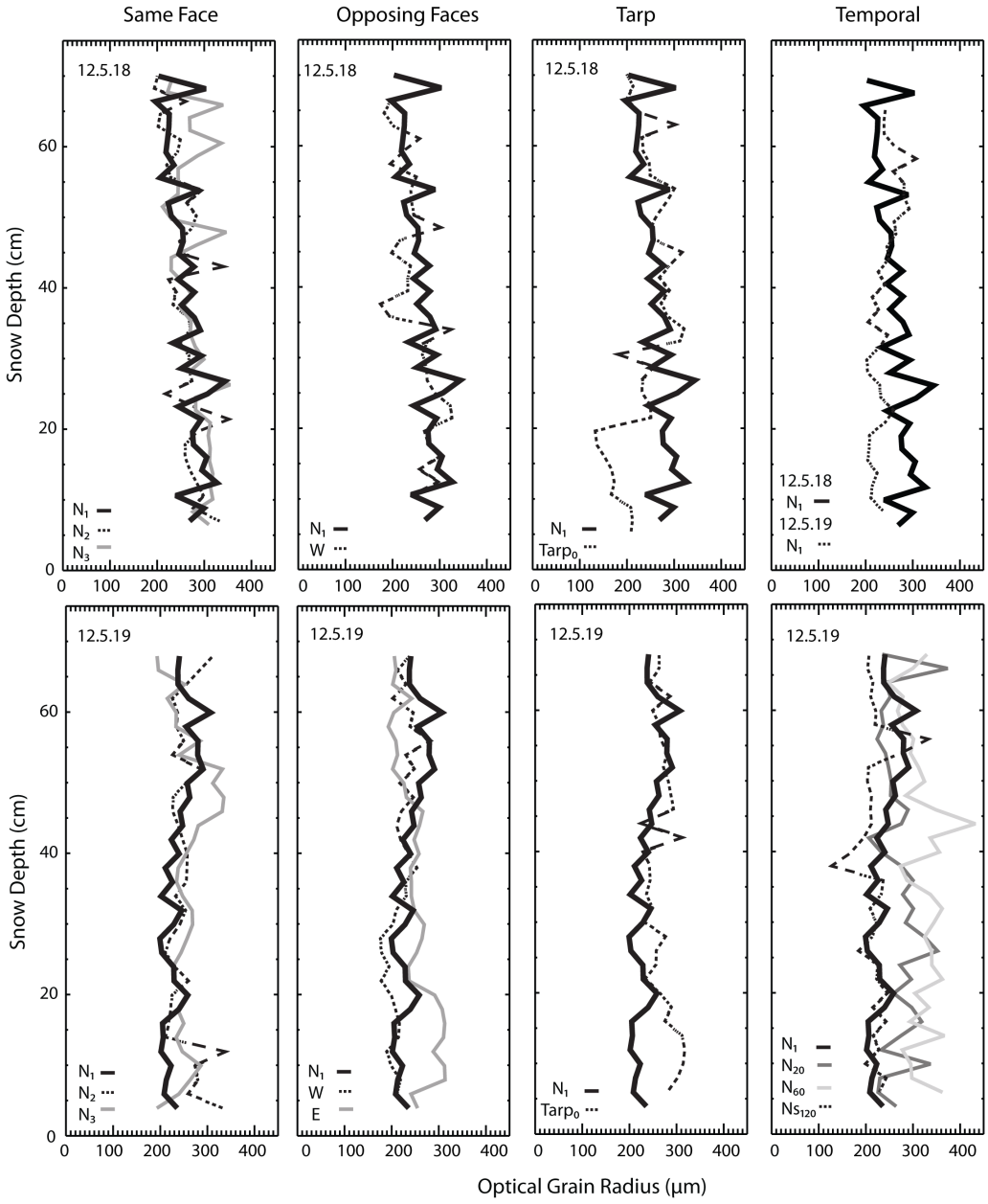

Figure 15 Optical grain size profiles plotted by sensitivity scenario.

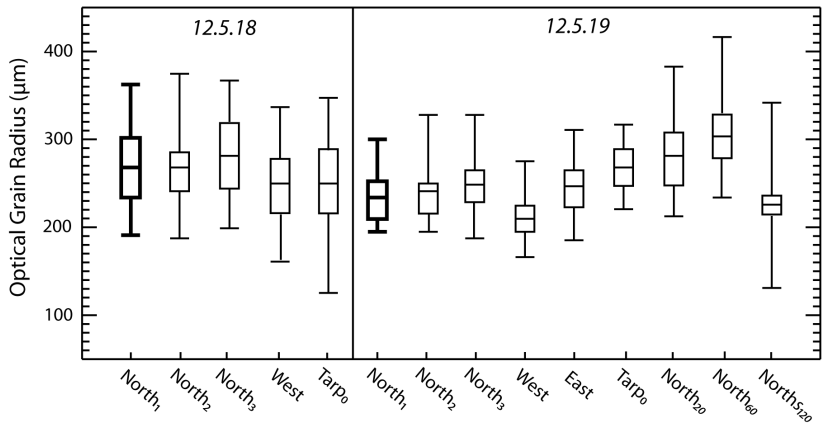

Figure 16 Box plots (1st, 2nd, 3rd Quartile, Max and Min) for OGR profiles. Reference profiles shown in bold.

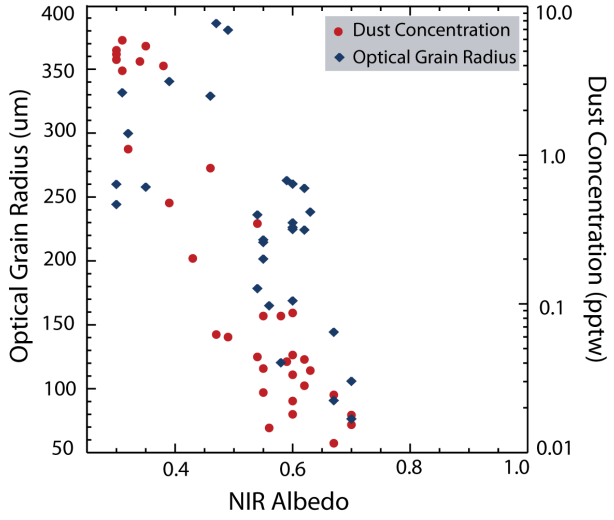
Dust Concentration
Optical Grain Radius
Optical Grain Radius (um)
Dust Concentration (pptw)
NIR Albedo
400
350
300
250
200
150
100
50
10.0
1.0
0.1
0.01
0.4
0.6
0.8
1.0

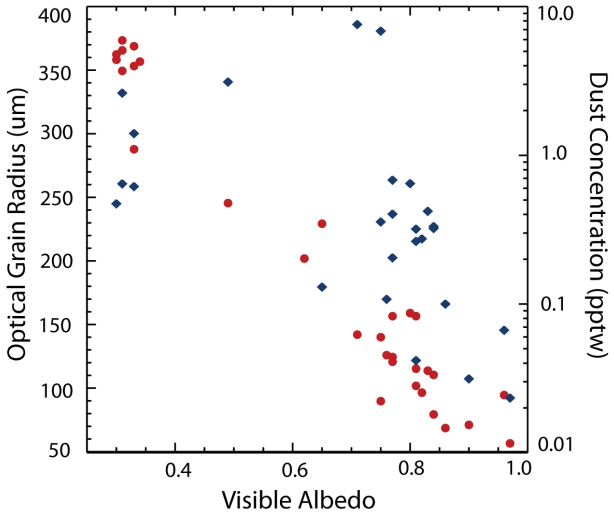
Optical Grain Radius (um)
Dust Concentration (pptw)
Visible Albedo
400
350
300
250
200
150
100
50
10.0
1.0
0.1
0.01
0.4
0.6
0.8
1.0

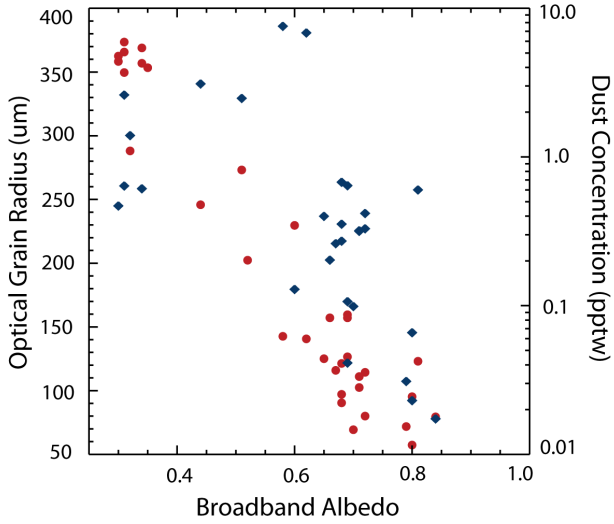
Optical Grain Radius (um)
Dust Concentration (pptw)
Broadband Albedo
400
350
300
250
200
150
100
50
10.0
1.0
0.1
0.01
0.4
0.6
0.8
1.0

Figure 17 The relationships between surface grain size, dust concentration, and albedo. The strongest is the log-linear relationship between surface dust concentration and visible/broadband albedo.

Table 1 Summary of sampling dates and measurements collected over the WY13 measurement dataset. Sky conditions are noted, as recorded in the field notes, to indicate when albedo could be collected accurately. No measurements were made on days with heavy snowfall, due to road conditions. If heavy snowfall started after site access, no spectroscopy was attempted to protect electronics.

Pit #	Date	DOY	Observer	Sky Conditions	Surface Albedo	Contact Spectroscopy	Density Profile	Visual Stratrigraphy	Gravimetric Samples
March									
1	130311	70	MS	full cloud			◆	◆	
2	130314	73	MS	full sun			◆	◆	◆
3	130318	77	MS	variable/cloud			◆	◆	◆
4	130325	84	MS	full sun	◆	◆	◆	◆	◆
5	130326	85	MS	full cloud	◆	◆	◆	◆	◆
6	130328	87	MS	variable/cloud		◆	◆	◆	◆
7	130329	88	MS	full sun	◆	◆	◆	◆	◆
8	130330	89	ID	variable		◆	◆		◆
9	130331	90	ID	consistent	◆	◆	◆		◆
April									
10	130401	91	ID	variable		◆	◆		◆
11	130402	92	ID	consistent	◆	◆	◆		◆
12	130403	93	ID	variable		◆	◆		◆
13	130404	94	ID	consistent	◆	◆	◆		◆
14	130405	95	ID	*snow*		◆	◆		◆
15	130406	96	ID	consistent	◆	◆	◆		◆
16	130410	100	MS	*snow*				◆	◆
17	130411	101	MS	*snow*		◆		◆	
18	130412	102	MS	full sun	◆	◆	◆	◆	◆
19	130413	103	MS	full cloud	◆	◆	◆	◆	◆
20	130414	104	MS	variable/cloud		◆	◆	◆	◆
21	130416	106	MS	variable/cloud		◆	◆	◆	◆
22	130418	108	MS	*snow*			◆	◆	
23	130424	114	MS	sun/cirrus	◆	◆	◆	◆	◆
24	130425	115	MS	full cloud	◆	◆	◆	◆	partial
25	130426	116	MS	full cloud	◆	◆	◆	◆	◆
26	130427	117	MS	full sun	◆	◆	◆	◆	◆
27	130428	118	MS	full sun	◆	◆	◆	◆	◆
28	130429	119	MS	full sun	◆	◆	◆	◆	◆
29	130430	120	MS	variable/cloud		◆		◆	partial
May									
30	130502	122	MS	full sun	◆	◆	◆	◆	◆
31	130503	123	MS	full sun	◆	◆	◆	◆	◆
32	130504	124	MS	full sun	◆	◆	◆	◆	◆
33	130508	128	MS	variable/cloud		◆	◆	◆	◆
34	130509	129	MS	variable/cloud		◆	◆	◆	◆
35	30511	130	MS	full sun	◆	◆	◆	◆	◆
36	130514	134	JD	-			◆	◆	◆
37	130515	135	JD	-			◆	◆	◆
38	130516	136	JD	-			◆	◆	◆
39	130517	137	MS	sun	◆	◆	◆	◆	◆
40	130518	138	MS	sun	◆	◆	◆	◆	◆

Table 2 Values for the mean profile OGR, mean difference (from the reference profile), and root mean square deviation (RMSD). Reference profiles were the first collected, and are indicated by bold text. The largest variations in mean OGR and RMSD's occurred for the No Tarp scenario on May 18th, and for the extended open pit scenarios on May 19th.

Profile	Average OGR	Difference	RMSD
12.5.18			
North$_1$	267.721	/	/
North$_2$	266.812	-0.909	49.239
North$_3$	282.443	14.722	52.499
West	250.068	-17.987	57.305
No Tarp	249.034	-18.686	81.622
12.5.19			
North$_1$	233.696	/	/
North$_2$	240.737	7.040	43.228
North$_3$	248.499	14.802	41.589
West	210.742	-22.954	34.135
East	246.313	12.616	56.531
No Tarp	268.797	35.101	53.889
North$_{20}$	280.922	47.225	72.505
North$_{60}$	305.116	71.419	87.927
Norths$_{120}$	226.168	-7.528	37.038

Chapter 3

A method to retrieve the complex refractive index and single scattering optical properties of dust deposited in mountain snow cover

Abstract

Dust on snow can have regionally important climatic and hydrologic impacts resulting from direct reduction of surface albedo and indirectly from the initiation of snow albedo feedbacks. Modeling the radiative impacts of dust deposited in snow requires knowledge of the optical properties of both components. Here we present an inversion technique to retrieve the effective optical properties of dust deposited in mountain snow cover from measurements of hemispherical dust reflectance and particle size distributions using radiative transfer modeling. First, modeled reflectance is produced from single scattering properties modeled with Mie theory for a specified grain size distribution over a range of values for the imaginary part of the complex refractive index (k=-0.00001 to 0.1). Then, a multi-step look-up table process is employed to retrieve the imaginary part of the complex index of refraction and single scattering optical properties by matching measured to modeled reflectance between 0.35 and 2.5 μm at 10 nm resolution. The real part of the complex refractive index for dust aerosols ranges between 1.5 and 1.6 and a sensitivity analysis shows the method is relatively insensitive to the choice of n within this range, 1.525 was used here. Using the values retrieved by this method to update dust optical properties in a snow+aerosol radiative transfer model reduces errors in spring time albedo modeling by 50% to 70%, matching measured albedo to within 2% on average in the visible wavelengths and 5% over the full range of snow reflectance.

1. Introduction

Mineral dust particles emitted from arid and disturbed landscapes are the most common atmospheric aerosol by mass [*Andreae*, 1995]. The global radiative impact of these dust aerosols can be positive or negative depending on how they influence cloud formation and on their optical properties, which describe the way they reflect, scatter and absorb electromagnetic radiation [*Myhre and Stordal*, 2001; *Tegen et al.*, 1996]. Given the importance of the optical properties on determining to magnitude of aerosol radiative forcing, there have been multiple direct analysis and indirect inversion techniques developed to determine the optical properties of aerosol dust and dust from geographic source regions [*De Luisi et al.*, 1976; *Grams et al.*, 1974; *Patterson et al.*, 1977; *Sokolik et al.*, 1993]. The bulk of this effort has focused on Saharan dust, which dominates dust aerosol mass loading [*Kandler et al.*, 2007; *Linke et al.*, 2006; *C L McConnell et al.*, 2008; *Patterson et al.*, 1977; *Wagner et al.*, 2012].

Dust aerosols also influence radiative forcing when deposited onto snow cover [*Painter et al.*, 2012; *Skiles et al.*, 2012]. Relatively clean snow is highly reflective in the visible wavelengths and even moderately absorbing dust aerosols modify albedo by darkening the surface, an important but highly regional process that has received less attention than atmospheric dust radiative forcing. The impacts of dust in snow have been most well studied in the mountain snow cover of the Colorado River Basin, which is at risk for dust deposition in the springtime when wind speeds and dust emission rates peak upwind in the semi-arid Colorado Plateau [*Flagg et al.*, 2013; *Painter et al.*, 2012]. Deposition of mineral dust has increased five fold in this region since settlement and disturbance of the west [*Neff et al.*, 2008], and extreme dust years may become more

frequent in the future as climate warms and vegetation dynamics shift [*Li et al.*, 2013; *Munson et al.*, 2011]. The springtime deposition of dust has been shown to shift timing and intensity of peak snow runoff and reduce total water yield [*Deems et al.*, 2013; *Painter et al.*, 2010; *Skiles et al.*, 2012]. This has water resource implications for the Colorado River, an essential and over allocated waterway system that is dependent upon springtime snowmelt in the upper basin to replenish lower basin reservoirs [*Christensen et al.*, 2004].

Dust also has also been shown to impact the snow albedo of glaciers in the Himalaya [*Gautam et al.*, 2013; *Kaspari et al.*, 2013; *Kaspari et al.*, 2009], Switzerland [*Oerlemans et al.*, 2009], annual snow cover of the Sierra Nevada [*Sterle et al.*, 2013], and the Greenland Ice Sheet [*Dumont et al.*, 2014]. Additional observational studies of dust in snow have occurred in the European Alps ([*De Angelis and Gaudichet*, 1991; *Franzén et al.*, 1994; *Grousset et al.*, 2003; *Schwikowski et al.*, 1995]), central/east Asia [*Wake and Mayewski*, 1994; *Xin et al.*, 2014], Antarctic Penninsula [*J R McConnell et al.*, 2007], and Greenland [*Bory et al.*, 2003]. It has also been suggested that dust on snow may be responsible northern China remaining ice free during the last glacial maximum [*Krinner et al.*, 2006].

So, while radiative forcing by dust in snow has been well recognized for decades, its precise value has largely remained unquantified. Most snow radiative forcing models justify neglecting dust because black carbon, a widespread light absorbing aerosol produced by incomplete combustion, can be orders of magnitude more absorbent by mass than dust and the effects of dust loading in snow should be similar to those of optically equivalent concentrations of black carbon [*Warren*, 1984; *Warren and Wiscombe*, 1980].

These assumptions are poorly justified and it is of interest to determine the optical properties in dust deposited in snow, which cannot be properly inferred from source region dust, as particle size distributions and overall composition are altered during atmospheric travel [Miller *et al.,* 2004], and exact source area is unknowable.

The radiative properties of dust aerosols, which are size- and wavelength-dependent, are described by the complex index of refraction:

(1) $$m = n + ik$$

The real part, *n,* also known as the simple index of refraction, is the ratio of how fast light travels through a medium relative to how fast it would travel through a vacuum. Values of *n* have been fairly well established for airborne mineral aerosols, and generally range from 1.5 to 1.6 for dust aerosols and between 1.4 and 1.6 for pure mineral phases [*Barthelmy*, 2006; *Grams et al.*, 1974; *Meng et al.*, 2010; *Patterson et al.*, 1977; *Sokolik et al.*, 1993; *Wagner et al.*, 2012; *Zhao et al.*, 1997].

The imaginary part, *k*, describes absorption loss as the wave propagates through the medium and despite a number of methods to determine it, it is less well established for dust aerosols. Methods can be generalized into two categorized: analysis based and inversion techniques. Analysis methods use laboratory measurements to determine k values, and can be classified as either radiation or composition based. Radiation methods use diffuse reflectance or transmitted light to retrieve *k* values from radiation theories, like the two flux Kubelka-Munk theory [*Patterson et al.*, 1977]. Composition based methods use mixture models to determine *k* values from known refractive indices of pure mineral components [*Ebert et al.*, 2004; *Sokolik and Toon*, 1999; *Sokolik et al.*, 1993].

Inversion methods for determining k values utilize measurements from one or more optical instruments, like nephelometers, photometers, and spectroradiometers, to determine scattering and reflectance. These instruments can be in the laboratory [*Wagner et al.*, 2012], in the field [*Grams et al.*, 1974], or on airborne remote sensing platforms [*C L McConnell et al.*, 2008; *Osborne et al.*, 2008; *Redemann et al.*, 2000]. Measurements are then used to retrieve k values by relating them to modeled scattering/reflection. These methods utilize various combinations of measurement techniques and modeling theories, which results in reported k values that vary by orders of magnitude, even for dust from the same source region.

Here, an inversion method is presented to determine the spectrally varying effective complex index of refraction for dust deposited in mountain snow cover in southwestern Colorado. Measured dust particle size distributions are used to model single scattering optical properties from Mie theory for varying values of k, and a specified value of n. Multiple scattering and reflectance is then modeled from single scattering optical properties, and the complex index of refraction is retrieved by matching measured hemispherical dust reflectance to modeled reflectance across the solar wavelengths. The single scattering optical properties, associated with retrieved k values, are incorporated in a snow/aerosol radiative transfer model to verify the validity of results by comparing modeled albedo of snow containing dust to albedo measured in the field.

2. Methods

2.1 Study Area and Field Sampling

In this paper, we work with dust collected from snow at Swamp Angel Study Plot (SASP), a subalpine study plot located in Senator Beck Basin Study Area (SBBSA), a

290 ha study basin located in the San Juan Mountains of southwestern, CO [*Painter et al.*, 2012]. The San Juan Mountains are the first major mountain range approached by dust aerosol plumes emitted from the southern Colorado Plateau, and SBBSA was established in 2004 to monitor the hydrologic impacts of dust in snow in the Colorado River Basin (CRB). The location of SBBSA location within the CRB and Colorado Plateau physiographic region is shown in Figure 1. The study area is managed by the Center for Snow Avalanche Studies in Silverton, CO, which maintains the sites, carries out snow sampling, and collects consistent observations of dust events. SASP is one of two study plots in SBBSA, and instrumentation at these sites has been monitoring wind speed and direction, air temperature and relative humidity, snowpack depth, incoming and outgoing broadband solar, and incoming longwave radiation since water year 2005. More detailed descriptions of the study area and data record can be found in *Painter et al.* [2012] and *Landry et al.* [2014].

Snow measurements at SASP have included weekly collections of snow samples for determination of dust stratigraphy in the top 30 cm of the snow column at 3 cm intervals (the approximate maximum depth at which radiative forcing is influenced by light absorbing impurities). These samples, referred to as gravimetric samples, are sent to the Snow Optics Laboratory at NASA's Jet Propulsion Laboratory in Pasadena, CA (hereafter 'SOL-JPL') where they are filtered and weighed to find dust concentration [*Painter et al.*, 2012; *Skiles and Painter*, 2014]. Additional sampling of individual dust layers occurs per dust event by collecting snow in a shallow layer over a 0.5 m^2 area, referred to as bulk samples. Bulk samples are sent to the Geosciences and Environmental Change Science Center of the United States Geological Survey in Denver, CO where they

are dried and preserved, and analyzed for physical, chemical and mineralogical compositions [*Lawrence et al.*, 2010].

This data record has been used to asses the interannual variability of dust deposition and dust composition [*Lawrence et al.*, 2010; *Skiles et al.*, 2012], but previous measurements were not carried out in a way to facilitate radiative transfer modeling. To address this void, a high-resolution record of snow properties and gravimetric dust concentrations were collected on a near daily basis over the last two months of snow cover in 2013. A detailed description of this data set was presented in Chapter 2. Briefly, measured snow properties included spectral snow albedo, grain size, and snow density. Spectral albedo, the ratio between the average of ten up-looking and ten down-looking hemispherical flux collections, was measured above the site of gravimetric snow sampling with a field spectrometer (ASD; FieldSpec3). The optical grain size, the size of the optically equivalent sphere which returns a similar hemispherical flux, was retrieved via contact spectroscopy [*Painter et al.*, 2007] using the Nolin-Dozier model [*Nolin and Dozier*, 2000] in 2 cm increments across the full vertical snow profile. Snow density in each of the 10 gravimetric samples in the top 30 cm was calculated from sample mass and volume. Below the top 30 cm, snow density was measured with a 1-L density cutter and field scale. Laboratory analysis of snow samples relevant to this study included dust concentrations and particle size distributions, described in Section 2.2.

2.2 Laboratory Measurements

The daily gravimetric samples were collected in Nasco brand Whirl-Pak bags, and to minimize disturbance samples were kept frozen and shipped in coolers packed with dry ice over night to SOL-JPL where they were stored in a walk-in freezer until time of

analysis. Prior to analysis, samples were removed from the freezer and allowed to melt in a stand-alone refrigerator to inhibit bacterial and algae growth in the melted samples. Samples were placed in an ultrasonic sonicator in the original sample bags for 20 minutes to agitate settled impurities and ensure samples were well mixed. Total sample mass was then recorded before drawing off a 50 ml aliquot for additional analysis, including particle size distribution. The remaining sample was filtered through individual pre-weighed Nuclepore 0.495 μm pore diameter filters. Filters containing impurities were then air dried, for at least two days, and reweighed after removing any large biological components (mainly pine needles). Dust concentrations are reported in milligrams of dust per gram of snow sample (mg g^{-1}) by taking the ratio between the differential dust mass and total snow sample mass [*Painter et al.*, 2012]. This is equivalent to parts per thousand by weight.

The optical property retrieval technique presented here does not account for individual constituents of the impurity mixture. While impurities are referred to as dust because they dominate the impurity mass, black carbon (BC), a byproduct of incomplete combustion, is another widespread and persistent light absorbing aerosol that is found in snow and ice cover all over the world [*Bisiaux et al.*, 2011; *Doherty et al.*, 2010; *Huang et al.*, 2011; *Kaspari et al.*, 2011; *Sterle et al.*, 2013]. The presence of BC could influence the selection of the real part of the refractive index, which has higher suggested values (n=1.75-1.95 [*Bond and Bergstrom*, 2006]) than dust aerosols. This was not accounted for here, though, because in WY13 BC represented a minute portion of the impurity volume fraction. Over the spring melt season BC concentrations ranged from 2-26 ppb,

which accounts for, on average, 0.01% of the total impurity concentration (see Chapter 2).

Particle size distribution (PSD) between 0.05 and 2000 μm were quantified utilizing laser light diffraction (Malvern Instruments; Mastersizer 2000E) from dust laden liquid snow samples introduced directly using a wet dispersion system on the same day that snow samples were melted and filtered. The obscuration constraints of the system limits PSD analysis to visibly dusty samples, but the extreme dust loading in spring 2013 enabled us to capture PSD's from 12 gravimetric samples, representing single and merged dust layers. Other than sonification, which was necessary to collect a representative aliquot, no treatments were applied to the 2013 samples to minimize sample disturbance. While there is variation in sample preparation, SOL-JPL PSD's are similar to USGS PSD's, which are freeze dried and digested to remove organics and carbonates to insure analysis of dust species only [*Lawrence et al.*, 2010].

Hemispherical reflectance of fully dry filtered dust was measured with an Analytical Spectral Devices (ASD) FieldSpec3 spectrometer (the same used to measured snow albedo) coupled to an ASD RTS-3ZC integrating sphere. The spectrometer contiguously samples the spectral region between 0.35-2.5 μm, with a spectral resolution ranging from 0.003 μm (at 0.7 μm) to 0.01 μm (at 1.4 and 2.1 μm) and splined reportage at 1 nm. The integrating sphere has an internal coating of Zenith® diffuse polymer material that is a highly reflective and Lambertian reflector over the instrument's spectral range, ensuring retrieval is insensitive to directional reflectance features coming from the sample. Close to solar irradiance level light is delivered by the collimated tungsten light source. Reported reflectance is the ratio between the measured reflectance from the

Zenith® diffuse reference standard and that from the sample. As with PSD measurements the heavy dust loading in 2013 allowed for reflectance measurement of multiple samples: there were a total of 7 optically thick dust samples, of ~1 mm thickness or more, representing both single and merged dust event layers (see picture in Figure 4).

2.3 Radiative Transfer Modeling

The modeling and analysis scheme described here is represented in Figure 2. Mie theory was used to model single scattering and absorption for a measured particle size distribution and specified value of n with a range of *k* values, for wavelengths between 0.35 and 2.5 μm at 10 nm resolution. The spectral range matches spectrometer measurements and the spectral resolution matches the snow/aerosol model used to validate results. The particle size distribution is described by the volume weighted mean radius and standard deviation of log(r) from the PSD measurements of dust samples. The use of Mie theory requires the assumption of spherical dust particles. This is reasonable, but not perfect assumption, and discussion of the limitations of treating dust aerosols as spheres can found in *Meng et al.* [2010] and *Yi et al.* [2011] and citations therein.

After a sensitivity analysis we determined outputs were relatively insensitive to the selected value of real part of the refractive index between n=1.5 and n=1.6, where the shift in the imaginary part was $1\text{-}3*10^{-5}$ (Figure 3). Similar insensitivity is reported in other studies [*Grams et al.*, 1974; *Kandler et al.*, 2007; *C L McConnell et al.*, 2008; *Yi et al.*, 2011]. Here n=1.525 was selected to match the value of *Grams et al.* [1974], which was measured for dust from the southwestern US using the immersion oil technique. The values for the imaginary part of the refractive index, *k*= -0.00001 to -0.1, at 0.00001 resolution, were selected to bracket the range of reported values for dust aerosols and

mineral components in the literature. The single scattering optical properties were used to model multiple scattering and reflectance using the plane parallel discrete ordinate radiative transfer algorithm DISORT [*Stamnes et al.*, 1988]. Reflectance was then catalogued by wavelength and *k* value to create a reflectance look up table (LUT; see Figure 4).

A two-step LUT process was used to retrieve spectrally varying optical properties from measured dust reflectance. First, *k* values were retrieved by matching measured reflectance to modeled reflectance at each wavelength, represented by an alignment of reflectance curves in Figure 4. In the initial production of the look up table differences between matches larger than 0.001 were flagged so additional reflectance curves could be modeled to fill in the hollow range. After iterations on this process the average difference in matched values was minimized to <0.002%. Index matching was then used to retrieve single scattering optical properties by *k* value and wavelength from separate LUTs.

The spectrally varying single scattering properties that correspond to the retrieved complex index of refraction are compiled as an optical properties look up table for the SNow, ICe, and Aerosol Radiation model, (SNICAR; offline version 8d) [*Flanner and Zender*, 2005; 2006]. SNICAR has been shown to accurately model snow reflectance based on theory from *Wiscombe and Warren* [1980], which uses Mie theory to calculate single-scattering by snow particles and the delta-Eddington approximation [*Joseph et al.*, 1976] for multiple scattering of solar radiation in the snowpack, and the two stream, multilayer radiative approximation of *Toon et al.* [1989]. The inputs for SNICAR include solar zenith angle, snow optical grain size, snow density, and concentrations of impurities. Output from SNICAR is snow albedo across 0.31-5.0 μm at 10 nm resolution

(here we utilize the subset of this albedo, 0.35-2.5 μm, that corresponds to the spectrometer range). The single scattering properties for ice and aerosol types that are needed for the radiative transfer calculations are extracted from lookup tables.

Currently, the dust optical properties in SNICAR are designed to represent general global characteristics of dust aerosols. The single scattering optical properties (albedo, asymmetry parameter, and mass extinction coefficient) for four partitions of a lognormal size distribution (0.1-1 μm, 1.0-2.5 μm, 2.5-5.0 μm, and 5.0-10.0 μm) are characterized by combinations of indices of refraction for a mixture of quartz, limestone, montmorillinite, illite, and hematite using the Maxwell-Garnett approximation (SNICAR-Online [*Flanner et al.*, 2007]). The modeling effort presented here was motived by the fact that generic/non-specific dust representations cannot accurately constrain radiative transfer modeling of snow albedo in the CRB, either in magnitude or reflectance shape. We compare SNICAR albedo, modeled with both the general dust characterization ('SNICAR dust') with the updated optical properties for dust on snow ('DOS') presented here, and assess modeled albedo scenarios by comparing them with spectral albedo, measured at the snow sampling site, and broadband albedo, measured at the nearby SASP instrumentation tower.

Spectral and broadband albedos were modeled with SNICAR for each day when measurements were made in the field between March 11th and May 18th, 2013. Snow property inputs were specified in 11 layers; the top 10 layers correspond to gravimetric snow sampling described in sections 2.1 (Figure 5). In each of these layers density, optical grain size (resampled from 2 to 3 cm resolution), and dust concentrations are specified. The lowest layer is the remainder of the snowpack, in which mean density,

mean grain size, and bulk dust concentration are specified. For albedo modeled with SNICAR dust measured dust concentrations are partitioned into the 4 size bins based on DOS PSD's. Measurement days spanned the transition from an accumulating to melting snowpack (peak snow water equivalent occurred on April 21st), as well as dust influenced snow evolution (98% of the total mass loading was deposited by 3 dust events in April).

Spectrally weighted albedo was calculated from SNICAR albedo over the broadband (BB; 0.35-1.5 μm), visible (VIS; 0.35-0.75 μm), and near-infrared wavelengths (NIR; 0.75-1.5 μm) by dividing the product of the summation of irradiance and albedo by the summation of irradiance, i.e. for broadband albedo:

$$\alpha = \frac{\sum_{\lambda=0.35\mu m}^{2.5\mu m} I * \alpha_{lai} \Delta\lambda}{\sum_{\lambda=0.35\mu m}^{2.5\mu m} I \Delta\lambda} \quad (2)$$

where I is spectral irradiance at a given solar zenith angle, α_{lai} is the modeled albedo with dust and/or BC at the same solar zenith angle, and λ is the wavelength (μm). Irradiance measured at the instrumentation tower is not spectrally resolved and therefore we model clear sky spectral irradiance with Santa Barbara DISORT Atmospheric Radiative Transfer model (SBDART) [*Ricchiazzi et al.*, 1998]. To account for daily variation in incoming solar irradiance SBDART irradiance was scaled by the broadband irradiance measured at the tower.

While snow grain size and impurity content mainly control inherent snow albedo, over the course of a day across a snow-covered landscape, the solar zenith angle, slope, aspect, cloud cover, and topography also act to influence net solar radiation [Conway et al., 1996; Flanner and Zender, 2006; Gardner and Sharp, 2010]. Care was taken to

minimize any additional uncertainty introduced by these factors when comparing modeled to measured albedo. Broadband albedo was selected for the same time each day (11:00 AM local time). Each SNICAR run correspondingly utilized the 11:00 AM solar zenith angle, which ranged from ~50^{o} in the beginning of March to ~30^{o} in mid-May. Reflected flux, which is used for error calculations, is corrected for variations in slope and aspect using the method described in *Painter et al.* [2012].

For spectral albedo comparison 14 of the 36 days were selected for comparison with SNICAR modeled albedo. Consistent sky conditions on these days allowed for an accurate collection of snow albedo with the field spectrometer. While this dataset is a smaller subset of the full record the days selected are representative of the range of snow conditions, from cold to melting snow and from relatively low to extremely high dust content (0.01 pptw to 5.7 pptw). In the SNICAR runs, the solar zenith angle specified corresponds to the time of albedo collection. Due to atmospheric absorption in the shortwave infrared (SWIR) we limit our spectral comparison to the 0.35 to 1.5 μm wavelength range, beyond this the signal becomes too noisy to capture an accurate albedo. We deem this acceptable as this is the range over which snow reflectance occurs, and beyond this solar irradiance is minimal.

3. Results and Discussion

3.1 Laboratory Measurements

Over the solar spectrum DOS reflectance is lowest at 0.35 μm, where it absorbs over 90% of irradiance (reflectance below 0.1). The albedo increases steadily over the visible wavelengths to ~ 0.3 at 0.75 μm (Figure 6). The rate of change is highest between 0.35 and 0.6 μm, with an average increase of 0.006 per 10 nm. The rate of change slows past

this point, increasing to ~0.4 around 1.35 μm, and then to ~0.5 at 2.5 μm. There is uncertainty in absolute reflectance value and trends beyond 1.85 μm, where a line of best fit was utilized to filter noise in the reflectance signal. For our purpose here, this simple approximation is acceptable, as it is most important to account for absorption by dust in the VIS and NIR where snow reflectance occurs.

Hemispherical DOS reflectance was consistent over the season, as shown in Figure 6. Variance between all reflectance curves is lowest at 0.35 μm at $2.8*10^{-5}$ and with a maximum variance of $7.4*10^{-4}$ occurring at 0.78 μm. There was minimal difference in reflectance between the different SOL-JPL sample preparations, which included dust evaporated from bulk samples, dust on filters, and dust scraped from filters. For retrieval of the imaginary part of the refractive index we use a SOL-JPL reflectance curve that represents the mean of all 2013 DOS samples.

Analysis of dust properties from mountain snow cover at 10 sites in Colorado, including SASP, by USGS confirm that dust deposited in snow the upper Colorado River Basin is broadly representative of dust originating in the four corners regions/southern Colorado Plateau [*Goldstein et al.*, 2014]. While we plan to assess variability in DOS optical properties in more detail in later studies visual comparison of reflectance from 2013 to reflectance from other years, and to an additional study site (Grand Mesa Study Plot (GMSP), located 150 km northwest from SASP) supports this finding (Figure 6). There is divergence between the SASP/GMSP reflectance curves between 0.6 and 1.1 μm, where GMSP DOS is slightly more reflective than SASP DOS, which is not unexpected given back-trajectory analysis indicates GMSP may receive dust from some more northern source regions than SASP (Chapter 1). Still, this difference is small

(maximum difference of 0.02 at 0.65 μm) and SASP/GMSP dust reflectance curves are more similar to each other than dust on snow collected from the Wasatch Mountain Range, UT, which is located northwest from SASP/GMSP and is not considered a deposition region for the four corners regions/southern Colorado Plateau (Figure 6). Therefore, the DOS samples collected in spring 2013 from SASP are considered representative of DOS in the Colorado River Basin, and hereafter refer to it as Colorado River Basin dust on snow (CRB DOS).

While slightly more variable than soil reflectance the particle size distributions for CRB DOS were fairly consistent across the spring. Variations mainly depended on the number of dust deposition events represented in the sample, where samples that contained dust from single events exhibited higher volume fraction peaks than snow samples that contained merged dust events (Figure 7). The particle size distribution used for the Mie modeling, a volume-weighted mean radius of 6 μm and standard deviation of log(r) of 0.28, was a mean of all wet PSD's including single and merged events. Like most dust samples, there was a fine mode present in the PSDs (Figure 7) and this characterization underrepresents the smallest particle range.

Using wet PSDs is suggested for this method, as might be expected we found that if the PSD was measured after the sample had been filtered, dried, and physically separated (but no further treatments were applied like sieving), then the mean radius increased by ~1-4 μm and the volume fractions shift toward larger particles sizes. This method is sensitive to the selected particle size distribution, and using a dry PSD returned unrealistic k values (k= -0.0005 at 0.35 μm), which were representative of weakly

absorbing mineral phases like quartz and were too low to describe absorption by CRB DOS.

3.2 DOS Optical Properties

The imaginary part of the complex refractive for CRB DOS ranged from 0.0018 at 0.35 μm to .00049 at 2.5 μm, with a ±0.0017 maximum difference between spectrally matched reflectance values and average difference of $3.63*10^{-5}$ (Figure 8). The most rapid decrease in *k* corresponded to the increase in reflectance across the visible wavelengths between 0.35 μm and 0.6 μm, where *k* decreases from 0.0018 to 0.0007. Some complex indices of refraction retrieved by this method across the visible wavelengths were 1.525-0.0018*i*, 1.525-0.00105*i*, and 1.525-0.00064*i at* 0.35 μm, 0.5 μm, and 0.75 μm respectively (see Table 1 for more values).

It was difficult to compare these values to others published for dust aerosols because the values are widely ranging. The complex refractive index suggested by *Grams et al.* [1974], determined from airborne dust in the southwestern US, m=1.525-0.005*i* (at 0.51 μm and 0.48 μm), uses the geometric mean *k* value from a set of retrievals that ranged from 0.0009 to 0.01. For Saharan dust, reported *k* values range from 0.0005 to 0.01 in the visible wavelengths [*C L McConnell et al.*, 2008; *Wagner et al.*, 2012], with values around 0.5 μm ranging from 0.0004 [*Osborne et al.*, 2008] to 0.008 [*Patterson et al.*, 1977].

The single scattering albedo, which is the probability that a photon will survive an extinction event (where 1 is fully scattering and 0 is fully absorbing), for CRB DOS ranged from 0.76 at 0.35 μm to 0.97 at 2.5 μm (Figure 9). Corresponding to the decrease in absorption and k values across the visible wavelengths, the largest rate of change in

SSA occurs between 0.35 μm and 0.7 μm, where it increases from 0.76 to 0.9. The asymmetry parameter '*g'*, the mean cosine of direction of scattering (where 1 is forward scattering and -1 is backward scattering), decreases slightly from 0.82 at 0.35 to 0.7 at 2.5 μm indicating a decrease in the forward scattering and penetration of photons into the snowpack by dust. An assumed particle density of 2.6 g cm^{-3} [*Hess et al.*, 1998; *Kandler et al.*, 2007; *Tegen and Fung*, 1995] was used to determine the mass specific extinction coefficient, which is highest at 0.35 μm decreasing to 0.7 μm and then remaining fairly constant to 2.5 μm (Figure 9).

The optical properties retrieved for CRB DOS are plotted with the optical properties for the four size bins of SNICAR dust in Figure 9. The optical properties for CRB DOS are most similar to properties for the largest size bin (D4; 5-10 μm), which is not surprising given the volume weighted mean radius for CRB DOS falls within this range. Notably, the main difference between scenarios is the higher CRB DOS absorption coefficient in the visible wavelengths relative to the D4 size bin.

In Figure 10 we plot the *k* values of ice and CRB DOS, along with CRB DOS reflectance, clean snow reflectance, and solar irradiance to illustrate why absorption by dust is highly effective at reducing snow albedo and influencing snow energy balance. Absorption by CRB DOS is highest across the visible wavelengths, where half of irradiance occurs and where clean snow is most reflective: *k* values for ice range from 10^{-10} to 10^{-8} between 0.4 and 0.7 μm [*Warren and Brandt*, 2008] where CRB DOS is ~10^{-3}. Snow becomes less reflective into the NIR, where snow grain size control absorption. Dust does not directly impact snow albedo in this wavelength range, but radiative forcing by dust contributes energy that enhances the rate of snow grain growth, which further

increases the amount of energy absorbed. Dust deposition thereby initiates a snow albedo feedback loop that increases the energy available for melt by reducing reflectance over the portion of the solar spectrum where snow reflectance occurs (VIS+NIR).

Sokolik and Toon [1999] presented a good summary of the limitations of retrieving dust optical properties from bulk samples, like the method presented here. Essentially, they argue that it is difficult to justify the representativeness of bulk samples when dust aerosols are highly variable in time and space and also questioned the appropriateness of attributing a single refractive index to mixtures of various particle sizes and chemical composition. We acknowledge the validity of these arguments for dust aerosols in transport but argue that using the reflectivity of bulk samples is an appropriate method to retrieve optical properties for dust in snow.

First, space-time variability is constrained by deposition region and seasonality of dust impacts, and we have found DOS reflectance and grain size distributions exhibit relatively limited intra- and interannual variability. This method utilizes hemispherical reflectance and is therefore not sensitive to issues associated with illumination angle. Additionally, approaching dust in snow with a forward, composition mixing approach neglects some absorbing components like organics (bacteria, plant matter) since these are typically removed by digestion/sieving prior to compositional analysis. Ultimately, we argue this method is useful because it improves radiative transfer modeling of snow+dust reflectance, as discussed in section 3.3.

3.3 Assessment of Optical Properties

3.3.1 Spectral Albedo

Conditions on spectral albedo measurement days could be generally classified into three time windows, the five relatively clean snow days when dust near the surface was less than 0.1 pptw (March 28th through April 24th), the four transitional days over which dust layers began to converge and emerge at the surface (April 26th-April 29th), and the five days when there was heavy dust loading of 4.0 pptw or more at the surface (May 2nd-4th, May 17th-18th). In Figure 11, we show 1) spectral albedo modeled with both snicar dust (α_{snicar}) and CRB DOS (α_{CRB}), 2) difference in modeled from measured albedo, 3) reflected flux, and 4) difference in modeled from measured reflected flux for a day in each of these time windows to illustrate the spectral variability between scenarios. In Figure 12 spectrally integrated BB, VIS, and NIR albedo is plotted for all 14 days. Time of snow albedo/snow property collection, surface grain size, and surface dust concentrations for these days are summarized in Table 2.

Broadband albedo errors for α_{crb} ranged from 0.01% to 11% difference, with an average error of 4.8% (Figure 12; data summary Table 3). The associated flux errors were -20 W m^{-2}, on average, and ranged from +0.07 to -36.12 W m^{-2} (where negative values reflects an underestimation of reflected flux). These errors were minimized across the visible wavelengths, 0.2% to 6% (+2.17 to -26.47 W m^{-2}), with an average error of 2% (-7.44 W m^{-2}). Errors in the NIR wavelengths were fairly low on the days prior to dust deposition (March 28th – April 24th) and on days when dust layers were still buried (April 26th - April 27th), ranging from 0.9% to 5.7% (+2.77 to -12.91 W m^{-2}). Errors increased

when dust is at or near the surface (April 28th - May 18th), ranging from 8% to 22% (-13.6 to -30.74 W m^{-2}).

Broadband errors for α_{snicar} ranged from 0.3% to 25.6% (-1.94 to -89.5 W m^{-2}), and averaged 10.7% (44 W m^{-2}), double the broadband error for α_{crb}. In the visible wavelengths errors ranged from 0.05% to 22.3% (+0.19 to -45.52 W m^{-2}), and averaged 10.2% (-26.15 W m^{-2}), five times the percent difference for α_{crb} and nearly four times the flux error. In the NIR α_{crb} and α_{snicar} were most similar, α_{snicar} errors range from 1.0% to 30.1% (-2.13 to 43.98 W m^{-2}), and average 11.6% (-17.76 W m^{-2}).

Due to the presence of dust in all the snow samples, α_{crb} was always lower than α_{snicar} because CRB DOS is more absorptive in the VIS wavelengths. Because SNICAR tends to overestimate albedo in the VIS, this higher absorption resulted in an improvement in albedo modeling of 50% on average across the full range of snow reflectance by α_{crb}. The most marked improvement occured across the VIS during the five days when dust was at the surface when errors for α_{crb}, which ranged from 0.7% to 2.9%, reduced errors almost 80% relative to errors for α_{snicar}, which ranged from 19.2% to 22.3%. This was due to α_{crb} being able to replicate the magnitude and steepness of snow+dust reflectance curves of measured snow albedo across the VIS (Figure 11). Therefore, utilizing CRB DOS optical properties allowed SNICAR to more accurately model the reduction in snow albedo due to dust in this region, particularly in the presence of heavy dust loading.

The largest variation between measured and modeled albedo for both scenarios occured in the NIR wavelengths in the presence of heavy dust loading, where SNICAR overestimated NIR albedo by ~15% for α_{crb} and 23% for α_{snicar}. Incoming irradiance is

lower in this wavelength range but the larger difference between measured and modeled albedo resulted in reflected flux errors that were greater than or similar to those in the VIS. Despite the presence of these errors, CRB DOS still improved NIR albedo modeling, reducing the average errors from 11.6% to 8.7%.

Albedo in the NIR should be a better match in all cases given that it is determined by the optical grain size input, which is estimated from measured reflectance from contact spectroscopy using the same theory and ice optical properties contained in SNICAR. Increasing the grain size to match measured albedo however does not resolve this issue, because a larger grain size reduces the albedo at all wavelengths (this was observed in test runs, also see [*Warren and Wiscombe*, 1980]). Therefore, this issue arises from the representation of dust absorption within SNICAR, and was not an error that could be attributed to inputs. The way SNICAR models NIR albedo in the presence of heavy dust loading is similar to the spectral albedo measurements presented in *Singh et al.* [2010], this study applied varying amounts of dust at the snow surface and observed a plateau of NIR albedo and increased shortwave infrared (SWIR) albedo with increasing amounts of dust. Essentially, the reflectance becomes more dust like and less ice like in the NIR/SWIR. As shown here, this is not representative of heavy dust absorption deposited by atmospheric deposition, where NIR albedo does not plateau and albedo still reduces close to 0 in the SWIR.

This issue may arise from how dust particles and snow grains are modeled as a mixture: SNICAR treats dust as an external mixture, while at SBBSA wet and dry deposition of dust is observed, resulting in dust that is both internally and externally mixed. This results in heterogeneous dispersions of dust amongst snow grains that

interact with solar radiation differently than homogenous external mixtures. This micro-scale variation in absorption manifests as spatially variable surfaces, for example, high surface roughness and vertical and planar patches of concentrated dust interspersed with cleaner snow (Figure 13). Even with high dust content, surfaces like these would have reflectance that is characteristic of both dust and ice. Perhaps representing a portion of dust concentrations as an internal mixture would allow modeled absorption in the NIR to better match observations.

There are no other studies we are aware of that present spectral albedo for such heavy dust loading from atmospheric deposition, so we are uncertain how these observations compare to those from other regions. These errors would only present themselves during period of melt in years with high dust concentrations. The current record indicates that there is a 30% chance that any given year may receive heavy dust loading akin to the levels that occurred in 2013. It is still a relatively short data record, so we unsure about this probability, but ideally we would be able to address this issue within SNICAR to accurately capture the reduction in snow albedo due to heavy dust loading over the full solar range. It is beyond the scope of this project to implement this change, but if observations were better matched in the NIR, w could expect errors across the full range of snow reflectance to be more similar to those in the VIS, ~2%.

3.3.2 Broadband Albedo Time Series

Snow albedo is spectrally varying, and therefore it is best to compare measured and modeled spectral albedo. Additionally, spectral albedo is best used in this analysis given that model inputs and albedo measurements were spatially and temporally coincident. However, due to sky condition limitations, the spectral albedo dataset was

small relative to the number of days when measurements were collected. Here, we use broadband albedo from tower pyranometers to present a near continuous time series of broadband albedo for all the days when snow sampling occurred (Figure 14).

Relative to measured albedo, α_{crb} overestimated flux over the full season by 20 W m^{-2} on average, a 5% difference from measured reflected flux and 2% of total irradiance (Figure 14). Relative to measured albedo, α_{crb} had an RMSE of 0.05 and R^2 value of 0.92. The RMSE for α_{snicar} was 0.07, with an R^2 value of 0.93, resulting in a reflected flux overestimation of 9.8%. This doubles the average flux error to 40 W m^{-2}, or 4% of total irradiance.

Similar to spectral results, both scenarios had higher albedos relative to the tower-measured albedo over the spring season. The exception is clean snow at the beginning of the measurements period and days with fresh snowfall, on these days surface dust concentrations were low, 0.025 pptw on average, and both scenarios modeled lower than measured albedo. Flux errors for both scenarios were small for these low-dust days, 1-2%, and these were the only days (11 total) when α_{snicar} modeled albedo better than α_{crb} (0.4% improvement). Spring dust concentrations and snowfall events (as measured at the SASP precipitation collector) are plotted in Figure 15.

Here, we are mainly interested in the 25 other days when dust concentrations at the surface were high enough to discern differences between dust optical properties, as it is on these days when CRB DOS should improve albedo modeling. For the 15 days between March 28th and April 28th, discounting the days when fresh snow was at the surface, surface concentrations were 0.1 pptw on average with a range of 0.01 to 0.35

pptw. Over this time frame α_{crb} improved albedo modeling by 2% and reduced flux errors from 43 to 33 W m^{-2}.

Between April 29th and May 5th surface dust concentrations increased from 0.5 pptw to 5.7 pptw, and over this time frame α_{crb} improved albedo modeling by 50%, reducing flux errors from 122 to 67 W m^{-2}. When dust was at the surface (after May 5th), concentrations were consistently greater than 4.0 pptw. On these days α_{crb} improved albedo modeling by ~70%, reducing flux errors from 91 to 30 W m^{-2}.

Due to spatial variability, the snow flux measured at the tower may not always be representative of snow in the nearby study plot, and it should be noted that snow melted out underneath the tower a day and half before snow all gone (SAG) occurred in the measurement plot. This may account for the large albedo errors for both scenarios between April 26th and April 30th (Figure 14), the time period when dust layers converged and emerged at the surface, which occurred more quickly at the tower than at the measurement site. Still, it is worthwhile to assess the variation between SNICAR modeled albedo and tower measurements over the full spring. While variation between measured and modeled albedo can be large under certain conditions, errors are similar to those found for the smaller spectral dataset, and relative to tower albedo CRB DOS improved broadband albedo modeling, reducing flux errors by 50% over the spring and 70% in the presence of heavy dust loading.

4. Concluding Thoughts

Here, we presented an inversion technique to determine the effective complex index of refraction and single scattering optical properties of dust deposited in mountain snow cover using measured particle size distributions and hemispherical reflectance. The

ultimate goal of this method was to improve the accuracy of radiative transfer modeling of dust in snow. We validated our retrievals by comparing measured albedo to albedo modeled by a snow+impurity radiative transfer model, and found utilizing the optical properties of CRB DOS reduced errors in broadband albedo modeling by 50% relative to optical properties for a 'global mean' dust characterization.

The study of light absorbing impurities in snow has focused on black carbon in permanent snow and ice in the high northern latitudes where even minor reductions in albedo can have important climatic impacts [*Hansen and Nazarenko*, 2004; *IPCC*, 2007]. Despite the importance of annual snowmelt runoff in the mid-latitudes, and the increased risk for dust emission and deposition with climate and land use change, the impacts of mineral dust on snow cover are not as well understood and observations are sparse.

A few recent studies have found that dust can dominate radiative forcing in mid-latitude mountain snow cover even in the presence of black carbon [*Kaspari et al.*, 2013; *Sterle et al.*, 2013]. The method presented here, which requires no more than an optically thick dust sample, could be employed to determine the region specific dust optical properties in mountain snow cover in remote regions like the Middle East, Central Asia, and the Himalaya to improve radiative transfer and hydrologic modeling efforts. Additionally, the validation of this method will facilitate the development of an additional inversion technique to retrieve dust concentrations from a snow reflectance library when the only snow albedo measurements are available, which has important implications for in situ and remote sensing retrievals in remote snow covered environments.

5. References

Andreae, M. O. (1995), *Climatic effects of changing atmospheric aerosol levels*, Elsevier Science, New York.

Barthelmy, D. (2006), Mineralogy Database, edited.

Bisiaux, M. M., R. Edwards, J. R. McConnell, M. Albert, H. Anschutz, T. A. Neumann, E. Isaksson, and J. E. Penner (2011), Variability of black carbon deposition to the East Antarctic Plateau, AD 1800-2000, *Atmospheric Chemistry and Physics Discussions*, *11*, 31091-31114.

Bond, T. C., and R. W. Bergstrom (2006), Light absorption by carbonaceous particles: an investigative review, *Aerosol Science and Technology*, *40*, 27-67.

Bory, A., P. E. Biscaye, and F. E. Grousset (2003), Two distinct seasonal Asian source regions for mineral dust deposited in Greenland (NorthGRIP), *Geophysical Research Letters*, *30*(4).

Christensen, N. S., A. W. Wood, D. P. Lettenmaier, and R. N. Palmer (2004), Effects of climate change on the hydrology and water resources of the Colorado River Basin, *Journal of Hydroclimatology*, *62*, 337-363.

Conway, H., A. Gades, and C. F. Raymond (1996), Albedo of dirty snow during conditions of melt, *Water Resources Research*, *32*(6), 1713-1718.

De Angelis, M., and A. Gaudichet (1991), Saharan dust deposition over Mont Blanc (French Alps) during the last 30 years, *Tellus*, *43B*, 61-75.

De Luisi, J. J., et al. (1976), Results of a comprehensive atmospheric aerosol-radiation experiment in the southwestern United States, *Journal of Applied Meteorology*, *15*, 441-463.

Deems, J., T. H. Painter, J. Barsugli, J. Belnap, and B. Udall (2013), Combined impacts of current and future dust deposition and regional warming on Colorado River Basin snow dynamics and hydrology, *Hydrology and Earth System Sciences Discussions*, *10*.

Doherty, S. J., S. G. Warren, T. C. Grenfell, A. D. Clark, and R. E. Brandt (2010), Light absorbing impurities in Arctic snow, *Atmospheric Chemistry and Physics Discussions*, *10*, 18807-18878.

Dumont, M., E. Brun, G. Picard, M. Michou, Q. Libois, J. R. Petit, M. Geyer, S. Morin, and B. Josse (2014), Contribution of light-absoring impurities in snow to Greenlands Darkening since 2009, *Nature Geoscience*, *7*, 509-512.

Ebert, M., S. Weinbruch, P. Hoffman, and H. M. Ortner (2004), The chemical composition and complex refractive index of rural and urban influenced aerosols determined by individual particle analysis, *Atmospheric Environment*, *38*, 6531-6545.

Flagg, C. B., J. C. Neff, R. L. Reynolds, and J. Belnap (2013), Spatial and temporal patterns of dust emissions (2004-2012) in semi-arid landscapes, southeastern Utah, USA, *Aeolian Research*.

Flanner, M. G., and C. Zender (2005), Snowpack radiative heating: Influence on the Tibetan Plateau climate, *Geophysical Research Letters*, *32*.

Flanner, M. G., and C. Zender (2006), Linking snowpack microphysics and albedo evolution, *Journal of Geophysical Research*, *111*(D12), doi:10.1029/2005JD006834.

Flanner, M. G., C. S. Zender, J. T. Randerson, and P. J. Rasch (2007), Present-day climate forcing and response from black carbon in snow, *Journal of Geophysical Research*, *112*.

Franzén, L. G., J. O. Mattsson, U. Mårtensson, T. Nihlén, and A. Rapp (1994), Yellow snow over the Alps and Subarctic from dust storm in Africa, March 1991, *Ambio*, *23*(3), 233-235.

Gardner, A., and M. J. Sharp (2010), A review of snow and ice albedo and the development of a new physically based broadband albedo parameterization, *Journal of Geophysical Research*, *115*.

Gautam, R., C. N. Hsu, K. M. Lau, and T. J. Yasunari (2013), Satellite observations of desert dust-induced Himalayan snow darkening, *Geophysical Research Letters*, *40*(5), 988-993.

Goldstein, H. L., R. Reynolds, and C. Landry (2014), Properties of dust deposited on Colorado mountain snow cover: effects on snow albedo*Rep.*, U.S. Geological Survey.

Grams, G. W., I. H. Blifford, D. Gillette, and P. B. Russell (1974), Complex Index of Refraction of Airborne Soil Particles, *Journal of Applied Meteorology*, *13*, 459-471.

Grousset, F. E., P. Ginoux, A. Bory, and P. E. Biscaye (2003), Case study of a Chinese dust plume reaching the French Alps, *Geophysical Research Letters*, *30*(6).

Hansen, J., and L. Nazarenko (2004), Soot climate forcing via snow and ice albedos, *Proceedings of the National Academy of Sciences*, *101*(2), 423-428.

Hess, M., P. Koepke, and I. Schult (1998), Optical Properties of aerosols and clouds: The software package of OPAC, *Bulletin of the American Meteorological Society*, *79*(5), 831-844.

Huang, J., Q. Fu, W. Zhang, X. Wang, R. Zhang, H. Ye, and S. G. Warren (2011), Dust and Black Carbon in Seasonal Snow Across Northern China, *Bulletin of the American Meteorlogical Society*.

IPCC (2007), Observations: Changes in Snow, Ice, and Frozen Ground., *Climate Change, 2007: The Physical Science Basis. Contribution of Working Group 1 to the Fourth Assessment Report of the Intergovernmental Panel on Climate Change*, *Chapter 7*.

Joseph, J. H., W. J. Wiscombe, and J. A. Wienman (1976), The delta-Eddington approximation for radiative flux transfer, *Journal of Atmospheric Sciences*, *33*, 2452-2459.

Kandler, K., N. Benker, U. Bundke, E. Cuevas, M. Ebert, P. Knippertz, S. Rodriguez, L. Schutz, and S. Weinbruch (2007), Chemical Composition and complex refractive index of Saharan Mineral Dust at Izana, Tenerife (Spain) derived by electron microscopy, *Atmospheric Environment*, *41*, 8058-8074.

Kaspari, S., T. H. Painter, M. Gysel, and M. Schwikowski (2013), Seasonal and elevational variations of black carbon and dust in snow and ice in the Solu-Khombu, Nepa and estimated radiative forcings, *Atmospheric Chemistry and Physics Discussions*(13).

Kaspari, S., M. Schwikowski, M. Gysel, M. G. Flanner, S. Kang, S. Hou, and P. A. Mayewski (2011), Recent increases in balck carbon concentrations from a Mt. Everest ice core spanning 1860-2000 AD, *Geophysical Research Letters*, *38*.

Kaspari, S., P. A. Mayewski, M. Handley, S. Kang, S. Hou, S. Sneed, K. Maasch, and D. Qin (2009), A High Resolution Record of Atmospheric Dust Composition and Variability since A.D. 1650 from a Mount Everest Ice Core, *Journal of Climate*, *22*, 16.

Krinner, G., O. Boucher, and Y. Balkanski (2006), Ice-free glacial northern Asia due to dust deposition on snow, *Climate Dynamics*, *27*, 613-125.

Landry, C., K. Buck, M. S. Raleigh, and M. P. Clark (2014), Mountain system monitoring at Senator Beck Basin, San Juan Mountains, Colorado: A new integrative data source to develop and evaluate models snow and hydrologic processes, *Water Resources Research*, *50*(2).

Lawrence, C. R., T. H. Painter, C. Landry, and J. C. Neff (2010), The contemporary composition of aeolian dust deposited in the San Juan Mountains, Colorado, USA, *Journal of Geophysical Research*, *115*.

Li, J., G. S. Okin, S. M. Skiles, and T. H. Painter (2013), Relating variation of dust on snow to bare soil dynamics in the western Unites States, *Environmental Research Letters*(8).

Linke, C., O. Mohler, A. Veres, A. Mohacsi, A. Bozoki, G. Szabo, and M. Schnaiter (2006), Optical properties and mineralogical composition of different Saharan mineral dust samples: a laboratory study, *Atmospheric Chemistry and Physics*, *6*, 3315-3323.

McConnell, C. L., E. J. Highwood, H. Coe, P. Formenti, B. Anderson, S. Osborne, S. Nava, K. Desboeufs, G. Chen, and M. A. J. Harrison (2008), Seasonal variations of the physical and optical characteristics of Saharan dust: Results from the Dust Outflow and Deposition to the Ocean (DODO) experiment, *Journal of Geophysical Research*, *113*.

McConnell, J. R., A. J. Aristarain, J. R. Banta, R. Edwards, and J. C. Simoes (2007), 20th-Century doubling in dust archived in an Antarctic Peninsula ice core parallels climate change and desertification in South America, *PNAS*, *104*(14), 6.

Meng, Z., P. Yang, G. W. Kattawar, L. Bi, K. N. Liou, and I. Laszlo (2010), Single-scattering properties of tri-axial ellipsoidal minderal dust aerosols: A database for application to radiative transfer calculations, *Journal of Aerosol Science*, *41*, 501-512.

Munson, S. M., J. Belnap, and G. S. Okin (2011), Responses of wind erosion to climate-induced vegetation changes on the Colorado Plateau, *PNAS*, *108*(10), 3854-3859.

Myhre, G., and F. Stordal (2001), Global sensitivity experiments of the radiative forcing due to mineral aerosols, *Journal of Geophysical Research*, *106*(D16), 193-204.

Neff, J. C., A. P. Ballantyne, G. L. Farmer, N. M. Mahowald, J. L. Conroy, C. C. Landry, J. T. Overpeck, T. H. Painter, C. R. Lawrence, and R. L. Reynolds (2008), Increasing eolian dust deposition in the western United States linked to human activity, *Nature Geosciences*.

Nolin, A. W., and J. Dozier (2000), A hyperspectral method for remotely sensing the grain size of snow, *Remote Sens Environ*, *74*(2), 207-216.

Oerlemans, J., R. H. Giesen, and M. R. Van den Broeke (2009), Retreating alpine glaciers: Increased melt rates due to accumulation of dust (Vadret da Morteratsch, Switzerland), *Journal of Glaciology*, *55*(192), 729-736.

Osborne, S., B. Johnson, J. Haywood, C. L. McConnell, A. J. Baran, and M. A. J. Harrison (2008), Physical and optical properties of mineral dust aerosol during the Dust ad Biomass Experiment (DABEX), *Journal of Geophysical Research*.

Painter, T. H., N. P. Molotch, M. P. Cassidy, M. G. Flanner, and K. Steffen (2007), Contact spectroscopy for the determination of stratigraphy of snow grain size, *Journal of Glaciology*, *53*(180), 6.

Painter, T. H., S. M. Skiles, J. Deems, A. Bryant, and C. Landry (2012), Dust Radiative Forcing in snow of the Upper Colorado River Basin: Part 1. A 6 year record of energy balance, radiation, and dust concentrations, *Water Resources Research*.

Painter, T. H., J. S. Deems, J. Belnap, B. Udall, A. F. Hamlet, and C. C. Landry (2010), Decreased water yield from the Colorado River Basin under dust-accelerated snowmelt, *PNAS*.

Patterson, E. M., D. Gillette, and B. H. Stockton (1977), Complex index of refraction between 300 and 700 nm for Saharan soils, *Journal of Geophysical Research*, *82*, 3153-3160.

Redemann, J., et al. (2000), Retrieving the vertical structure of the effective aerosol complex index of refraction from a combination of aerosol in situ and remote sensing measurements during TARFOX, *Journal of Geophysical Research*, *105*(D8), 9949-9970.

Ricchiazzi, P., S. R. Yang, C. Gautier, and D. Sowle (1998), SBDART: A research and teaching software tool for plane-parallel radiative transfer in the Earth's atmosphere, *Bulletin of the American Meteorological Society*, *79*(10), 2101-2114.

Schwikowski, M., P. Seibert, U. Baltensperger, and H. W. Gaggeler (1995), A study of an outstanding saharan dust event at the high-alpine site Jungfraujoch, Switerland, *Atmospheric Environment*, *29*(15), 1829-1842.

Singh, S. K., A. V. Kulkarni, and B. S. Chaudhary (2010), Hyperspectral analysis of snow reflectance to understand the effects of contamination and grain size, *Annals of Glaciology*, *51*(54).

Skiles, S. M., and T. H. Painter (2014), A 9-yr record of dust on snow in the Colorado River Basin, paper presented at 12th Biennial Conference of Science and Management on the Colorado Plateau, Flagstaff, AZ.

Skiles, S. M., T. H. Painter, J. Deems, C. Landry, and A. Bryant (2012), Dust radiative forcing in snow of the Upper Colorado River Basin: Part II. Interannual variability in radiative forcing and snowmelt rates, *Water Resources Research*, *48*.

Sokolik, I., and O. B. Toon (1999), Incorporation of mineralogical composition into models of the radaitvie properties of mineral aerosols from UV to IR wavelengths, *Journal of Geophysical Research*, *104*(D8), 9423-9444.

Sokolik, I., A. Andronova, and T. E. Johnson (1993), Complex refractive index of atmospheric dust aerosols, *Atmospheric Environment*, *27*(16), 2495-2502.

Stamnes, K., S.-C. Tsay, W. J. Wiscombe, and K. Jayaweera (1988), Numerically stable algorithm for discrete-ordinate-method radiative transfer in multiple scattering and emitting layered media, *Applied Optics*, *27*, 2502-2509.

Sterle, K. M., J. R. McConnell, J. Dozier, R. Edwards, and M. Flanner (2013), Retention and radiative forcing of black carbon in the Eastern Sierra Nevada snow, *The Cryosphere*, *7*.

Tegen, I., and I. Fung (1995), Contribution to the atmospheric mineral aerosol load from land surface modifications, *Journal of Geophysical Research*, *100*(18).

Tegen, I., A. Lacis, and I. Fung (1996), The influence on climate forcing of mineral aerosols from disturbed soils, *Nature*, *380*, 419-422.

Toon, O. B., C. P. McKay, T. P. Ackerman, and K. Santhanam (1989), Rapid calculation of radiative heating rates and photodissociation rates in inhomogeneous multiple scattering atmospheres, *Journal of Geophysical Research*, *94*(D13), 16,287-216,301.

Wagner, R., T. Ajtai, K. Kandler, K. Lieke, C. Linke, T. Muller, M. Schnaiter, and M. Vragel (2012), Complex Refractive Indices of Saharan dust samples at visible and near UV wavelengths: a laboratory study, *Atmospheric Chemistry and Physics*, *12*, 2491-2512.

Wake, C. P., and P. A. Mayewski (1994), Modern eolian dust deposition in central Asia, *Tellus*, *46*(B), 220-233.

Warren, S. G. (1984), Optical constants of ice from the ultraviolet to the microwave, *Applied Optics*, *23*, 1206-1225.

Warren, S. G., and W. J. Wiscombe (1980), A model for the spectral albedo of snow, II, Snow containing atmospheric aerosols, *J. Atmos. Sci. (USA)*, *37*(12), 2734-2745.

Warren, S. G., and R. E. Brandt (2008), Optical constants of ice from the ultraviolet to microwave: A revised compilation, *Journal of Geophysical Research*, *113*.

Wiscombe, W. J., and S. G. Warren (1980), A Model for the Spectral Albedo of Snow. I: Pure Snow, *Journal of Atmospheric Sciences*, *37*, 2712-2733.

Xin, W., X. Baiqing, and M. Jing (2014), An Overview of the Studies on Black Carbon and Mineral Dust Deposition in Snow and Ice Cores in East Asia, *Journal of Meteorlogical Research*, *28*, 354-370.

Yi, B., C. N. Hsu, P. Yang, and S.-C. Tsay (2011), Radiative Transfer simulation of dust-like aerosols: Uncertainties from particle shape and refractive index, *Journal of Aerosol Science*(42), 631-644.

Zhao, F., Z. Gong, H. Hu, M. Tanaka, and T. Hayasaka (1997), Simultaneous determination of the aerosol complex index of refraction and size distribution from scattering measurements of polarized light, *Applied Optics*, *36*(30), 7992-8001.

Figures

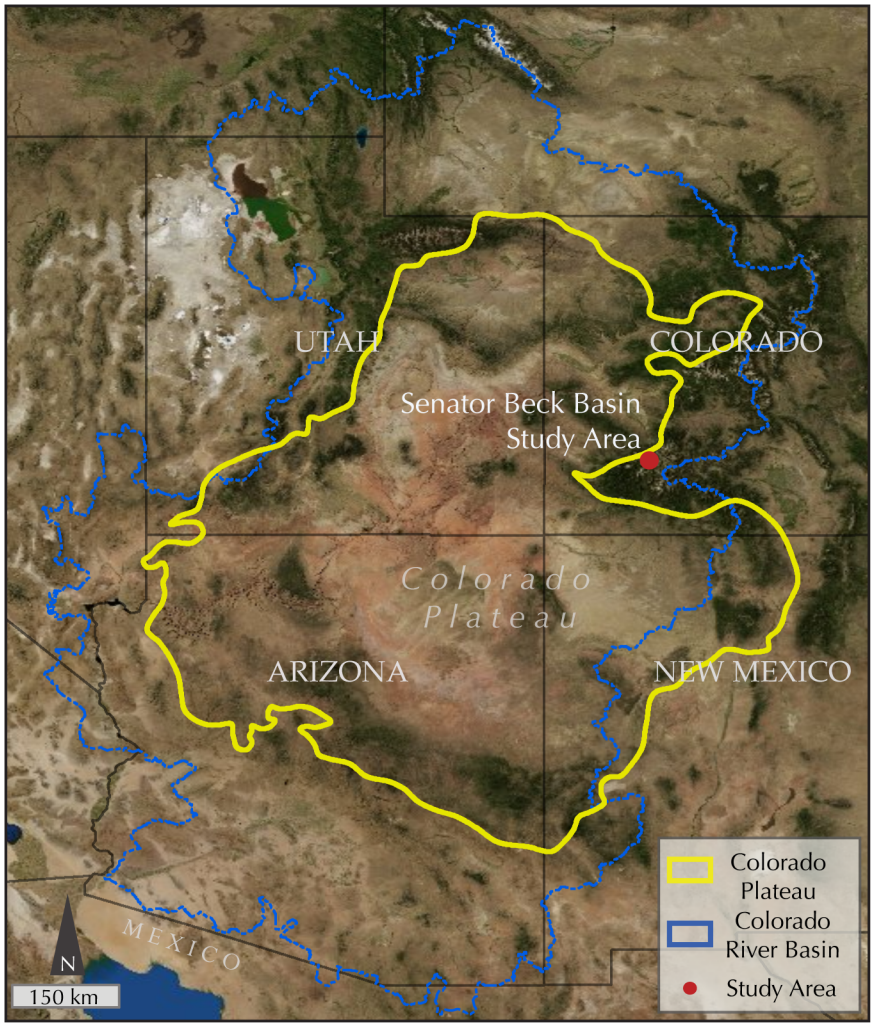

Figure 1 Overview of cross section between the Colorado River Basin and the Colorado Plateau, and location of study area.

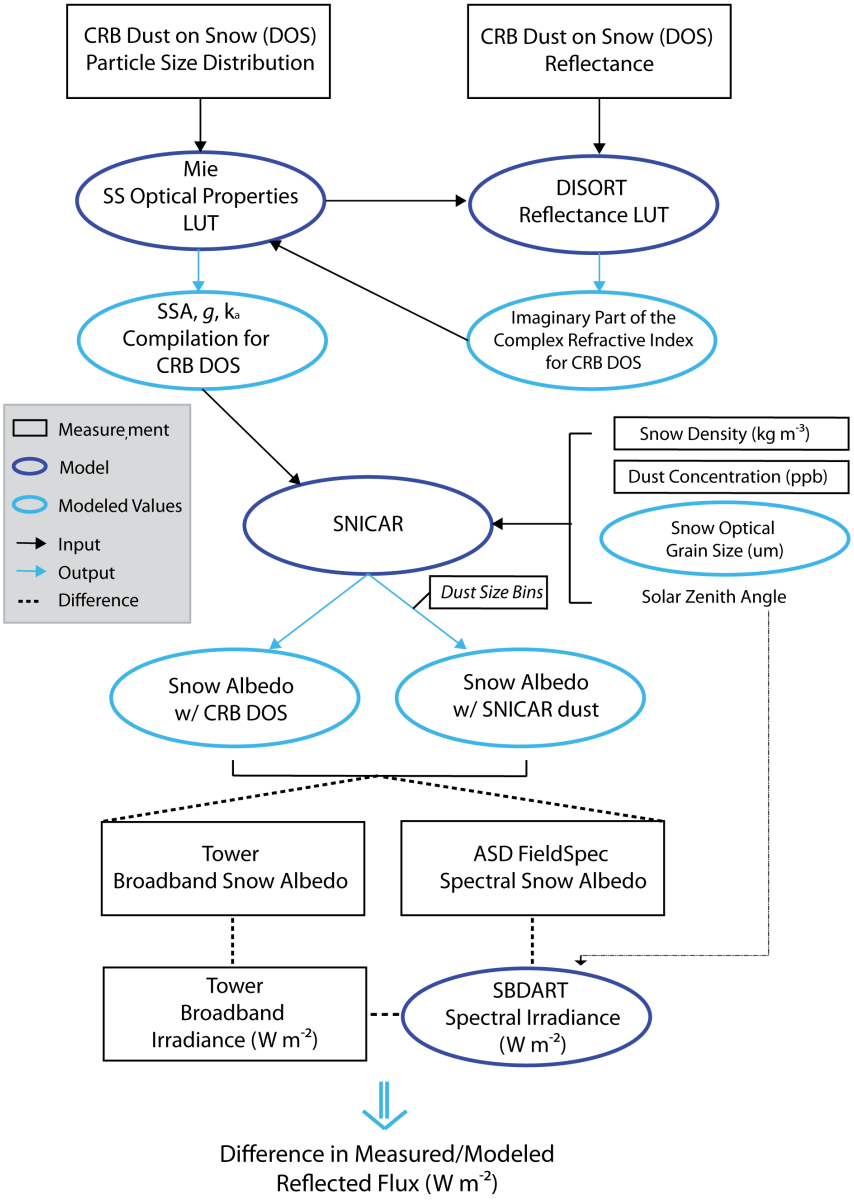

Figure 2 Methodology to retrieve and validate dust on snow optical properties.

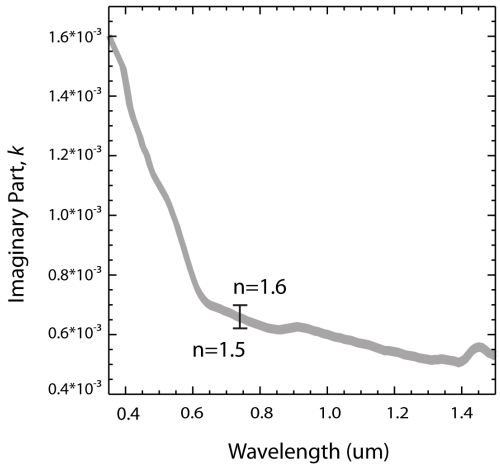

Figure 3 The shaded area is the range of retrieved values for the imaginary part of the complex refractive index, k, for specified values for the real part, n, between 1.5 and 1.6.

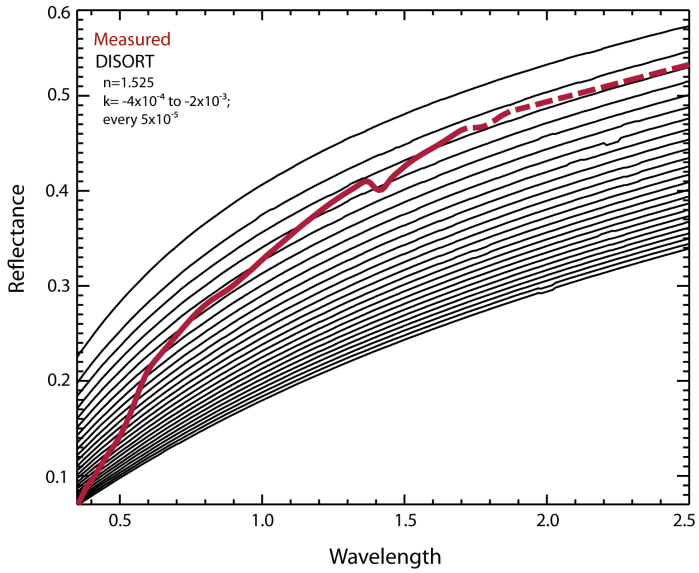

Figure 4 Visual representation of DISORT LUT used to retrieve the imaginary part of the complex index of refraction. The dashed part of the measured reflectance line indicates where reflectance is estimated due to noise in the signal. The actual LUT is more densely populated; the resolution is limited here so that reflectance curves remained discernible.

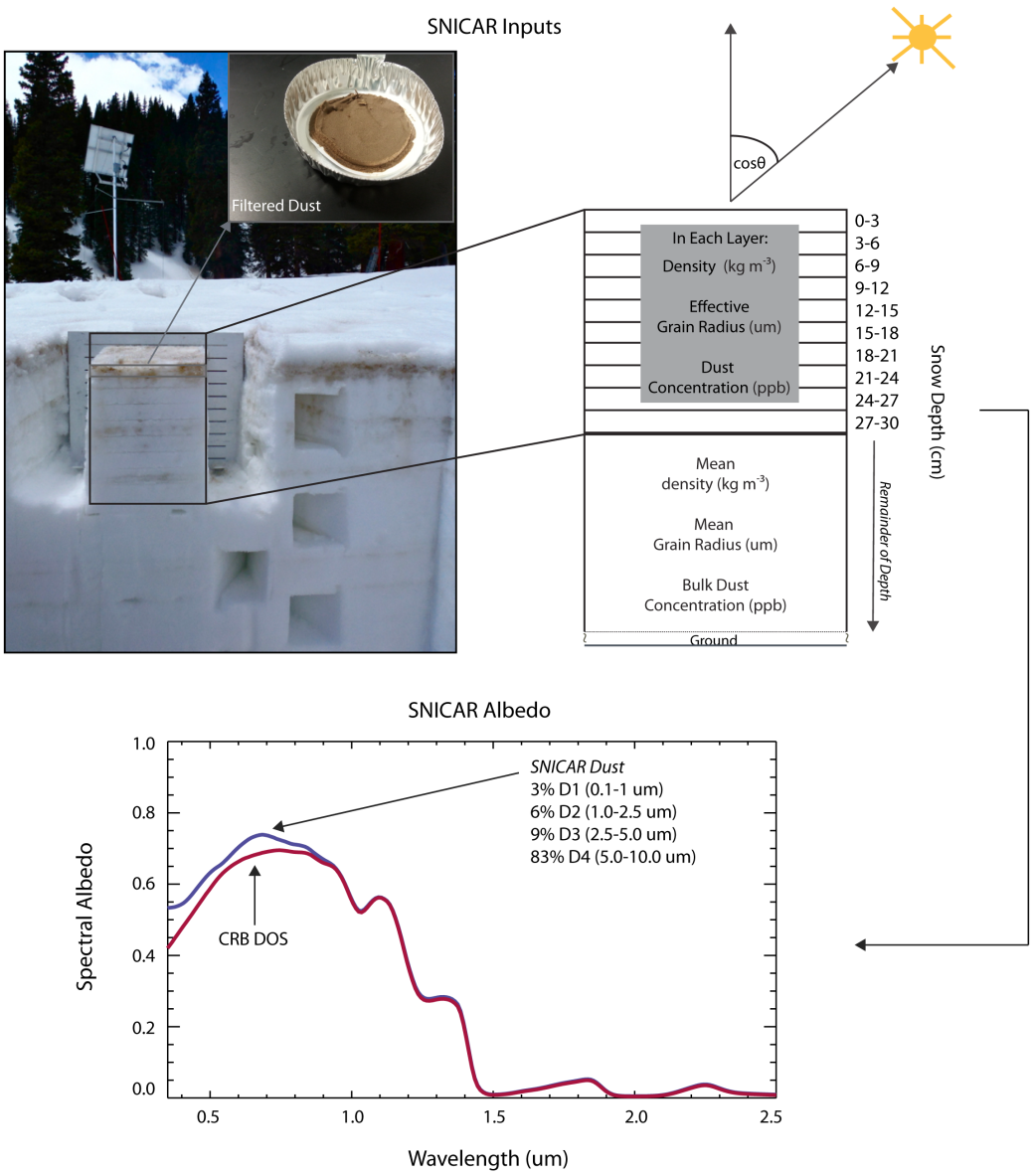

Figure 5 A representation of SNICAR inputs and output for May 11th, 2013. Snow properties and dust concentrations are specified in 11 layers, 10 3-cm surface layers and a single layer for the remainder of the snowpack.

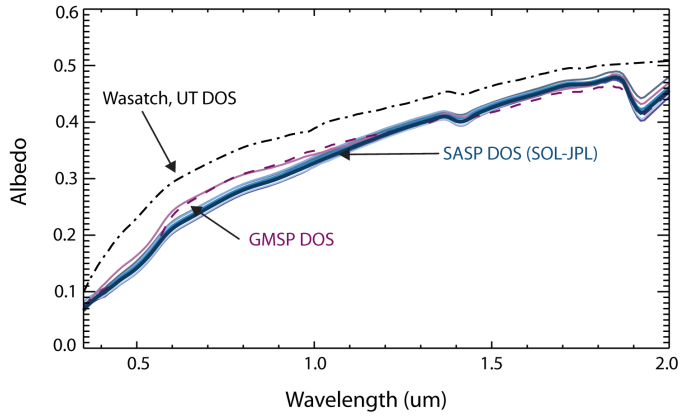

Figure 6 Dust on snow reflectance for SASP 2013 dust on snow (DOS) samples (blue lines), GMSP 2013 DOS (purple line), and Wasatch Mountain Range, UT DOS from 2009 (dotted line).

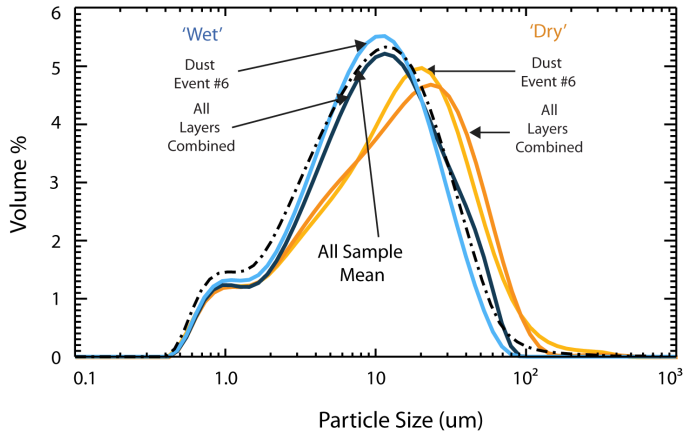

Figure 7 Particle size distributions of SASP 2013 dust on snow, as measured with laser light diffraction. The 'All Sample Mean' represents the average of particles size distribution, from all wet samples.

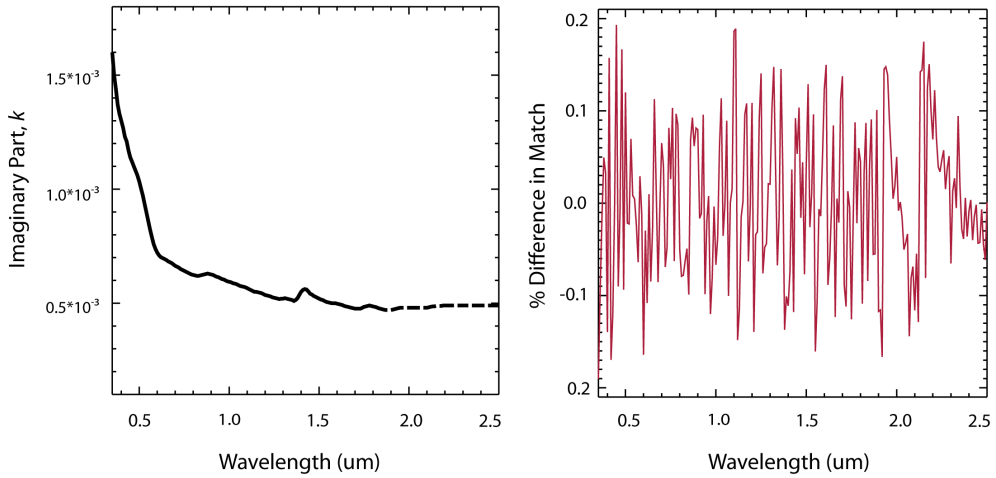

Figure 8 (Left) The imaginary part of complex index of refraction, k, for CRB DOS between 0.35 and 2.5 µm. Dotted line indicates where reflectance was estimated to account for noise. (Right) Percent difference between measured and modeled reflectance used to retrieve the *k* values.

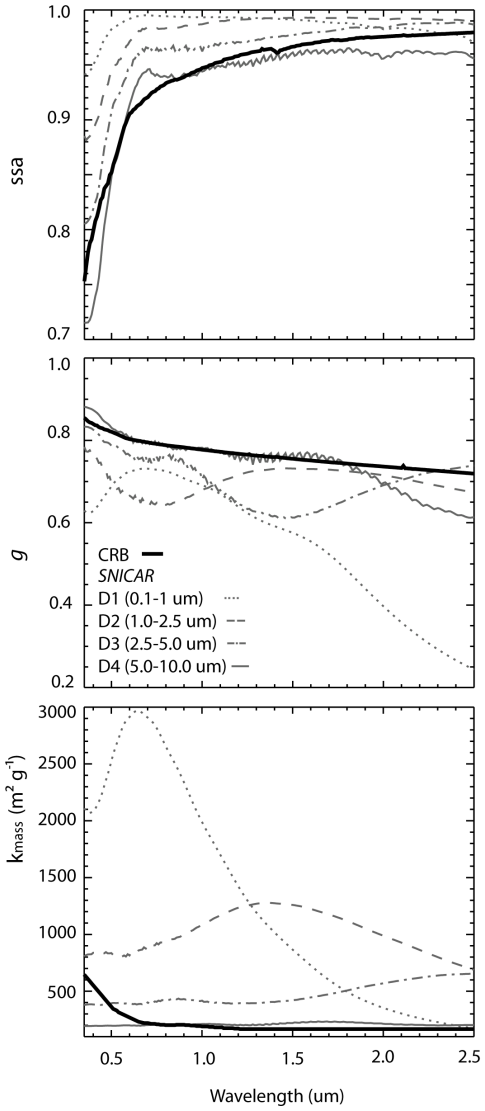

Figure 9 Optical property inputs for SNICAR (single scattering albedo, asymmetry parameter, and mass absorption coefficient) for CRB DOS and SNICAR dust.

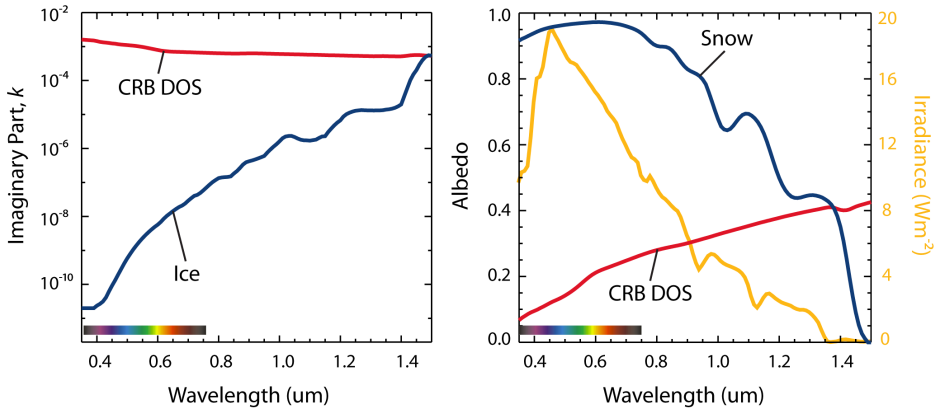

Figure 10 CRB DOS is highly effective at reducing snow albedo because it is most absorbing in the visible wavelengths, where incoming solar radiation is greatest, ice is least absorbing, and snow is most reflective.

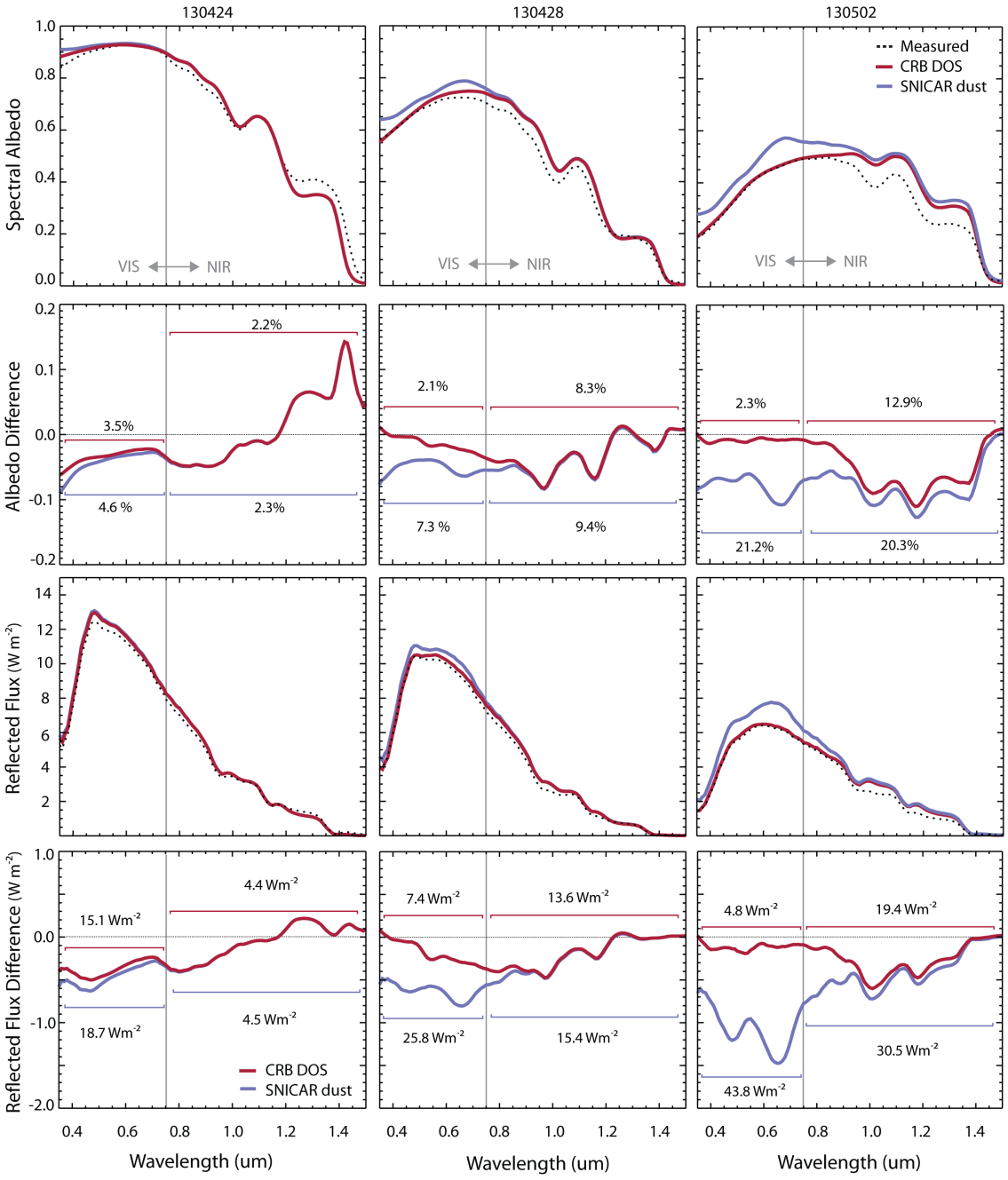

Figure 11 Measured and modeled spectral albedo, and reflected flux, for three days. The spectrally varying error metrics, difference from measured albedo and reflected flux, are plotted for the same three days. Spectrally integrated albedos for all days are plotted in Figure 13. Error metrics are summarized for all days in Table 1. The March 2nd albedo plot exhibits SNICAR overestimation of NIR albedo in the presence of heavy dust loading.

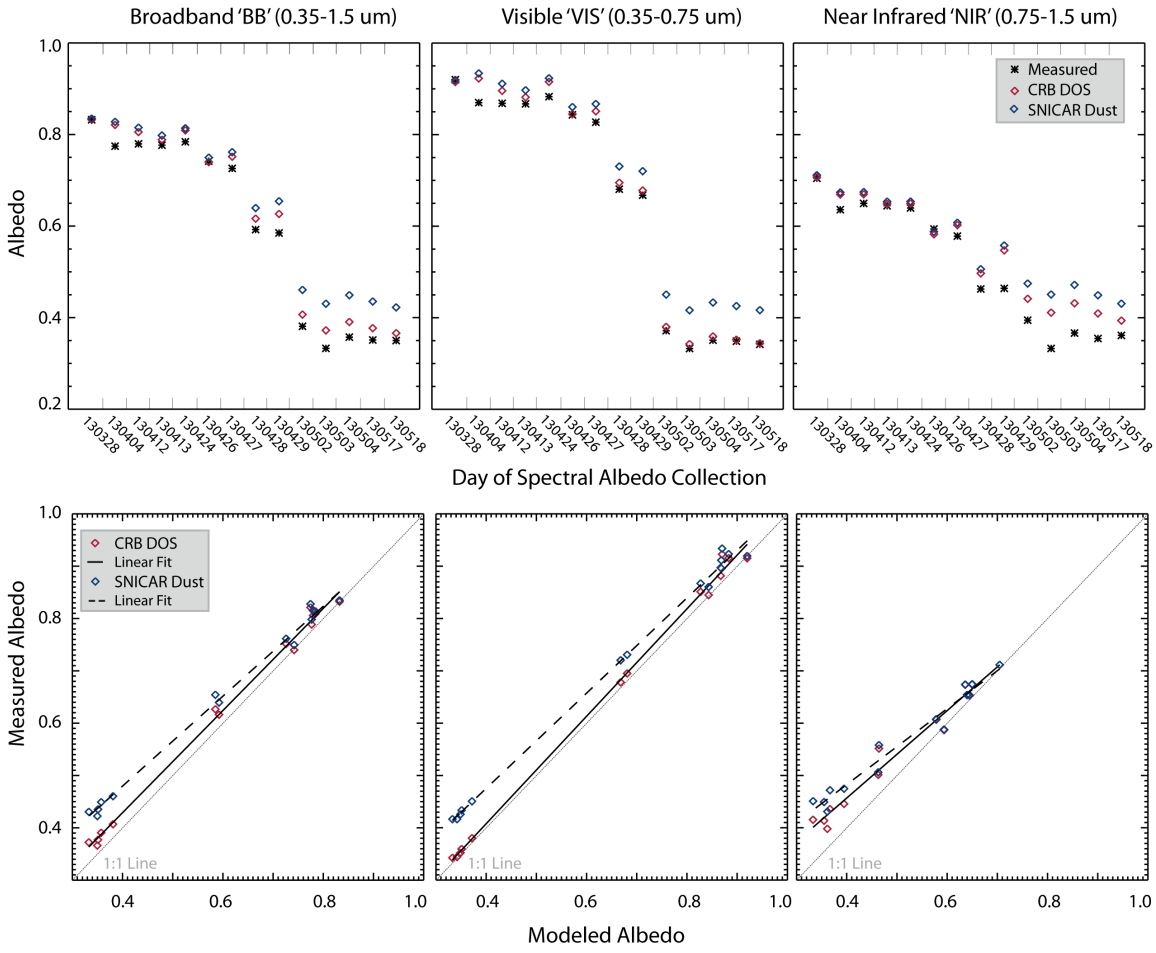

Figure 12 Measured and modeled broadband, visible, and NIR albedo calculated from spectral albedo using SBDART irradiance. For all wavelength ranges CRB DOS closely approximates measured albedo, with R^2 values of 0.995, 0.997, and 0.974 for BB, VIS, and NIR wavelength ranges, respectively. Similar to results found at the tower, this reduces total flux errors relative to SNICAR dust by 50% for BB, and by 70% and 25% for the VIS and NIR.

Figure 13 Rather than a continuous externally mixed layer of dust, like that which would result from artificial deposition, atmospheric deposition results in dust that is distributed amongst snow grains as internal and external mixtures, as exhibited in this DOS picture from SASP on May 10th, 2013. The inability of SNICAR to capture absorption by such a heterogeneous mixture may account for NIR errors in the presence of heavy dust.

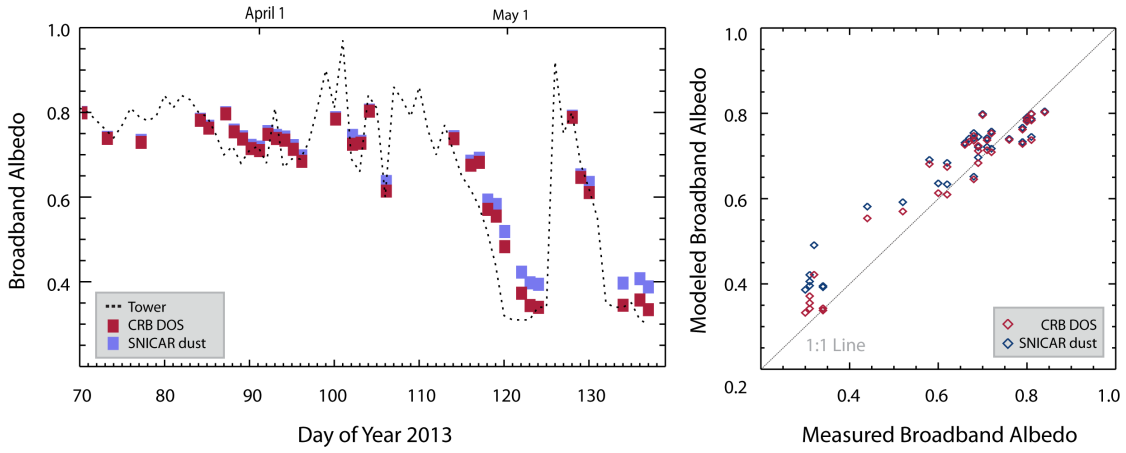

Figure 14 (Left) Modeled broadband albedo for 36 days between March 11 and May 18 plotted over to 11:00 AM broadband albedo from the SASP instrumentation tower. (Right) Scatter plot of measured and modeled albedo. The correlation coefficient is 0.966 (R^2= 0.92) for CRB DOS and 0.95 (R^2=0.93) for SNICAR dust. This results in flux differences (less absorption/more reflection) of 20 W m^{-2} for CRB DOS and 41 W m^{-2} SNICAR dust.

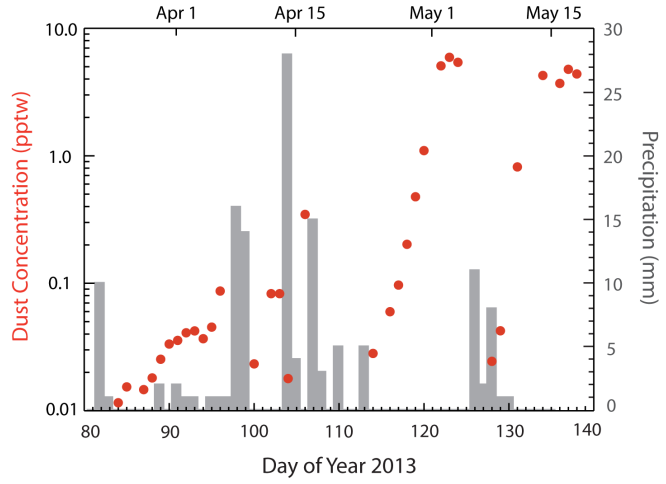

Figure 15 Dust concentration and snowfall events between March 21st and May 18th, 2013.

Table 1 Complex index of refraction for CRB DOS over a range of wavelengths.

Wavelength	Complex Refractive Index
0.35	1.525-0.0018i
0.40	1.525-0.0016i
0.45	1.525-0.0013i
0.50	1.525-0.0011i
0.55	1.525-0.0009i
0.60	1.525-0.0008i
0.65	1.525-0.0007i
0.70	1.525-0.00067i
0.75	1.525-0.00064i
0.80	1.525-0.00062i
0.90	1.525-0.00063i
1.00	1.525-0.00059i
1.10	1.525-0.00057i
1.20	1.525-0.00054i
1.30	1.525-0.00052i
1.40	1.525-0.00055i
1.50	1.525-0.00052i
1.60	1.525-0.0005i
1.70	1.525-0.00048i

Table 2 Time of albedo collection, surface snow density, grain size, and dust concentration for days of spectral albedo analysis. Surface measurements represent SNICAR inputs for the uppermost layer.

Date	DOY	Time of Albedo Measurement	Surface Snow Density (kg m^{-3})	Surface Grain Size (um)	Surface Dust Concentration (pptw)
130328	87	11:58	277.0	151.86	0.013
130404	94	11:02	313.5	383.11	0.034
130412	102	12:29	239.9	270.04	0.074
130413	103	13:31	239.9	316.19	0.075
130424	114	14:09	221.8	326.48	0.025
130426	116	11:59	307.5	278.95	0.055
130427	117	11:34	329.3	450.44	0.057
130428	118	13:17	282.4	364.00	0.183
130429	119	10:51	273.5	313.83	0.431
130502	122	11:33	295.0	448.81	4.599
130503	123	11:38	271.6	512.41	5.317
130504	124	10:43	250.3	496.66	5.772
130517	137	10:59	288.9	387.56	4.324
130518	138	13:45	267.6	312.27	3.725

Table 3 Summary of spectral albedo analysis, average errors are summarized at the bottom of each column and the largest errors are in bold.

		Measured				CRB DOS			SNICAR Dust		
	Date	DOY	Irradiance (Wm^{-2})	Reflected Flux (Wm^{-2})	Albedo	Albedo	% Difference	Difference ($W m^{2}$)	Albedo	% Difference	Difference ($W m^{2}$)
Broadband 'BB' (0.35-1.5 um)	130328	87	766.54	637.96	0.832	0.832	0.01%	0.07	0.835	0.3%	-1.94
	130404	94	846.02	655.22	0.774	0.821	5.8%	**-39.38**	0.828	6.6%	-45.07
	130412	102	993.92	774.81	0.780	0.806	3.3%	-25.86	0.815	4.5%	-35.34
	130413	103	627.07	487.04	0.777	0.789	1.5%	-7.46	0.798	2.7%	-13.41
	130424	114	784.94	615.49	0.784	0.809	3.1%	-19.57	0.814	3.7%	-23.32
	130426	116	944.29	700.51	0.742	0.740	0.3%	1.85	0.750	1.0%	-7.28
	130427	117	913.67	663.27	0.726	0.752	3.5%	-23.50	0.762	4.8%	-32.51
	130428	118	872.54	516.76	0.592	0.616	4.0%	-20.98	0.639	7.7%	-41.22
	130429	119	820.87	480.14	0.585	0.627	6.9%	-34.19	0.654	11.2%	-56.91
	130502	122	934.40	356.07	0.381	0.407	6.6%	-24.13	0.461	18.9%	-74.24
	130503	123	916.82	305.17	0.333	0.372	**11.2%**	-36.12	0.430	**25.6%**	**-89.50**
	130504	124	835.78	298.70	0.357	0.391	8.9%	-27.72	0.449	22.7%	-76.66
	130517	137	924.49	324.69	0.351	0.377	7.1%	-24.00	0.435	21.4%	-77.80
	130518	138	544.95	190.68	0.350	0.366	4.5%	-8.85	0.422	18.8%	-39.55
							4.8%	*-20.7033*		*10.7%*	*-43.9111*
Visible 'VIS' (0.35-0.75 um)	130328	87	454.41	418.02	0.920	0.915	0.5%	2.17	0.919	0.05%	0.19
	130404	94	500.69	435.57	0.870	0.923	**5.9%**	**-26.47**	0.934	7.1%	-32.00
	130412	102	589.72	512.12	0.868	0.896	3.1%	-16.14	0.911	4.8%	-25.30
	130413	103	372.10	322.69	0.867	0.882	1.6%	-5.36	0.897	3.4%	-11.09
	130424	114	465.80	411.30	0.883	0.915	3.6%	-15.12	0.923	4.5%	-18.77
	130426	116	560.34	472.48	0.843	0.845	0.2%	-0.92	0.860	2.0%	-9.62
	130427	117	542.05	448.36	0.827	0.851	2.9%	-13.01	0.867	4.7%	-21.60
	130428	118	517.91	352.62	0.681	0.695	2.1%	-7.38	0.731	7.1%	-25.83
	130429	119	486.67	325.00	0.668	0.678	1.5%	-5.02	0.720	7.6%	-25.57
	130502	122	554.40	206.09	0.372	0.380	2.3%	-4.75	0.451	19.2%	-43.79
	130503	123	544.01	181.04	0.333	0.343	2.9%	-5.38	0.416	**22.3%**	**-45.52**
	130504	124	495.49	173.93	0.351	0.359	2.4%	-4.18	0.433	21.0%	-40.86
	130517	137	548.39	191.26	0.349	0.352	1.0%	-1.89	0.426	19.9%	-42.24
	130518	138	323.51	110.64	0.342	0.344	0.7%	-0.74	0.417	19.7%	-24.15
							2.2%	*-7.4429*		*10.2%*	*-26.1536*
Near Infrared 'NIR' (0.75-1.5 um)	130328	87	312.13	219.94	0.705	0.711	0.9%	-2.10	0.711	1.0%	-2.13
	130404	94	345.33	219.65	0.636	0.673	5.7%	-12.91	0.674	5.8%	-13.07
	130412	102	404.20	262.68	0.650	0.674	3.6%	-9.72	0.675	3.8%	-10.04
	130413	103	254.97	164.36	0.645	0.653	1.3%	-2.10	0.654	1.4%	-2.32
	130424	114	319.14	204.19	0.640	0.654	2.2%	-4.44	0.654	2.2%	-4.55
	130426	116	383.95	228.03	0.594	0.587	1.2%	2.77	0.588	1.0%	2.34
	130427	117	371.62	214.91	0.578	0.607	4.8%	-10.49	0.608	5.0%	-10.91
	130428	118	354.63	164.14	0.463	0.501	8.0%	-13.60	0.506	9.0%	-15.39
	130429	119	334.20	155.14	0.464	0.552	17.2%	-29.18	0.558	18.3%	-31.34
	130502	122	380.00	149.98	0.395	0.446	12.1%	-19.38	0.475	18.4%	-30.46
	130503	123	372.81	124.13	0.333	0.415	**22.0%**	**-30.74**	0.451	**30.1%**	**-43.98**
	130504	124	340.29	124.77	0.367	0.436	17.2%	-23.54	0.472	25.1%	-35.80
	130517	137	376.09	133.43	0.355	0.414	15.3%	-22.11	0.449	23.5%	-35.56
	130518	138	221.44	80.04	0.361	0.398	9.6%	-8.10	0.431	17.5%	-15.39
							8.7%	*-13.26*		*11.6%*	*-17.76*

Chapter 4

Estimating radiative forcing by light absorbing impurities in snow from vertically resolved measurements of snow properties and impurity concentrations

Abstract

The deposition of light absorbing impurities accelerates snowmelt through reduction of albedo (direct impact), further indirect reduction of albedo by accelerating the growth of snow grain size (first indirect impact), and earlier uncovering of darker substrate (second indirect impact). Here, a daily time series of direct radiative forcing by dust and black carbon (BC) in snow is presented for the last two months of snow cover in 2013 at Senator Beck Basin Study Area, San Juan Mountains, CO using the snow/aerosol radiative transfer model SNICAR. Following measurements presented in Chapter 2, snow property inputs (density, optical grain radius, and dust/BC concentrations) were specified in 11 total layers, ten of which spanned the top 30 cm of the snowpack. To accurately capture absorption by dust, which dominates the impurity mass, the dust optical properties used for radiative transfer calculations were updated to represent dust deposited in snow in the Colorado River Basin. Over the measurement period, instantaneous radiative forcing (RF) by LAIs in snow (dust+BC) ranged from 0.25 W m^{-2} to 525 W m^{-2} with 12-hr daily averages ranging from 10 W m^{-2} to 347 W m^{-2}. The majority of RF occurred in the visible wavelengths (~90%; 0.35-0.75 μm), but expansion into the near infrared occurred with increasing LAI concentrations. The portion of LAI RF accounted for by BC, 1-5%, decreased as dust concentrations increased, illustrating the reduced radiative impact of BC in the presence of heavy dust loading. The RF values calculated from measurements typically fell within the range of RF values estimated indirectly from changes in surface reflectance (Chapter 1), on average, they were 25 W m^{-2} lower than reported RF values (direct+first indirect impact), but 12 W m^{-2} higher than minimum RF (direct impact only).

1. Introduction

A high temporal, spectral, and vertical resolution snow property dataset, collected at Swamp Angel Study Plot (SASP), Senator Beck Basin Study Area (SBBSA), San Juan Mountains, CO, was presented in Chapter 2. Variability in snow density, grain size, and dust/black carbon (BC) content over a full ablation season was determined from this time series, and the impact to surface albedo investigated. The regional specific optical properties of deposited impurities were determined from hemispherical reflectance and particle size distributions using an inversion technique, presented in Chapter 3. Here, these measurements are used to quantify radiative forcing by dust and BC in snow across the visible, near infrared, and broadband solar wavelength ranges. Unique radiative transfer model runs for only dust, only BC, and dust+BC partition the radiative contribution from each constituent and determine radiative forcing ratios. Additionally, radiative forcing estimated from measurements are compared to radiative forcing estimated from changes in surface reflectance following the method presented in *Painter et al.* [2007].

2. Methods

2.1 Radiative Transfer Model

Snow albedo was simulated with the offline version of the SNow, ICe, and Aerosol Radiation (SNICAR; version 8d) model [*Flanner and Zender*, 2005; 2006], which has been used to study radiative forcing by impurities in snow from the point [*Kaspari et al.*, 2011; *Sterle et al.*, 2013] to regional scale [*Flanner et al.*, 2007; *Flanner et al.*, 2009]. The model computes multiple scattering and reflectance from snow+aerosol mixtures across 470 bands (0.3 to 5.0 μm) at 10 nm resolution with a

single layer version of the two stream, multilayer radiative approximation of *Toon et al.* [1989]. Snow property inputs include snow optical grain size, snow density, and concentrations of light absorbing impurities. Other inputs include ground/substrate albedo and the cosine of the solar zenith angle. The single scattering optical properties for ice are extracted from lookup tables, which are included for a large range of grain sizes (between 10 μm to 5 mm at 1 μm resolution) and have been updated to reflect the revised ice optical property compilation of *Warren and Brandt* [2008]. Look up tables are also provided for several aerosol types including two types of BC (sulfate coated/uncoated), dust in four size bins, and volcanic ash.

2.2 Measurement Inputs

Albedo was estimated for each day snow sampling and spectroscopy took place between March 25th and May 18th. This time frame captured the transition from a relatively clean, accumulating snowpack, to a dust laden melting snowpack. Snow property inputs were specified in 11 total layers. In the upper ten layers, which spanned the top 30 cm in 3 cm increments, density and LAI concentrations were layer-specific following gravimetric sampling described in Part 1, and optical grain radius (OGR) values were resampled from 2 to 3 cm resolution. The lowest layer represented the remainder of the snow pack, and density and OGR inputs were daily average values below the top 30 cm. Dust and BC concentrations, which tend to be stationary in the bulk snowpack, remained constant to reflect the average concentration sampled across the lower snowpack profile (1-L samples in 10 cm increments, from beneath the top 30 cm to the ground) on March 25th. This lower layer was needed to represent the full depth of the snowpack but should not impact surface albedo, as the extinction depth of solar radiation

is shallow (exponential past 40 cm in clean snow) [*Warren*, 1982], and the estimated maximum depth to which LAIs impact albedo is ~30 cm.

The model was run hourly by holding snow inputs constant and varying the cosine of the solar zenith angle to account for daily variation in snow albedo, irradiance, and radiative forcing (Figure 1). The hourly solar zenith angle was calculated from the site latitude and longitude (SASP; 37°54'24.89" N, -107°42'40.76" W). The daily average albedos and radiative forcings reported here represent average values across hours with positive solar zenith angles only. These values differ from daily means (like those reported in Chapter 1), which for account for positive and zero values across the full 24-hour day.

Albedo was estimated for four scenarios: snow with dust only, snow with BC only, snow with dust and BC, and clean snow (no impurities). Technically, the dust scenario was not uniquely dust, as concentrations and optical properties have been determined from filtered impurities, which are mixtures. Using dust only, though, likely underrepresents absorption by BC, as it is a small volume fraction of the total impurity mass. Therefore, BC only and dust+BC runs are used to investigate the relative and combined impacts of each LAI constituent. Only impurity concentration inputs were altered between scenarios, measured densities and grain sizes remained the same. Therefore, radiative forcing in this context represents the direct impact of LAIs (enhanced surface absorption), and not the indirect impacts (enhanced grain growth and reduction of snow covered area) [*Hansen and Nazarenko*, 2004; *Painter et al.*, 2007].

Measured BC concentrations were specified as the uncoated variety, the optical properties of which have been tuned to have a mass absorption cross section of 7.5 m^2 g^{-1}

at 550 nm, corresponding to the value suggested by *Bond and Bergstrom* [2006] [*Flanner et al.*, 2007]. Dust concentrations were specified in a new dust category, incorporated into SNICAR to reflect the optical properties of dust deposited in snow in the Colorado River Basin. The single scattering optical properties required for radiative transfer calculations were retrieved from measured dust reflectance and particle size distributions using the inversion technique described in Chapter 3. Briefly, reflectance was modeled from single scattering properties, modeled with Mie theory, over a range of values for the imaginary part of the complex refractive index (k=-0.00001 to -0.1), for the measured grain size distribution and a specified value for the real part of the complex refractive index (n= 1.525; *Grams et al.* [1974]). This representation more accurately captures absorption by dust in this region and reduces errors in albedo modeling by 50% relative to a more general dust characterization.

2.3 Uncertainty

Optical grain radius is an important factor in modeling snow albedo as it determines reflectance in the NIR, and mainly controls clean snow albedo. The uncertainty in grain size retrievals from contact spectroscopy, as described in Chapter 2, were accounted for here by perturbing OGR inputs by ±20 μm in all layers/scenarios, to assess the propagations of the grain size uncertainty through albedo and radiative forcing estimates. To gain an understanding of general uncertainty in the time series estimated broadband albedo was compared to measured broadband albedo at the SASP instrumentation tower, at hourly and daily time steps. Spectral albedo was used to assess spectral variation over a smaller subset of the measurement record.

2.4 Radiative Forcing

Snow reflectance varies spectrally, and therefore estimating radiative forcing (in W m^{-2}) requires the spectral distribution of incoming solar radiation. The irradiance measurements at SBBSA instrumentation towers are not spectrally resolved, and therefore clear sky spectral irradiance was modeled hourly between 0.35 and 2.5 μm at 10 nm resolution with the Santa Barbara DISORT Atmospheric Radiative Transfer model (SBDART) [Ricchiazzi et al., 1998]. To account for daily variation in sky conditions, the modeled spectral irradiance was scaled such that the summation equaled broadband irradiance measured at the instrumentation tower (*Kipp and Zonen pyranometer*; 0.35-2.5 μm). From SNICAR albedo and SBDART irradiance spectrally weighted albedo between 0.35 and 0.75 μm (visible; VIS), 0.75 and 2.5 μm (near/shortwave infrared; NIR), and 0.35 μm and 2.5 μm (broadband; BB), was calculated by dividing the product of the summation of irradiance and albedo by the summation of irradiance, i.e. for broadband albedo:

(1) $$\alpha = \frac{\sum_{\lambda=0.35\mu m}^{2.5\mu m} I * \alpha_{lai} \Delta\lambda}{\sum_{\lambda=0.35\mu m}^{2.5\mu m} I \Delta\lambda}$$

where I is scaled spectral irradiance at the given solar zenith angle, α_{lai} is the modeled albedo with dust and/or BC at the same solar zenith angle, and λ is the wavelength (μm).

Radiative forcing is estimated by taking the summation of the product of spectral irradiance and the difference between the spectrally weighted dust/BC albedo and clean snow albedo, which represents the enhanced surface absorption due to dust/BC, again for broadband wavelengths:

(2) $$RF = \sum_{\lambda=0.35\mu m}^{2.5\mu m} I * (\Delta\alpha)\Delta\lambda$$

where $\Delta\alpha = \alpha_{clean} - \alpha_{lai}$, which is the difference between clean snow albedo and dust/BC albedo at the same hour, for the same snow grain size and density.

2.5 Radiative Forcing Comparison

Radiative forcings estimated directly using the method described above were compared to the existing dust radiative forcing record at SASP (as presented in Chapter 1), which are estimated indirectly from surface reflectance following the method first presented by *Painter et al*. [2007]. This method calculates radiative forcing for two scenarios: the minimum case, which accounts for albedo reduction in the visible wavelengths (the direct impact) and the maximum case, which additionally accounts for expansion of RF into the NIR, and enhanced grain growth (first indirect impact; *i*1). This is done by partitioning the proportion of the change in NIR/SWIR albedo due to the presence of dust versus grain coarsening in the absence of dust, a relationship which was developed at SBBSA [*Painter et al.*, 2007]. Reported radiative forcings are then the average of these two scenarios.

The minimum radiative forcing ($F_{d\min}$) case:

(3) $$F_{d\min} = E_{vis}\Delta_{vis}$$

where E_{vis} is visible irradiance (W m^{-2}), $\Delta_{vis} = 0.92 - \alpha_{vis}$, with α_{vis} being measured visible albedo and 0.92 being the mean visible albedo for relatively dust-free snow at SBBSA [*Painter et al.*, 2007].

The maximum radiative forcing ($F_{d\max+i1}$):

(4) $$F_{d\max+i1} = 0.5(E_{vis}\Delta_{vis} + E_{nir}\alpha_{nir}((1/\xi) - 1)$$

where if

$\Delta_{vis} \leq 0.17$ then $\xi = 1 - 1.689\Delta_{vis}$

else if,

$\Delta_{vis} > 0.17$ then $\xi = 0.67$

and E_{nir} is the NIR/SWIR net shortwave flux, and α_{nir} is the NIR/SWIR albedo.

Spring radiative forcings are reconstructed at the end of each water year from March 15th [*Painter et al.*, 2007; *Skiles and Painter*, 2014; *Skiles et al.*, 2012]. The record is continuous, not discrete, as it is based on tower measurements and requires no snow sampling.

3. Results and Discussion

3.1 Modeled Albedo

Due to the control that $\Delta\alpha$ has on radiative forcing, it is of interest to discuss the trends in modeled albedo between SNICAR clean snow/impurity scenarios (Figure 2). Daily broadband albedo in the absence of impurities (α_{clean}) ranged from 0.82 to 0.74. Due to the optical properties of snow, ice absorption in the NIR is determined by OGR, and therefore NIR α_{clean} exhibited a greater range (0.66 to 0.5; 23% difference) than VIS α_{clean} (0.98 to 0.97; 2% difference), where absorption is determined by concentrations of LAIs (Figure 4). While there were periodic increases in α_{clean}, due to new snowfall, the trend was decreasing over the measurement period corresponding to increasing grain size (Figure 3).

Daily snow albedo in the presence of BC only (α_{BC}) exhibited a similar range to α_{clean} with a maximum $\Delta\alpha$ of 0.009. This is due to the low BC concentrations sampled in WY13 (1-26 ppb), resulting in a α_{BC} that was only slightly more absorptive than clean

snow (0.5-1% reduction in albedo). The changes in VIS α_{BC} over the measurement period were slightly greater that that of VIS α_{clean} (2.4% vs. 2%), this absorption was minor though, and the relationship between BC concentrations, OGR, and VIS/NIR albedo indicate trends in α_{BC}, like α_{clean}, are mainly controlled by trends in OGR (Figure 4).

Albedo in the presence of dust and BC (α_{D+BC}) exhibited a far greater range than either α_{clean} or α_{BC}, from 0.80 to 0.30, with a corresponding $\Delta\alpha$ range of 0.01 to 0.5. Reduction in α_{D+BC} over the measurement period was mainly controlled by dust concentration in the surface layer, with no significant relationship with grain size or BC concentrations. The relationship between dust concentrations is negative log-linear, where α_{D+BC} decreased linearly with exponential increases in surface dust concentrations. The majority of this absorption occurred in the VIS, but expanded to the NIR as $\Delta\alpha$ increased, with NIR α_{D+BC} noticeably diverging from α_{clean} when $\Delta\alpha$ increased above 0.2 (Figure 2). Albedo in the presence of dust only (α_D) was similar to α_{D+BC}, ranging from 0.81 to 0.32 ($\Delta\alpha$ range of 0.01 to 0.48).

3.2 Model Performance

The smallest difference between measured and modeled albedo was α_{D+BC}, with an average difference of +0.02 over the measurement period, next was α_D with an average difference of +0.04 (Figure 5). Because SNICAR consistently overestimated albedo relative to measured albedo, mainly in the VIS wavelengths but also in NIR wavelengths in the presence of heavy dust loading (see Chapter 3), representing BC as a unique constituent improved the representation of absorption by LAIs. The largest difference between measured and modeled albedo occurred between April 27th and May 2nd, when dust emerged more quickly at the tower than at the sampling site, resulting in faster melt

and reduction in measured albedo. When this time period is excluded, the difference between α_{D+BC} and measured albedo reduces to +0.01.

These differences can be quantified in terms of reflected flux by taking the difference between spectrally integrated reflected flux and measured reflected flux. This difference was as great as 150 W m^{-2} overestimation/underestimation at the hourly time scale, a product of driving hourly estimates over a day with measurements collected at a single point in time. Over the full measurement period, though, the differences in reflected flux averaged to -19 W m^{-2}, a 5% overestimation of reflected flux for α_{D+BC} (Figure 6).

Difference between measured and modeled spectral albedo for 14 days across the measurements period is discussed in detail in Chapter 3. Briefly, across the range of snow reflectance the difference was 5%, a -20 W m^{-2} difference, similar to that found for the hourly broadband comparison above. Snow albedo was best matched in the visible wavelengths, to within 2% on average, a -7 W m^{-2} difference. Spectral albedo was most poorly matched in NIR in the presence of heavy dust loading, when the differences as great as 25% result in flux errors of -30 W m^{-2}. On average, the NIR difference was 9%. While this is 4 times the difference in the VIS, the lower solar irradiance in these wavelengths results in a flux difference that is less than half that in the VIS (13 W m^{-2}). This analysis was completed for dust only; when BC was included (α_{D+BC}) spectral albedo modelin improved by 1 W m^{-2} over the full range of snow reflectance. Figure 7 shows an example of spectral albedo scenarios for two days, April 26th when layers D6-8 are still in the lower surface layers, and May 2nd, when D6-9 have combined at the surface.

3.3 Grain Size Uncertainty

Perturbing grain size by ±20 μm resulted in a maximum difference in α_{clean} of -0.008 to 0.007, and an average difference of ±0.004. For α_{D+BC} the maximum difference was -0.01 to 0.009, with an average difference of ±0.006. The higher differences occurred on days when cleaner snow lies at the surface, allowing changes in grain size to manifest. The smaller differences occurred on days with high dust content at the surface, when dust strongly dominated absorption. For α_{D+BC} changes in grain size impacted the full range of snow reflectance, while for α_{clean} the changes only manifested in the NIR. The impact on radiative forcing was between -0.9 and +1.4 W m^{-2}, ±1 W m^{-2} on average, for all scenarios.

3.4 Radiative Forcing

3.4.1 Dust+BC

Intraseasonal variation and general trends in radiative forcing by dust+BC (RF_{D+BC}) are determined by dust events, new snowfall, and snowmelt rates, which control LAI concentrations in the surface and near-surface layers (Figure 8). In the first two weeks of the measurement period (March 25th - April 8th) when dust concentrations in the surface layers were lower, from 7.9 x 10^{-4} to 6.0 x 10^{-2} pptw, daily average RF_{D+BC} (hereafter, simply 'RF_{D+BC}') ranged from 10 to 39 W m^{-2} (Figure 9). In the following week (April 8th - April 16th) RF_{D+BC} was similar, 38 W m^{-2}, despite the occurrence of dust events 6-8 (D6-8), which deposited 98% of the season total dust mass. A large increase in RF_{D+BC} did not immediately accompany these dust deposition events because a series of snowfall events kept dust content in the top 12 cm (4 layers) low, 0.08 pptw on average. The precipitation free period at the end of April resulted in snowmelt that led to the

emergence, and then convergence, of the D6-8 individual dust layers. As this process took place RF_{D+BC} increased from 39 W m^{-2} on April 26th to 146 W m^{-2} on April 30th, when D8 first emerged and D9 was deposited.

The highest RF_{D+BC} values occurred between May 2nd and May 4th corresponding the highest dust concentration in the surface layer (>5.0 pptw). Instantaneous values over this time period peaked beween 400 and 500 W m^{-2} (more than half of incoming solar irradiance). Daily average RF_{D+BC} peaked on May 3rd, corresponding to the highest sampled dust concentration (341 W m^{-2}; 5.9 pptw dust). The total absorption by the snowpack, over 70% of incoming solar radiation, over this time period resulted in rapid melt and scavenging of both mass from snow grains and dust concentrations (see Figure 11 and 13 in Chapter 2), leading to a decrease in RF_{D+BC} to 270 W m^{-2} on May 4th. Dust was buried by snowfall on May 8th, briefly reducing RF_{D+BC} to below 100 W m^{-2} for a few days. The dust quickly resurfaced, accompanied by a rise in radiative forcing to 221 W m^{-2} on May 14th and then 281 W m^{-2} on May 17th. On the final day of sampling, RF_{D+BC} decreased to 158 W m^{-2}, which is again attributed to lower dust concentrations due to scavenging of dust from the surface layers and lower irradiance (see Chapter 2; Figures 11, 13 and this chapter Figure 3, Figure 6).

The portion of RF that occurred in the NIR increased with dust concentrations (Figure 10). Since clean scenario and LAI scenario runs utilized the same grain size input, this is mainly determined by the wavelength range over which there is a divergence between clean/LAI albedo curves ($\lambda\alpha_C - \lambda\alpha_{D+BC} > 0$) (see Figure 7). The wavelength of divergence increased from 0.7 μm, for relatively clean snow at the beginning of the measurement period, to 1.2 μm when D6-9 was present as a merged layer at the surface.

Correspondingly, the NIR contribution increased from 5% to 20% of total radiative forcing when concentration increased from 0.1 pptw to >4.0 pptw. When $\Delta\alpha$ was less than 0.05, at the beginning of the season and on days with new snowfall, less than <1 W m^{-2} (5% of RF_{D+BC}) occurred past 0.75 μm. Over the month of April, as dust concentrations in the surface layers increased, $\Delta\alpha$ increased from 0.06 to 0.25 and NIR RF_{D+BC} increased from 1 - 10 W m^{-2} of total RF_{D+BC} (5 to 10%). On April 30th when D6-9 was at the surface, $\Delta\alpha$ reached 0.3 and NIR RF_{D+BC} increased to 22 W m^{-2} (15%). After this, when D6-9 was at the surface, $\Delta\alpha$ was greater than 0.4 and NIR RF_{D+BC} was 40 - 60 W m^{-2} (~20% of total). Given the spectral albedo errors between NIR albedo in the presence of heavy dust loading (see Chapter 3), this is likely an underestimate of the NIR contribution on these days (and an underestimate of total RF).

3.4.2 Dust/BC Only

There was a minor reduction in radiative forcing between daily average RF_{D+BC} and dust only (RF_D) scenarios, 2 W m^{-2} on average over the measurement period, but the same patterns were exhibited: the lowest RF_D values occurred in the beginning of the measurement period and on days with new snowfall (9 to 37 W m^{-2}), increased with snowmelt as dust came to the surface (40 to 143 W m^{-2}), and peaked when D6-9 was present as a merged layer at the surface (337 W m^{-2} peak, 257 W m^{-2} average). Again, similar to RF_{D+BC}, the NIR contribution to radiative forcing increased with rising dust concentrations, from ~4% in the beginning of the measurement period to ~18% when dust was at the surface.

Daily average radiative forcing by BC only (RF_{BC}) was 3.5 W m^{-2} on average, between 85% and 98% (92% average) less than that by RF_D. Patterns were similar to

those exhibited by RF_{D+BC}, as BC concentrations co-varied with dust concentrations. The lowest RF_{BC} occurred prior to D6 (1.5 to 2.8 W m^{-2}), increased over the time period that dust layer D6-8 deposited/emerged (3.1 to 4.8 W m^{-2}), and were highest when there is high dust content at the surface (7 W m^{-2} peak, 5 W m^{-2} average). The NIR contribution never increased above 10%, with absorption past 0.75 μm accounting for 0.02 - 8% of absorption (4% on average). It is likely that RF_{BC} is overestimated by this method, because the measured OGR inputs are dust influenced and would be smaller in the presence of BC only.

The difference between RF_D and RF_{D+BC} is the radiative impact of BC in the presence of dust. This difference, between 0.2 and 4.5 W m^{-2}, increased as radiative forcing increased, but the percent difference, between 1% and 5%, decreased as radiative forcing increased. Therefore, the proportion of RF accounted for by BC decreased with increasing dust concentrations. On average, the RF contribution by BC was 1.6 W m^{-2} less in the presence of dust relative to RF_{BC} alone, a 50% reduction. This result, a reduced absorption efficacy, is consistent with another study that uses SNICAR to investigate the impacts of dust and BC in a region of heavy dust loading in the Himalaya [*Kaspari et al.*, 2013].

While the BC in SNICAR is 30 times more absorbing than the dust from the Colorado River Basin (Chapter 3), the BC contribution was relatively small here because it was a minor fraction of total impurity concentration (0.0002% to 0.1%, 0.01% on average). To exhibit the relative absorption efficacy of sampled BC concentrations in the presence of such heavy dust loading, dust and BC concentrations are scaled by their respective mass extinction coefficients at .55 μm in Figure 11, where the mass extinction

coefficient is the absorption efficiency scaled by the particle density, and describes the magnitude of absorption per unit mass.

3.4.3 Radiative Forcing Comparison

Daily mean radiative forcing estimated via the *Painter et al.* [2007] (RF_{P07}) method was 45 W m^{-2} over the measurement period, with instantaneous values ranging from 0 to 440 W m^{-2}. In Figure 12, the gray shading indicates maximum (RF_{maxP07}) and minimum (RF_{minP07}) RF_{P07} cases. Over the measurement period, the average difference between RF_{maxP07} and RF_{minP07}, the portion of RF that would be attributed to enhanced grain growth, was 24 W m^{-2} (±12 W m^{-2} from average). This difference was lowest over periods of frequent snowfall (April 7th-April 20th; 8 W m^{-2}) and highest when dust was at the surface (May 1-5th, May 12th-17th; 53 W m^{-2}).

Due to the fact the direct radiative forcing estimated here accounts for only the direct effect, we would expect it to be less than RF_{P07}, which accounts for both enhanced absorption in the visible wavelengths and enhanced grain growth. Up until April 29th RF_{D+BC} was 34 W m^{-2} less than RF_{P07}, consistently falling below even RF_{minP07}. This difference was 15 W m^{-2}, on average, prior to dust deposition (March 25th-April 6th) and 4 W m^{-2}, on average, when dust was present in the surface layers, but still buried beneath fairly clean snow (April 10th – April 29th).

When dust first came to the surface (April 30th – May 4th) hourly RF_{D+BC} increased above RF_{P07}, by 22 W m^{-2} on average, but still fell below RF_{maxP07}. The exception was May 4th, when RF_{D+BC} briefly increased above RF_{maxP07} for a few hours spanning peak solar irradiance (~12 W m^{-2} greater over the length of the day). Over the remainder of May RF_{D+BC} remained slightly elevated above RF_{P07}, by 7 W m^{-2} on

average, but remained below RF_{maxP07} by 32 W m^{-2}, on average. Over the full measurement period, RF_{D+BC} was, on average, 25 W m^{-2} less than RF_{P07}, 63 W m^{-2} less than RF_{maxP07}, and 12 W m^{-2} greater than RF_{minP07}. While RF_{D+BC} was lower than RF_{P07} prior to dust emergence, these results suggest that RF_{D+BC} and RF_{P07} are fairly well matched when averaged across the full spring season, given that the difference between them is only slightly more than the difference in reflected flux attributed to the overestimation of albedo from SNICAR (-20 W m^{-2}).

5. Concluding Thoughts

Here a time series of radiative forcing by dust and black carbon in snow was simulated directly from snow measurements collected between March 25th and May 18th, 2013 in the San Juan Mountains, Colorado. This was the first time a dataset has been collected with high enough temporal, spectral, and vertical resolution to directly account for the impact of dust and optical grain size stratigraphy on radiative forcing over a full spring season. Together with the consistent record of snow energy balance fluxes at SBBSA, it is the most complete set of coincident radiation and microphysical snow observations of which we are aware.

Dust dominated both impurity mass and absorption, with hourly RF ranging from 0.25 W m^{-2} to 525 W m^{-2}, and daily average RF_D ranging from 9 W m^{-2} to 342 W m^{-2}. There was only a minor increase in daily average RF from RF_D to RF_{D+BC}, which ranged from 10 W m^{-2} to 347 W m^{-2}. The difference between RF_D and RF_{D+BC}, the portion accounted for by BC, was about half of RF_{BC} (1 W m^{-2} to 7 W m^{-2}), indicating absorption by LAIs is reduced in the presence of multiple constituents. Hourly values typically fell

within, or below, the range of RF estimated indirectly from changes in surface reflectance.

Absorption by LAIs occurred mainly in the VIS, but RF expanded into the NIR as dust concentrations increased and the wavelength of divergence occured at longer wavelengths. This relationship between dust concentrations and VIS/NIR albedo is important, as it may allow for the estimation of dust content from surface albedo when measurements of dust concentrations cannot be made, such as snow albedo inferred from radiance measurements by remote imaging spectroscopy platforms, like NASA's Airborne Snow Observatory (http://aso.jpl.nasa.gov/). Because clean snow albedo is mainly controlled by optical grain radius, it could be modeled by extracting OGR from snow reflectance using the Nolin-Dozier inversion model [*Nolin and Dozier*, 2000]. Dust concentration could then be estimated via a look up table populated with dust concentration and corresponding wavelength of divergence.

The next step in advancing modeling techniques of dust in snow is accounting for dust stratigraphy and absorption explicitly in a numerical multi-layer snow melt model, an exercise that has been previously limited by lack of measurements. Building upon the dataset presented in Chapter 2, the dust optical properties presented in Chapter 3, and the modeling presented here, the next chapter presents the coupling of SNICAR to the physically based snowmelt model SNOWPACK [*Bartelt and Lehning*, 2002; *Lehning et al.*, 2002]. By building into the model the ability to track dust layers, and then calling SNICAR to update absorption of solar radiation directly from SNOWPACK modeled snow/impurity properties, the vertically resolved impacts of dust on snow evolution can be modeled physically. This controlled modeling environment, which is constrained and

validated by measurements, facilitates the understanding of dust influenced snow metamorphism and albedo feedbacks. These can be difficult to assess from measurements, as snow/climate interactions are temporally and spatially variable, and logistical constraints limit high-resolution measurement capabilities in most snow-covered environments.

5. References

Bartelt, P., and M. Lehning (2002), A physical SNOWPACK model for avalanche warning systems. Part 1: numerical model, *Cold Regions Science and Technology*, *35*(3), 123-145.

Bond, T. C., and R. W. Bergstrom (2006), Light absorption by carbonaceous particles: an investigative review, *Aerosol Science and Technology*, *40*, 27-67.

Flanner, M. G., and C. Zender (2005), Snowpack radiative heating: Influence on the Tibetan Plateau climate, *Geophysical Research Letters*, *32*.

Flanner, M. G., and C. Zender (2006), Linking snowpack microphysics and albedo evolution, *Journal of Geophysical Research*, *111*(D12), doi:10.1029/2005JD006834.

Flanner, M. G., C. S. Zender, J. T. Randerson, and P. J. Rasch (2007), Present-day climate forcing and response from black carbon in snow, *Journal of Geophysical Research*, *112*.

Flanner, M. G., C. S. Zender, P. G. Hess, N. M. Mahowald, T. H. Painter, V. Ramanathan, and P. J. Rasch (2009), Springtime warming and reduced snow cover from carbonaceous particles, *Atmospheric Chemistry and Physics*, *9*, 2481-2497.

Grams, G. W., I. H. Blifford, D. Gillette, and P. B. Russell (1974), Complex Index of Refraction of Airborne Soil Particles, *Journal of Applied Meteorology*, *13*, 459-471.

Hansen, J., and L. Nazarenko (2004), Soot climate forcing via snow and ice albedos, *Proceedings of the National Academy of Sciences*, *101*(2), 423-428.

Kaspari, S., T. H. Painter, M. Gysel, and M. Schwikowski (2013), Seasonal and elevational variations of black carbon and dust in snow and ice in the Solu-Khombu,

Nepa and estimated radiative forcings, *Atmospheric Chemistry and Physics Discussions*(13).

Kaspari, S., M. Schwikowski, M. Gysel, M. G. Flanner, S. Kang, S. Hou, and P. A. Mayewski (2011), Recent increases in balck carbon concentrations from a Mt. Everest ice core spanning 1860-2000 AD, *Geophysical Research Letters*, *38*.

Lehning, M., P. Bartelt, B. Brown, C. Fierz, and P. Satyawali (2002), A physical SNOWPACK model for the Swiss avalanche warning. Part II: snow microstructure, *Cold Regions Science and Technology*, *35*(3), 147-167.

Nolin, A. W., and J. Dozier (2000), A hyperspectral method for remotely sensing the grain size of snow, *Remote Sens Environ*, *74*(2), 207-216.

Painter, T. H., A. P. Barrett, C. C. Landry, J. C. Neff, M. P. Cassidy, C. R. Lawrence, K. E. McBride, and G. L. Farmer (2007), Impact of disturbed desert soils on duration of mountain snow cover, *Geophysical Research Letters*, *34*.

Ricchiazzi, P., S. R. Yang, C. Gautier, and D. Sowle (1998), SBDART: A research and teaching software tool for plane-parallel radiative transfer in the Earth's atmosphere, *Bulletin of the American Meteorological Society*, *79*(10), 2101-2114.

Skiles, S. M., and T. H. Painter (2014), A 9-yr record of dust on snow in the Colorado River Basin, paper presented at 12th Biennial Conference of Science and Management on the Colorado Plateau, Flagstaff, AZ.

Skiles, S. M., T. H. Painter, J. Deems, C. Landry, and A. Bryant (2012), Dust radiative forcing in snow of the Upper Colorado River Basin: Part II. Interannual variability in radiative forcing and snowmelt rates, *Water Resources Research*, *48*.

Sterle, K. M., J. R. McConnell, J. Dozier, R. Edwards, and M. Flanner (2013), Retention and radiative forcing of black carbon in the Eastern Sierra Nevada snow, *The Cryosphere*, *7*.

Toon, O. B., C. P. McKay, T. P. Ackerman, and K. Santhanam (1989), Rapid calculation of radiative heating rates and photodissociation rates in inhomogeneous multiple scattering atmospheres, *Journal of Geophysical Research*, *94*(D13), 16,287-216,301.

Warren, S. G. (1982), Optical properties of snow, *Reviews of Geophysics and Space Physics*, *20*(1), 67-89.

Warren, S. G., and R. E. Brandt (2008), Optical constants of ice from the ultraviolet to microwave: A revised compilation, *Journal of Geophysical Research*, *113*.

Figures

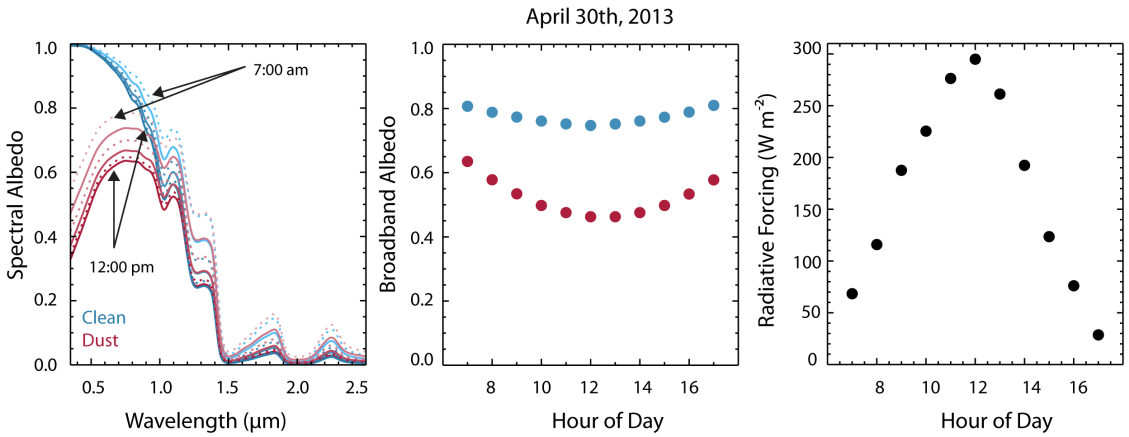

Figure 1 Daily variation in spectral albedo, broadband albedo, and radiative forcing modeled with SNICAR, from measurements collected on April 30th, 2013.

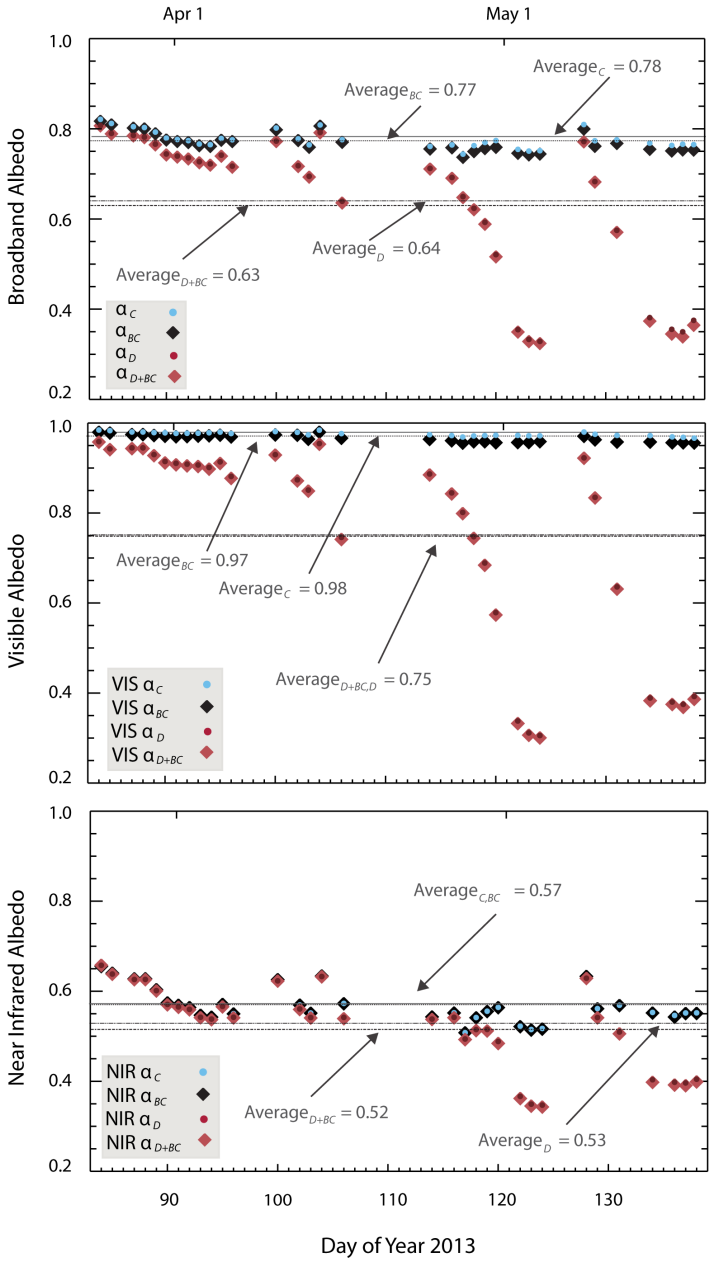

Figure 2 Daily average broadband, VIS, and NIR albedo modeled with SNICAR, for different impurity scenarios, from measurements presented in Chapter 2 (also see Figure 3), between March 25th and May 18th (snow all gone), 2013.

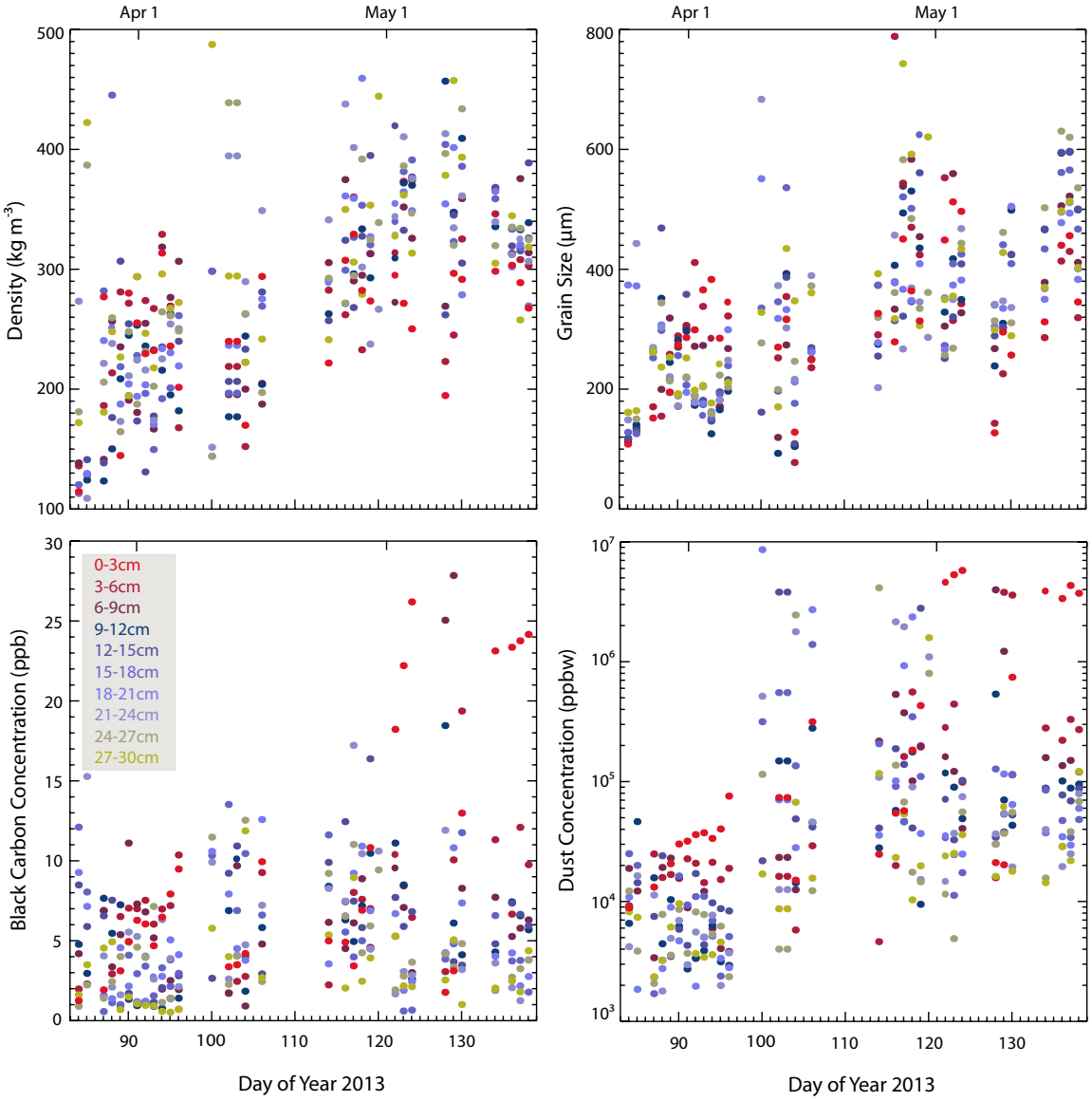

Figure 3 Measured snow property inputs for the upper ten surface layers in SNICAR runs, from gravimetric sampling presented in Chapter 2. For the clean snow scenario only density (upper left) and optical grain size (upper right) are specified, impurity scenarios additionally include BC only (lower left), dust only (lower right), and dust+BC.

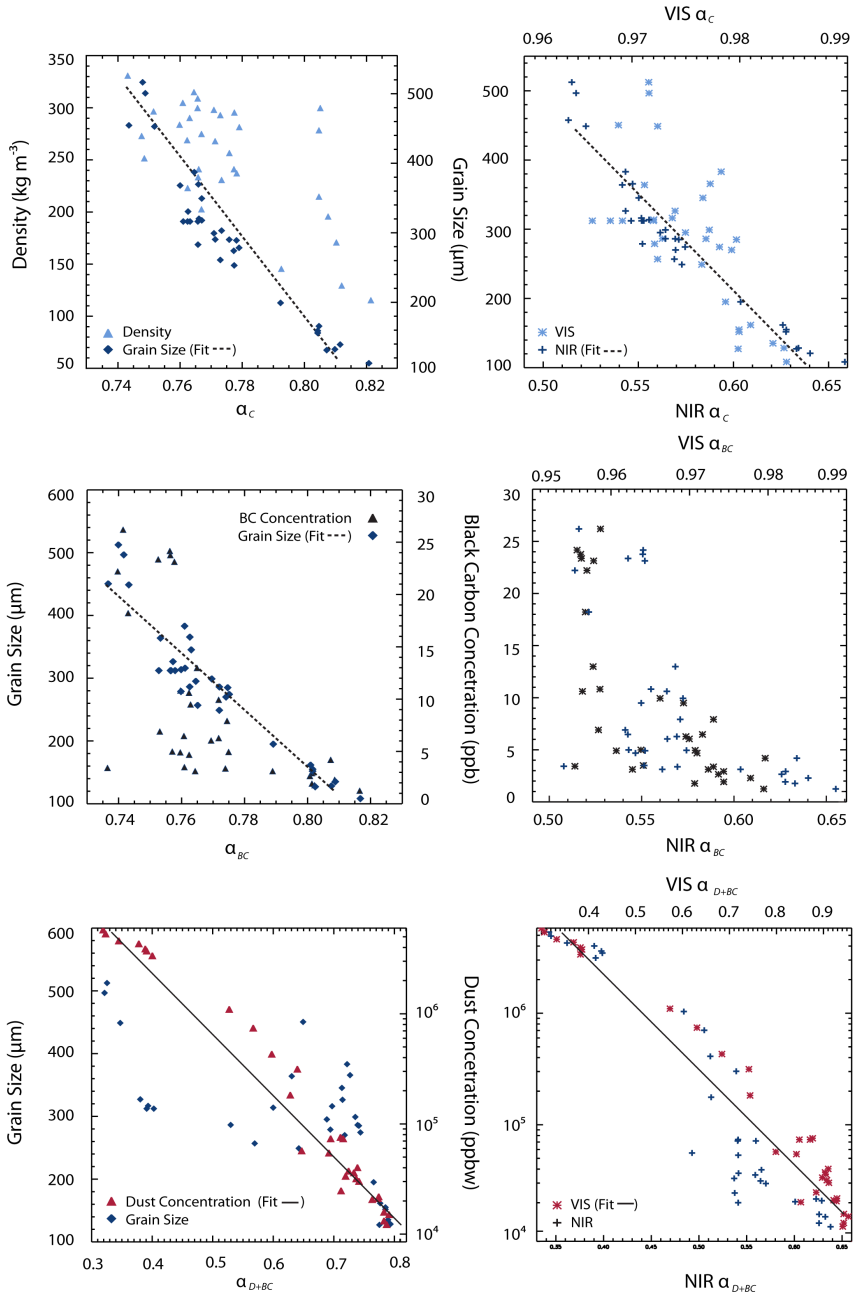

Figure 4 The relationship between SNICAR modeled albedo and snow inputs, with statistically significant relationships indicated with fit lines. With an R^2 value of -0.95, α_C is correlated with grain size in the surface layer (top, left) as determined by NIR absorption (R^2=-0.96; top, right), α_{BC} is also mainly controlled by grain size with an R^2 value of -0.94 (middle, left), and not BC concentration (middle, right). With a log-linear R^2 value of -0.96 α_{D+BC} is strongly correlated with dust concentration in the surface layer (bottom, left), which is dominated by absorption in the VIS (R^2= -0.97; bottom, right).

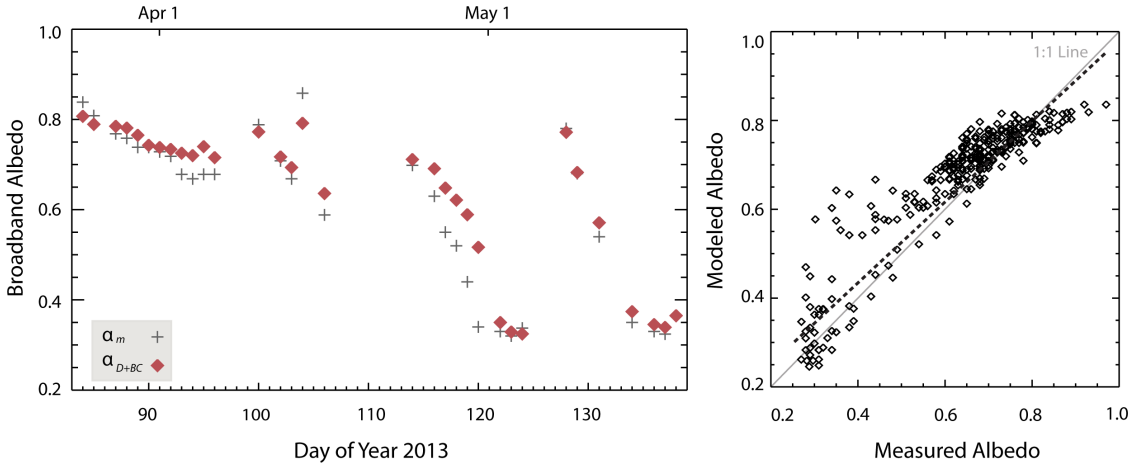

Figure 5 (Left) Comparison of measured and modeled albedo over time. Over the full measured period α_{D+BC} is 0.02 higher than measured albedo with the greatest difference occurring over the albedo decrease between April 26th and April 30th as dust layers converge at the surface. Outside of the window the difference reduces to 0.01. (Right) Hourly albedo scatter plot of measured and modeled values: SNICAR tends to overestimate albedo except for at the highest values, when it is underestimated relative to measured albedo. These differences average out over the measurements period, and the hourly comparison also returns an average difference of 0.02, though it exhibits more variation (hourly R^2= 0.85, daily R^2= 0.96).

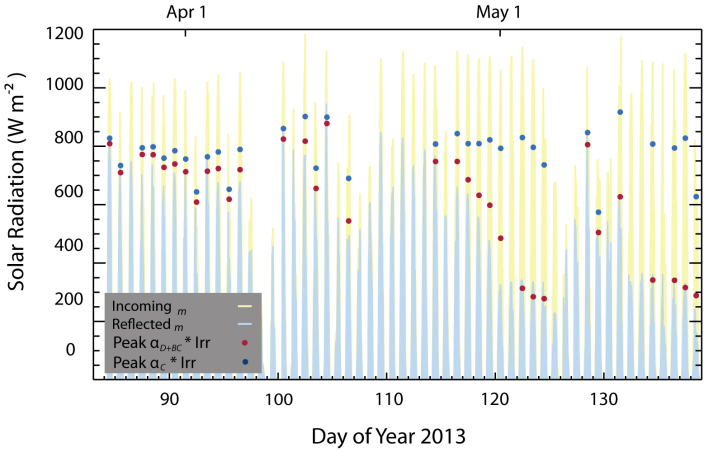

Figure 6 Daily peak values for modeled reflected flux from clean and dust+BC scenarios, plotted over hourly broadband irradiance and reflected flux as measured at the SASP instrumentation tower. The summation of modeled spectral irradiance matches measured broadband irradiance, as it is scaled to do so.

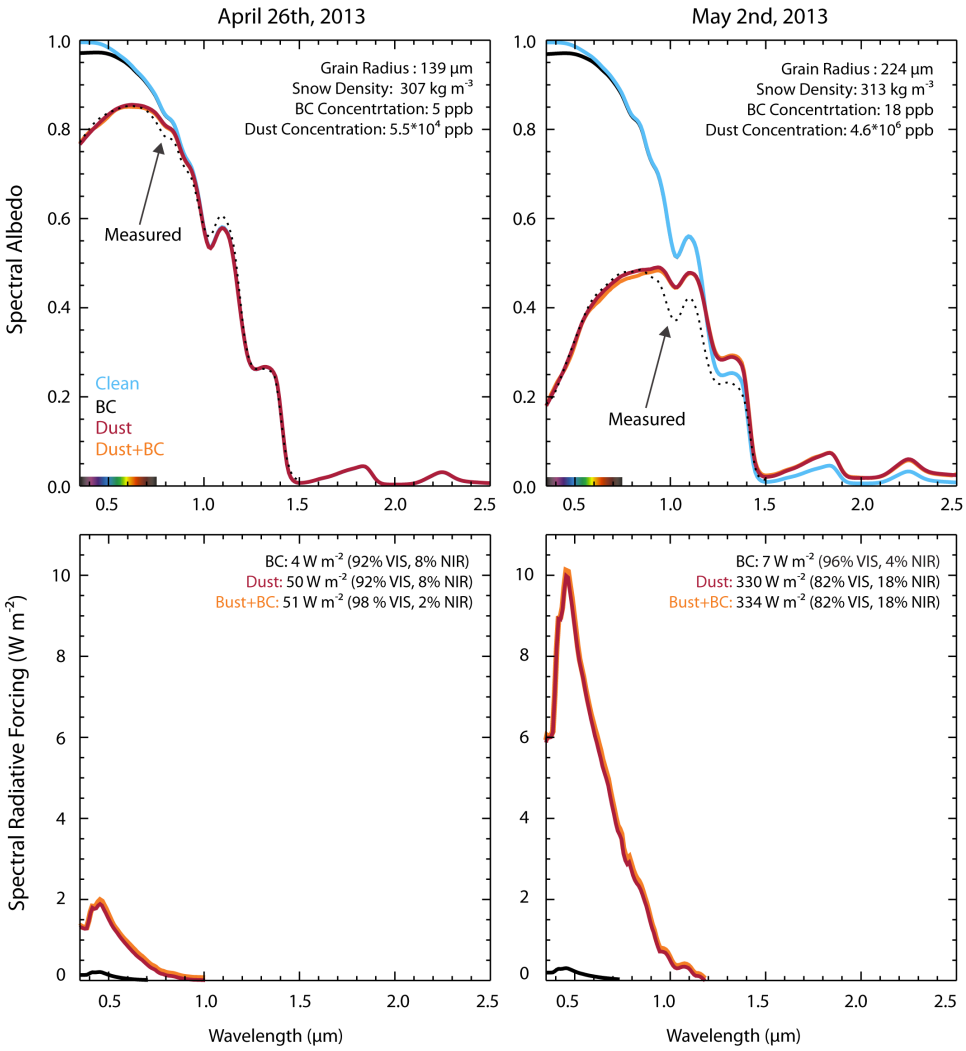

Figure 7 Spectral albedo and radiative forcing for two days. Difference from measured over the full range of snow reflectance is 0.3% for April 26th, and 7% for May 2nd. The expansion of radiative forcing into the NIR at high dust concentrations is exhibited in the lower right plot.

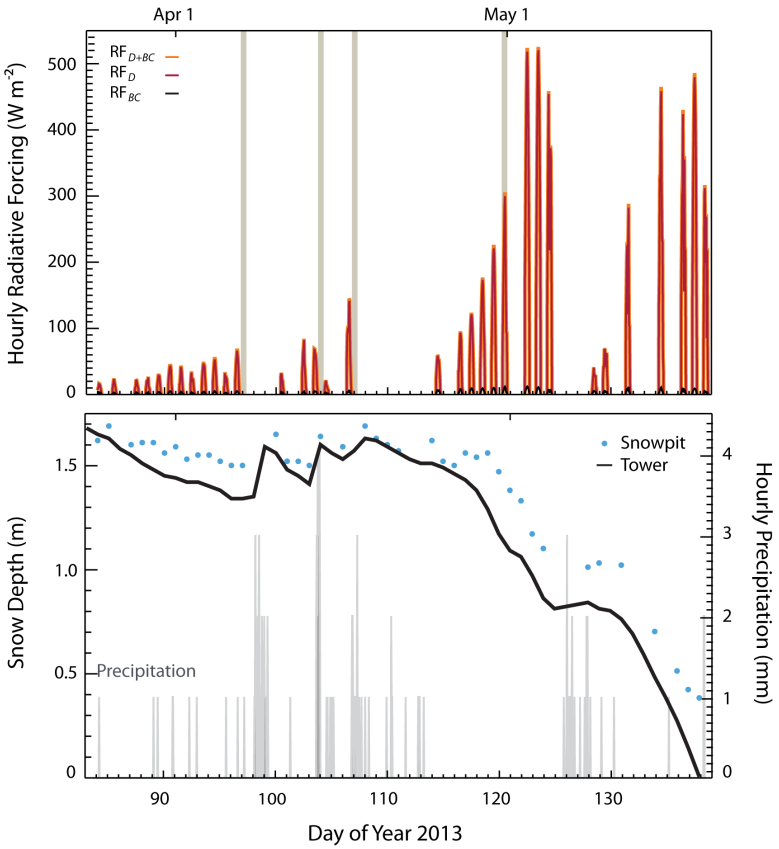

Figure 8 Hourly radiative forcing, dust event timing (beige lines), precipitation, and snow depth over the measurement period. Increases in RF are associated with dust concentrations at or near the surface, and decreases are associated with new snowfall. Gaps in the record indicate days where the measurements did not take place, and not zero radiative forcing.

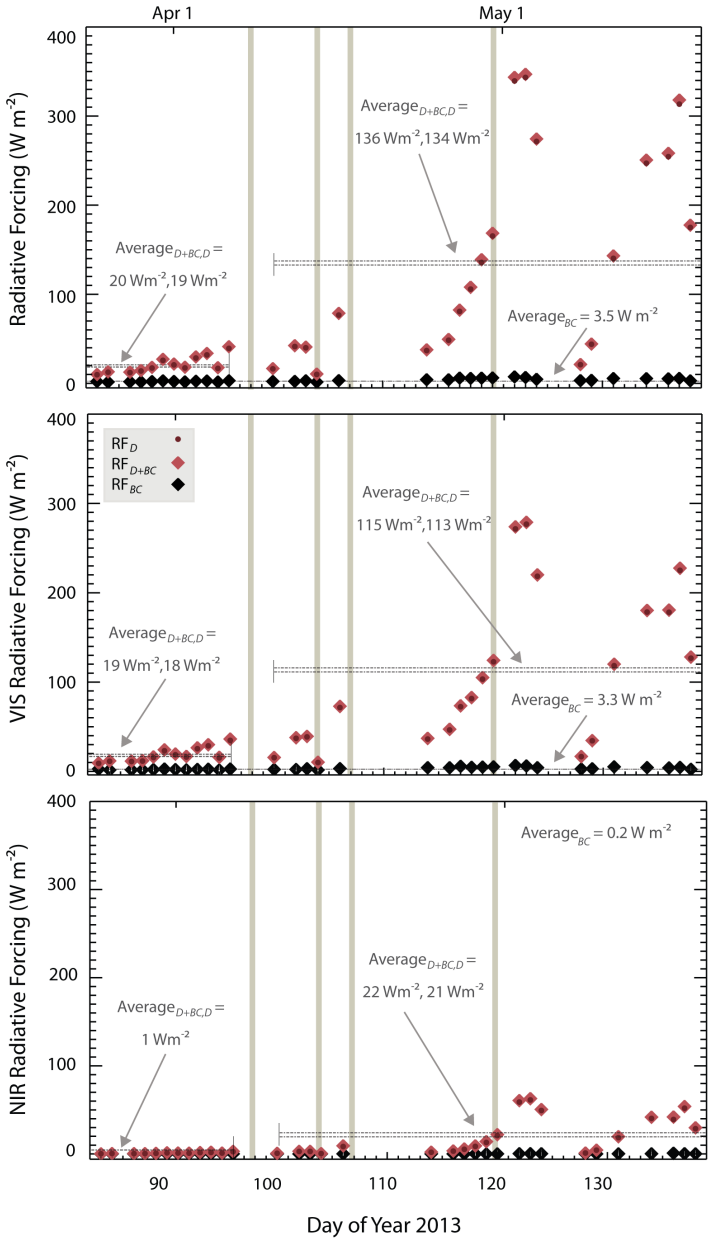

Figure 9 Daily average radiative forcing, partitioned for impurity scenarios across broadband, visible, and near/shortwave infrared wavelengths. Average time period radiative forcing is summarized before and after the heavy dust deposition associated with dust events D6-9 (beige lines), which deposited 98% of the WY13 total dust mass. The bulk of radiative forcing is due to absorption in the visible wavelengths (middle), although this expands to the NIR in the presence of heavy dust (bottom).

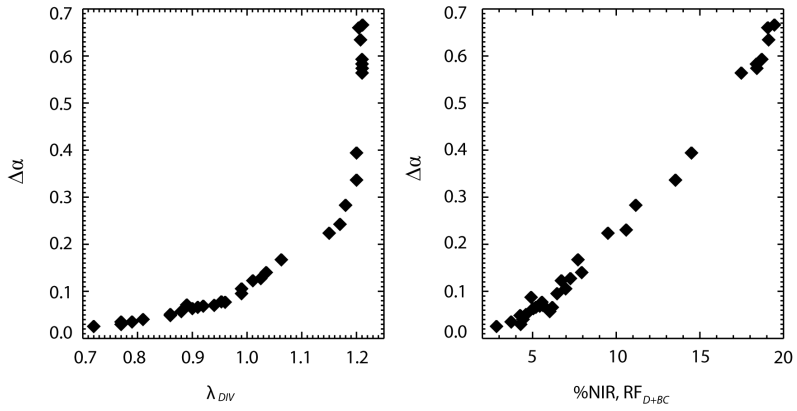

Figure 10 The relationship between Δα and the wavelength of divergence, and Δα and percent of radiative forcing that occurs in the NIR wavelengths. As Δα increases the wavelength of divergence (λ_{DIV}) between spectral albedo curves extends further into the NIR, which leads to an increase in the fraction of RF_{D+BC} that occurs in the NIR wavelengths.

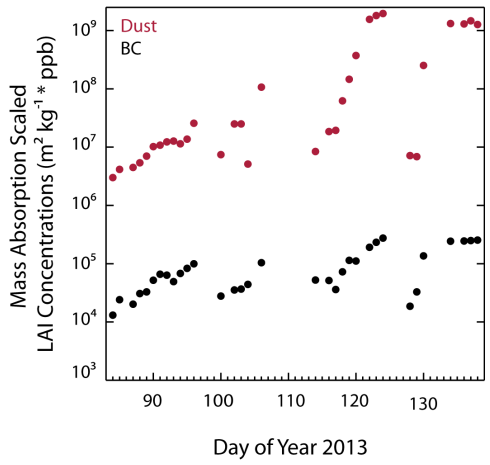

Figure 11 Absorption efficacy of dust and BC, exhibited by scaling measured concentrations by their respective mass absorption co-efficient at 0.55 μm.

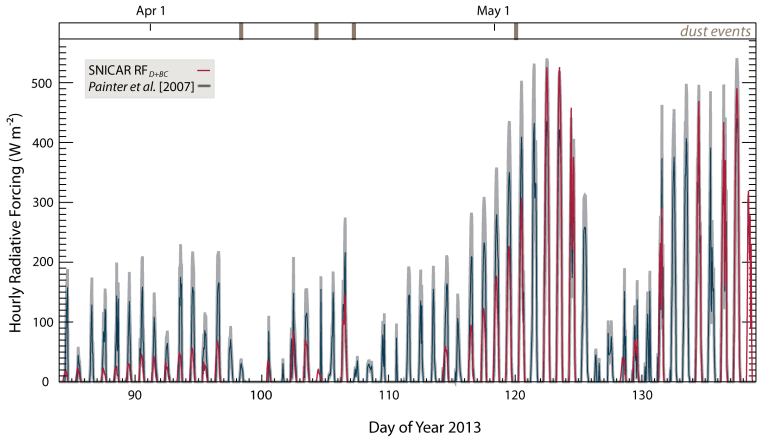

Figure 12 Comparison of directly and indirectly calculated radiative forcing. Prior to heavy dust deposition RF estimated here (RF_{D+BC}) fell below the range of RF estimated using method presented in *Painter et al*., [2007] (RF_{P07}), where values are reported as the average of minimum (LAI absorption only) and maximum radiative forcing (LAI absorption+ enhanced grain growth) scenarios. After high dust content is near or at the surface RF_{D+BC} increases to fall within the range of RF_{P07}, only exceeding max RF_{P07} on May 4th by ~7 W m^{-2} over the course of the day.

Chapter 5

Simulating dust deposition and radiative forcing with the numerical snow model SNOWPACK coupled to the snow/aerosol radiative transfer model SNICAR

Abstract

The darkening of the snow surface by light absorbing impurities (LAIs) impacts snow albedo directly by increasing absorption of shortwave radiation in the visible wavelengths. This process indirectly enhances the rate of snow grain growth, which determines absorption in the near-infrared wavelengths, and combined the direct and indirect impact of LAIs reduces snow albedo over the full range of snow reflectance. The presence of LAIs has been established in many snow-covered regions, and accurate parameterizations of snow albedo should represent this LAI snow albedo feedback. Here, dust influenced snow cover evolution was simulated at Senator Beck Basin Study Area, San Juan Mountains, CO with the multi layer snow process model SNOWPACK, modified to track dust stratigraphy, coupled to a snow/aerosol radiative transfer model, SNICAR. SNICAR modeled albedo updates the reflected shortwave radiation (RSWR) input, based on modeled snow properties and region specific dust optical properties. Decreases in RSWR with increasing dust content influences snow metamorphism, simulating LAI enhanced grain growth. Results showed that model tracked dust stratigraphy was well simulated, to within 3 cm on average, and dates of dust layer emergence corresponded with observations. A low bias in optical grain size, determined from modeled grain size using an empirical relationship, created a high bias in albedo until dust was at or near the surface, when modeled values more closely matched observed values. Correspondingly, dust radiative forcing was best simulated when dust was at or near the snow surface. A partitioning of direct and indirect radiative impacts, carried out by swapping grain sizes between dust and clean snow runs, shows that absorption by dust dominates radiative forcing (~80% dust, ~20% grain growth).

1. Introduction

In Chapter 1, the spatio-temporal impacts of dust on snow radiative forcing in the Colorado River Basin were investigated using the semi-empirical energy balance approach first presented in *Painter et al.* [2007b]. This methodology is useful because it reconstructs dust radiative forcing continuously from changes in surface reflectance, and does not require snow sampling, or explicit knowledge of dust deposition or stratigraphy. It is of interest, though, to simulate dust stratigraphy and microphysical interaction with snow grains explicitly to advance process modeling, improve model simulation of snow albedo, and develop methods of simulating and forecasting dust radiative forcing in the absence of energy balance tower measurements for forcing variables.

In Chapter 4, I demonstrated the ability to track dust radiative forcing directly from vertically resolved measurements of snow density, snow optical grain size, and dust/black carbon concentrations, presented in Chapter 2, utilizing region specific DOS optical properties, presented in Chapter 3. Here, the radiative transfer model, SNICAR [*Flanner and Zender*, 2005; 2006] is forced not with measurements, but with simulated snow property variables modeled by the physically based snow model SNOWPACK [*Lehning et al.*, 1999], in order to understand the relative contributions to total radiative forcing by impurities of direct radiative forcing and the grain-size growth first feedback. The multi-layer model, updated here to track dust stratigraphy, utilizes SNICAR snow albedo to update reflected shortwave radiation to simulate absorption by dust in snow in a physically based manner.

2. Methods

2.1 Model Coupling Overview

The model coupling scheme described here, SNOWPACK plus dust and radiative transfer, or SNOWPACK DRT, is visually represented in Figure 1. Briefly, after model initiation, modeled snow property outputs in the active layer (layer heights, density, grain size, and dust concentrations) were used as inputs to the snow+aerosol radiative transfer model SNICAR. SNICAR uses snow properties to calculate broadband snow albedo, which are then applied to measured incoming shortwave radiation to update reflected shortwave radiating at the next time step.

SNOWPACK DRT was run for two scenarios. In the first, dust was specified, to represent observed conditions. In the second, the same modeling scheme was applied, but with no dust, to represent clean snow cover evolution (in the absence of dust). Total dust radiative forcing was determined by taking the difference in absorbed shortwave radiation between the dust and clean snow scenarios. An additional two scenarios were modeled with standalone SNICAR, from SNOWPACK outputs, one for direct radiative forcing, with the grain growth impact removed, and one for indirect radiative forcing, which accounted for only the grain growth impact. The following sections provide details on SNOWPACK, dust accounting, SNICAR, forcing and verification data, and radiative forcing partitioning.

2.2 SNOWPACK Model

The one-dimensional numerical snow process model SNOWPACK, the snow cover model of the Swiss Federal Institute for Snow and Avalanche Research SLF (www.slf.ch), was selected here for three reasons: it evolves the snow cover based on

atmospheric and radiation forcings, represents the snow cover as a variable number of layers, and tracks snow metamorphism. It was originally developed to predict snow development in fine stratigraphic detail to support avalanche warning [*Lehning et al.*, 1999] and a full model description can found in a suite of papers published in 2002 [*Bartelt and Lehning*, 2002; *Lehning et al.*, 2002a; *Lehning et al.*, 2002b]. The model, which has been shown to accurately predict the accumulation and melt of mountain snow cover by predicting snowpack settlement, layering, surface energy exchange, and mass balance, is currently used in operational avalanche forecasting in Switzerland. Validation studies have also been carried out in Montana [*Lundy et al.*, 2001] and Finland [*Rasmus et al.*, 2007], and the model has been applied to study glacier mass balance [*Michlmayr et al.*, 2008], snow hydrology [*Lehning et al.*, 2006], climate change scenarios [*Bavay et al.*, 2009], and alpine permafrost [*Leutschg et al.*, 2008]. While SNOWPACK relies on energy balance data from meteorological instrumentation towers for model inputs, running the model with forecasted weather data has also been investigated [*Bellaire et al.*, 2011].

The SNOWPACK model predicts snow cover formation and deformation based on atmospheric forcing inputs, with layers being defined in terms of height, snow density, and snow microstructure. Snow is represented as a three-phase porous medium consisting of volumetric fractions of ice, water, and air, for which principles of mass, energy, and momentum conservation are maintained [*Bartelt and Lehning*, 2002]. Snow density in the bulk snowpack is the summation of volumetric fractions and constituent density, and new snow density is estimated from air temperature, relative humidity, and wind speed [*Lehning et al.*, 2002a]. Snow microstructure is defined by the parameters *sphericity*,

dendricity, *grain size*, and *bond size*, which are used to predict bulk snow properties including thermal conductivity (from which the temperature profile is determined) and viscocity [*Lehning et al.*, 2002b].

Snow accumulation, settlement, and melt take place within a Lagrangian coordinate system, i.e. it is not a fixed computational grid but rather a coordinate system that moves with the ice matrix, allowing for a more realistic representation of snow density and snow microstructure. This representation also maintains mass conservation of the ice phase, which reduces the number of governing differential equations [*Bartelt and Lehning*, 2002]. Snow settlement is controlled by metamorphic relationships defined for, (1) equitemperature metamorphism using mixture theory [*Brown et al.*, 1999], (2) kinetic metamorphism using an empirical relationship between the ice matrix and the pore space [*Lehning et al.*, 2002b], and (3) wet snow metamorphism using an empirical relationship based on fraction of liquid water [*Brun et al.*, 1989]. These are thermally based regimes, which are a function of surface energy exchanges and heat conductivity.

At a minimum, the atmospheric forcing data required by SNOWPACK is air temperature, relatively humidity, and wind speed, reflected and/or incoming shortwave radiation, and either measured snow heights or precipitation [*Lehning et al.*, 2002a]. Additionally, incoming longwave radiation, atmospheric emissivity, and/or snow surface temperature can be specified, but are not required by the model. The ground temperature can be specified, if measured; otherwise it is assumed to be 0^{o}C. The model can be initiated prior to snow accumulation, which requires only forcing data, or from measured/observed snow properties, which additionally requires initiation data that must

include layer depth, layer temperature, volumetric constituent fractions, and snow microstructure parameters, across the full snow profile.

Snow depth or precipitation inputs are used to determine accumulation (the addition of elements). Sensible and latent heating fluxes are estimated from temperature, relative humidity, and wind speed inputs based on an assumption of neutral atmospheric surface layer using Monin-Obhukov similarity [*Lehning et al.*, 2002a]. Turbulent flux parameterizations account for wind interaction (or 'wind pumping') within the surface layers, which alters heat and vapor transport relative to termination of wind interaction at the upper snow interface and improves simulations of the thermal regime in the uppermost snow layers [*Lehning et al.*, 2002a]. If incoming longwave radiation is not provided, the longwave radiation balance depends on surface temperature: when surface temperatures are $< -1.3^{o}C$, the surface temperature is utilized as the upper boundary condition, when it warms to a temperature at which phase changes could occur ($> -1.3^{o}C$), atmospheric emissivity and longwave radiation balance is estimated from air temperature and relative humidity inputs using the Brutsaert equation [*Brutsaert*, 1975].

Snow albedo is determined from a statistical relationship developed at a single alpine plot over three years in Switzerland, and is based on meteorological and snowpack properties [*Lehning et al.*, 2002a]. This parameterization is required operationally in Switzerland, where weather stations measure reflected shortwave radiation but not incoming shortwave radiation. The amount of shortwave radiation absorbed by the snowpack is determined from a calculation is based on distance below the snow cover surface and an extinction coefficient, which varies linearly with snow density [*Lehning et al.*, 2002a].

It should be noted that this a description of SNOWPACK, and not SNOWPACK DRT, as implemented here. Also, this is only a brief summary of the highly complex SNOWPACK model. It reflects the current understanding of model parameters and interactions, and does not include any recently implemented model updates.

2.2.1 Tracking Dust Stratigraphy

The observations presented in Chapter 2, as well as *Painter et al.* [2007b; 2012] and *Skiles et al.* [2012] confirm that dust mass is stationary in the layer in which it is deposited, except under conditions of rapid melt, behavior which has also been observed in other snow covered environments [*Conway et al.*, 1996; *Doherty et al.*, 2013]. This is important as it allows for straightforward representation of dust stratigraphy within SNOWPACK. A new variable was defined, dust density, that acts as a simple marker, which means that the specified value is retained in the layer in which it was defined, is summed with adjacent layers as snow settles, and does not change or interact with other snow properties. When there was an observed dust event, the additional dust content was added to the dust content in the surface element.

Light absorbing impurities in snow are commonly reported as concentrations, in parts per thousand or parts per billion, or as a loading, in g m^{-2}. Here, the dust density marker has units of g m^{-3}. This dust metric was selected so that dust concentration, which is defined in terms of dust mass per unit of snow mass, could be properly determined from modeled snow density:

$$\text{Concentration}_{\text{Dust}}(\text{g kg}^{-1}) = \text{Density}_{\text{Dust}}(\text{g m}^{-3}) / \text{Density}_{\text{Snow}}(\text{kg m}^{-3}) \quad (1)$$

The units, g kg^{-1}, is equivalent to mg g^{-1}, or parts per thousand, the units in which dust concentrations are reported across the other chapters. Dust density inputs are

determined from dust mass ((g); see Chapter 2), the measured mass of dust filtered from snow samples during laboratory analysis, and gravimetric sample volume area (3 cm x 500 cm^2). Snow density is SNOWPACK modeled snow density at the same time step, in the same layer. Black carbon was not included in this analysis as it was determined in previous chapters to have a minimal contribution to impurity mass and radiative forcing in this region (see Chapters 2,3), but could be included in future model runs in a similar fashion.

2.3 SNICAR Model

The SNow, Ice, Aerosol radiative transfer model SNICAR [*Flanner and Zender*, 2005; *Flanner et al.*, 2007] is described in both Chapter 3 and Chapter 4. Briefly, the model uses solar zenith angle, optical snow grain size (μm), snow layer thickness (m), snow density (kg m^{-3}), and concentrations of light absorbing impurities (ppb) to estimate radiative transfer by applying a single-layer version of the multiple scattering approximation of *Toon et al.* [1989] [*Flanner et al.*, 2007]. Snow and impurity optical properties are called from look up tables based on grain size and impurity type. Here, dust is specified in a new impurity category that corresponds to regional specific dust on snow optical properties (Colorado River Basin dust on snow; CRB DOS), which was determined from filtered dust reflectance and particles size distributions as described in Chapter 3. It should be noted that SNICAR broadband albedo is spectrally integrated over a set irradiance curve, which is representative of clear sky mid-latitude winter.

2.4 Initiating and Forcing Data

For the model runs presented here, snow cover was simulated with SNOWPACK version 3.2.0, and was run at an hourly time step using a 15-minute integration time step.

The initiating, forcing, and verification data came from Swamp Angel Study Plot (SASP), located in an opening below tree line in Senator Beck Basin Study Area (SBBSA), San Juan Mountains, CO [*Painter et al.*, 2012]. The study area, managed by the Center for Snow and Avalanche Studies (CSAS) in Silverton, CO, was established in 2004 to study the hydrologic impacts of dust on snow [*Painter et al.*, 2007b]. More details on SASP/SBBSA can be found in Chapters 1 and 2, *Painter et al.* [2012], and *Landry et al.* [2014].

The model was initiated at 12:00 PM local time on March 25th, from snowpack measurements collected within the study plot boundaries between 10:30 and 11:45 AM local time. Initial layer depths were 3 cm across the top 30 cm of the snowpack, corresponding to gravimetric samples, and 10 cm below this to the ground, corresponding to 1-L density cutter samples. The snow cover retained cold content (snow temperatures were below 0 ^{o}C across the full profile) and therefore volumetric constituents were assumed to consist of ice and air, and were estimated from measured snow density and snow water equivalent. Snow temperatures, which were measured every 10 cm along the snow profile, were resampled to 3 cm intervals across the surface layers. The snow microstructure parameters, grains size and bond size, were taken from observed snow grain size and type, collected by Chris Landry, CSAS director, within study plot boundaries on March 22nd, the snow microstructure parameters, sphericity and dendricity were estimated from observed snow grain types utilizing the relationship in *Colbeck et al.* (1990).

Initial dust densities, initialized from a separate file, were determined from March 25th snow samples, which were bagged and analyzed across the full profile. To minimize

shipping costs and the number of snow samples to be analyzed, this was one of only two days when full profile snow samples were bagged for analysis. During model runs, dust density in new snow layers was set to the average dust density (0.02 g m^{-3}) sampled for visually identified clean snow across the bulk snowpack (early season snow accumulation) on March 11th, the other full profile collection day.

During the simulation, dust was placed into the snow surface layer, via an external file consisting of a time stamp and dust density, at times that corresponded to each of the 4 observed spring dust events: seasonal dust event number 6 (D6) occurred on April 8th, D7 on April 14th, D8 on April 16th, and D9 on April 30th. For D6 through D8, which were identifiable distinct dust layers, the prescribed dust density was taken from the corresponding dust layer on the next sampling day. Deposition event number D9 was deposited after D8 had emerged at the surface, known as a dust-on-dust event, and density was calculated by taking the difference between measured dust density on April 30th, and measured dust density in the D8 layer on April 29th.

Forcing data, taken from the SASP meteorological and energy balance tower, included hourly averages of air temperature (K), relative humidity (%), wind speed (m s^{-1}), incoming shortwave radiation (W m^{-2}), incoming longwave radiation (W m^{-2}), and snow depth (m). Snow precipitation (mm) was taken from measurements at the standalone precipitation gauge nearby the tower. These variables are plotted in Chapter 1, Figure 2, and Chapter 2, Figure 6. Reflected shortwave radiation, which is measured at SASP, was specified in the input file, but was updated by SNICAR beginning at 11:00 am local time on March 26th, 23 time steps after model initiation, as described in section

2.4. The shortwave input was set to 'both' to specify both incoming and reflected shortwave radiation inputs.

2.5 SNOWPACK Outputs/SNICAR Inputs

When absorbed shortwave radiation was modeled as being non-zero within the SNOWPACK surface layers, defined here as the active layer (Figure 2), then SNICAR was used to estimate snow albedo based on SNOWPACK modeled snow profile properties within each of the active layers. Active layer snow thicknesses, the difference between the top of current element and the top of the next element, define the number of layers within SNICAR, and snow grain size and density is then specified in each of those layers.

Snow grain size was transformed from observable snow grain size (OSGS), in mm, to optical grain size (OGR), in μm, by the following empirical relationship between OGR, OSGS, and liquid water content (LWC):

$$OGR = (OSGS / 0.014) + (LWC / 0.2) \quad (2)$$

This relationship matches observed trends by allowing optical grain radius to remain small in the beginning of the measurement period, and grow more quickly in the presence of liquid water (Figure 3). The simple alternative would be to scale OSGS from mm to μm, but relative to this approach the empirical relationship applied here reduced the average differences across the simulation period from 77 μm to 17 μm (and to within the uncertainty range of the retrieval method). The relationship was determined from the average SNOWPACK modeled OSGS across the top 30 cm, simulated using only measured forcing inputs, and average measured OGR across the top 30 cm (collected for the SASP WY13 dataset: Chapter 2), and needs to be further validated.

Dust concentration inputs were calculated from modeled dust density and modeled snow density following the relationship in Equation 1, and a scalar was applied to convert concentrations from ppt to ppb. Two runs were completed with same initiating and forcing data, with dust ('dust' scenario), and without dust ('clean snow' scenario). In the clean snow scenario, SNICAR outputs represent clean snow albedo for a given grain size and density.

Solar zenith angle was precalculated from SASP latitude and longitude using the 'sunang' user command of the Image Processing Workbench (IPW; www.nwrc.ars.usda.gov/ipw). These were stored in a look up table based on time stamp. When snow depth was estimated at greater than 40 cm, the substrate layer albedo was set to 0.93, to replicate the remainder of the snowpack, in case radiative transfer was simulated beneath the SNOWPACK active layers. When the snow depth was estimated at less than 40 cm, the substrate albedo was set to 0.2, so that absorption by the ground could be accounted for in thin snow layers just prior to snow depletion.

2.6 Verification

Snowpack DRT outputs were assessed by comparing measured to modeled snow properties, including snow depth, snow water equivalent, snow density, optical grain size, and dust concentrations. Snow properties were measured on a near-daily basis in a series of snow pits, located nearby the instrumentation tower, between March 25th and May 18th, 2013, as described in Chapter 2. There are 34 days from this measurement dataset that fall within the SNOWPACK simulation time frame presented here. Measurements included density and snow optical grain size, measured across the full profile, and dust concentrations across the top 30 cm of the snowpack. The higher resolution surface

samples are used here to verify modeled values in the SNOWPACK active layer, as these are the modeled snow properties called by SNICAR.

Modeled snow water equivalent was compared to snow water equivalent (SWE) calculated from snow density at the snow pit site. Modeled SWE was also compared to SWE simulated with the two-layer snow energy balance model SNOBAL [*Marks et al.*, 1998]. This is the model that is currently implemented at SBBSA to estimate the hydrologic impacts of dust on snow [*Painter et al.*, 2007b; *Skiles et al.*, 2012] (see also Chapter 1).

The broadband snow albedo modeled by SNICAR from modeled snow properties was compared to broadband albedo measured at the SASP instrumentation tower, with albedo being the ratio between incoming and reflected shortwave radiation. Modeled snow albedo was also compared to albedo modeled by stand-alone SNICAR, forced with measured snow properties, as presented in Chapter 4. Additionally, modeled daily mean reflected shortwave radiation was compare to measured, which was corrected for plot scale variations in slope and aspect following the method described in *Painter et al*. [2012].

Radiative forcing, the difference in absorbed shortwave radiation between dust and clean snow, was compared with continuous radiative forcing time series estimated from measured surface reflectance using the relationship described in *Painter et al.* [2007b]. This is likewise the radiative forcing parameterization currently implemented in SBBSA to quantify the radiative and hydrologic impacts of dust on snow. More details on this method can be found in *Painter et al.* [2007b] and *Skiles et al.* [2012], and it is described in both Chapter 1 and Chapter 4.

2.7 Partitioning Radiative Forcing Impacts

To partition the direct and indirect radiative forcing impacts due to dust absorption and dust enhanced grain growth, respectively, standalone SNICAR runs were made over the simulation time frame by applying the modeled clean snow grain size to the dust scenario (direct impact alone) and modeled dust influenced snow grain size to clean scenario (indirect impact alone):

(3) $$\text{Direct}_{\alpha} = (\text{Dust Absorption} - \text{Dust Enhanced Grain Growth})$$

(4) $$\text{Indirect}_{\alpha} = (\text{Clean Snow} + \text{Dust Enhanced Grain Growth})$$

The broadband albedo outputs were then applied to measured incoming shortwave radiation to estimate reflected/absorbed shortwave radiation. Radiative forcing was estimated by taking the difference in absorbed shortwave radiation from the clean snow scenario. The relative proportion of radiative forcing accounted for by each impact was calculated by taking the ratio between the dust/indirect scenarios and the dust scenario, which represents total radiation forcing.

3. Results and Discussion

3.1 Modeled Snow Properties

3.1.1 Density and Snow Water Equivalent

SNOWPACK DRT modeled a broader range of snow densities than was observed at the measurement site (Figure 4). Maximum modeled densities, which typically corresponded to the lowest snow layers (exhibited in snow profiles; Figure 5), ranged from 499 to 554 kg m^{-3}, and were always higher than measured maximum density, by 25 to 112 kg m^{-3}, 70 kg m^{-3} on average. Minimum modeled densities, which ranged from 30 to 315 kg m^{-3}, typically correspond to the uppermost surface layers. These were

underestimated by 43 kg m^{-3} on average, while for roughly 1/3 of the measurements days minimum densities were overestimated, by 5 to 94 kg m^{-3}, they were more frequently underestimated, by 1 to 191 kg m^{-3}. Average snow density, which typically fell within the interquartile range of measured densities, was overestimated by 55 kg m^{-3} across the simulation period.

Densities that are too high across the bulk snowpack are important, because they introduce a high bias in snow water equivalent estimates. Densities in the surface layers are also important they influence active layer depth, which was reduced over the season as surface layers densified. Densities also determine dust concentrations, and densities that are too low/high in the active layers result in dust concentrations that are too high/low, which would impact radiation balance. Active layer densities and dust concentrations are compared to measurements in section 3.1.5.

Snow water equivalent, the product of depth and density, was overestimated over the simulation by 105 mm on average relative to measurements, and 82 mm relative to SWE simulated with SNOBAL (Figure 6). The high bias was consistent and exhibited an upward trend (relative to SNOBAL), increasing from 44 mm on March 26th to more than 180 mm between May 2nd and 4th. While SWE is not directly related to the radiation balance study carried out here, it is the most hydrologically relevant snow property, and if SNOWPACK DRT were to be applied operationally in the future, accurate SWE estimates would be important. An overestimation of spring/ablation season SWE is also exhibited in the water equivalent plots presented in *Bartelt and Lehning* [2002], across five seasons at a study plot in Switzerland, though better agreement was shown during the accumulation season. It is useful to compare SWE modeled with SNOWPACK DRT

to the continuous time series modeled with SNOBAL, as SWE cannot be continuously calculated from tower measurements alone and previous results show SNOBAL reconstructs snow cover evolution well at SASP, with an average SWE RMSE of 20 mm [*Painter et al.*, 2007b; *Skiles et al.*, 2012].

3.1.2 Dust Content

Dust concentration stratigraphy, across the full profile, as simulated by SNOWPACK DRT is visualized in Figure 7. Visually, dust stratigraphy was well tracked, with depth below the surface corresponding with observations to within a few centimeters across four snow profiles (Figure 5), additionally, modeled dates of dust layer emergence (after being buried by new snowfall) occurred within a day of observed date of emergence. Due to variations in depth and density between measured and modeled snow cover it was difficult to carry out a quantitative analysis of dust content and dust stratigraphy. Here, the simple metric, max dust density (D_{max}) was selected, along with the relative depth below the snow surface, to compare to measurements. These are both relevant to radiation balance, as absorption by dust is directly related to the amount of dust in a given layer and how close that layer is to the surface. While the range of modeled dust concentrations are compared to measurements for the active layer in section 3.1.3 below, this assesses SNOWPACK DRT's ability to track the direct dust input, outside of the influence from modeled density.

Of all years on record at SBBSA (2005-2013), 2013 received the heaviest dust loading, with 90% of dust mass being deposited in a single event (D6; April 8th). Therefore, D_{max} exhibited a wide range of values; modeled D_{max} ranged from 3 to 1246 g m^{-3}, and measured D_{max} ranged from 3 to 1444 g m^{-3} (Figure 8). Prior to D6, modeled

D_{max} was lower than measured but the difference was small, from 1.1 to 4.5 g m^{-3}, 2 g m^{-3} on average (for context, by applying an average density of 350 kg m^{-3}, this would be 0.005 mg g^{-1}). After D6 was placed into the model, but prior to it coming to the surface, the average underestimation increased to 156 g m^{-3} (~ 0.44 mg g^{-1}). Over this time period, between April 8th and April 29th, D7 and D8 were also placed in the model. On April 29th, D9 was placed into the model. The next set of measurements, between May 2nd and May 4th, show an average overestimation of D_{max} by 186 g m^{-3} (~0.5 mg g^{-1}), which corresponds to the timing of convergence/emergence of all dust layers (modeled and observed). These were the only three days when dust was consistently overestimated. Between May 8th and May 16th, the time frame over which dust was buried by new precipitation and then re-emerged, D_{max} was again underestimated by 66 to 300 g m^{-3} (153 g m^{-3} average; ~0.4 mg g^{-1}).

On the last day of sampling, D_{max} was only slightly overestimated, by 5 g m^{-3} (0.02 mg g^{-2}), the lowest D_{max} difference for D6-9 layers. This close accounting at the every end of the season is promising, as dust content on the final sampling day represents a convergence of all seasonal dust layers, and in previous work [*Painter et al.*, 2007b; *Skiles et al.*, 2012] and Chapter 1, this is an important metric that is referred to as the end of year dust concentration. On average, over the whole season, D_{max} was underestimated by 47 g m^{-3} (~0.3 mg g^{-1}). This may be due to the fact that dust was only placed into the model during observed dust events, while observations show that dust content steadily increases over the spring, even for new snowfall events, as atmospheric dust loading peaks in this region in the spring [*Sorooshian et al.*, 2013] (see Chapter 2; Figure 8).

The location of modeled D_{max} was never greater than 30 cm below the snow surface, and therefore could be compared to measurements across all 20 days that a full gravimetric sample set was collected for analysis. Depths beneath the surface are calculated from the top of the element and top of the gravimetric sample, respectively. Depth was matched for 11 of the 20 days, including April 4th-7th, May 2nd-4th, and 14th-18th, when dust was both modeled and observed as being at the surface. Across the other days when depth was not matched, the difference from measured ranged from +7 cm (farther from the surface) to -5 cm (closer to the surface), and was +3 cm on average, an uncertainty that corresponds to the thickness of a gravimetric sample.

3.1.3 Grain Size

Grain size stratigraphy was assessed by comparing modeled to measured optical grain radius (OGR) across four full profiles, collected on March 26th, April 14th, April 29th, and May 11th (Figure 5). These days were selected as they represent the range of conditions across the simulation and observation period (fairly clean, high dust content below the surface, and high dust content near the surface), and correspond to the measurement profiles discussed in Chapter 2 (see Chapter 2, Figure 12). The comparison of the range of active layer OGR across all measurement days can be found in section 3.1.4.

As shown in Figure 3, OGR estimated from modeled OSGS using Equation 2 followed measured trends, but the relationship results in an overestimation early in the simulation, and then an underestimation later in the simulation for OGR in the top 30 cm. Across the full profiles used here, snow grain size was always underestimated. Average OGR across the March 26th profile was 212 μm, whereas the modeled average was 202

μm, a -10 μm difference. With the exception of the ice layer at ~150 cm, OGR trends were well matched in this profile. On April 14th, the average difference across the profile was -35 μm (219 μm measured, 184 μm modeled), while grain sizes were well matched in the surface layers, the complex dust influenced stratigraphy between 120 and 130 cm, which had higher optical grain sizes, was not captured by the model. Outside of these layers, the trend in OGR was well matched and the difference in the median OGR, 216 μm measured and 200 μm modeled, was smaller than the average difference. In neither profile did the average grain size difference exceed the 50 μm uncertainty reported for the contact spectroscopy method [*Painter et al.*, 2007a].

The highest difference in average OGR occurred on April 29th, with an average difference of 98 μm between measured OGR, 346 μm, and modeled OGR, 247 μm. OGR values in the ice and melt freeze layers in this pit were up to 60% greater than the modeled OGR values at the same depth. Still, the trend of smaller OGR values in the surface layers and increasing OGR toward the ground was captured and the difference in median values, -65 μm, was smaller than the overall average difference. The largest difference in snow depth was on May 11th, when simulated snowfall was retained for longer than observed, which resulted in lower than observed OGR across ~ the top 40 cm. In the mid-pack (below 80 cm) OGR trends were better matched, but still underestimated. Over the full profile, modeled OGR was 232 μm, and measured was 282 μm, a 49 μm difference. The average difference across all four profiles was 48 μm (underestimation), an average error that falls within the uncertainty range for the OGR retrieval method.

3.1.4 Active Layer Density, Grain Size, and Dust Concentrations

The modeled snow properties across the active layer are of particular interest as these are used as inputs to SNICAR, and therefore influence the radiation balance by determining albedo directly, and by determining the response to dust concentrations. Here, the max/min range and average values are assessed to verify that SNOWPACK DRT simulates physically reasonable values (

Figure 9). It should be noted that this is not a strict quantitative assessment, as, (1) simulated snow depth and layer thicknesses did not correspond to observations, and (2) active layer depth was variable, and ranged from 30 cm at the beginning of the assessment to 16 cm on May 18th, whereas snow measurements were always across the top 30 cm.

Reflecting the full profile density results, modeled active layer densities spanned a greater range of values than measured. Modeled densities ranged from 34 to 546 kg m^{-3}, averaging 313 kg m^{-3} over the simulation. This was 30 kg m^{-3} higher than the average measured density, which was 283 kg m^{-3}. Modeled maximum densities were consistently higher than measured densities, while minimum modeled densities were consistently lower. The largest differences in minimum density occurred in the surface layers with new snowfall, where observations indicate the new snow fall did not become dense enough quick enough, until it reached a density of ~200 kg m^{-3}, at which point densification was too quick.

Between modeled initiation on March 26th and April 8th (D6), the range of active layer dust concentration values were fairly well matched, with modeled maximum values falling slightly below maximum measured values (following too high density values and

underestimation of max dust density over this time frame). Minimum modeled values fell both above and below measured values, where the lowest measured values occurred on days with new snowfall. The measured dust concentrations in these layers was never lower than the specified background dust in simulated new snow layers, but rather, the modeled surface densities were too low and therefore modeled dust concentrations in low dust content layers was higher than observed.

On April 8th, when D6 was placed into the model, the concentration was higher than ever measured (> 8 mg g^{-1}) due to the low density of the surface layer in which it was placed. As the layer became more dense, layer concentration dropped to 5.3 mg g^{-1} on April 12th, which was closer but still elevated relative to the ~ 4.0 mg g^{-1} typically measured for the D6 layer. As the layer continued to become denser concentrations dropped, decreasing from 3.7 mg g^{-1} on April 13th to 2.58 mg g^{-1} on April 25th. The convergence with D7 and D8 on April 29th brought the concentration in the combined layer back up to 4.4 mg g^{-1}. It increased further to 5.4 mg g^{-1} with the placement of D9.

Modeled concentrations in the converged D6-9 layer were lower than observed between May 2nd and May 4th, when dust was at the surface. Observed concentrations ranged from 5.1 to 5.9 mg g^{-1}, whereas modeled values ranged from 3.6 to 5.2 mg g^{-1}. After this, until snow depletion, the combined dust layer concentration averaged 4.5 mg g^{-1}, slightly higher than measured, which averaged 4.2 mg g^{-1}. Concentrations were well matched just prior to snow depletion, when measured and modeled values were around 4.7 mg g^{-1}. Over the full simulation time frame, dust concentrations were underestimated by 0.1 mg g^{-1}, on average. Minimum modeled dust concentration were always lower than measured, due to low background dust content in new snow layers that become denser

over time, and to the steady increase in observed dust concentrations over the spring. Due to this fact, and the log scale range of modeled/observed dust concentrations introduced by extremely high D6 dust content, an overall average comparison was not carried out.

Active layer OGR follows the trends that have previously been discussed. Briefly, average OGR were overestimated between March 26th and April 6th, by 38 μm on average. Between April 10th and April 16th, modeled values transitioned to being lower then measured, with average underestimation of 50 μm. The largest average difference, of 108 μm, occurred between April 24th and May 4th. At the very end of the season values were underestimated again, by 9 μm, just prior to snow depletion. Relative to the OGR dataset used to determine the OGR/OSGS relationship, which used average values over the top 30 cm, the underestimation of OGR in the active layer was greater as averages are taken only over the more shallow active layers. Still, over the full the simulation these errors balanced out, modeled OGR was 46 μm higher, on average, then measured OGR, and differences typically fell with or near the uncertainty range of the method. Maximum OGR was the only measurement that consistently fell outside the range of modeled values, where peaks in measured OGR correspond to dust influenced ice/melt freeze conglomerate layers, and previously discussed profiles showed that SNICAR does not capture the magnitude of grain size increase in these layers.

Average OGR is not necessarily the most important indicator for impacts on radiation balance, but rather, OGR in the uppermost surface layers where interaction with shortwave radiation first occurs. In these layers, minimum OGR was modeled between 52 and 282 μm, 98 μm average. Measured minimum OGR ranged from 51 μm to 217 μm, 153 μm average. Minimum OGR was underestimated by more than 100 μm on certain

days and by 49 μm on average across the full simulation. This is the due to the minimum grain size value in SNOWPACK (0.4 mm), to which new snowfall is typically set, and the low liquid water content in these layers, which means they are not influenced higher by the OGR relationship implemented here. This low bias in surface grain size has important implications for the radiation balance, as discussed in section 3.2.

3.1.5 Grain Size Difference

The difference in grain size between dust and clean scenarios (Δ_{GS}) is an indicator of the indirect impact of dust on snow (Figure 10). Those across the active layer are particular interest (Figure 11), as swapping these between dust and clean scenarios determines direct/indirect radiative forcing. Except for in a few instances, active layer dust OGR (average 184 μm) was always higher than clean OGR (average 139 μm), with daily average Δ_{GS} ranging from 1 to 130 μm. In the beginning of the simulation there was a steady upward trend in daily Δ_{GS}, increasing from 5 μm on March 26th, to 131 μm on April 8th. Over this time period new snowfall was retained for longer and did not settle as fast in the clean snow scenario. New snowfall simulated in both scenarios resulted in low surface OGR in both scenarios between April 8th and 18th, and the average Δ_{GS} was 38 μm.

Between April 20th and April 29th, the time period over which buried dust layers began to emerge at the surface, dust scenario OGR was consistently higher then clean scenario OGR, but Δ_{GS} was fairly stagnant, ranging from 31 to 64 μm and averaging 43 μm. This attributed to the slow but steady grain growth of rounded grains in both scenarios under the equitemperature (low temperature gradient) metamorphism regime [*Lehning et al.*, 2002b]. The snowpack/air temperatures were not cold enough to dictate

kinetic growth, nor were the water contents high enough for wet snow metamorphism. While small complex grains (i.e. fresh dendritic snow) can grow rapidly under equitemperature conditions [*Brown et al.*, 1999], there was no snowfall over this time frame (simulated or observed).

Across the days when dust was first at the surface in early May (May 1st- 5th), Δ_{GS} ranged from 23 to 69 μm, and average 48 μm. A decrease in Δ_{GS} occurred again between May 6th and May 12th (1-20 μm, 9 μm average), with simulated snowfall. A diverging Δ_{GS} trend initiated again on May 12th as dust surfaced, with Δ_{GS} increasing from 8 μm to 96 μm on May 15th, before declining again to 7 μm on May 19th. These large differences just prior to snow depletion are attributed to the higher liquid water content present in the dust scenario at the end of the season.

3.2 Shortwave Radiation Balance

3.2.1 Modeled Albedo and Reflected Shortwave Radiation

Two metrics were selected to evaluate the modeling of shortwave radiation balance; broadband albedo and daily mean reflected shortwave radiation (RSWR). For consistency across chapters, broadband snow albedo comparisons were carried out across the 11 AM hour (spanning 11:00 AM to 12:00 PM). This was typically the hour over which snow properties were being collected. Daily mean RSWR was selected to compare reflected flux inputs across the full day instead if higher instantaneous values in the middle of the day.

SNOWPACK DRT modeled albedo (for the dust scenario) was consistently higher than measured albedo over the full simulation (Figure 12). The most apparent difference occurred between March 26th and April 27th, the first half of the simulation,

when modeled albedo fluctuated between 0.74 and 0.84 (0.78 average), whereas measured albedo ranged from 0.58 to 0.9 (0.74 average). Correspondingly, measured daily mean RSWR was 184 W m^{-2}, while modeled RSWR was 196 W m^{-2}, an 11 W m^{-2} daily mean error, or 5% of total irradiance (Figure 13).

For reference, SNICAR albedo, modeled from measurements, is also plotted in Figure 12 (see Chapters 3,4), along with the difference in albedo from the dust scenario (which represent albedo modeled from measured snow properties and albedo modeled from modeled snow properties, respectively). SNICAR (from measured values) are better matched with measured albedo, which shows that the high bias in modeled albedo was not an albedo overestimation by SNICAR, but rather can be attributed to SNOWPACK DRT inputs to SNICAR. Therefore, this is attributed to the low bias in surface grain size, as discussed in section 3.1.4.

Between April 27th and May 4th, when dust layers were simulated as converging and emerging at the surface modeled albedo dropped from 0.79 to 0.34 (average; 0.45). Measured albedo was lower the modeled over this time period (average; 0.38), and began the dust-influenced decline earlier, but the trend and magnitude of dust influenced albedo reduction was well captured by modeled albedo. The daily mean RSWR error was as high as 78 W m^{-2} on April 27th (21% of irradiance), but decreased to 6 W m^{-2} on May 4th (2% of irradiance).

Measured and modeled albedos both increased between May 6th and May 10th, with simulated/observed snowfall. The decrease in measured albedo after new snowfall, which dropped from 0.9 on May 6th to 0.55 on May 11th, was quicker than simulated for modeled albedo, which remained above 0.69 over this same time period (due to the

modeled OGR being too high in the new snow layers). The difference in daily mean RSWR was fairly low, though, with an 8 W m^{-2} error, or 4% of total irradiance, between 144 W m^{-2}, measured, and 152 W m^{-2}, modeled. On April 12th both measured and modeled albedo dropped below 0.4 as dust surfaced again, which suggests that the low bias in grain size was only effective at influencing a high bias in albedo when dust was not at the surface.

Modeled and measured albedo remained low until modeled/observed snow depletion, with modeled albedo falling below measured over the final 6 days of snow cover (May 17th, observed SAG). Over this time frame modeled albedo averaged 0.31, 0.02 lower than measured (0.33). Daily mean RSWR was 119 W m^{-2}, for measured, and 115 W m^{-2}, for modeled (4 W m^{-2} overestimation; 1% of irradiance). During the two final days of simulated snow cover there was less than 40 cm of snow, and modeled absorption by the substrate resulted in an average modeled albedo of 0.25 just prior to snow depletion. Over the full simulation period, average modeled albedo was 0.68, 0.04 higher than average measured albedo (0.64). Daily mean RSWR over the simulation period was 177 W m^{-2} versus 165 W m^{-2} measured (12 W m^{-2} error; 4% of total irradiance). Despite the sometimes large differences between modeled albedo/RSWR inputs and measured values, the largest impact on radiation balance occurs when dust concentrations in the surface layers are higher, and it is promising that SNOWPACK DRT can capture this behavior.

3.2.2 Albedo Difference

Dust radiative forcing is mainly determined by the difference in SNICAR modeled albedo between the dust and clean scenarios (Figure 12). These differences are

briefly summarized here, as modeled clean snow albedo remains high across the simulation, and modeled dust scenario albedo was just discussed. Differences in albedo were lowest across the first half of the simulation, and on days with simulated snowfall, when dusty snow albedo was 0.02 – 0.1 lower than clean snow albedo (0.03 average) and difference in daily mean RSWR were 10 W m^{-2} on average. Differences were greatest when dust was at the surface, when dusty albedo ranged from 0.34 to 0.48 lower than clean snow albedo, with an average difference of 0.44. Differences in daily mean RSWR were 115 W m^{-2} on average (daily mean clean RSWR, 250 W m^{-2}, and dust RSWR, 135 W m^{-2}).

3.2.3 Radiative Forcing

Daily mean radiative forcing ranged from 2 to 109 W m^{-2}, and was 30 W m^{-2} over the full simulation (Figure 14), with instantaneous values greater than 400 W m^{-2} when dust was at the surface. Radiative forcing mainly followed the trends in albedo and RSWR previously discussed. Briefly, RF was lowest over the first half of the simulation, between 2 and 27 W m^{-2} prior to April 27th, corresponding to the low bias in OGR and the resultant low difference between clean and dusty snow albedo. When dust first came to the surface RF quickly increased from 27 W m^{-2} on April 27th to 100 W m^{-3} on May 2nd. Over the May snowfall event, values ranged from 9 to 43 W m^{-2}. As dust resurfaced RF increased from 72 W m^{-2} on May 12th, to 109 W m^{-2} on May 17th (peak RF).

The daily mean RF values predicted here were consistently lower than values predicted by $RF_{p07,}$ which ranged from 0 to 141 W m^{-2} (simulation daily means: 46 W m^{-2}/ 30 W m^{-2}). In the beginning of the simulation, March 26th-April 27th, RF_{p07} was 19 W m^{-2}, more than triple RF simulated here (8 W m^{-2}). The lowest differences occurred when

precipitation was simulated, in mid-April and the beginning of May (~5 W m^{-2} difference). When dust was at or near the surface, the differences in daily mean RF were between 20 and 30 W m^{-2}, despite being lower than RF_{p07} the trends in RF were captured, with peak values coinciding for both RF estimations. In Chapter 4 I showed that RF_{p07} could be closely simulated when SNICAR was forced with measured snow properties, which suggests that there is room for improvement in accounting for snow properties, particularly surface layer grain size, within SNOWPACK DRT. While the trends in radiative forcing were captured, the magnitude of radiative forcing was lower than expected.

3.3 Direct/Indirect Radiative Forcing

Albedo estimated for direct/indirect effects were similar to those estimated for dust/clean snow across the first half of the simulation, when albedo in all scenarios remained relatively high (Figure 15). As would be expected, direct albedo was slightly higher than dusty albedo (~0.03), and indirect albedo was slightly lower than clean albedo (~0.02). When dust came to the surface on April 30th, direct albedo dropped to ~0.42, ~0.06 higher than dusty albedo, due to lower OGR inputs, and indirect albedo dipped below clean snow albedo by 0.05, due to the higher OGR inputs. Over the remainder of the season direct albedo remained higher than dusty snow albedo by 0.06 on average, and indirect albedo remains lower than clean snow albedo by 0.03 on average. Lower OGR in the dust case resulted in a larger impact on albedo (0.04 higher albedo) than higher OGR in the clean case (0.02 lower albedo).

Daily mean radiative forcing by grain size impacts alone ranged from 1 to 28 W m^{-2}, and were 7 W m^{-2} on average (Figure 16). When dust concentrations in uppermost

surface layers were low, at the beginning of the season and during simulated precipitation events, the proportion of radiative forcing accounted for by differences in OGR (27 - 60%) was higher than when dust was present near or at the surface (14-22%). While the contribution of indirect forcing to total forcing was lowest when dust was at the surface, this when the highest indirect radiative forcing values occurred (daily mean; 13 W m^{-2}). The cumulative radiative forcing at the end of the simulation was 30 MJ m^{-2} day^{-1}, ~20% of cumulative radiative forcing for the total impact (149 MJ m^{-2} day^{-1}).

Daily mean radiative forcing by dust absorption alone ranged from 1 to 83 W m^{-2}, and was 21 W m^{-2} on average. The impact due to dust was balanced with changes in grain size early in the season and on days that snowfall was simulated, when total radiative forcing, and dust concentrations in the surface layers were lower. When dust came to surface, though, the control of radiative strongly shifted to the direct effect, dominating 75-85% of total radiative forcing, with daily mean direct radiative forcings above 70 W m^{-2}. On average, the cumulative RF for direct absorption by dust was 120 MJ m^{-2} day^{-1}, ~80% of total radiative forcing over the full simulation.

4. Concluding Thoughts

The energy balance measurements and current model implementations at SASP/SBBSA do not necessitate an application of SNOWPACK DRT, but currently the direct/indirect impacts of dust radiative forcing are accounted for semi-empirically. The combined high resolution energy balance and snow property dataset at SASP in WY13 allowed for the development and verification of the modeling approach presented here, which physically accounts for the direct and indirect radiative impacts of dust on snow deposition, first, by building dust into the numerical SNOWPACK model and then, by

coupling it to the snow+aerosol radiative transfer model SNICAR. Increased absorption by dust was simulated by using modeled snow properties, including optical grain size and dust concentrations, to force SNICAR and update the reflected shortwave radiation input with SNICAR modeled albedo. The direct impact, enhanced absorption, and indirect impact, enhanced grain growth, were partitioned by running the model with and without dust and then using differences in grain size to force individual radiative transfer runs with and without dust influenced grain growth.

SNOWPACK DRT overestimated snow depth, density, and SWE, but SAG was modeled to within two days of SAG at the SASP instrumentation tower, and within 1 day of SAG at the measurement site. Results show that dust content was slightly underestimated (~43 g m^{-3}), but that dust stratigraphy was well simulated, to within 3 cm on average, and dust emergence corresponded to within a day of observations. Optical grain radius, which was converted from modeled observable grain radius using an empirical relationship, was underestimated by ~50 μm, on average across four representative snow profiles and in the active layers.

A low bias in OGR in the surface layers resulted in a high bias in albedo, but observations were better matched when dust emerged and dominated the radiation balance. Lower than measured albedo directly influenced estimated dust radiative forcing, the difference in absorbed shortwave radiation between dust and clean scenarios, which was underestimated across most of the simulation until dust emergence. The partitioning exercise confirmed that the majority of radiative forcing, ~80%, was accounted for by direct dust absorption. The portion is that was accounted for by

difference in grain size, ~20%, was greatest prior to dust deposition and lowest when dust was at the surface.

The single greatest improvement to SNOWPACK DRT would be further development on the optical grain radius relationship, to address the low bias in surface grain sizes. This would allow for snow albedo be more accurately simulated, which would improve radiative forcing retrievals. This is not as simple as increasing the minimum grain size value in SNOWPACK, as sometimes the OGR of new snowfall can be quite low, it just does not remain as low for as long as SNOWPACK DRT simulates. Rather, for future use, a more in depth statistical analysis will need to be undertaken to see if there is a better predictor/s of observed OGR than the simple relationship implemented here between observable grain size and liquid water content. SNOWPACK does allow for user-configured models, and as such SNICAR could be implemented directly in the model in the future along with a direct interaction between dust and grain growth, which could improve results. Executing this implementation was outside the scope of this study.

Still, these are promising results for further applications, I have established that SNOWPACK can track dust stratigraphy, and that increased absorption by dust influenced grain growth within the model. In the future, SNOWPACK DRT could prove to be useful for studying the impacts dust on weak layer formation for avalanche forecasting applications. There are many other possibilities, as well, SNOWPACK DRT could be further coupled to dust transport model to simulate dust deposition in the absence of observations. Building dust into the spatially distributed version of SNOWPACK, Alpine 3D [*Lehning et al.*, 2006], could be used to investigate regional

impacts of dust on snow. SNOWPACK DRT could also be initiated on the day of a dust event, and forced with forecasted atmospheric forcing data to forecast, instead of reconstruct, dust influenced snow evolution. Using a combination of these approaches, it may also be possible to inform SNOWPACK with snow properties retrieved from remote sensing, like NASAs Airborne Snow Observatory (ASO; www.aso.jpl.nasa.gov), to investigate radiative forcing impacts in regions where observations are sparse or non-existent, like the Himalaya.

5. References

Bartelt, P., and M. Lehning (2002), A physical SNOWPACK model for avalanche warning systems. Part 1: numerical model, *Cold Regions Science and Technology*, *35*(3), 123-145.

Bavay, M., M. Lehning, T. Jonas, and H. Lowe (2009), Simulations of future snow cover and discharge in Alpine headwater catchments, *Hydrological Processes*, *23*, 95-108.

Bellaire, S., J. B. Jamieson, and C. Fierz (2011), Forcing the snow-cover model SNOWPACK with forecasted weather data, *The Cryosphere*, *5*, 1115-1125.

Brown, R. L., M. Q. Edens, and M. Barber (1999), Mixture theory of mass transfer based upon snow mictrostructure, *Defence Science Journal*, *49*(5), 363-370.

Brun, E., E. Martin, V. Simon, C. Gendre, and C. C. (1989), An energy and mass model of snow cover suitable for operation avalanche forecasting, *Journal of Glaciology*, *35*(121), 333-342.

Brutsaert, W. (1975), On a derivable formula for long-wave radiation from clear skies, *Water Resources Research*, *11*(5), 2.

Conway, H., A. Gades, and C. F. Raymond (1996), Albedo of dirty snow during conditions of melt, *Water Resources Research*, *32*(6), 1713-1718.

Doherty, S. J., T. C. Grenfell, S. Forsstrom, D. Hegg, R. E. Brandt, and S. Warren (2013), Observed vertical redistribution of black carbon and other insoluble light-absorbing particles in melting snow, *Journal of Geophysical Research: Atmosphere*, *118*.

Flanner, M. G., and C. Zender (2005), Snowpack radiative heating: Influence on the Tibetan Plateau climate, *Geophysical Research Letters*, *32*.

Flanner, M. G., and C. Zender (2006), Linking snowpack microphysics and albedo evolution, *Journal of Geophysical Research*, *111*(D12), doi:10.1029/2005JD006834.

Flanner, M. G., C. S. Zender, J. T. Randerson, and P. J. Rasch (2007), Present-day climate forcing and response from black carbon in snow, *Journal of Geophysical Research*, *112*.

Landry, C., K. Buck, M. S. Raleigh, and M. P. Clark (2014), Mountain system monitoring at Senator Beck Basin, San Juan Mountains, Colorado: A new integrative data source to develop and evaluate models snow and hydrologic processes, *Water Resources Research*, *50*(2).

Lehning, M., P. Bartelt, B. Brown, and C. Fierz (2002a), A physical SNOWPACK model for the Swiss avalanche warning Part III: meterological forcing, thin layer formation and evaluation, *Cold Regions Science and Technology*, *35*, 169-184.

Lehning, M., P. Bartelt, B. Brown, C. Fierz, and P. Satyawali (2002b), A physical SNOWPACK model for the Swiss avalanche warning. Part II: snow microstructure, *Cold Regions Science and Technology*, *35*(3), 147-167.

Lehning, M., P. Bartelt, B. Brown, T. Russi, U. Stoekli, and M. Zimmerli (1999), SNOWPACK model calculations for avalanche warning based upon a new network of weather and snow stations, *Cold Regions Science and Technology*, *30*(1-3), 145-157.

Lehning, M., I. Volksch, D. Gustafsson, T. A. Nguyen, M. Stahli, and M. Zappa (2006), ALPINE3D: a detailed modeld of mountain surface processes and its application to snow hydrology, *Hydrological Processes*, *20*(2111-2128).

Leutschg, M., M. Lehning, and W. Haeberli (2008), A sensitivity study of factors influencing warm/thin permafrost in the Alps, *Journal of Glaciology*, *54*, 696-704.

Lundy, C. C., R. L. Brown, E. E. Adams, K. W. Birkeland, and M. Lehning (2001), A statisitical validation of the snowpack model in a Montana climate, *Cold Regions Science and Technology*, *33*, 237-246.

Marks, D., J. Kimball, D. Tingey, and T. Link (1998), The sensitivity of snowmelt processes to climate conditions and forest cover during rain-on-snow: a case study of the 1996 Pacific Northwest flood, *Hydrological Processes*, *12*, 24.

Michlmayr, G., M. Lehning, H. Holzmann, G. Koboltschnig, R. Mott, W. Schoner, and M. Zappa (2008), Applications of Alpine3D for glacier mass balance and runoff studies at Goldbergkees, Austria, *Hydrologic Processes*, *22*(19), 3941-3949.

Painter, T. H., N. P. Molotch, M. P. Cassidy, M. G. Flanner, and K. Steffen (2007a), Contact spectroscopy for the determination of stratigraphy of snow grain size, *Journal of Glaciology*, *53*(180), 6.

Painter, T. H., S. M. Skiles, J. Deems, A. Bryant, and C. Landry (2012), Dust Radiative Forcing in snow of the Upper Colorado River Basin: Part 1. A 6 year record of energy balance, radiation, and dust concentrations, *Water Resources Research*.

Painter, T. H., A. P. Barrett, C. C. Landry, J. C. Neff, M. P. Cassidy, C. R. Lawrence, K. E. McBride, and G. L. Farmer (2007b), Impact of disturbed desert soils on duration of mountain snow cover, *Geophysical Research Letters*, *34*.

Rasmus, S., T. Gronholm, M. Lehning, K. Rasmus, and M. Kulmala (2007), Validation of the SNOWPACK model in five different snow zones in Finland, *Boreal Environment Research*, *12*, 467-488.

Skiles, S. M., T. H. Painter, J. Deems, C. Landry, and A. Bryant (2012), Dust radiative forcing in snow of the Upper Colorado River Basin: Part II. Interannual variability in radiative forcing and snowmelt rates, *Water Resources Research*, *48*.

Sorooshian, S., T. Shingler, A. Harpold, C. W. Feagles, T. Meixner, and P. D. Brooks (2013), Aerosol and precipitation chemistry in the southwestern United States: spatiotemporal trends and interrelationships, *Atmospheric Chemistry and Physics*(13).

Toon, O. B., C. P. McKay, T. P. Ackerman, and K. Santhanam (1989), Rapid calculation of radiative heating rates and photodissociation rates in inhomogeneous multiple scattering atmospheres, *Journal of Geophysical Research*, *94*(D13), 16,287-216,301.

Figures

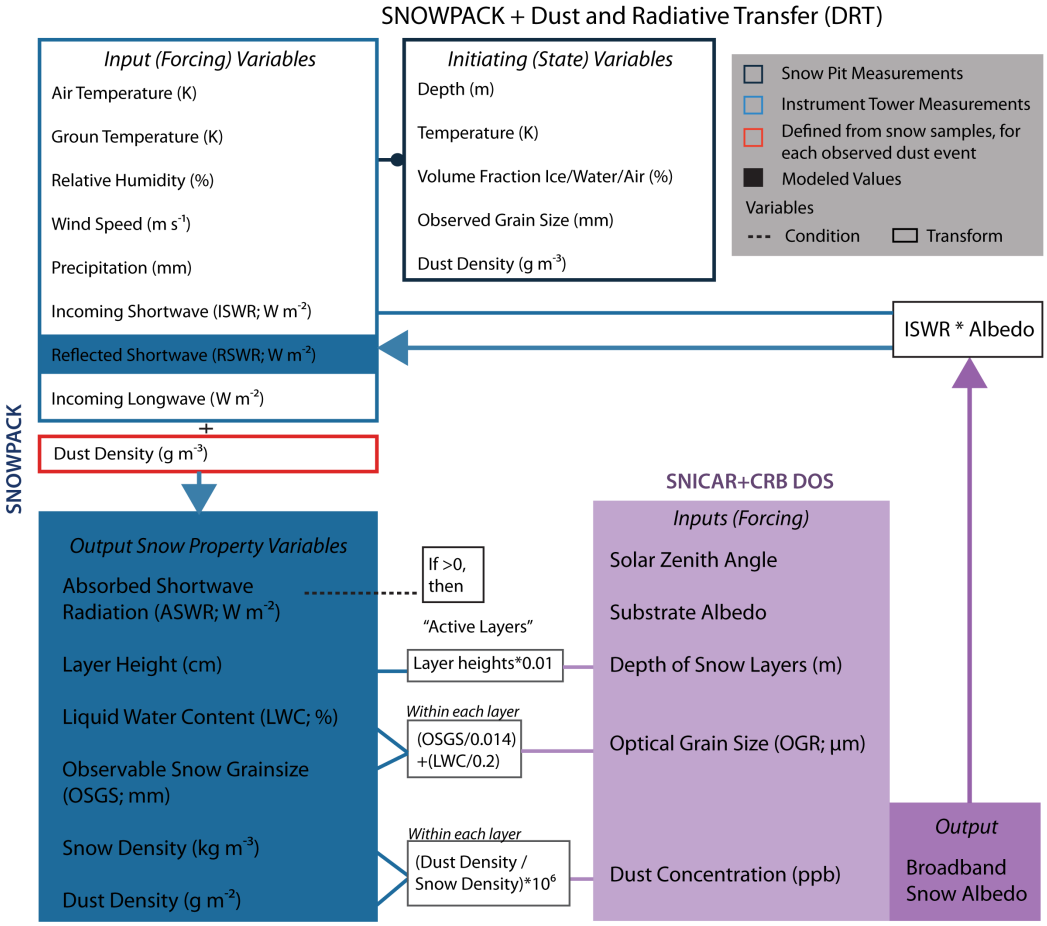

Figure 1 Diagram of model coupling between the numerical snow model SNOWPACK, modified to track dust stratigraphy, and the snow and aerosol radiative transfer model SNICAR.

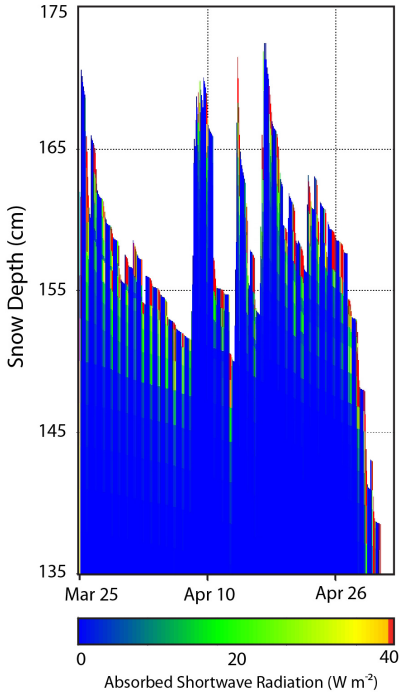

Figure 2 Visualization of absorbed shortwave radiation (ASWR) across the snowpack surface layers between March 25th and May 2nd, 2013. This snow property is used to define the snow active layers.

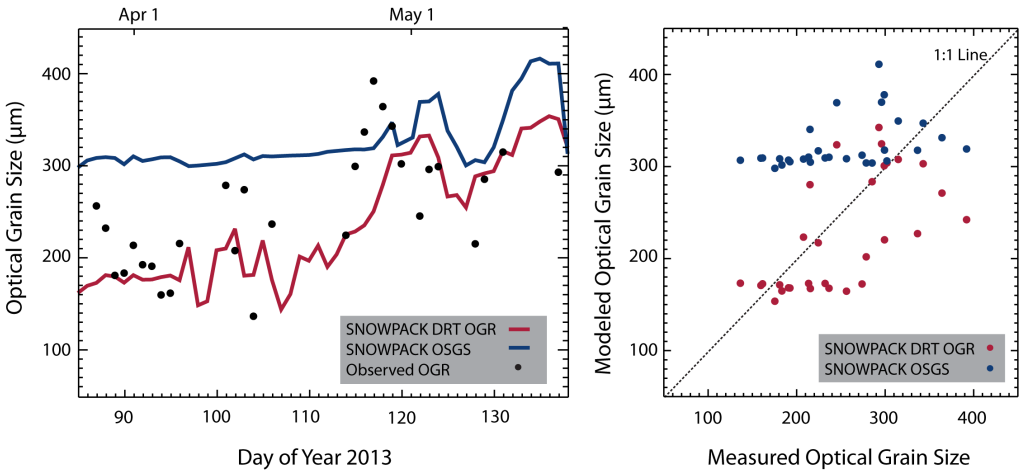

Figure 3 Comparison of SNOWPACK modeled observable snow grain size (OSGS), SNOWPACK DRT optical grain radius (OGR) determined via the empirical relationship in Equation 2, and measured OGR. All values represent averages across the top 30 cm of the snow cover, and modeled values are from a SNOWPACK run forced only with measured values. While the empirical relationship generally underestimates OGR, it captures the trends in grain size and minimizes errors relative to simply scaling OSGS from mm to μm.

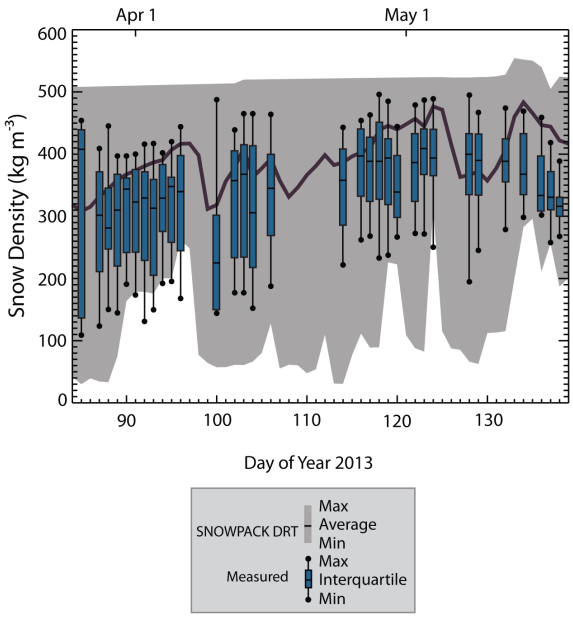

Figure 4 The range of modeled and measured snow densities across the full snow profile. The densest layer corresponds to the lowest layers, and the least dense layer typically corresponds to the uppermost layer. In combination with the high bias in snow depth the high bias in lower layer density impacts modeled SWE.

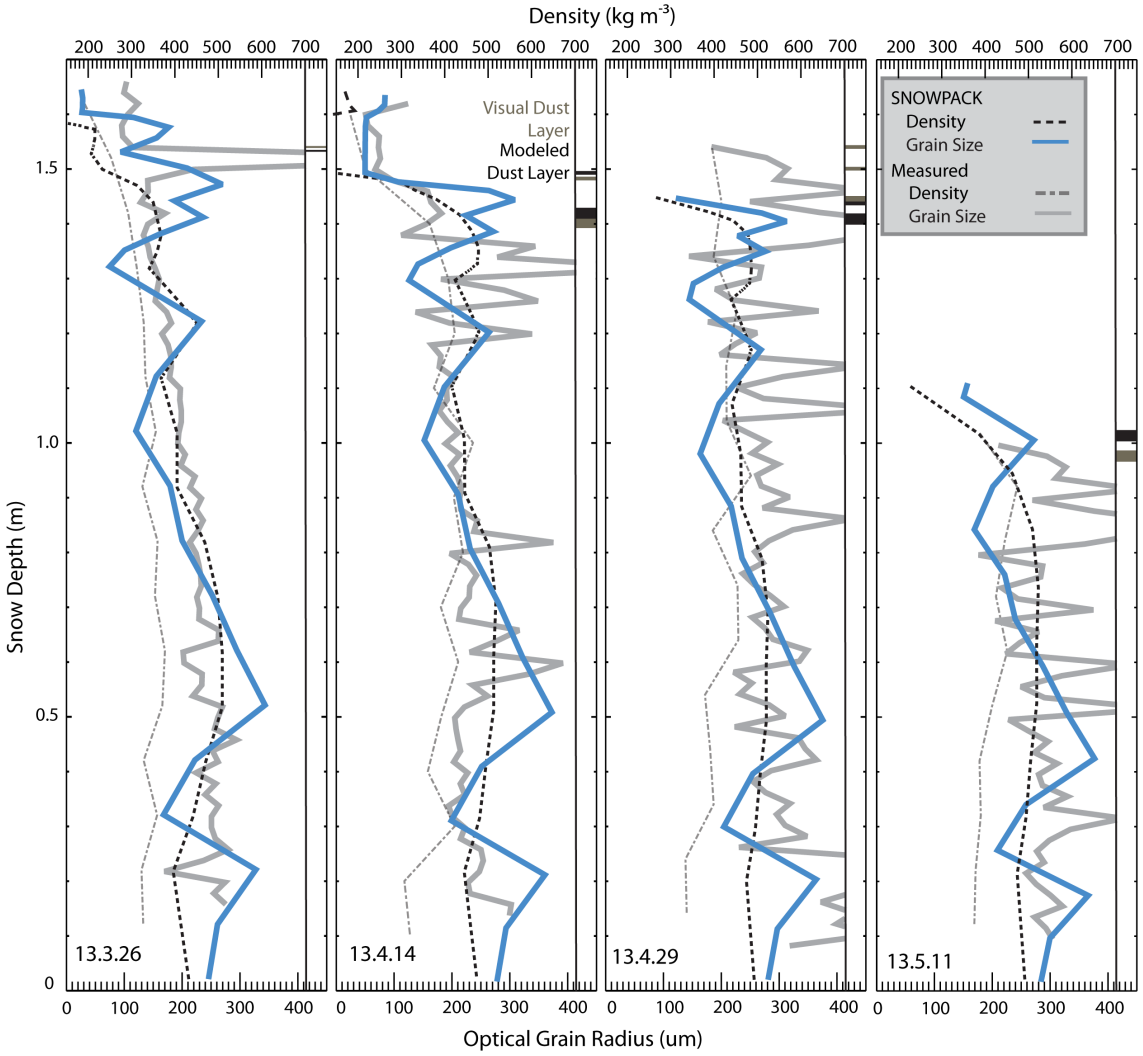

Figure 5 Comparison of modeled and measured dust stratigraphy and snow density/OGR profiles, for four days across the SASP WY13 measurement time frame. Relative to measurements, modeled density was too low in the near-surface layers, and too high in the bulk snowpack. Grain size was better matched; while they also tend to be low in the surface layers, full profiles trends were simulated well. Dust stratigraphy was well simulated by SNOWPACK DRT, while snow surface height do not always match, the depth below the surface of dust layer is matched to within a few cm.

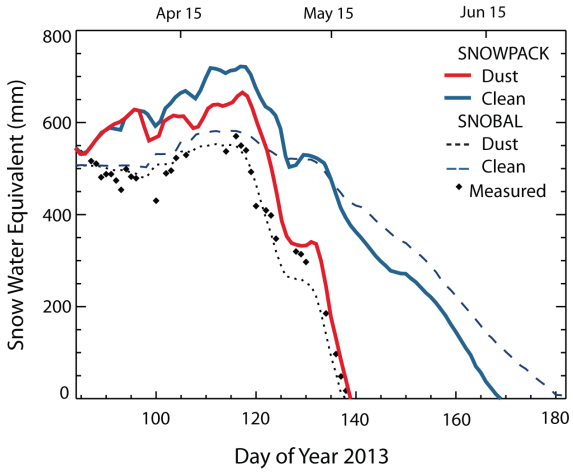

Figure 6 Snow water equivalent depletion modeled with SNOWPACK DRT. Here, it is compared with density from snow pit measurements and SWE modeled with the snow energy balance SNOBAL, which is a two layer model that is forced with similar atmospheric and radiation inputs.

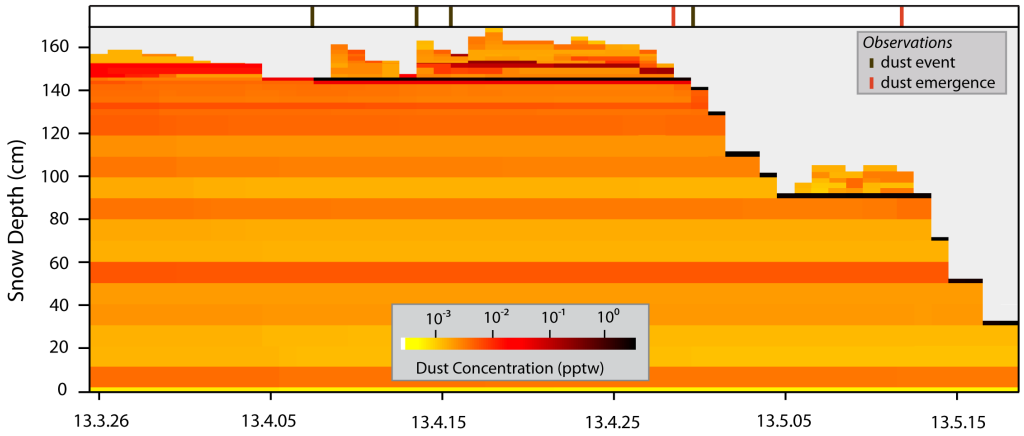

Figure 7 A visualization of noontime SNOWPACK DRT dust stratigraphy. The plot is based on a fixed grid and therefore does not fully capture the behavior of the Lagrangian based snow cover simulated by SNOWPACK. Dust concentrations were calculated by dividing dust density by snow density. Timing of observed dust events, which correspond to when dust was placed into the model, are indicated at top of plot along with observed date of dust emergence.

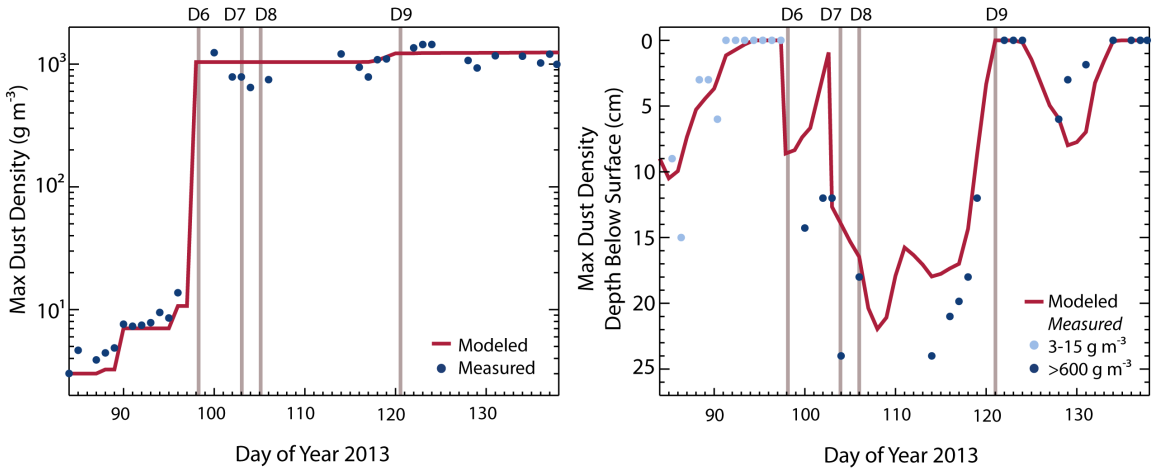

Figure 8 To compare how well SNOWPACK DRT tracks dust, the layer with the maximum dust density (D_{max}) was identified and compared to measurements. The trend in D_{max} (left) was well matched but dust densities were generally underestimated, with a total overall error of -47 g m^{-3}. The corresponding depth below the surface of each D_{max} layer is best matched when it was most important, when daily max dust content was observed at the surface. The average difference across the other days is ~3 cm, on average.

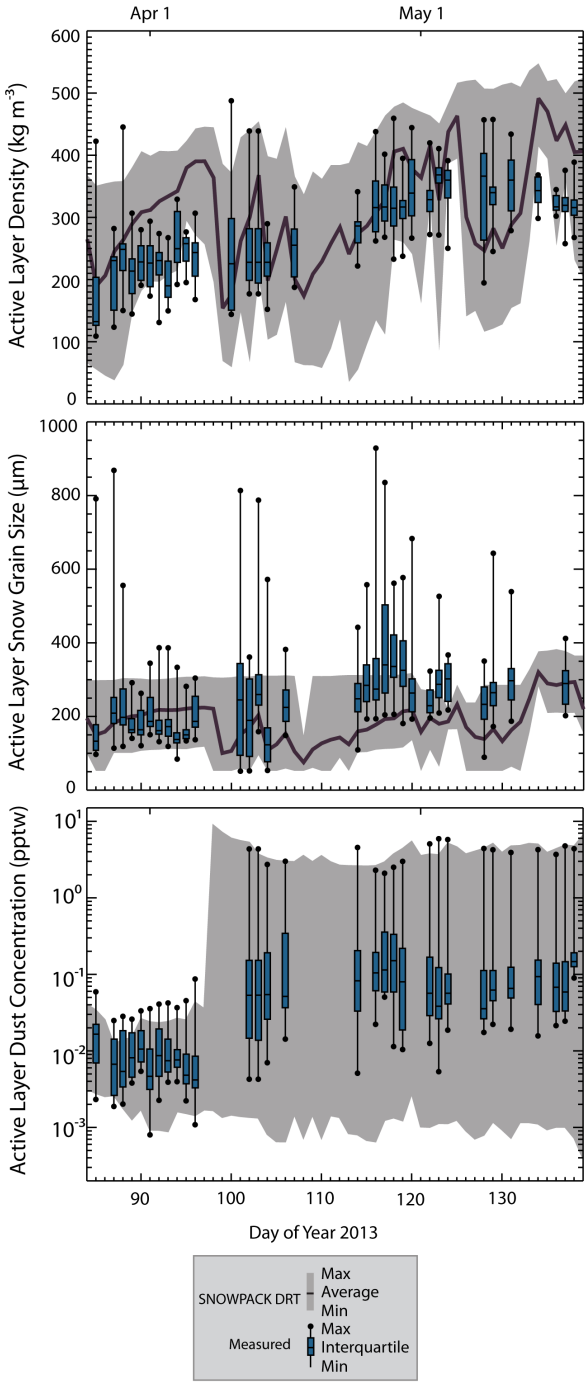

Figure 9 Comparison of the range of values for snow densities, dust concentrations, and OGR across the active layers, which were the modeled values used as inputs to SNICAR.

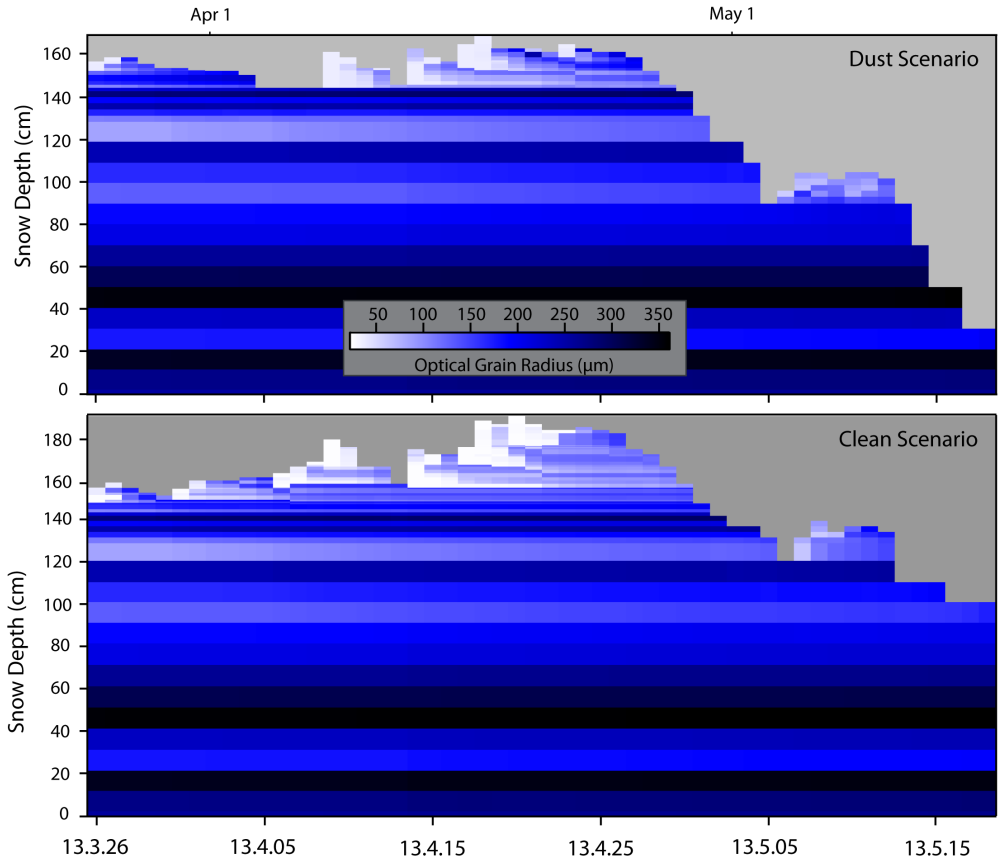

Figure 10 A visualization of modeled noontime optical grain radius (OGR) stratigraphy for dust and clean scenarios. OGR was calculated from observable snow grain size and liquid water content, based on an empirical relationship developed from the SASP WY13 OGR measurement dataset. The difference in OGR between dust and clean scenarios represents the impact of dust radiative forcing on grain growth. As for dust concentration plotted in Figure 7, this plot is based on a fixed grid and therefore does not fully capture the behavior of the Lagrangian based snow cover simulated by SNOWPACK, and is only meant for visualization.

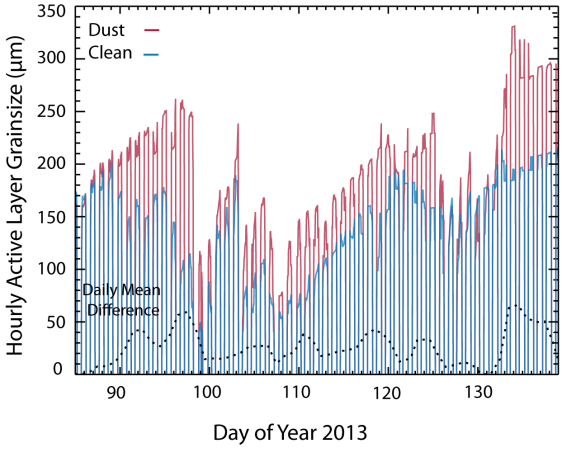

Figure 11 Hourly active layer OGR averages for dust and clean scenarios, plotted with daily mean difference.

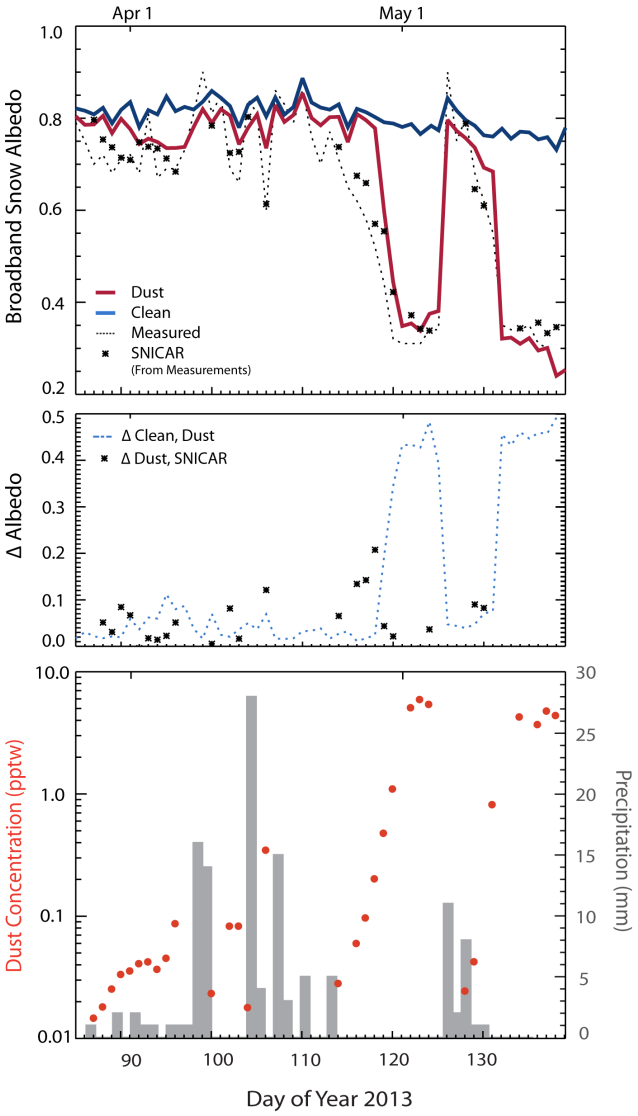

Figure 12 SNICAR modeled broadband albedo for dust and clean scenarios (top), plotted with measured albedo (SASP instrumentation tower) and albedo modeled by SNICAR forced with measured snow properties (see Chapter 3,4). The albedo difference between dust and clean scenarios, and the difference between albedo modeled from modeled values (dust) versus measured values (SNICAR) are plotted in the middle. For reference, snowfall and measured dust concentrations, factors that influence abrupt changes in albedo, are plotted below over the same time period.

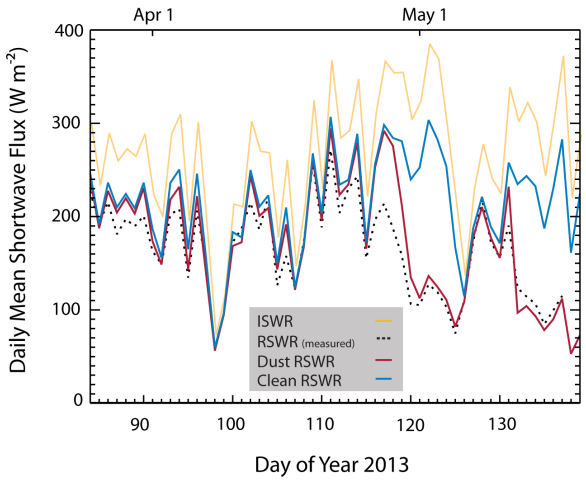

Figure 13 Daily mean reflected shortwave radiation (RSWR) inputs for the dust and clean scenarios, plotted with measured daily mean incoming shortwave radiation (ISWR) and RSWR.

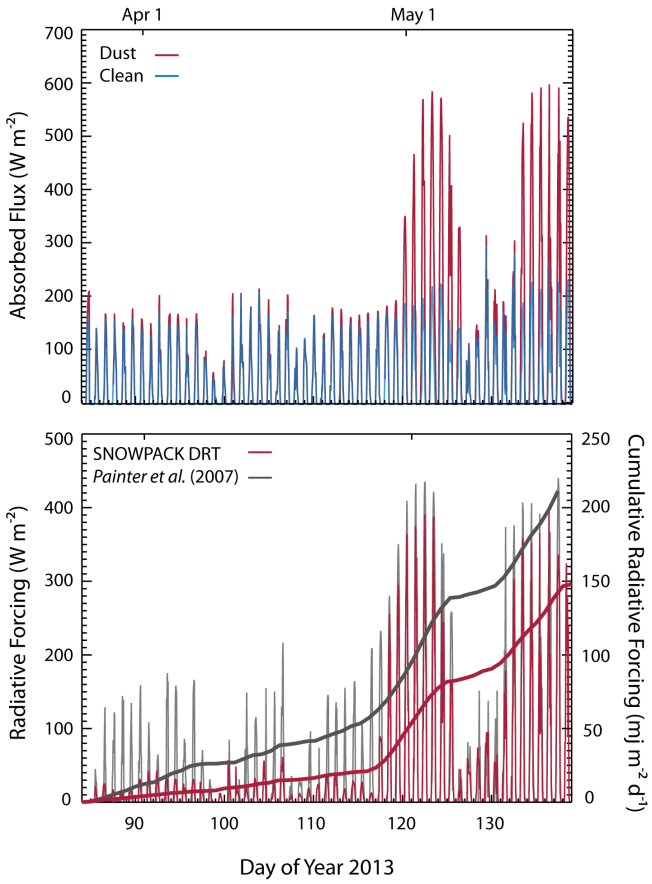

Figure 14 Absorbed shortwave radiations for dust and clean scenarios (top). Dust radiative forcing is plotted below, with radiative forcing calculated indirectly from changes in surface reflectance following *Painter et al.* [2007] (see Chapters 1,4). Due to the overestimation of albedo in the beginning of the simulation period, SNOWPACK DRT radiative forcing was lower than that estimated by *Painter et al.* [2007] method.

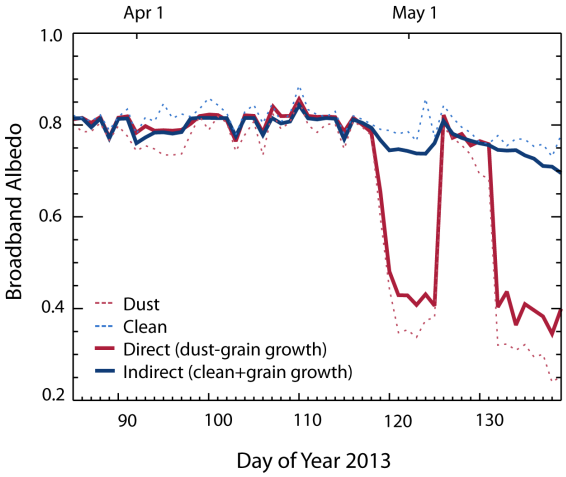

Figure 15 Broadband snow albedo for direct and indirect radiative forcing scenarios: the direct scenario, which represents the radiative forcing due only to absorption by dust, is simulated with smaller grain sizes from the clean scenario. The indirect scenario, which represents increased absorption due to dust influenced grain growth, is simulated with no dust but larger grains from the dust scenario. Simulations are completed with standalone SNICAR model runs from modeled snow properties.

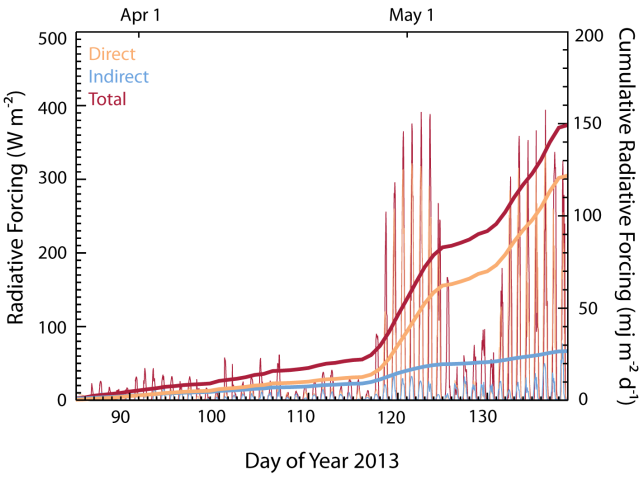

Figure 16 Modeled radiative forcing for direct/indirect radiative forcing scenarios. The partitioning between direct and indirect radiative forcing is ~80% and ~20%, respectively, over the simulation time frame.